Intermittency, Singularity & Reversibility on Log-lattices

Guillaume Costa

université PARIS-SACLAY

Intermittency, Singularity & Reversibility on Log-lattices

Intermittence, singularité et réversibilité sur grilles logarithmiques.

Thèse de doctorat de l'université Paris-Saclay

École doctorale n° 564, Physique Île-de-France (PIF)
Spécialité de doctorat: Physique
Graduate School : Physique. Référent : Faculté des sciences d'Orsay

Thèse préparée dans l'unité de recherche **SPEC (Université Paris-Saclay, CEA, CNRS)**, sous la direction de **Bérengère DUBRULLE**, directrice de recherche.

Thèse soutenue à Paris-Saclay, le 18 Juin 2024, par

Guillaume COSTA

Composition du jury

Membres du jury avec voix délibérative

Sergio CHIBBARO Professeur, Université Paris-Saclay	Président
Luca BIFERALE Professeur, Università degli Studi di Tor-Vergata & INFN	Rapporteur & Examinateur
Giorgio KRSTULOVIC Chercheur, HDR, CNRS, Université Côte d'Azur	Rapporteur & Examinateur
Isabelle GALLAGHER Professeur, École Normale-Supérieure	Examinatrice
Giovanni GALLAVOTTI Professeur émérite, Università La Sapienza	Examinateur

THESE DE DOCTORAT
NNT : 2024UPASP040

université PARIS-SACLAY

ÉCOLE DOCTORALE
Physique en Île-de-France (PIF)

Titre: Intermittence, singularité et réversibilité sur grilles logarithmique.
Mots clés: Turbulence, réversibilité, singularités, intermittence, grilles logarithmiques, simulations numériques.

Résumé: En 2019, Campolina & Mailybaev ont développé un nouveau cadre, les *grilles logarithmiques* permettant de réaliser des simulations à haute résolution grâce à l'utilisation de modes exponentiellement espacés dans l'espace de Fourier. Une telle construction rappelle les *shellmodels* bien connus. En utilisant ce nouveau cadre, cette thèse aborde le sujet de l'intermittence, des singularités et de la réversibilité dans les écoulements turbulents. Nous nous intéressons tout d'abord à la capacité du système à reproduire des caractéristiques intermittentes, telles que des bursts de dissipation d'énergie, observées dans des écoulements réels. Une explication possible de ce phénomène est l'existence de singularités complexes des champs de vitesses dont les parties imaginaires pilotent la dissipation. En atteignant l'axe réel (i.e une partie imaginaire nulle), elles génèrent un burst de dissipation et peuvent conduire à des scénarios de blowup. A travers l'étude de l'existence de blowups dans différents scénarios (écoulements hyper, hypovisqueux et classique), nous étudions l'existence de singularités complexes dans notre modèle. En introduisant la notion d'efficacité, nous montrons qu'il est possible d'observer des blowups visqueux dans le contexte des *équations de Navier-Stokes réversibles*, introduites pour la première fois par Gallavotti en 1996. En utilisant ces équations modifiées, nous étudions l'existence d'une solution faible dissipative. Enfin, nous étudions les propriétés statistiques des équations de Navier-Stokes réversibles mettant en évidence l'existence d'une transition de phase du second ordre et examinons la conjecture de Gallavotti concernant l'équivalence d'ensemble entre les équations de Navier-Stokes et leur homologue réversible.

Title: Intermittency, Singularity & Reversibility on Log-lattices.
Keywords: Turbulence, reversibility, singularities, intermittency, logarithmic grids, numerical simulations.

Abstract: In 2019, Campolina & Mailybaev developed a new framework, the *Log-lattices* allowing for simulations at high resolution through the use of exponentially spaced modes in the Fourier space. Such construction recalls the well known *shellmodels*. Using this new framework, this thesis tackles the subject of intermittency, singularities and reversibility in turbulent flows. We first focus on the ability of the system to reproduce intermittent features, such as bursts of energy dissipation, observed in real flows. A possible explanation to this phenomenon is the existence of complex singularities of the velocity fields which imaginary parts pilot the dissipation. By reaching the real axis (i.e a null imaginary part), they generate a burst of dissipation and can lead to blowup scenarios. Through the study of the existence of blowup in various scenarios (hyper, hypoviscous and classical flows) we investigate the existence of complex singularities in our model. Introducing the notion of efficiency, we then show that it is possible to observe viscous blowups in the context of the *Reversible Navier-Stokes equations*, first introduced by Gallavotti in 1996. Using these modified equations, we study the existence of weak dissipative solutions. Finally, we study the statistical properties of the Reversible Navier-Stokes equations highlighting the existence of a second order phase transition and investigate the Gallavotti's conjecture stating the equivalence of ensembles between Navier-Stokes equations and its reversible counterpart.

Contents

0 - Introduction

0.1 . Glossary

As every field if not every individual has his own symbols, this section sets notations and definitions of all the notions and quantities contained in this thesis.

$\boldsymbol{\rho}$ Density of the fluid.

$\boldsymbol{\nu}$ Viscosity of the fluid.

$\boldsymbol{u}$ Velocity field.

$\boldsymbol{\nabla}$ Differential operator nabla.

$\boldsymbol{i}$ Notation for complex numbers such that $\boldsymbol{i}^2 = -1$.

$\Re$ Real part of a complex number.

$\Im$ Imaginary part of a complex number.

E Kinetic energy.

Ω Enstrophy.

II Energy transfers between scales.

ϵ Energy dissipation.

$\mathcal{W}$ Work of a force.

Re Reynolds number of a flow.

$\mathcal{R}_\mathrm{r}$ "Reversible" Reynolds number defined for the Reversible Navier-Stokes equations.

$\mathcal{E}$ Efficiency, definied in the context of Reversible Navier-Stokes.

Nu Nusselts number.

Pr Prandlt number.

Ra Rayleigh number.

λ Spacing parameter of the grid in the Fourier space.

$\boldsymbol{k}$ Wavenumber associated to the Fourier transform.

$\|.\|_2$ Euclidean norm.

$*$ Convolution product.

S_p Structure functions of order p.

ξ_p Exponent of the structure functions of order p.

$\langle . \rangle$ Time average of a given quantity.

Var Variance of a given distribution.

σ Standard deviation of a given distribution.

PDF Probability Density Function.

DNS Direct Numerical Simulation.

0.2 . Context

The dynamics of simple fluids are described by the incompressible Navier-Stokes equations (1).

$$\partial_t \boldsymbol{u} + (\boldsymbol{u} \cdot \boldsymbol{\nabla})\boldsymbol{u} = -\boldsymbol{\nabla} p + \nu \boldsymbol{\Delta} \boldsymbol{u}, \quad (1)$$

$$\nabla \cdot \boldsymbol{u} = 0. \quad (2)$$

In the absence of viscosity, referred as ν, the system is time-reversible as it is invariant under the transformation $\mathcal{T} : t \to -t; \boldsymbol{u} \to -\boldsymbol{u}$. The addition of viscosity leads to energy dissipation through the term $\nu \Delta \boldsymbol{u}$. It follows that the equation is no longer invariant under the transformation $\mathcal{T}$. The dynamics of viscous fluids are then intrinsically irreversible, due to the presence of a constant viscosity ν that breaks the time reversal symmetry. Turbulent flows are then inherently *out of equilibrium* systems a rather new field of study. Therefore, they can not be accurately studied using most of the well known physics as it only applies to *equilibrium* systems.

To make up for that, Gallavotti (1) introduced a reversible version of the Navier-Stokes equations, called RNSE, that restores the time reversal symmetry $\mathcal{T} : t \to -t; \boldsymbol{u} \to -\boldsymbol{u}$, by conserving the total enstrophy through a time dependent viscosity $\nu_r(t)$. Thanks to the regained time-reversibility, one can then study this new equation using the tools of statistical mechanics. A point of great interest lies in the Gallavotti conjecture (1) stating that RNSE and NSE are statistically equivalent under specific conditions. Such conjecture holds a lot of importance as statistical properties of RNSE, found using our usual tools, could be transposed to NSE where these exact same tools can no longer be used. More specifically, this conjecture and the use of the RNSE could shed some light on a puzzling phenomenon known as *anomalous dissipation*. This phenomenon refers to the behavior of the energy dissipation ϵ of fluids in the limit of large Reynolds number. A simple glance at Eq. 1 points towards an energy dissipation ϵ proportional to the viscosity ν. Yet, such property only holds in the laminar regime (i.e moderate Reynolds number), while achieving the turbulent limit (i.e high Reynolds number) the dissipation reaches a plateau becoming independent of the viscosity. This scenario suggests a spontaneous breaking of the time-reversal symmetry that could be studied through the RNSE.

The existence of a dissipation in the turbulent limit is referred to as the Onsager's conjecture, stating that solutions of the inviscid Navier-Stokes equation that are irregular enough can dissipate energy even in the absence of viscosity (2). Unlike its viscous counterpart, the dissipative effect of singularities is thought to occur through bursts of dissipation, a phenomenon referred to as *intermittency*. Possible empirical characterization of this dissipative solution may be obtained through the multi-fractal theory (3). This

theory allows to measure the probability of apparition of a singularity with a given exponent, characterizing how the velocity gradients diverge in the inviscid limit. Results of experimental or numerical data (4; 5; 6; 7; 8) reveal a wide interval of possible exponents (Fig. 1, $C(h) = 3 - D(h)$, where $D(h)$ is the dimension of the fractal set in the multifractal theory), with highest probability near the Kolmogorov value $1/3$, and with values corresponding to dissipative ($h < 1/3$) or non-dissipative ($h > 1/3$) weak solutions of Euler equations.

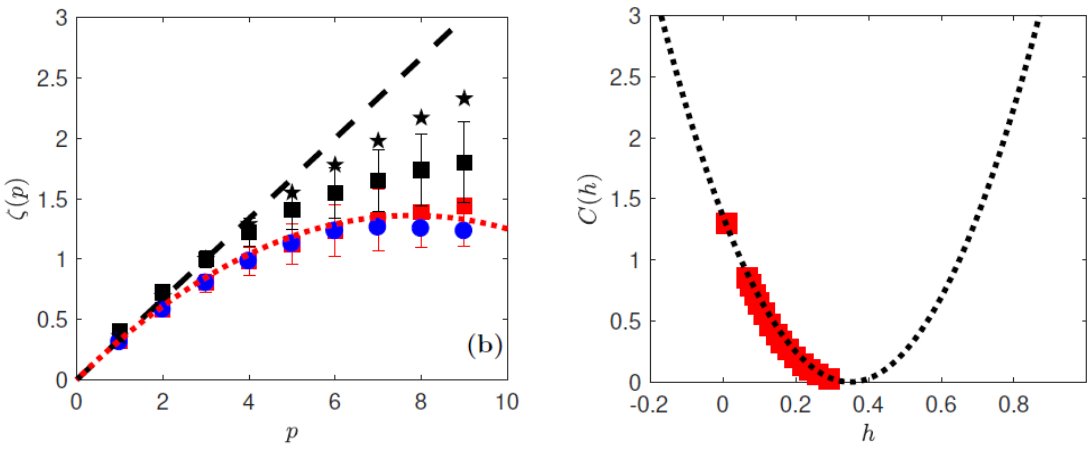

(a) (b)

Figure 1: **Deviation from KG41 and multifractal theory, results extracted from the PhD of Hugues Faller (9).** (1a) Exponents of the structures functions blue circles correspond to numerical simulations while red squares are associated to experimental data. Results are obtained on wavelet transforms for which $\zeta(3) \neq 1$. Hence black squares correspond to the rescaling $\zeta(p)/\zeta(3)$ of red squares. Black stars are rescaling of experimental results from (10). (1b) Multifractal spectrum of experimental data of Fig. 1a. $C(h)$ is obtained through an inverse Legendre transform of $\zeta(p)$ and corresponds to $3 - D(h)$, where $D(h)$ is the fractal dimension of the fractal set associated to h.

In 1981, Frisch and Morf (11) proposed a tracking method for complex singularities based on the fitting of the exponential decay of the energy spectrum. Through the study of a 1D non-linear Langevin system, they shed light on possible connections between intermittency and the collapse of complex singularities onto the real axis that generates bursts of dissipation. Despite their various manifestations, observing singularities remains a real challenge in both experiments and numerical simulations due to the necessity of reaching extremely high Reynolds number. Indeed, the complexity of DNS being roughly $\mathcal{O}(\mathrm{Re}^3)$, approaching the turbulent limit with DNS remains, for now, an impossible feat as $\mathrm{Re} \to \infty$. One must then discard the smaller scales by introducing a cut-off that impacts the dynamics of singularities (11). Hence, this tracking method was abandonned.

Nonetheless, *anomalous dissipation* and singularities are still subjects of active research as Onsager's conjecture was recently proved by Buckmeister (12), who constructed weak solutions of inviscid NSE that were able to dissipate a finite amount of energy. The exact link between real solutions of the NSE and this construction remains unclear.

In this thesis, we propose to perform simulations using *Log-lattices*, a new framework developped by Campolina & Mailybaev (13). Its exponential spacing of modes, in the Fourier space, allows for high resolution simulations at the cost of reducing the number of interactions between modes. Such construction recalls the *shellmodels* (GOY (14), SABRA (15), Desnyansky-Novikov (16)), a class of 1D models that also use an exponential spacing of modes in the Fourier space. Shellmodels were extensively studied (15; 17; 18; 19) [1] as they make up for the lack of resolution of DNS. Yet, due to the absence of some fundamental symmetries and their inherent 1D nature, they fail at reproducing some features of the NSE (such as intermittency in the dyadic model). This is where Log-lattices come into play as it allows for n-D simulations, with formal equivalence to the usual shellmodels for $n = 1$, while conserving most of the symmetries of the NSE. These features allow us to study properties yet out of reach of current DNS, such as the development of complex singularities through the previously mentioned Frisch and Morf method but also to extend various studies about the RNS e.g the existence of a phase transition in the conserved energy case (20) or the Gallavotti conjecture (1).

0.3 . Brief overview of the chapters

The first chapter introduces the logarithmic lattices (LL) and their constructions along with several important quantities. In addition, it briefly presents the algorithm used to solve the Navier-Stokes equation and its reversible counterpart.

The second chapter focuses on the tracking of complex singularities on LL through a numerical method called "Singularity strip", introduced by Frisch and Morf (11). The first part of the chapter tackles the form of the dissipation domain as shellmodels usually exhibit a stretched exponential decay. We show that LL exhibits no stretching making possible the tracking of complex singularities. More specifically, it develops the link between singularities and blowup in different scenarios (1D Burgers, Euler, 3D NSE...).

Frisch and Morf established connection between the presence of complex singularities and the development of intermittent features. Building on the results of Chapter 2, we investigate in this third chapter for hints of intermittency, an essential component of turbulence, on LL as it had not been clarified by C.Campolina & A.Mailybaev.

As previously highlighted in previous chapters, the presence of complex singularities affects the dissipation of energy in the system and could explain the *anomalous dissipation*. In this fourth chapter, we investigate the conjecture stated by Onsager in 1949. Using a modified version of the NSE called "Reversible Navier-Stokes equations" (RNSE) that restores the time-reversibility of the NSE through a time dependent viscosity. In particular, we emphasize the existence of two phases in RNSE: an unstable one where we build blowup solutions, at constant energy, for forced systems leading to possible weak-solutions upon regularization and a stable NS-like phase.

The fifth chapter connects the notion of singularity to the existence of the two phase found in Chapter 4, highlighting the presence of two attractors with behaviors that ressemble those of phase transitions.

The sixth chapter investigates the properties of RNSE, confirming the presence of a phase transition expected from the results of Chapter 5 but also previously observed in

[1] To only name a few.

small DNS. In particular, we study the effects of resolution on the transition highlighting a convergence to a mean field Landau second order phase transition in the infinite resolution limit.

In 1996, G.Gallavotti introduced the RNSE, albeit with conserved enstrophy. He conjectured a statistical equivalence, under some hypothesis, between the irreversible system and its reversible counterpart. This equivalence is particularly interesting as the reversible system allows for the use of the tools of statistical mechanics. Chapter 7 focuses on the validity of the conjectures for different conserved quantities, using LL to build on previously obtained DNS results.

Finally, the last chapter contains all my - submitted or published - contributions that are unrelated to the topic of this PhD, albeit for them being numerical simulations on LL.

1 - Numerical details

1.1 . Log-lattices

1.1.1 . Introduction

With the rapid development of computers, performing simulations has become a fundamental tools for physicists in order to tackle subjects yet beyond reach of experiments. Still, the most traditionnal and straight forward way of performing simulations is rather costly. Indeed, Direct Numerical Simulations (DNS) of a simple flow has a complexity of the order $\mathcal{O}(\mathrm{Re}^3)$ making tedious the task of simulating small scales.

To overcome the resolution limitations of DNS, Campolina & Mailybaev (13) proposed a new framework in which the Fourier space is discretized following a geometric progression $k_n = k_0\lambda^n$. Such construction is reminiscent of the discretization of shell-models (16; 14; 15) allowing for high resolution simulations using a limited number of modes. Note that in 1D, Log-lattices are formally equivalent to well known shell models, depending on the considered value of λ. Their main improvement lies in the extension of such shellmodels to higher dimensions. Therefore, it allows for high resolutions simulations of 3D flows while conserving almost all of the system's symmetries.

1.1.2 . Definitions

Log-lattices (LL) are discretized logarithmic grids, composed of exponentially spaced modes:

$$k = k_0\lambda^n,$$

where λ is the log-lattice spacing parameter. This construction is detailed in Campolina & Mailybaev (21; 22). We start by taking the Fourier transform of Eq. 1, to get the NS equations in spectral space:

$$\partial_t\hat{u}_i + \boldsymbol{i}k_j\hat{u}_j * \hat{u}_i = -\boldsymbol{i}k_i\hat{p} - \nu k_j k_j\hat{u}_i + \hat{f}_i, \tag{1.1}$$

where Einstein summation over repeated indices is used, $\boldsymbol{i}$ is the square root of -1, k_i is the i^{th} component of the wavenumber $\mathbf{k} = (m,n,q)\mathbf{k}_0$, $\hat{g}$ is the Fourier transform of g, and $*$ is the convolution product which couples modes in triadic interactions such that $\boldsymbol{k} = \boldsymbol{p} + \boldsymbol{q}$.

We then project this equation onto the log-lattice. For this, we consider from now on that the velocity modes $\hat{u}_i$ only depend on the wavevectors on the log-lattice. This projection is then valid provided that the convolution operator is "well-defined", i.e. that it respects the symmetries of a convolution operator and has a nonempty set of triadic interactions. We thus require that

$$\lambda^m = \lambda^n + \lambda^q, \text{(m,n,q)} \in \mathbb{Z}^3 \tag{1.2}$$

admits solutions, which restricts the values of λ to three families of solutions, each having z interactions in D dimensions:

- $\lambda = 2$ ($z = 3^D$).
- $\lambda = \sigma \approx 1.325$, the plastic number ($z = 12^D$).

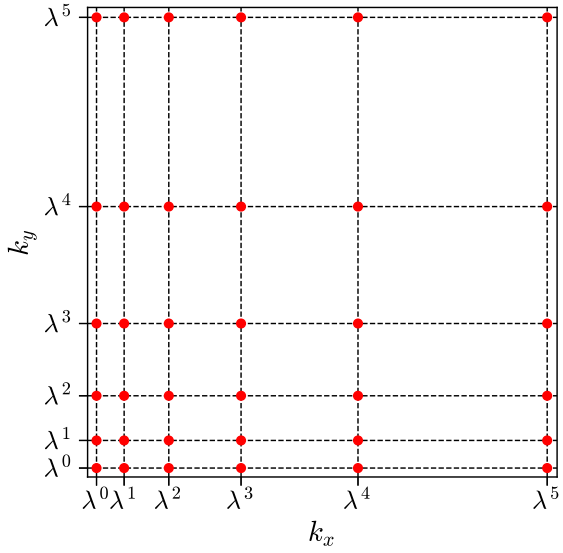

Figure 1.1: Example of 2D log-lattice with spacing parameter λ.

- λ such that $1 = \lambda^b - \lambda^a$ for some integers $0 < a < b$. $(a, b) \neq (1, 3), (4, 5)$ with $\gcd(a, b) = 1$ ($z = 6^D$).

Note that for the lowest possible values of a and b, which is $(1, 2)$, λ is the golden number ($\phi \approx 1.618$). The 2D geometry of such a lattice is shown in Fig. 1.1.

Besides the convolution product, log-lattices are also endowed with a scalar product given by:

$$(f, g) = \Re\left(\sum_{\boldsymbol{k}} f(\boldsymbol{k})\overline{g(\boldsymbol{k})}\right). \tag{1.3}$$

1.1.3 . Quantities of interest

Throughout our study, we can compute two large scale quantities of interest:

- The energy spectrum $E(k,t) = \dfrac{1}{(\lambda-1)kN_k} \displaystyle\sum_{k\leq|\boldsymbol{k'}|<\lambda k} \left\|\hat{\boldsymbol{u}}(\boldsymbol{k'},t)\right\|_2^2$, where N_k is the number of points in the shell of radius k (proportional to $\log^{D-1}(k)$).
- The total enstrophy $\Omega(t) = \displaystyle\sum_k k^2 E(k,t)$.

We also compute the mean energy transfer at scale k through:

$$\Pi(k) = \langle -2\Im(\boldsymbol{u}, \boldsymbol{k}\cdot\boldsymbol{u} * \boldsymbol{u})\rangle\,, \tag{1.4}$$

where $\|\mathbf{k}\|_2 = k$ and $\langle\cdot\rangle$ refers to temporal averages over shells of radius k.

To study intermittency we propose to use an ansatz of the structure functions, using the following convention:

$$S_p(k) = \langle\|\hat{\boldsymbol{u}}(\boldsymbol{k},t)\|_2^p\rangle\,. \tag{1.5}$$

Note that the structure functions are also commonly defined, in shell models, as

$$S_p(k_n) = \left\langle \left|\frac{\Pi_n}{k_n}\right|^{p/3}\right\rangle. \tag{1.6}$$

1.2 . Numerical implementation: viscous splitting

In our study, we propose to first solve the inviscid Navier-Stokes equation (1.7). Using an implicit 4th order Runge-Kutta solver with adaptative time-steps we obtain the inviscid velocity field $u_0(\boldsymbol{k}, t+dt)$.

$$\partial_t \hat{u}_i = P_{ij}\left(-\boldsymbol{i}k_q\hat{u}_q * \hat{u}_j + \hat{f}_j\right), \tag{1.7}$$

where $P_{ij} = \delta_{ij} - \frac{k_i k_j}{k^2}$ accounts for the pressure term under zero divergence hypothesis.

The viscosity ν is then taken into account using a method similar to viscous splitting, where the velocity field is divided by a viscous contribution such that:

$$\boldsymbol{u}(\boldsymbol{k_n}, t+dt) = \boldsymbol{u}(\boldsymbol{k_n}, t+dt)_{\nu=0} e^{-\nu dt \|\boldsymbol{k_n}\|_2^2}. \tag{1.8}$$

This method allows for bigger time steps as it frees the solver from too small values of the velocity fields. Note that, in the context of the Reversible Navier-Stokes equation (RNS), the viscosity depends on time and therefore is no longer a constant. In such case, one could wonder if this method gives proper results in the case of time dependent viscosity $\nu_r(t)$.

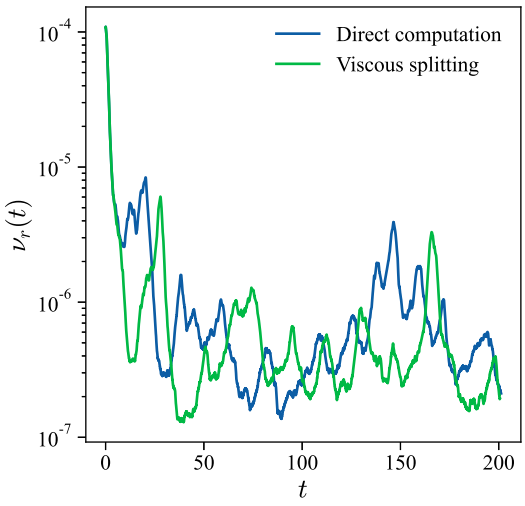

Figure 1.2: **Evolution of the reversible viscosity ν_r at each step.** Both simulations are performed for $\lambda = \phi \approx 1.618$, $N = 12^3$, $f_0 = 0.27$. The green curve is obtained using the viscous splitting method while the blue curve is obtained by directly solving the RNS equation, where the reversible viscosity is computed in order to conserve the total kinetic energy.

Both methods lead to similar behavior of the viscosity (Fig. 1.2), with mean values $\nu_{r,\text{Splitting}} \approx 4.9 \cdot 10^{-7}$ and $\nu_{r,\text{Direct}} \approx 6.4 \cdot 10^{-7}$. It is expected to find a slight difference as the number of time step is still relatively small. Moreover, the direct computation is performed using the analytical expression of the reversible viscosity and therefore leads to deviation from E_0.

Still, both methods give similar results (Fig. 1.2). However, the "viscous splitting" method allows us to “perfectly” (with floating-point accuracy) conserve a chosen quantity (here the total kinetic energy) without deviation. In the sequel, we thus adopt this method in all our simulations.

We are now equipped with a new framework, allowing for precise, high resolutions simulations that conserves all the flavors of the Navier-Stokes equations allowing us to investigate properties yet out of reach of DNS such as the development of blowups and their link to complex singularities.

1.3 . Initial conditions and forcing

In all our simulations the following initial conditions, adapted from (20) to LL, are used:

$$\begin{aligned} \hat{u}_x(\mathbf{k}) &= U(\boldsymbol{k}), \\ \hat{u}_y(\mathbf{k}) &= -\hat{u}_x(\boldsymbol{k})\frac{k_x}{k_y}, \\ \hat{u}_z(\mathbf{k}) &= 0, \end{aligned} \tag{1.9}$$

where U is an initial field, with initial energy centered on the large scales.

When necessary, a forcing term is added such that $\boldsymbol{f}$ is a constant field of norm f_0, symmetric by time-reversal, with non-zero contributions for $\boldsymbol{k}$ such that $15 < \|\boldsymbol{k}\|_2 < 16$:

$$\begin{aligned} \hat{f}_x(\mathbf{k}) &= f_0 \text{ if } 15 < \|\boldsymbol{k}\|_2 < 16 \text{ else } 0, \\ \hat{f}_y(\mathbf{k}) &= f_0 \text{ if } 15 < \|\boldsymbol{k}\|_2 < 16 \text{ else } 0, \\ \hat{f}_z(\mathbf{k}) &= 0. \end{aligned} \tag{1.10}$$

Unless written otherwise, simulations are performed using $\lambda = \phi$.

2 - Singularity and blowups

2.1 . Motivations

In 1981, Frisch and Morf (11) postulated the existence of complex singularities in solutions of Navier-Stokes equations. Using a simple one-dimensional non-linear Langevin system, they demonstrated that the dynamics of such complex singularities could be directly connected to intermittency as dissipation bursts (such as in Fig. 3.10b) occur whenever a complex singularity approaches the real axis.

Following this, the scenario was further explored in the one-dimensional Burgers equation – a 1D surrogate of the Navier-Stokes equation. Where it was discovered that real singularities can be observed in the inviscid limit and manifest as shocks, i.e. finite jumps in the velocity which dissipates energy in agreement with the dissipation anomaly (23).

Extending these results to 3D represents a real challenge. In 3D Euler singularities emerge as blow-ups, believed to occur in finite time, of vorticity. Adding a viscosity ν acts as a repellent, prohibiting the collapse of singularities onto the real axis and preventing the infinite growth of vorticity. Consequently, observing singularities requires high Reynolds numbers (i.e low viscosities) implying simulations at high numerical resolutions as truncation could affect the dynamics of singularities (11). Yet, the computational power needed for such DNS is currently beyond reach, hindering further progress on the matter. This is where *Log-lattices* come into play. Their moderate numerical cost, allowing for simulations which resolutions far exceed those of the current DNS, coupled with the singularity strip method opens new perspectives on these issues.

This chapter consists of two parts. First, we show that the dissipation in Log-lattices is well described by an exponential and unlike shell models, presents no stretching. We then move on to an article, currently in review in *Non-linearity* (24) dealing with the development of complex singularities in various scenarios.

This article is a collaborative work with other fellow PhD students of the group and the founders of log-lattices, namely C.Campolina & A.Mailybaev.

2.2 . Energy dissipation on Log-lattices

The tracking of the position of a complex singularity, through the *analiticity strip method* is based on the fitting of the exponential decay $e^{-\delta k}$ of the turbulent energy spectrum. Where δ is the singularity's y-coordinate, in the complex plane. The physical meaning of δ and therefore the success of the extraction is bound to an *exact* exponential dissipation. Yet, it has been shown that shellmodels actually exhibit a stretched exponential dissipation $e^{(\delta k)^x}$, where x is the stretching exponent. More specifically, L'vov et.al (15) found that $x \approx 0.69$ in the SABRA shellmodel (i.e the formal 1D equivalent of LL with $\lambda = \phi$). We then propose to address the form of the dissipative range in the context of Log-lattices, focusing on the case $\lambda = \phi$

For more informations about Log-lattices and numerical details, please refer to Chapter. 1.

2.2.1 . Dissipative range on Log-lattices

As previously mentioned, it has been shown (15) that the SABRA shell model behaves as a stretched exponential in the dissipative range such that

$$u_n \propto e^{-(k_n/k_\eta)^x}, \text{where } x = \log_\lambda \phi \approx 0.69. \tag{2.1}$$

This exponent was extracted by fitting $\log(-\log E_k)$ in the dissipative range.

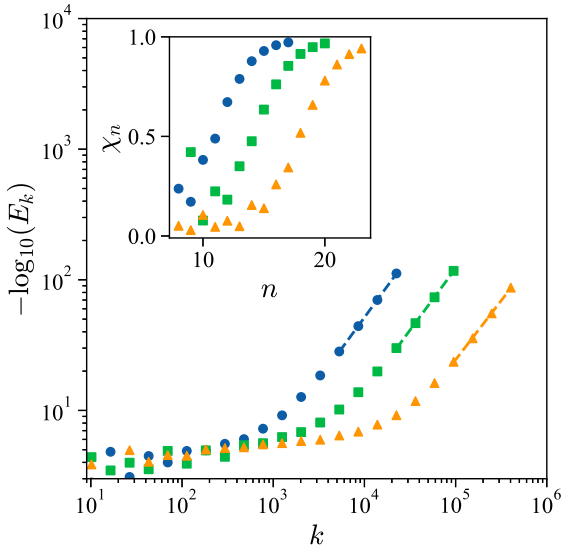

Figure 2.1: **Fitting of the stretching exponent x** for a 1D Log-lattice with $\lambda = \phi$. Simulations are performed using $\nu = 1e-05, 1e-06, 1e-07$. The colored dashed lines correspond to the fitting over the last few populated modes of each simulation. The inset shows the value of the local stretching exponent χ_n as a function of the shell number n highlighting a convergence towards $x = 1$.

According to this formula, one should then recover for $\lambda = \phi$ (i.e LL parameters) an exponential dissipation without stretching as $x = \log_\phi \phi = 1$. This property is extremely interesting as it allows for the use of the *analyticity strip* (25), a method of Frisch & Morf, that relies on the fitting of the energy spectrum in the dissipative range to extract the position of a singularity in the complex plane.

Similarly to (15), we perform 1D simulations, on LL, for various viscosities. The stretching exponent x is then extracted by fitting over the last few - populated - modes obtaining $x \approx 1$. Following (26), we introduce a local stretching exponent χ_n such that:

$$\chi_n = \log_\phi |\ln \langle |u_{n+1}|^2 \rangle| - \log_\phi |\ln \langle |u_n|^2 \rangle|. \tag{2.2}$$

Assuming that $u_n \sim e^{-(k_n/k_\eta)^x}$ in the dissipative range, one obtains $\chi_n \xrightarrow[n\to\infty]{} x$.

Figure 2.1 gathers the results for three different viscosities, highlighting slopes, in the dissipative range, close to 1 for $-\log_{10}(E_k)$. In addition, the local stretching exponent converges to $x \approx 1$ in all simulations confirming the prediction of Eq. 2.1 albeit for $\lambda = \phi$. The smaller value of χ_n observed for $\nu = 5e-07$ (blue circles) is associated to statistical errors due to an unsufficient time resolution.

The absence of exponential stretching allows for proper fitting of the dissipative range. Still, the numerical accuracy in such domain has to be taken into account as LL exhibits energy spectra with energy of the order of 10^{-256} in the last shell.

2.2.2 . Effect of the tolerance on the dissipative range

While performing numerical simulations, one must be careful to fulfill the Courant Friedrichs Lewy (CFL) conditions (27) as to ensure the correctness of the computation. However, due to the large achievable resolutions on Log-lattices, CFL conditions become almost impossible to fulfill after a certain threshold k_{CFL}.

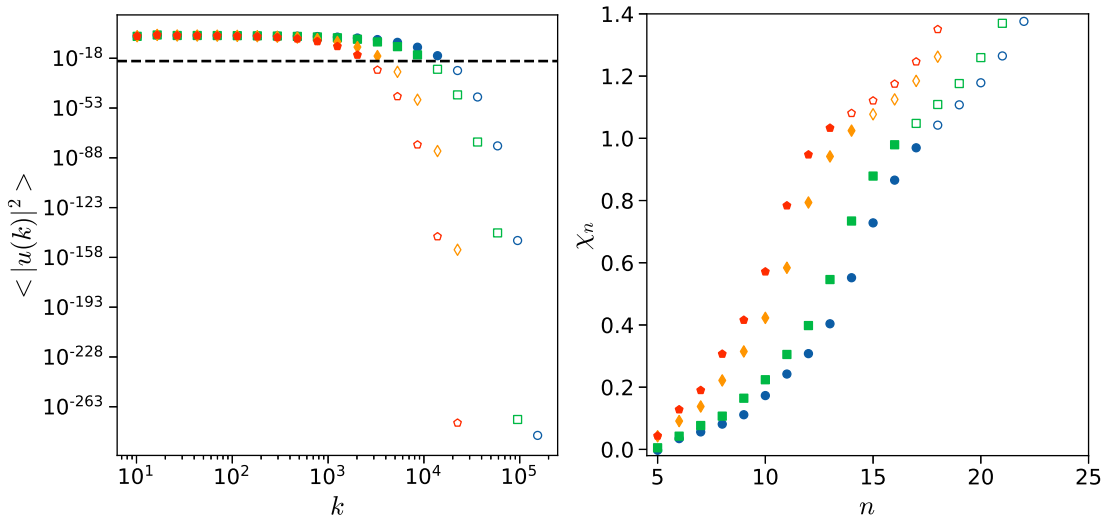

(a) (b)

Figure 2.2: **Effect of the tolerance on the dissipative range for 3D simulations.** (2.2a) Time average of the energy in each shell, the black dashed line corresponds to $a_{tol}^2 = 1e-20$. (2.2b) Local stretching exponents. Simulations are performed using various viscosities $\nu = 1e-05, 5e-06, 1e-06, 5e-07$. Empty symbols are associated to under-resolved modes.

One can then wonder what are the effects of the tolerance on the results ? Well, fortunately enough, the inertial range always lies in the *well-resolved* region provided that the

tolerance is set to usual values of the order $a_{tol} = 1e-06$. Still, modes in the dissipative range can exhibit energy of the order of $1e-256$. Therefore, it is unclear if whether or not the smallest scales are *well-resolved*.

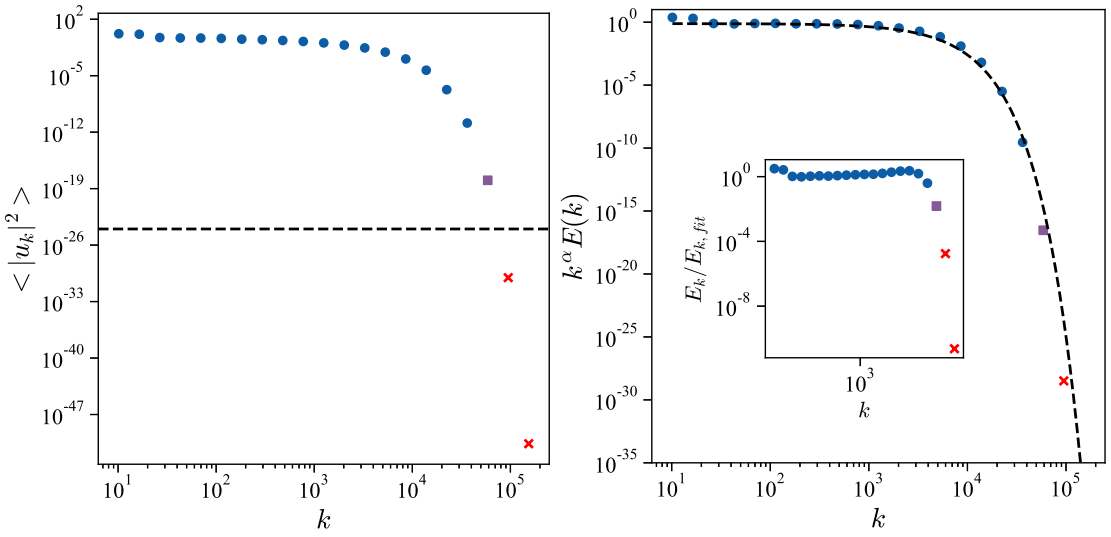

(a) (b)

Figure 2.3: **Fitting procedure for the energy spectrum applied to a 3D simulation.** The simulation is performed using $\lambda = \phi$, $N = 22^3$ and $\nu = 1e-07$. (2.3a) Time average of the energy in each shell, the black dashed line corresponds to $a_{tol}^2 = 1e-24$. The red crosses correspond to highly under resolved shells while the purple squares correspond to shells in which the energy of individual modes is close to a_{tol}^2. (2.3b) Fitting of the compensated energy spectrum. The fitting is only performed on the blue circles. The inset presents the ratio of the energy spectrum over the fitted spectrum, highlighting a good matching for the blue circles.

To illustrate this point, we perform 3D simulations on LL with $\lambda = \phi$ for $\nu = 1e-05, 5e-06, 1e-06, 5e-07$. The number of mode is set to $N = 30^3$ [1], reaching a resolution $k_{max} \approx 7 \times 10^6$. The solver tolerance is set to $a_{tol} = 1e-10$. Figure 2.2a shows the total energy of each shell [2] highlighting that the last five shells of every simulations are *under-resolved* according to CFL conditions. The local stretching exponents χ_n first increase up to $\chi_n \approx 1$ before observing a change of slope for the five last extracted values. This change of slope appears more clearly for the high viscosity cases as the steady state is well established. It is striking to notice that the change of slope, associated to an hyper-dissipative scheme ($\chi_n > 1$) appears for *under-resolved shells* (i.e empty symbols). This results suggest that, upon setting a low enough value for the tolerance, one can accurately fit, up to roughly $\left\langle \|\boldsymbol{u}(\boldsymbol{k})\|_2^2 \right\rangle \approx a_{tol}^2$, the dissipative range with exponent $\chi_n = 1$ corresponding to the usual, physical, dissipation. Figure 2.3 presents the fitting procedure of an energy spectrum, the expected shape is the following $E(k) = Ck^{-\alpha}e^{-k/k_\eta}$. The exponent α is first extracted in

[1] We denote N^D the number of modes, meaning that each direction has N modes.

[2] Note that the energy in a n-D shell is a sum of the contribution of every $\boldsymbol{k}$ such that $k' \leq \|k\|_2 < \lambda k'$. Therefore, the actual contribution of a single model is way below the total shell energy.

the inertial range such that $\alpha \approx 1.7$, close to the usually observed $\alpha_{DNS} = 1.72$. We then fit the dissipative range of the compensated energy spectra $Ck^{\alpha}E(k)$ to extract $k_{\eta} \approx 1750$. Note that, according to our previous explanation, the fitting procedure is only performed over *well-resolved modes*. Therefore, red crosses, lying way below a_{tol}^2 and purple square are not taken into account. The reason for discarding the purple square is that, for n-D simulations (with $n > 1$) each point of the energy spectra is a sum of many contributions, whose individual values are close to a_{tol}^2. Yet, we show that for all other points the fitting procedure gives acceptable results.

2.2.3 . Hyperviscous and hypoviscous cases

In previous sections, we performed simulations of the usual Navier-Stokes equations 1 characterized by a dissipative term $\nu\boldsymbol{\Delta u}$. In such case, energy spectra are accurately described - for *well-resolved modes* - by $E(k) = Ck^{-\alpha}e^{-k/k_{\eta}}$.

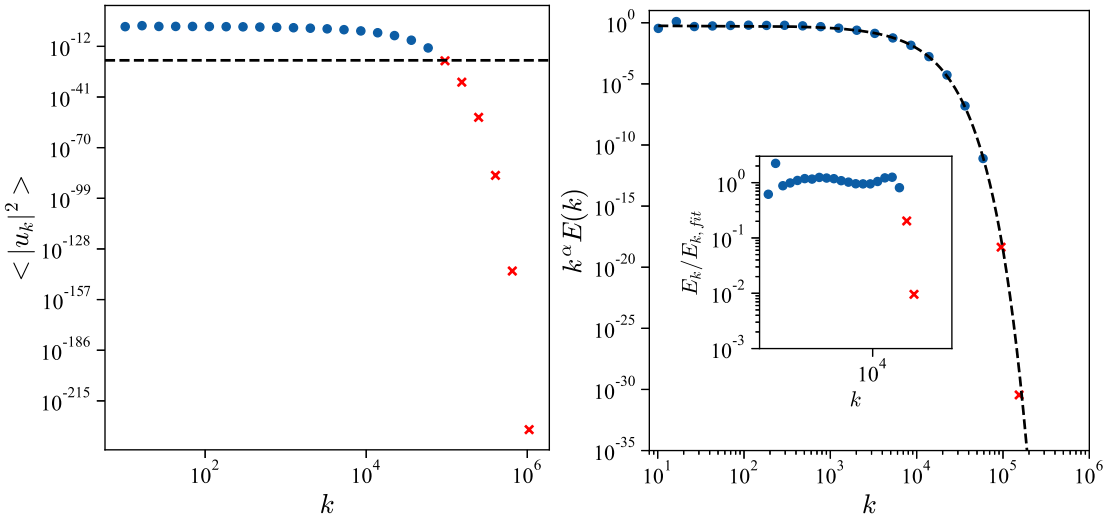

(a) (b)

Figure 2.4: **Fitting procedure for the energy spectrum applied to a 3D hypoviscous simulation.** The simulation is performed using $\lambda = \phi$, $N = 30^3$, $\nu = 1e-05$ and $\gamma = 0.7$. (2.4a) Time average of the energy in each shell, the black dashed line correspond to $a_{tol}^2 = 1e-20$. The red crosses correspond to highly under resolved modes. (2.4b) Fitting of the compensated energy spectrum. The fitting is only performed on the blue circles. The inset presents the ratio of the energy spectrum over the fitted spectrum, highlighting a good matching for the blue circles.

Yet, it is possible to slightly change the dissipative mechanism by introducing an exponent γ such that the equation now reads:

$$\partial_t \boldsymbol{u} + (\boldsymbol{u}\cdot\boldsymbol{\nabla})\boldsymbol{u} = -\boldsymbol{\nabla}p + \nu\boldsymbol{\Delta}^{\gamma}\boldsymbol{u}, \quad (2.3)$$

$$\nabla\cdot\boldsymbol{u} = 0, \quad (2.4)$$

Simulations at $\gamma > 1$ (resp. $\gamma < 1$) are called hyperviscous (resp. hypoviscous). By varying γ one can explore properties associated to the dissipative process such as the development of singularites (24). In addition, hyperviscosity is often used to increase the size of

the inertial range at fixed resolution as it allows for lower values of viscosity. It is therefore interesting to see if the energy spectrum conserves the same shape and how our fitting algorithm performs. Figure 2.4 presents the results of the fitting procedure applied to an hypoviscous case with $\gamma = 0.7$. The energy spectrum is accuretaly described by the usual Kolmogorov spectrum albeit for a steeper slope $\alpha_{\gamma=0.7} = 1.77$ in the inertial range.

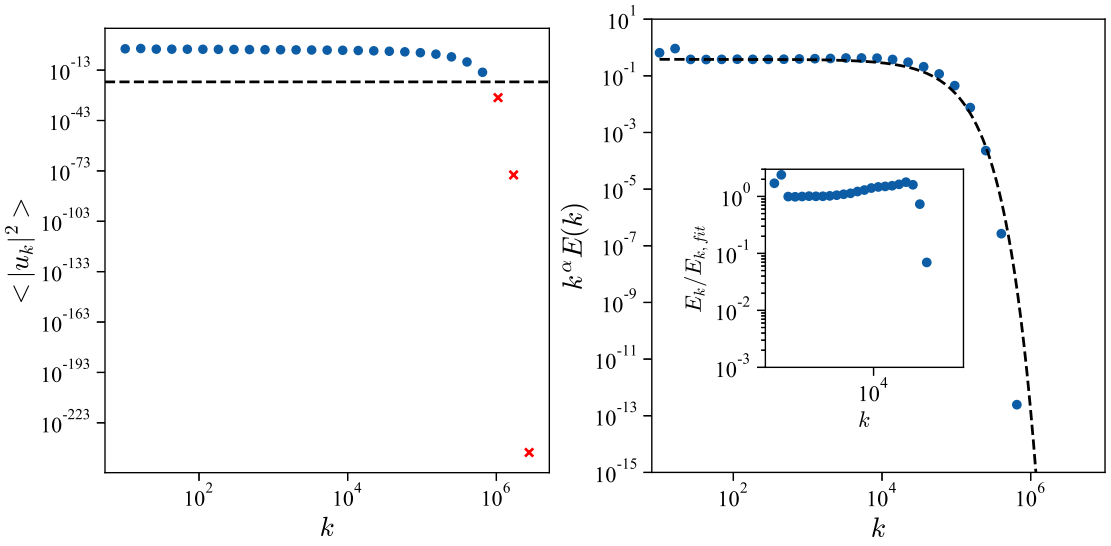

(a) (b)

Figure 2.5: **Fitting procedure for the energy spectrum applied to a 3D hyperviscous simulation.** The simulation is performed using $\lambda = \phi$, $N = 30^3$, $\nu = 1e-14$ and $\gamma = 1.5$. (2.5a) Time average of the energy in each shell, the black dashed line corresponds to $a_{tol}^2 = 1e-20$. The red crosses correspond to highly under resolved modes. (2.5b) Fitting of the compensated energy spectrum. The fitting is only performed on the blue circles. The inset presents the ratio of the energy spectrum over the fitted spectrum, highlighting bottleneck effects.

By performing hyperviscous simulations, one achieves at fixed ν a greater inertial range that can then be used for various purposes. Yet, the question remains: does hyperviscosity impact the form of the dissipation ? Figure. 2.5 shows a fitting less accurate than the other cases. The recovered slope $\alpha = 1.64$ is close to the usual Kolmogorov slope $-5/3$. Yet, it appears in the inset that the energy spectrum becomes less steep around the Kolmogorov scale k_η. This small effect is associated to a small bottleneck, known to be aggravated by hyperviscosity (28). In order to overcome this problem one must then be careful as to properly set the fitting range for the dissipative part.

Although the fitting procedure gives acceptable results in both hypoviscous and hyperviscous simulations, the latter exhibit small bottleneck effects. Such bottleneck, if aggravated by the hyperviscous factor γ could already be present in traditional simulations (i.e $\gamma = 1$).

2.2.4 . Bottleneck effect in Log-lattices

The previous section highlighted the existence of small bottleneck effects on Log-lattices, aggravated by hyperviscosity. Still, these effects can also be seen in traditionnal simulations with $\gamma = 1$. Indeed, in the transition range between the inertial and dissipative domains, one observes an excess of energy slightly above the fitted spectrum. Yet, this fitted spectrum exhibits good behavior outside of this transition range.

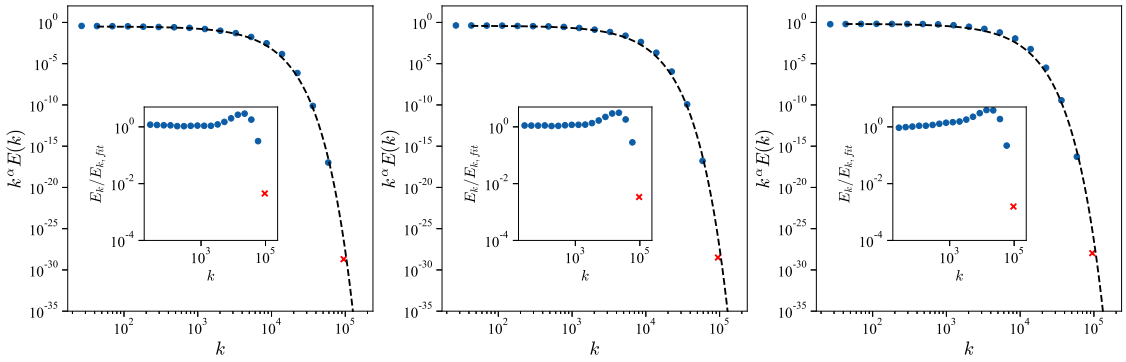

(a) (b) (c)

Figure 2.6: **Fitting procedure for the energy spectrum applied to a 3D simulation.** The simulation is performed using $N = 22^3$, $\nu = 1e-07$ and $a_{tol} = 1e-12$. The fitting protocol is applied using a fixed exponent α in the inertial domain. (2.6a) $\alpha = 1.52$. (2.6b) $\alpha = 1.56$. (2.6c) $\alpha = 5/3$. A lower value of α makes up for the excess of energy in the transition range with a small impact on k_η, varying between 1600 and 1650.

This is especially true for simulations presenting short inertial domains, of length of the order of a decade. In such cases, energy spectra seem to exhibit an excess of energy in the transition range that impedes a complete fitting of the energy spectrum. Fig. 2.6 presents the results of the fitting protocol with fixed exponent α in the inertial range highlighting that smaller α leads to a better fitting of the transition area with little impact on the value of k_η. Setting a lower value of α accounts for more energy in the transition range, hence highlighting the bottleneck. Nonetheless, the bottleneck effect being associated to a too small inertial domain and k_η being only slightly impacted, the usual fitting protocol should be applied as to ensure a correct physical interpretation of the results.

It is to be noted that, for simulations with small inertial domain, extracting the α exponent using a purely linear fitting is imprecise as the exponential dissipation can not be overlooked. Indeed, for the simulations of Fig. 2.6, a direct linear fitting of the inertial range of the fitted spectrum, with imposed slope α, gives a slope $\beta = \alpha - 0.1$. This steeper slopes takes into account the effect of the viscosity in the inertial range that should vanish as ν decreases. In such context, setting a smaller value for α could improve the fitting quality.

2.2.5 . Energy dissipation in the $\lambda = 2$ case

In the previous sections, we focused on the $\lambda = \phi$ case which 1D equivalent is a SABRA shell model. Yet, unlike classical shell models, the statistical model in LL changes upon the choice of the grid parameter λ. Upon choosing $\lambda = 2$, one can perform even quicker simulations, due to fewer interactions. Indeed, the 1D equivalent of this system is the

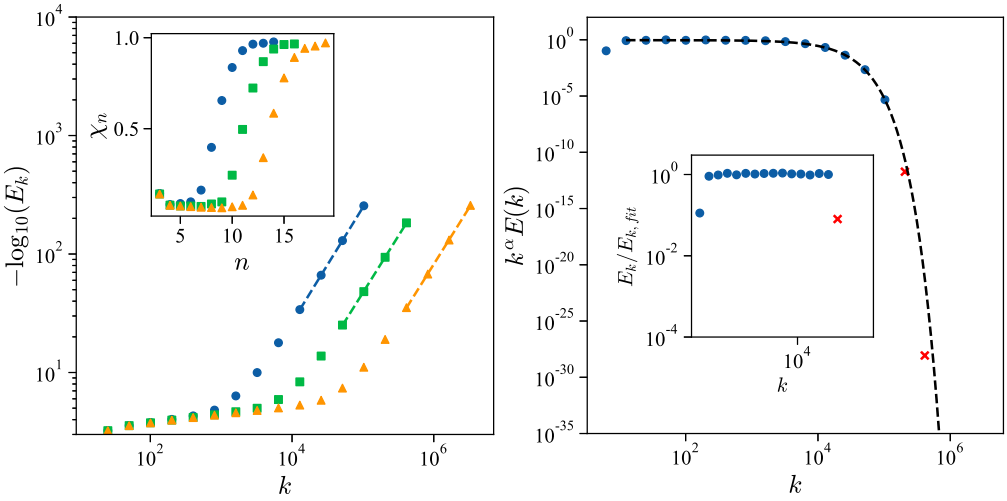

Figure 2.7: **Dissipative range in 1D & 3D** for Log-lattices with $\lambda = 2$. (2.7a) 1D simulations performed using $\nu = 1e-05, 1e-06, 1e-07$. The colored dashed lines correspond to the fitting over the last few populated modes of each simulation. The inset shows the value of the local stretching exponent χ_n as a function of the shell number n higlighting a convergence towards $x = 1$. (2.7b) Fitting procedure applied to a 3D energy spectrum. The black dashed line correspond to the fitted spectrum. The inset presents the ratio of the energy spectrum over the proposed fitting highlighting a ratio of 1 for all the *well-resolved shells*. The *under-resolved shells* are represented with a red cross.

Desnyansky-Novikov model (16), considering only nearest neighbour interactions. As for the Log-lattices with $\lambda = \phi$, the dissipative range is well described by a pure exponential decay $u_n \propto e^{k_n/k_\eta}$ for *well-resolved shells* for both 1D (Fig. 2.7a) and 3D (Fig. 2.7b). Note that the tolerance has the same effects on the simulations as red crosses (Fig. 2.7b) lie below the exponential fitting implying an excessive dissipation.

2.2.6 . Conclusion

In this section, we have performed 1D and 3D simulations of the Navier-Stokes equations on Log-lattices, mainly using a spacing parameter $\lambda = \phi$. For such parameter, the 1D Log-lattice is equivalent to the SABRA shellmodel and exhibits an exponential dissipation with no stretching as $x = \log_\phi \phi = 1$ regardless of the γ factor in the dissipative term.

This result is interesting as it allows for the use of the analyticity strip method on Log-lattices. Such method, previously performed on DNS was quickly abandonned due to the lack of resolution in the dissipative range. Yet, one must be careful as to set a proper value for the solver tolerance and refrain himself from fitting the exponential dissipation below this threshold as such scales might not be well resolved. Furthermore, this fitting procedure appears also as a great tool for the extraction of structure function's exponents, as it permits a complete fitting of energy spectra and thus an increase in precision. These results also stand for LL with $\lambda = 2$.

In addition, we showed the existence of slight bottleneck effects in Log-lattices with $\lambda = \phi$, aggravated by hyperviscosity. In such case, special care has to be taken while performing the fitting in the dissipative range.

As it had been shown LL exhibit no stretching in the dissipation range. Therefore, we propose to apply the Frisch & Morf method coupled to our fitting procedure to track complex singularities of fluids, on LL, in various scenarios.

2.3 . Tracking complex singularities of fluids on log-lattices

We showed in previous section that the dissipative range is accurately described, for *well-resolved shell*, by a non-stretched exponential decay. This property allows for the tracking of complex singularities through the use of the analiticity strip method.

This section is an article, submitted to *Non-linearity* and currently under review.

Tracking complex singularities of fluids on log-lattices

Quentin Pikeroen[1], Amaury Barral[1], Guillaume Costa[1], Ciro Campolina[2], Alexei Mailybaev[3] & Berengere Dubrulle[1]

[1]SPEC/IRAMIS/DSM, CEA, CNRS, University Paris-Saclay, CEA Saclay, 91191 Gif-sur-Yvette, France

[2]Université Côte d'Azur, CNRS, Inria, Institut de Physique de Nice, France

[3]Instituto de Matemática Pura e Aplicada, 22460-320 Rio de Janeiro, Brazil

E-mail: `berengere.dubrulle@cea.fr`

Abstract. In 1981, Frisch and Morf [1] postulated the existence of complex singularities in solutions of Navier-Stokes equations. Present progress on this conjecture is hindered by the computational burden involved in simulations of the Euler equations or the Navier-Stokes equations at high Reynolds numbers. We investigate this conjecture in the case of fluid dynamics on log-lattices, where the computational burden is logarithmic concerning ordinary fluid simulations. We analyze properties of potential complex singularities in both 1D and 3D models for lattices of different spacings. Dominant complex singularities are tracked using the singularity strip method to obtain new scalings regarding the approach to the real axis and the influence of normal, hypo and hyper dissipation.

1. Introduction

Viscous fluids dissipate mechanical energy into heat due to the first law of thermodynamics. Observations and numerical simulations reveal that this dissipation is not homogeneous within the flow but occurs via spatially or temporally intermittent bursts, a phenomenon classically referred to as intermittency. Moreover, after spatial and temporal averaging, the mean energy dissipation becomes independent of the viscosity in the inviscid limit, according to the empirical "zeroth law of turbulence". Onsager explained these observations in 1949 [2], conjecturing that strong enough singularities in the inviscid flow could provide an anomalous dissipation. While this conjecture has been proven mathematically [3], its application to fluids is still debated. In fact, the developement of finite-time singularities in Euler flows is until now an unsolved problem [4], while the same question formulated for the Navier-Stokes equations is among the open Millennium Prize Problems of the Clay Mathematics Institute [5]. This debate concerns the existence of singularities in real space. In 1981, Frisch and Morf [1] paved the way to another possibility based on the existence of complex singularities. They proved on a simple one-dimensional non-linear Langevin system that the dynamics of such complex singularities could be directly connected to intermittency, as dissipation bursts occur whenever a complex singularity approaches the real axis.

Since then, this scenario was also confirmed in the one-dimensional Burgers equation – a 1D surrogate of the Navier-Stokes equation. In this system, real singularities can be observed in the inviscid limit and manifest as shocks, i.e. finite jumps in the velocity. Shocks dissipate energy in agreement with the dissipation anomaly [6]. They correspond to the collapse of two complex conjugate singularities onto the real axis [7, 8]. When a viscosity ν is added, the singularities are repelled from the real axis, the closest one being constantly at a distance greater than $O(\nu^{3/4})$ to the real axis. The complex singularities follow Calogero-Moser (CM) dynamics [9], with long-range interactions (decaying in $1/r$). There is an exact mapping between such CM dynamics and the solution of the PDE, which can be described exactly via pole decomposition coupled to the integration of the CM equations [8].

The generalization of these findings to 3D is challenging [10]. The computational burden to resolve the Navier-Stokes equation for a fluid with typical velocity U and length L scales like Re^3, where $\mathrm{Re} \sim UL/\nu$ is the Reynolds number. Most of the earlier attempts to track complex singularities in the inviscid limit were performed using the "singularity strip" method [11], which is based on the observation that the behaviour of the energy spectrum at large wavenumber k is dominated by the position of the singularity closest to the real axis, and decays like $\exp(-2\delta k)$, where δ is the imaginary part of corresponding singularity. Fitting the large wavenumber tail of the energy spectrum as a function of time, one then gets an estimate of $\delta(t)$, and a real singularity occurs when $\delta(t) = 0$. So far, studies have only identified exponentially decaying regimes for $\delta(t)$ [12] which suggests the absence of finite time blow-up. However, we cannot

guarantee that this extrapolation is correct due to numerical limitations.

New perspectives on these issues were opened recently by Campolina and Mailybaev [13], exploring fluid dynamics on log-lattices. This technique may be viewed as a generalization of the so-called "shell models" [14, 15] and solves the equations of motion in Fourier space using a sparse set of Fourier modes. The modes are evenly spaced points in log space ("logarithmic lattices"). They interact via nonlinear equations derived from the fluid equations by substituting for the convolution product a new operator, which can be seen as a convolution on the log-lattice, while preserving most symmetries of the original equation. The model is valid for all dimensions. In 1D, it was shown to encompass [13] the dyaic and Sabra shell models of turbulence [14, 15]. In 3D, its solutions have the same behaviour as the Navier-Stokes equation in Fourier space (energy spectrum, energy transfers), over an unprecedented wide range of scales [13]. In the inviscid equations, a finite-time blow-up is observed [16] in connection with a chaotic attractor that propagates at a constant average speed in a renormalized Fourier space, like a wave. However, Campolina and Mailybaev did not attempt to track possible complex singularities in connection with such a blow-up.

This is the purpose of the present paper. In the first part, we validate the close connection between fluid dynamics on log-lattice and real fluid dynamics by focusing on the 1D Burgers equation, where dominant complex singularities are tracked using the singularity strip method. In the second part, we extend this technique to 3D to obtain new scalings regarding the approach to the real axis and the influence of normal, hypo and hyper dissipation.

2. Log-lattice framework

2.1. Definitions and notations

We consider a d-dimensional complex vector field $u(t,k) = (u_1, \dots, u_d)$ depending on time $t \in \mathbb{R}$ and on the wave vector $k = (k_1, \dots, k_d)$. We shall interpret u as the Fourier components of the velocity field. For this reason, we require them to satisfy the Hermitian symmetry $u(t,-k) = \overline{u(t,k)}$ with respect to k, which is the Fourier property of a real-valued function in physical space. The wave vector k is embedded on a *logarithmic lattice* (in short, *log-lattice*), which means that its components follow geometric progressions $k = k_0(\pm\lambda^{m_1}, \dots, \pm\lambda^{m_d})$ for integers $m_1, \dots, m_d$, where $k_0 = 2\pi$ is a fixed positive reference scale, and $\lambda > 1$ is the spacing factor of the lattice. The dependence of u on t and k is henceforth implicit and specified only when ambiguity prevails.

Fluid dynamics on log-lattice [13] is the set of vector fields u which are solutions of

the equations

$$k_\beta u_\beta = 0, \tag{1a}$$

$$\partial_t u_\alpha + ik_\beta (u_\alpha * u_\beta) = -ik_\alpha p - \nu k^{2\gamma} u_\alpha + f_\alpha, \tag{1b}$$

$$(u_\alpha * u_\beta)(k) = \sum_{q+r=k} u_\alpha(q) u_\beta(r), \tag{1c}$$

where p is the complex pressure field that enforces incompressibility (1a), f is a vectorial forcing, and ν is a non-negative viscosity parameter. When $\nu > 0$, the exponent γ measures the dissipation degree: we say the flow has *viscous* (or *usual*) *dissipation* if $\gamma = 1$, it has *hypo-dissipation* if $\gamma < 1$, and it has *hyper-dissipation* if $\gamma > 1$. Similarly to the dynamics of continuous media, system (1) is the *incompressible Navier-Stokes equations* on the log-lattice. When $\nu = 0$, the flow is *inviscid*, and the system reduces to the *incompressible Euler equations* on the log-lattice.

The convolution in eq. (1c) defines triadic interactions on the logarithmic lattice, which are nontrivial only if the equation $\lambda^m = \pm\lambda^q \pm \lambda^r$ has integer solutions m, q, r. As shown in [13], this is possible only for particular values of λ, which determine the number of possible interactions on the grid. In this paper, we consider the following three values: $\lambda = 2$, with 3 interactions per direction; $\lambda = \phi \approx 1.618$ (the golden number), with 6 interactions per direction; and $\lambda = \sigma \approx 1.325$ (the plastic number), with 12 interactions per direction. As λ decreases from 2 to σ, the density of nodes and the number of interactions on the grid increase. We recall, however, that the interactions for these log-lattices are all local.

2.2. Global quantities

By analogy with the Fourier representation of classical fluid flows, we define the global quantities representing the *total energy* E and the *helicity* H as

$$E = \sum_k |u|^2, \tag{2}$$

$$H = \sum_k u_\alpha \overline{\omega}_\alpha, \tag{3}$$

where $\omega_\alpha = \epsilon_{\alpha\beta\gamma} i k_\beta u_\gamma$ is the *vorticity* field; here, $\epsilon_{\alpha\beta\gamma}$ is the Levi-Civita symbol. Regular solutions of the unforced three-dimensional inviscid system (1) conserve these quantities in time [13].

Moreover, we define the energy spectrum $E(k)$ as

$$E(k) = \langle |u|^2 \rangle_{S_k}, \tag{4}$$

where the average $\langle \cdot \rangle_{S_k}$ is taken over the wave vectors in the shell S_k delimited by spheres of radii k and λk. More explicitly,

$$\langle |u|^2 \rangle_{S_k} = \frac{1}{N_k(\lambda k - k)} \sum_{k \le |q| < \lambda k} |u(q)|^2, \tag{5}$$

where $N_k \sim (\log k)^{d-1}$ is the number of wave vectors in the shell S_k.

2.3. Regularity

The solutions of fluid dynamics equations on log-lattices (1) share some regularity properties with the original models. The main mathematical results are for the inviscid Euler equations [13]. For this system, the local-in-time existence of strong solutions and a Beale-Kato-Majda blow-up criterion were proved. Exploiting the conservation of enstrophy, one proves the global regularity of two-dimensional flows. In the three-dimensional case, high-resolution numerical log-lattice simulations disclosed a finite-time blow-up, characterized by a chaotic wave travelling with constant average speed along a renormalized set of variables [16]. Such blow-up scenario was confirmed for $\lambda = \phi$ and $\lambda = \sigma$, presenting the same asymptotic blow-up scalings [13]. In the viscous case, numerical simulations suggest the expected global regularity of solutions.

2.4. Singularity strip method for log-lattices

If a potential singularity is due to an imaginary pole crossing the real axis, one can track its distance to the real axis via the *singularity strip method* [11]. This method considers the analytic continuation $u(z)$ of the physical-space velocity field and is based on the following property: if

$$u(z) \sim 1/(z - z_*)^{\xi}, \quad \text{for } z \to z_* \tag{6}$$

in a neighborhood of the complex singularity $z_* = a + i\delta$, then its Fourier transform $\hat{u}_k$ satisfies

$$\hat{u}_k \sim k^{-d-\xi} e^{ika} e^{-\delta k}, \quad \text{as } k \to \infty. \tag{7}$$

Asymptotics of (7) provide the corresponding exponential decay $E(k) \sim e^{-2\delta k}$ for the energy spectrum over a typical length 2δ. Therefore, one can measure the distance of the dominant pole to the real axis by monitoring the decay of the energy spectrum in Fourier space. A finite-time singularity at instant t_b would occur if $\delta \to 0$ as $t \to t_b$.

Extension of this notion to the log-lattice framework is natural. It relies on the observation that if a flow (1) on log-lattice satisfies $u(k) \sim k^{-d-\xi} e^{-\delta k}$, then its inverse Fourier transform obeys a relation similar to (6). Therefore, we can generalize the singularity strip method to log-lattices, where 2δ is estimated from the slope of $\log E(k)$ as a function of k.

2.5. Numerical methods

Equations (1) are numerically integrated using a technique analogous to viscous splitting. Considering a time step dt, we obtain $u(t + dt)$ from $u(t)$ employing the following strategy. Using $u(t)$ as initial condition, we first solve the inviscid equation

$$\partial_t u_\alpha = P_{\alpha\beta} \left[-ik_\sigma (u_\beta * u_\sigma) + f_\beta \right], \tag{8}$$

where $P_{\alpha\beta} = \delta_{\alpha\beta} - \frac{k_\alpha k_\beta}{k^2}$ accounts for the pressure term under the incompressibility hypothesis (1a). For that, we use an explicit 4th order Runge-Kutta method. This

yields $u(t+dt)_{\nu=0}$. Then, the viscosity is taken into account through $u(t+dt) = u(t+dt)_{\nu=0} e^{-\nu k^{2\gamma} dt}$. In this whole process, we adapt dynamically the time step dt.

3. 1D Burgers equation

Before going to the full three-dimensional Navier-Stokes system on log-lattices, we take an intermediate step by studying the simpler one-dimensional Burgers equation. For this system, several exact mathematical results are available. This allows us to probe the singularity strip method on log-lattices, by comparing our numerical computations with the exact expected results.

The one-dimensional Burgers equation on log-lattices is obtained from system (1) as follows. We consider a compressible pressureless flow on a one-dimensional log-lattice. Mathematically, this translates into setting $p = 0$ and dropping eq. (1a) from the system, which reduces to

$$\partial_t u + u * \partial_x u = -\nu k^{2\gamma} u + f, \tag{9a}$$

$$(u * \partial_x u)(k) = \sum_{q+r=k} ir\, u(q) u(r). \tag{9b}$$

It was shown [17] that, up to a prefactor in the convolution (9b), the Burgers equation on log-lattices is equivalent to well-known shell models of turbulence for specific choices of parameters. Particularly, when $\lambda = 2$, system (9) (but with a factor 2 added in the convolution and restricting to imaginary solutions) is the dyadic model [18], while for $\lambda = \phi$ (but with a factor $-\phi^2$ added in the convolution) it is the Sabra model [19] in a three-dimensional parameter regime (second invariant is not sign defined). Because of this relation with shell models of turbulence, the Burgers equation on the one-dimensional log-lattice inherits several results concerning the regularity of its solutions, which we briefly review now.

For the dyadic model ($\lambda = 2$) with $\nu > 0$, there are theorems [20] for global existence of weak solutions (satisfying the energy inequality at almost all time), local regularity when $\gamma > 1/3$, global regularity when $\gamma \geq 1/2$, and finite-time blow-up when $\gamma < 1/3$ for sufficiently large initial conditions. Note that for the *continuous* version of the 1D Burgers equations, global existence and analycity holds whenever $\gamma \geq 1/2$, while finite-time blow-ups are present whenever $\gamma < 1/2$ [21]. In contrast, we have presently no rigorous statements about the dyadic model for the parameter range $1/3 \leq \gamma < 1/2$. This means that the mathematical techniques used in the currently available theorems are not sharp enough to separate the finite-time blow-up and the global regularity regimes. The finite-time singularity in the inviscid case was also rigorously established [22].

For the viscous Sabra model ($\lambda = \phi$) with usual dissipation $\gamma = 1$, there are proofs [23] of global regularity of strong solutions. Like the Navier-Stokes equations, the dynamics of the Sabra model develops within finite degrees of freedom. Indeed, the finite dimensionality of the global attractor and the existence of a finite-dimensional

Table 1: Exponents of the inviscid scalings of various quantities measured for the 1D Burgers and the 3D Euler equations within different values of the grid spacing λ. The scalings are with respect to $\tau = 1-t/t_b$, where t_b is the blow-up time. By definition, the energy spectrum scales like $E(k) \sim k^{-1-2\alpha}$, the maximum value of the vorticity scales like $\omega_{\max} \sim \tau^{-\beta}$, and the width of the singularity strip scales like $\delta \sim \tau^{\mu}$. The $^{(0)}$ superscript indicates a simulation performed with no forcing. The * superscript indicates a simulation made with a different initial condition.

	λ	t_b	α	β	μ
1D Burgers	2	0.3898	0.37	1	1.55
	ϕ	0.5193	0.37	1	1.55
	σ	0.4300	0.37	1	1.55
	$2^{(0)}$	0.2687	0.37	1	1.55
	$\phi^{(0)}$	0.1460	0.37	1	1.55
3D Euler	2	0.8481	0.67	1	2.81
	ϕ	5.8005	0.67	1	2.83
	ϕ^*	0.1542	0.67	1	2.82
	σ^*	0.8430	0.67	1	2.67

inertial manifold were proved [23]. On the other hand, the inviscid model has [24] global-in-time existence of weak solutions with finite energy, local-in-time regularity, and a Beale-Kato-Majda blow-up criterion. Despite the absence of rigorous proofs, it is well-known [25] that Sabra (in the three-dimensional parameter regime) develops a self-similar finite-time blow-up, characterized as a travelling wave in a renormalized system of variables (cf. [26]). Following the dynamical systems approach, such blow-up can be seen as a fixed-point attractor of the associated Poincaré map [27].

To our knowledge, there are no systematic results about the development of singularities in Sabra with general dissipation exponents γ, nor in the case of our third lattice parameter $\lambda = \sigma$.

3.1. Inviscid flow

We start with the inviscid ($\nu = 0$) Burgers equation with and without forcing. When forcing, initial conditions are equal to zero, and the forcing is equal to the imaginary unit i on the first mode (k_0) for $\lambda = 2$, the first two modes when $\lambda = \phi$, and the first three modes when $\lambda = \sigma$. Without forcing, initial conditions are taken such that total energy $E = 1$, and first mode, two first modes or three first modes have positive uniform real value, depending on $\lambda = 2$, ϕ or σ, while initial smaller scales are zero. We observe finite-time blow-up for all three values of λ in the two cases. Numerical results are plotted in fig. 1, and scaling exponents are summarized in table 1.

The maximum of the gradient $\omega_{\max}(t) = \max_k |ku(k)|$ blows up in finite time,

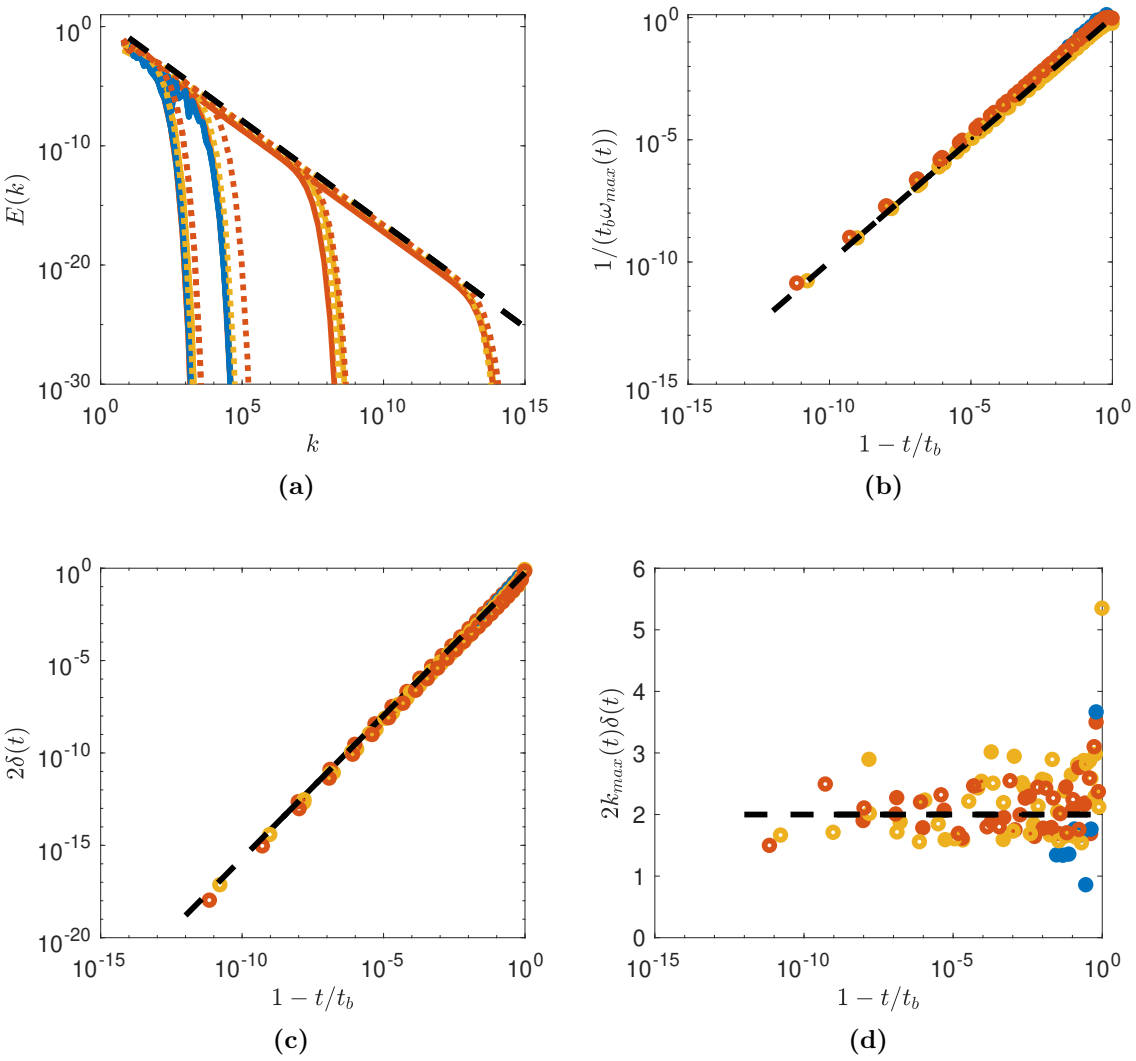

Figure 1: Inviscid blow-up for the 1D Burgers equation for $\lambda = 2$ (yellow), $\lambda = \phi$ (red) and $\lambda = \sigma$ (blue). Continuous lines and filled symbols indicate simulations with constant forcing, while dotted lines and open symbols indicate simulations without forcing. (1a) Spectra at different renormalized relative time $\tau = 1 - t/t_b$. The black dotted line has a slope of -1.733. (1b) Maximum value of the derivative $1/t_b\omega_{\max}$ as a function of τ; The black dotted line is the theoretical value from eq. (10). (1c) Width of the analyticity strip 2δ as a function of τ. The black dotted line has a slope given in table 1. (1d) Renormalized width $k_{\max}\delta$ as a function of τ. The black dotted line has a slope of 0.

following the self-similar law

$$t_b\omega_{max} \sim \frac{1}{\tau}, \quad \tau = 1 - \frac{t}{t_b}, \tag{10}$$

displayed in fig. 1b. While the blow-up time depends on the forcing and the value of λ, the self-similar law (10) is independent of these variables. This law also holds for the original continuous model. Indeed, differentiating the classical Burgers equation $\partial_t u + u\partial_x u = 0$ with respect to x, we get that the space derivative $\omega = -\partial_x u$ obeys

$d\omega/dt = \partial_t\omega + u\partial_x\omega = \omega^2$, whose solution is exactly eq. (10) with $t_b = 1/\omega(t=0)$.

We also check that the energy spectrum evolution is universal, in the sense that it only depends on τ. This is illustrated in fig. 1a, where spectra for different λ but similar τ are shown to overlap. As τ approaches zero, the energy spectrum gradually widens towards larger values of k, developing a power-law $E(k) \sim k^{-2\alpha-1}$ with $1+2\alpha = 1.733$, which corresponds to the scaling law $u(k) \sim k^{-\alpha}$ with $\alpha = 0.367$. Such asymptotics agrees with exact results from the renormalization group formalism applied to the Sabra shell model [28].

Finally, we compute the analyticity strip width δ as the solutions approach the blow-up. This is done using the formula (7) with $\xi + 1 = \alpha$. The result is shown in fig. 1c. We verify that δ decays to zero in finite time, following a power law $\delta \sim \tau^\mu$, with $\mu = 1.546$. This decay is also universal and does not depend on the value of λ or the forcing. The width of the analyticity strip is closely associated with $k_{\max}$, defined as the wavenumber at which ω attains its maximum value. Indeed, we see in fig. 1d that $k_{\max}\delta$ is approximately constant in time. This is in agreement with the asymptotic eq. (7), which implies that $\omega_{\max}$ is achieved at $k_{\max} \sim 1/\delta$.

The self-similar law (10) is valid for all λ in average only. The figures show that the blow-up looks truly self-similar only for the values $\lambda = 2$ and $\lambda = \phi$. The oscillations in the case $\lambda = \sigma$ suggest a different blow-up scenario (e.g. quasi-periodic or chaotic). A detailed analysis of this is left for future work.

3.2. Viscous dissipation

We now introduce viscous dissipation ($\gamma = 1$) and study how the dynamical behaviour depends upon the viscosity parameter ν. This section restricts the analysis to the value $\lambda = 2$. We introduce a force at the large scale, whose amplitude is adapted dynamically so that the total power input is constant in time ($f_{k=k_0} = P u_{k=k_0}/|u|^2_{k=k_0}$, where $P = 1$).

In this setup, the dissipative term is strong enough to prevent the blow-up, and the solution reaches stationarity. The energy spectrum develops a power law in the intermediate scales (called the *inertial range*) followed by an exponential decay at larger k – see fig. 2a. In the inertial range, $E(k) \propto k^{-5/3}$, corresponding to $u(k) \propto k^{-1/3}$.

The maximum value of the derivative $\omega_{\max}$ is inversely proportional to the viscosity, following the power law $\omega_{\max} \sim \nu^{-\beta}$ with $\beta = 0.5$, as shown in fig. 2b. This scaling law can be derived when assuming a viscosity-independent *anomalous dissipation* $\epsilon > 0$ in the inviscid limit $\nu \to 0$. Under this assumption, we have the balance $\nu\omega^2 \sim \epsilon$, which provides $\omega \sim (\epsilon/\nu)^{1/2}$.

Accordingly, the width of the analyticity strip does not decline to zero. However, it stabilizes at a finite value that depends on the viscosity – see fig. 2c – and follows the power-law scaling $\delta \sim \nu^\mu$, with exponent $\mu = 0.7067$. This is smaller than expected from a dimensional argument "a la Kolmogorov", in which $\epsilon = \nu u^2/\delta^2$, with $u \sim \delta^{1/3}$, would instead predict $\delta \sim \nu^{3/4}$. The strip width follows approximately the scaling $\delta \sim 1/k_{\max}$, as shown in fig. 2d.

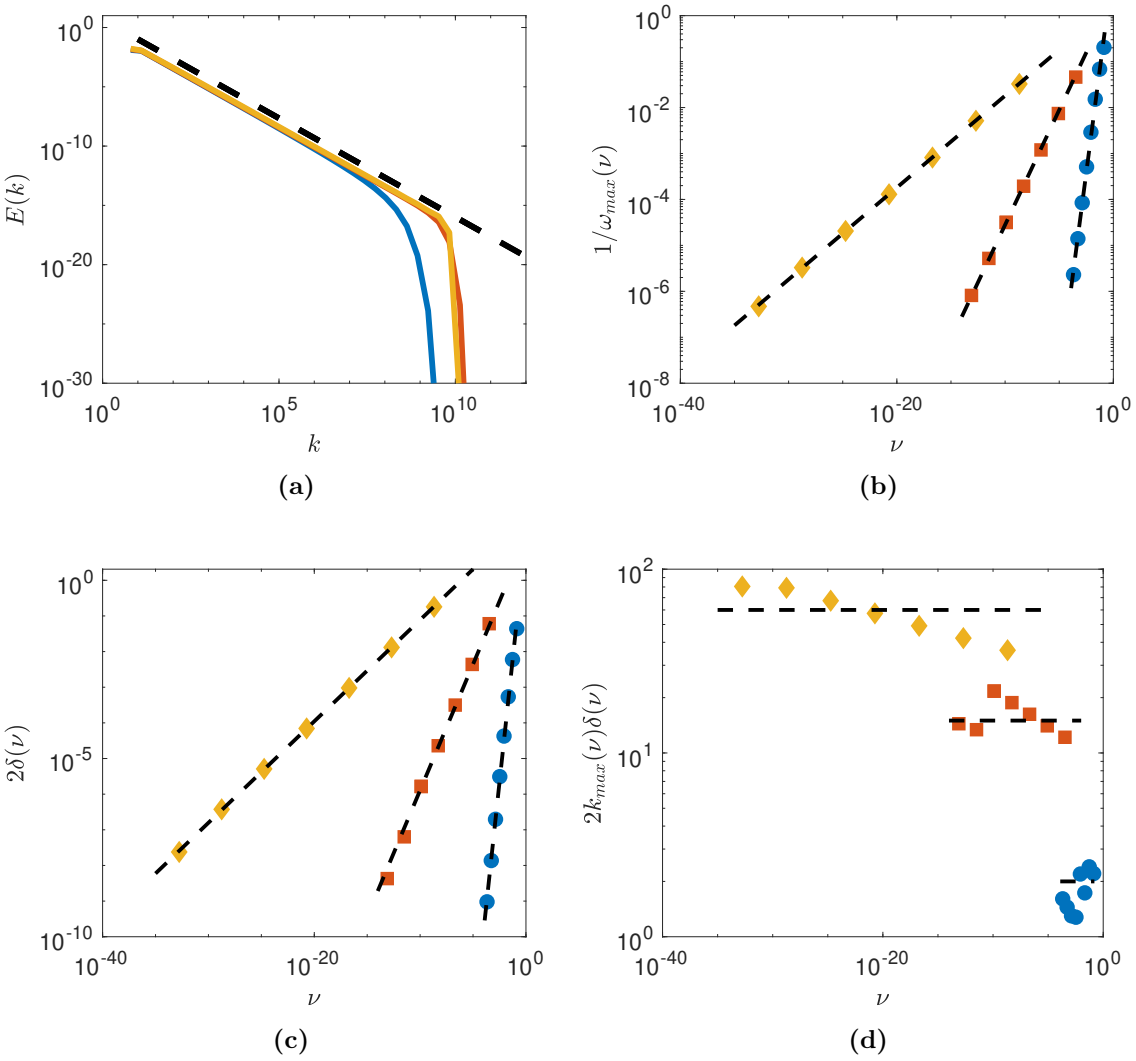

Figure 2: Influence of the type of viscosity on the stationary dynamics of the viscous 1D Burgers equation for $\lambda = 2$ and $\gamma = 0.5$ (hypo-viscous case, blue circle), $\gamma = 1$ (viscous case, red squares) and $\gamma = 2$ (hyperviscous case, yellow diamond). (2a) Energy spectrum. The black dotted line has a slope $-5/3$; (2b) Maximum value of the derivative $1/\omega_{\max}$ as a function of viscosity. The black dotted line has a slope given in table 2 for each case. (2c) Width of the analyticity strip 2δ as a function of viscosity. The black dotted line has a slope given in table 2 for each case. (2d) Renormalized width $k_{\max}\delta$ as a function of viscosity.

3.3. Hyper- and hypo-dissipation

We have also studied the influence of the dissipation degree γ on the various scaling laws. This is summarized in fig. 2 and table 2. The slope of the spectrum is insensitive to γ and displays a $E(k) \sim k^{-5/3}$ law with no intermittency correction. On the other hand, the slopes of both the inverse of the maximum gradient and the singularity width increase in absolute value as γ is decreased towards $1/3$. We defer the discussion about those results to section 5.1.

Table 2: Scaling exponents of various quantities as a function of γ measured for the 1D Burgers and the 3D Navier-Stokes equations with grid spacing $\lambda = 2$. The scalings are with respect to the viscosity ν. By definition, the energy spectrum scales like $E(k) \sim^{-1-2\alpha}$, the maximum value of the vorticity scales like $\omega_{\max} \sim \nu^{-\beta}$ and the width of the analyticity strip scales like $\delta \sim \nu^{\mu}$.

	1D Burgers			3D Navier-Stokes		
γ	α	β	μ	α	β	μ
1/3	–	–	–	2/3	1	2.81
1/2	1/3	1.80	2.78	0.5	0.78	1.53
1	1/3	0.50	0.71	0.40	0.39	0.65
2	1/3	0.20	0.28	0.37	0.19	0.27
8	1/3	0.045	0.06	1/3	0.05	0.06

Table 3: Exponents in the critical case $\gamma = 1/3$ of various quantities measured for the 1D Burgers and the 3D Navier-Stokes equations with different values of the grid spacing λ. The scalings are with respect to $\tau = 1 - t/t_b$, where t_b is the blow-up time. By definition, the energy spectrum scales like $E(k) \sim k^{-1-2\alpha}$, the maximum value of the vorticity scales like $\omega_{\max} \sim \tau^{-\beta}$ and the width of the analyticity strip scales like $\delta \sim \tau^{\mu}$.

	1D Burgers				3D Navier-Stokes			
λ	t_b	α	β	μ	t_b	α	β	μ
2	0.8497	0.37	1	1.55	7.8194	2/3	1	2.81
ϕ	0.5193	0.37	1	1.55	6.51	2/3	1	2.83
σ	0.4546	0.37	1	1.84	–	–	–	–

3.4. Critical dissipation degree $\gamma = 1/3$

According to [20], there are finite time blow-up solutions for the Burgers equation (9) with $\lambda = 2$ whenever $\gamma < 1/3$. However, the theorems say nothing about the limit case $\gamma = 1/3$. For this reason, we call this value as being the *critical dissipation degree*. It is natural to ask whether the blow-up might or might not occur in this specific situation. Here we consider not only $\lambda = 2$, but also extend this question to the other two lattice parameters.

We initialized the flow with the same data as in the inviscid case and set the small viscosity $\nu = 10^{-7}$. We observed a finite time blow-up for all three λ, illustrated in fig. 3. The blow-up time is larger than in the inviscid case, but the scaling laws are the same – both the prefactor and the scaling exponents – as in the inviscid case. The exponents are summarized in table 3. The only exception is for the scaling law of δ in the case $\lambda = \sigma$. This might be due to the oscillations in the energy spectrum, making it harder to fit the exponential decreasing, see fig. 3a.

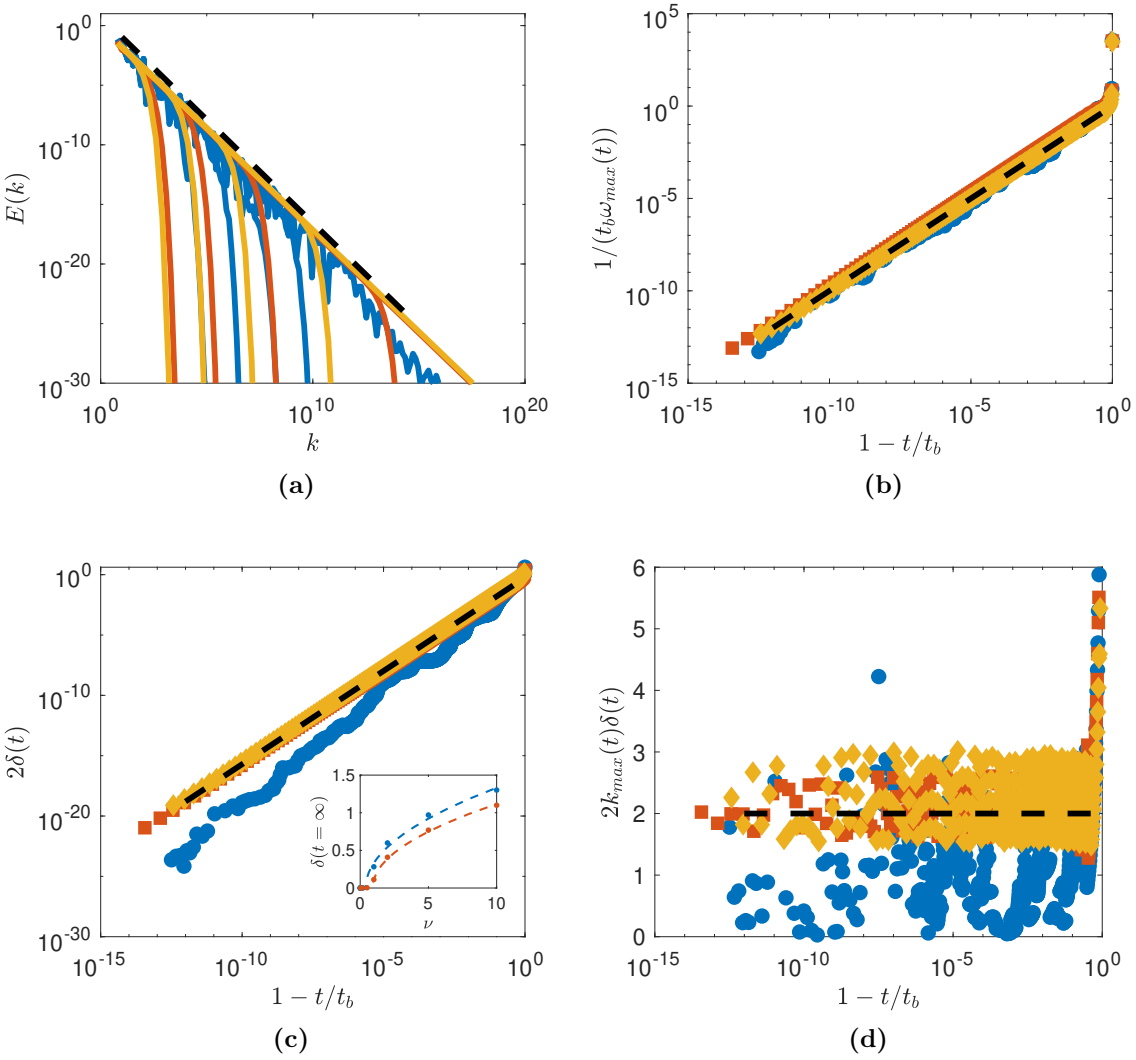

Figure 3: Blow-up for the critical ($\gamma = 1/3$) 1D Burgers equation, with $\nu = 10^{-7}$ and for $\lambda = 2$ (yellow), $\lambda = \phi$ (red) and $\lambda = \sigma$ (blue). (3a) Spectra at different renormalized relative time $\tau = 1 - t/t_b$; (3b) Maximum value of the derivative $1/t_b\omega_{\max}$ as a function of τ (3c) Width of the analyticity strip 2δ as a function of τ. The insert shows the behaviour of the width of the analyticity strip at $t = \infty$ when the viscosity is increased, for $\gamma = 1/3$ (blue data points) (resp. $\gamma = 1/4$ (red data points)). The dotted lines are fits of the type $\sqrt{\nu - \nu_c}$, with $\nu_c = 0.4$ (resp. $\nu = 0.9$). (3d) Renormalized width $k_{\max}\delta$ as a function of τ. The dotted line has the same scaling and prefactor as in the inviscid blow-up case, see fig. 1

In this small-viscosity run, viscosity only delays the blow-up but does not influence the development of the singularity. However, we observed a surprising behaviour change when increasing the viscosity to larger values. There is a transition between a small-viscosity regime, where finite time blow-up occurs, and a large-viscosity regime, where the blow-up disappears, and the width of the analyticity strip saturates to a finite value – see insert of fig. 3c. The amplitude of δ seems to follow a critical mean-field behaviour, as it varies like $\delta \sim \sqrt{\nu - \nu_c}$, with $\nu_c \sim 0.4$. A similar transition is observed at a lower value of γ, with ν_c increasing as γ decreases.

This transition is in fact not contradicting the mathematical results by [20], since they prove existence of blow-up only for initial conditions larger than a threshold that depends linearly in the viscosity. In all our calculations, we start with the same initial conditions. This means that for large enough values of viscosity, the initial condition becomes smaller than the threshold, therefore invalidating the hypothesis of the theorem. More than that, our numerical results suggest that this hypothesis is actually essential for the result of the theorem and might not be dropped in general.

4. 3D Euler and Navier-Stokes equations

4.1. Inviscid flow – Euler equations

We now turn to the full three-dimensional incompressible fluid dynamics on log-lattices, starting with the inviscid Euler equations. We consider here the three lattice spacings λ. In order to test universality, we ran the case $\lambda = \phi$ with two different incompressible random initial conditions, differing by their range of scales. Default initial conditions are defined at large scale $|k| < 3k_0$, while the other (denoted by a star $*$) are defined at scales $|k| < k_0\lambda^3$. We observed a finite-time blow-up in all setups, in agreement with previous results documented in [16, 13]. Here, we observe that while the blow-up time depends on the initial conditions, the dynamics become universal when plotted in non-dimensional variables, as illustrated in fig. 4. The spectra for distinct values of λ overlap when plotted at the same non-dimensional times $\tau = 1 - t/t_b$, as evidenced in fig. 4a. The slope of the power law in the inertial range is steeper than in 1D Burgers, with a value very close to $-7/3$. This is the slope expected for a helicity cascade. Our exponent is slightly smaller than those found in some direct numerical simulations of the Euler equations, where a $E(k) \sim k^{-3}$ spectrum is observed [29, 30], but comparable to the value 2.33 obtained in more recent simulations [31].

The maximum value of the vorticity $\omega_{\max}$ diverges during the blow-up, as shown in fig. 4b. Its asymptotic scaling is the same as for the maximum gradient in the 1D Burgers equation, given by eq. (10). However, contrarily to the 1D case, the constant in front of the power law varies as a function of λ and is not simply given by $1/t_b$. This is not too surprising given the 3D nature of the flow, which prevents the application of the simple blow-up argument used for 1D Burgers. However, as λ is decreased towards 1, the non-dimensional curve becomes closer to the exact asymptotic law.

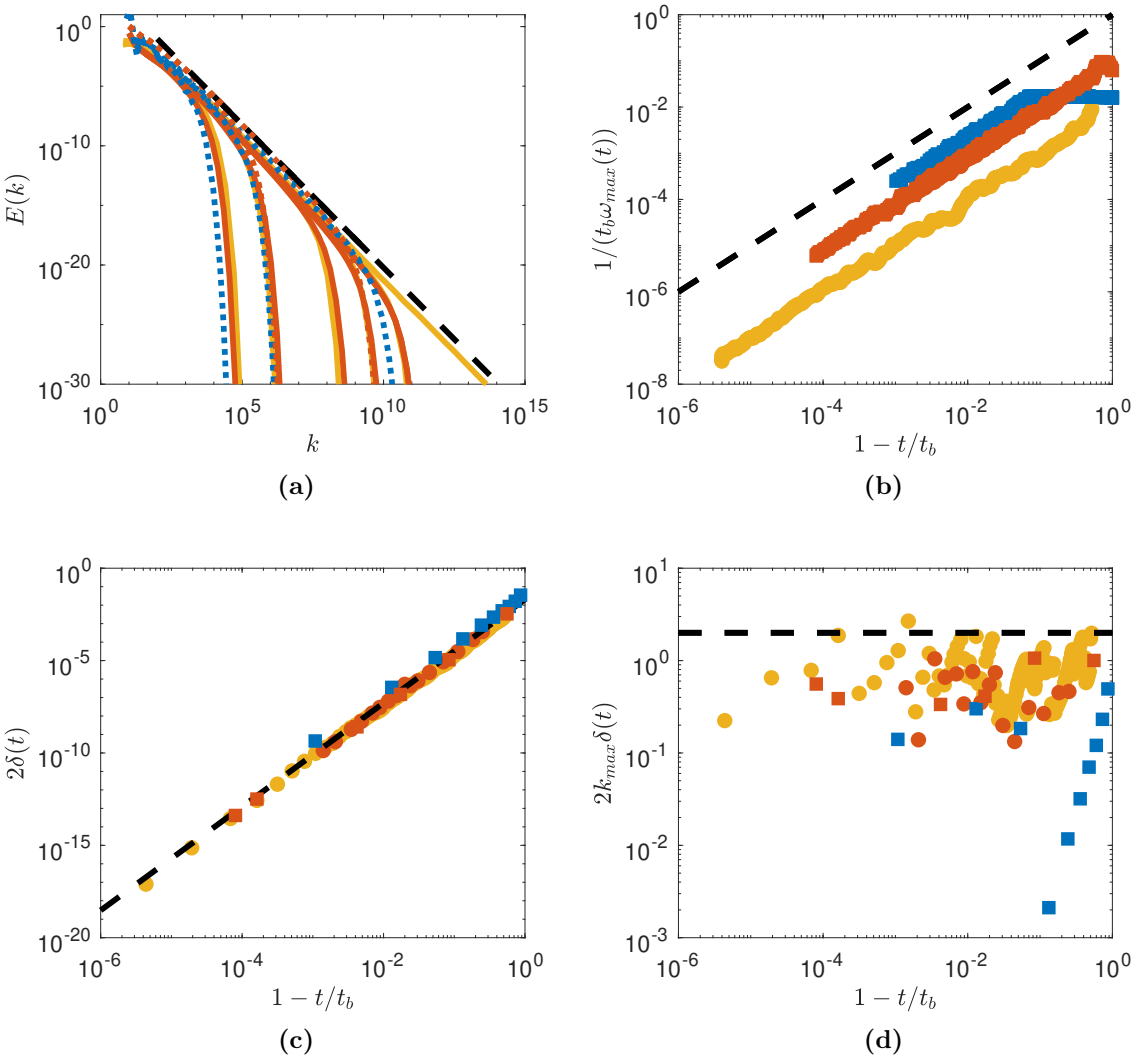

Figure 4: Inviscid blow-up for the 3D Euler equations for $\lambda = 2$ (yellow), $\lambda = \phi$ (red) and $\lambda = \sigma$ (blue). (4a) Spectra at different renormalized relative time $\tau = 1 - t/t_b$, from 0.2542 to 0.00001 from left to right. Spectra with continuous lines and dotted lines correspond to different initial conditions. The black dotted line has a slope of $-7/3$; (4b) Maximum value of derivative $1/t_b\omega_{\max}$ as a function of τ. The black dotted line has a slope of 1; (4c) Width of analyticity strip 2δ as a function of τ; The black dotted line has a slope 2.805. (4d) Renormalized width $k_{\max}\delta$ as a function of τ. In panels 4b, 4c and 4d, we used different symbols for different initial conditions: circles, and squares.

Approaching the blow-up, the width of the analyticity strip decays to zero with a power law $\delta \sim \tau^{\mu}$ with exponent $\mu \approx 2.81$ – see fig. 4c. This is larger than in 1D Burgers. This decay is also universal, as it does not depend on λ. However, it does not show a simple dependence with $k_{\max}$ as seen in fig. 4d. This might be related to the chaotic nature of the blow-up attractor [13].

4.2. Viscous dissipation – Navier-Stokes equations

We now add the viscous term with $\gamma = 1$ and a constant-power forcing. The solutions achieve a statistically stationary state in this framework, whose average scalings are depicted in fig. 5. Like in 1D Burgers, the energy spectra display a power law until the solution reaches the viscous scale, with an inertial range widening as ν decreases. The slope of the energy spectrum is slightly steeper than Kolmogorov's $-5/3$, with an intermittency correction of around 0.13. Accordingly, the scaling exponent α for $u(k) \sim k^{-\alpha}$ is $\alpha = 0.40$, slightly larger than $1/3$. The maximum vorticity $\omega_{\max}$ increases with decreasing viscosity, following the power law $\omega_{\max} \sim \nu^{-\beta}$ with an exponent $\beta = 0.39$ lower than Kolmogorov's $1/2$.

The width of the analyticity strip decays with viscosity as $\delta \sim \nu^{\mu}$ with an exponent $\mu = 0.65$ – see fig. 5c. Such decay is less intense than in the 1D Burgers equation. Nevertheless, the dependence of δ on $1/k_{\max}$ in the Navier-Stokes case is sharper, as one verifies by comparing fig. 5d with fig. 2d.

4.3. Hyperviscous dissipation

We now consider what happens in the hyperviscous case $\gamma > 1$. We keep the constant-power forcing to reach stationary states.

For $\gamma = 2$, we still observe a power-law energy spectrum followed by an exponential cut-off at the viscous scales – see fig. 5a. The inertial range keeps widening as ν is decreased. The slope of the energy spectrum is very close, but slightly steeper than $-5/3$. The exact fitting provides us an intermittency correction around 0.07, corresponding to $\alpha = 0.37$, see table 2. The maximum vorticity $\omega_{\max}$ increases with decreasing viscosity like a power law, with an exponent $\beta = 0.19$ lower than usual ($\gamma = 1$) viscous case. The width of the analyticity strip decays with viscosity with an exponent $\mu = 0.26$. Like in the viscous case, δ appears to scale simply like $1/k_{\max}$, as seen on fig. 5d.

The above results suggest that the intermittency corrections in the energy spectra are smaller for hyperdissipation. Indeed, as the dissipation degree γ increases, the exponent α converges towards Kolmogorov's $1/3$, see table 2. We checked that for the stronger degree $\gamma = 8$, they vanish completely, and the dependence of $\omega_{\max}$ and δ on ν become very weak. This is explained by the very sharp viscous cut-off due to the hyperviscous dissipation. Indeed, the equivalent of the Kolmogorov scale k_d in the hyperviscous case relates to ν as $k_d \sim \nu^{1/(1-1/3-2\gamma)}$, becoming independent of viscosity in the limit $\gamma \to \infty$. For $\gamma = 2$ the dependence is $\delta \sim k_d^{-1} \sim \nu^{0.3}$, close to what is observed for the scaling of the singularity strip width.

4.4. Hypoviscous dissipation

The case with hypoviscous dissipation $1/3 < \gamma < 1$ is qualitatively similar to the viscous and hypervisous cases – see fig. 5. Exponents, however, are steeper. The corresponding values are reported in table 2. The energy spectrum develops a slope corresponding to

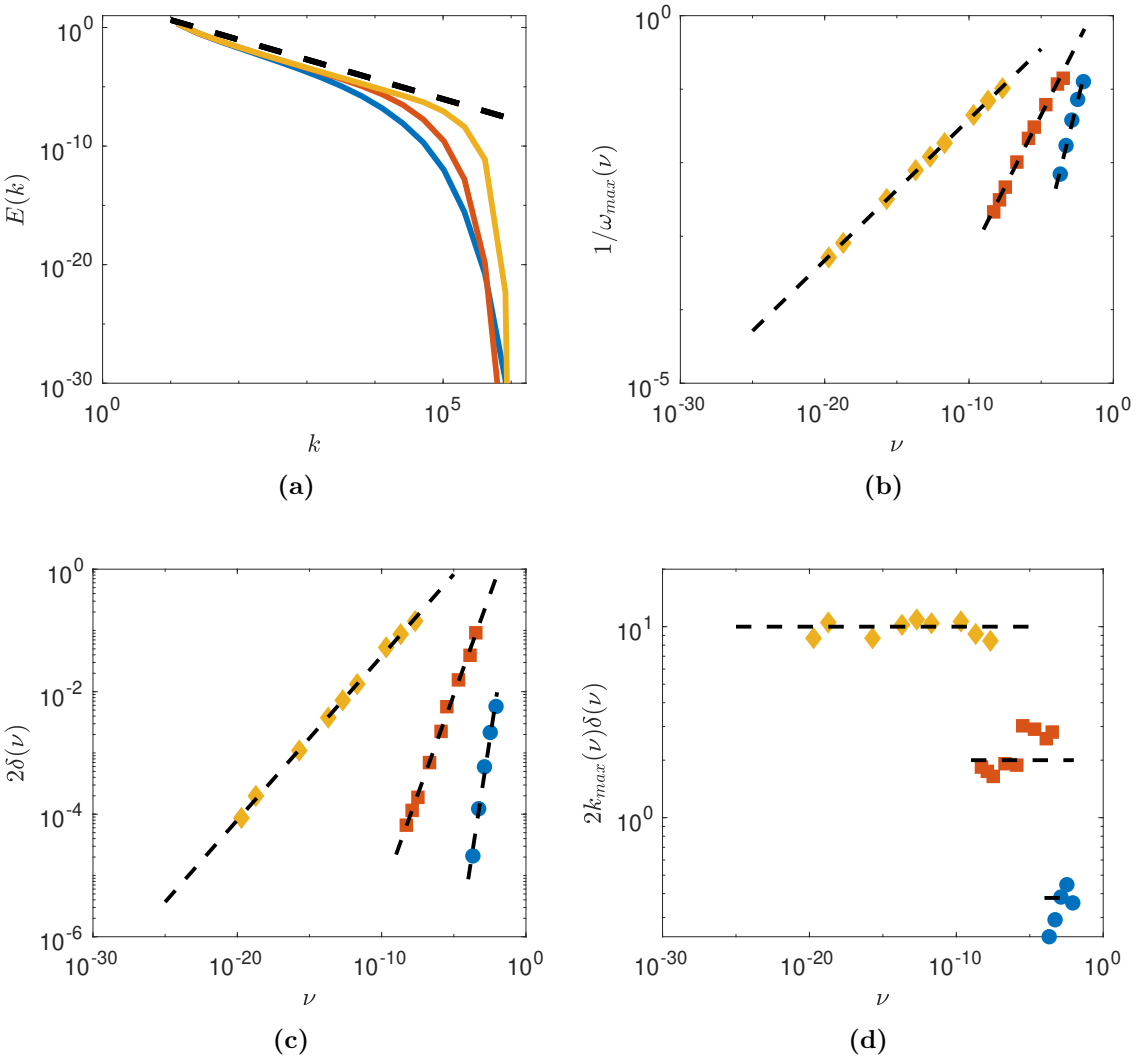

Figure 5: Stationary dynamics for the 3D Navier-Stokes equations for $\lambda = 2$ and $\gamma = 0.5$ (hypo-viscous case, blue circle), $\gamma = 1$ (viscous case, red squares) and $\gamma = 2$ (hyperviscous case, yellow diamond). (5a) Energy spectrum. The black dotted line has a slope $-5/3$; (5b) Maximum value of the derivative $1/\omega_{\max}$ as a function of viscosity. The black dotted line has a slope given in table 2 for each case. (5c) Width of the analyticity strip 2δ as a function of viscosity. The black dotted line has a slope given in table 2 for each case. (5d) Renormalized width $k_{\max}\delta$ as a function of viscosity.

the exponent $\alpha = 0.5$, which is steeper than Kolmogorov's $1/3$ but milder than Euler's $2/3$ on log-lattices. The singularity width appears again to be controlled by the wave number corresponding to the maximum vorticity – see fig. 5d. On the other hand, the maximum vorticity grows much more rapidly than in the viscous case, with an exponent twice as big, as shown in fig. 5b. This may indicate that we are approaching a critical dissipation degree, below which finite-time blow-up will occur.

4.5. Critical dissipation degree $\gamma = 1/3$

The asymptotics of Kolmogorov's length scale for a flow with a general dissipation degree predicts the breakdown of the viscous cut-off when γ approaches the critical value $1/3$. Indeed, the dissipation scale k_d is obtained from the dimensional balance between the convective and the dissipative terms $k_d u_d^2 \sim \nu k_d^{2\gamma} u_d$. On the other hand, Kolmogorov's theory states that $u_d \sim \epsilon^{1/3} k_d^{-1/3}$ for the energy dissipation rate ϵ, which has a finite positive value in the inviscid limit. Together, these expressions yield

$$k_d \sim \epsilon^{\frac{1}{6(\gamma-1/3)}} \nu^{\frac{1}{2(1/3-\gamma)}}, \tag{11}$$

which, for sufficiently small ν, provides $k_d \to +\infty$ when $\gamma \searrow 1/3$. For this reason, we call $\gamma = 1/3$ the *critical dissipation exponent*, the value at which we expect that the dissipative term is no longer strong enough to prevent a finite-time singularity. We recall this was the case for the 1D Burgers equation on log-lattices.

Motivated by the above arguments, we investigate the critical hypo-diffusive degree in the full 3D system on log-lattices. The following analysis considers the spacings $\lambda = 2$ and $\lambda = \phi$. The initial data is the same as we used in the inviscid simulations, and viscosity is the same $\nu = 10^{-7}$.

In this regime, we observed a finite time blow-up for the two values of λ, illustrated in fig. 6. Like in 1D Burgers, the blow-up time is larger than in the inviscid case, but the scaling laws are the same. This is summarized in table 3. The slope of the energy spectrum remains $-7/3$. For $\lambda = 2$ and $\nu = 10^{-3}$, the dynamics becomes stationary, meaning there is as in 1D a phase transition, but between $\nu = 10^{-3}$ and 10^{-7}, smaller than $\nu_c \sim 0.4$ in 1D.

5. Discussion

5.1. Scaling laws

The variations of the scaling exponents with respect to the diffusion exponent γ are shown in fig. 7.

Predictions for the scaling laws are possible using simple dimensional arguments if we impose $\delta \sim 1/k_{\max}$, as empirically observed. Indeed, from $u \sim k^{-\alpha}$ and $\omega \sim ku$, we get $\omega_{\max} \sim k_{\max}^{1-\alpha} \sim \delta^{\alpha-1}$ so that we get:

$$\beta = \mu(1-\alpha). \tag{12}$$

This fixes a link between the 3 exponents that is well satisfied – see fig. 7b. On the other hand, one can connect μ and α by extending the argument fixing the Kolmogorov scale to hypo and hyper-viscous cases: we impose that $k_{\max}$ is fixed by the condition that the viscous term balances the non-linear term $\nu k_{\max}^{2\gamma} u_{\max} \sim k_{\max} u_{\max}^2$. Using $u_{\max} \sim k_{\max}^{-\alpha}$ and $\delta \sim 1/k_{\max}$ we then get:

$$\mu = -\frac{1}{1-\alpha-2\gamma}, \tag{13}$$

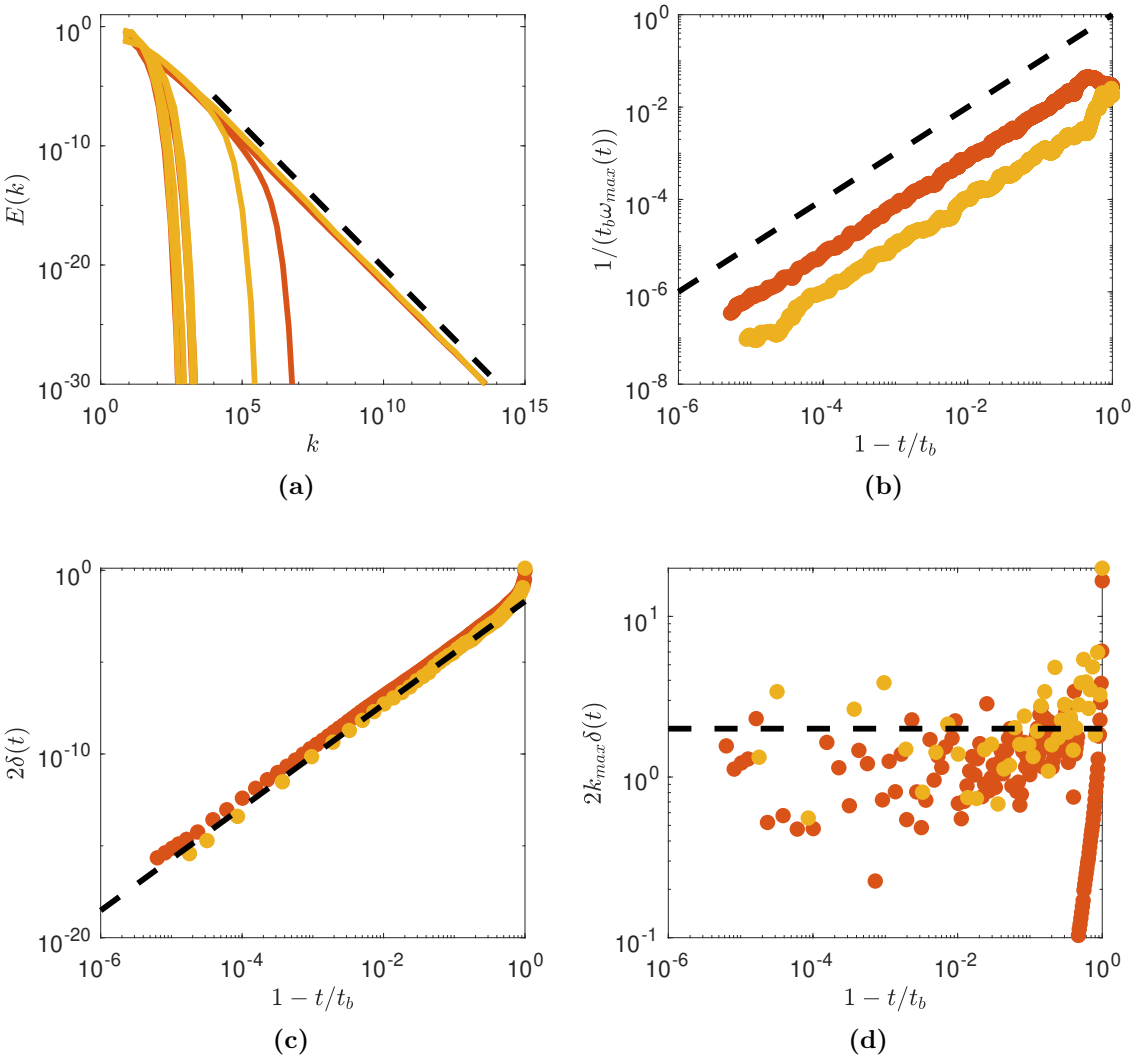

Figure 6: Blow-up for the critical ($\gamma = 1/3$) 3D Navier-Stokes equations, for $\lambda = 2$ (yellow) and $\lambda = \phi$ (red). (6a) Spectra at different renormalized relative time $\tau = 1 - t/t_b$; (6b) Maximum value of the derivative $1/t_b\omega_{\max}$ as a function of τ (6c) Width of the analyticity strip 2δ as a function of τ (6d) Renormalized width $k_{\max}\delta$ as a function of τ. The dotted line has the same scaling and prefactor as in the inviscid blow-up case, see fig. 4

This prediction is tested in fig. 7c and is well satisfied. Without loss of generality, the only free parameter can be taken as $\alpha(\gamma)$. In the limit $\gamma \to 1/3$, we can fix it by imposing that $\beta = 1$, which is the scaling corresponding to conservation of the circulation of u [32]. From eqs. (12) and (13), we then get $\alpha = 1 - \gamma = 2/3$, corresponding to a helicity cascade. In all other cases, we have no clear theories to predict the variations of α with γ. Notably, when $\gamma \to \infty$, we recover $\alpha = 1/3$ corresponding to an energy cascade.

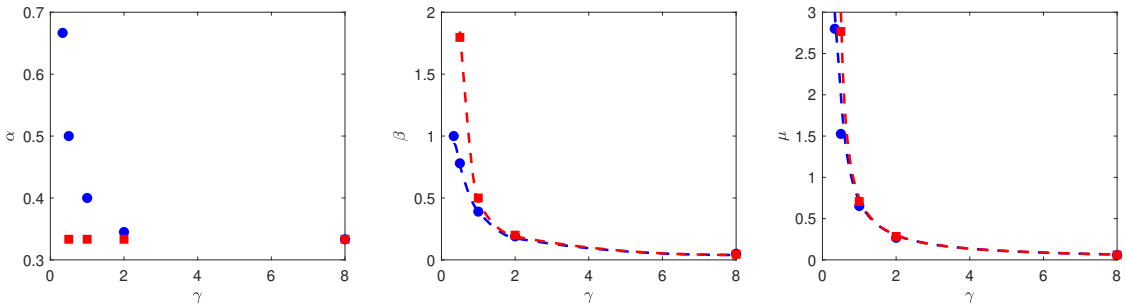

(a) **(b)** **(c)**

Figure 7: Variation of the scaling exponents as a function of the dissipation degree γ for the 1D Burgers (blue circle) and the 3D Navier-Stokes (red square) equations with $\lambda = 2$. (7a) For the scaling of the velocity $u \sim k^{-\alpha}$. (7b) For the scaling of the maximum vorticity $\omega_{\max} \sim \nu^{-\beta}$. The data points are reported from tables 2 and 3, while the dotted lines correspond to eq. (12); (7c) For the scaling of the singularity strip $\delta \sim \nu^{\mu}$. The data points are reported from tables 2 and 3. while the dotted lines correspond to eq. (13).

5.2. Interest of the critical case

The critical case $\gamma = 1/3$ is more than purely academic: renormalization group (RNG) analysis of NSE in Fourier space [33] indeed shows that the fixed point of the equations corresponds to a Navier-Stokes equation with turbulent viscosity scaling like $A\epsilon^{1/3}k^{-4/3}$, where A is a constant with value $A = 0.1447$ in 1D and $A = 0.4926$ in 3D. This corresponds exactly to eq. (1), with $\gamma = 1/3$ and $\nu = A\epsilon^{1/3}$. This model is sometimes used as a subgrid model of turbulence [34]. In that respect, it is interesting that the transition viscosity found in sections 3.4 and 4.5 (at constant injected power, i.e. $\epsilon = 1$) is very close to the RNG value in 1D. On the one hand, this guarantees that the size of the inertial range is very wide, in agreement with the RNG picture of scale invariant solutions. On the other hand, this means that the solution is very close to a blow-up, which could have implications regarding the stability of this subgrid scheme.

5.3. Implications for real Euler or Navier-Stokes?

The log-lattices simulations we performed cannot be seen as an exact model of the Euler or Navier-Stokes equations because they remove by construction many non-linear interactions of the original equations, especially the non-local one. Nevertheless, because they obey the same conservation laws and symmetries, they may capture some scaling laws of the original equation more accurately. Comparing our findings with the few results on the topic is engaging.

Regarding the Euler equation, recent high-resolution numerical simulation in the axisymmetric case by [35] explored the scaling of the singularity strip in the blowing situation proposed by [36]. They found an exponent $\mu = 2.6 \pm 0.5$, which is compatible with the value 2.8 ± 0.1 that we get from table 2. Unfortunately, they do not provide an

estimate of the slope of the energy spectrum. Previous older results in the Taylor-Green vortex [37, 30] found a steeper spectrum corresponding $\alpha \sim 1$. However, spectra with exponent matching our $-7/3$ value were observed in the early stage of recent simulations at larger resolution [31]. Therefore, the main characteristics of blow-up in log-lattices simulations agree with the most recent results observed in the traditional DNS of the Euler equation.

Regarding the Navier-Stokes equations, we can look at two recent results. The first one by [38] finds a value of $\mu = 0.89$ using recent DNS of NSE. This value is larger than the value we found in the present paper, corresponding to $\mu = 0.65$. Another recent result [39] estimates β in 3D NSE. They indeed found that the tail of the PDF of enstrophy scales like $\nu^{0.77}\tau_K^{-2}$, where $\tau_K \sim \nu^{1/2}$ is the Kolmogorov time. Identifying such extreme events of enstrophy with $\omega^2_{\max}$, we thus get $\beta_{DNS} \sim 0.88$, which is also much larger than the value we observe in log-lattices $\beta_{LL} \sim 0.39$. Note, however, that both DNS values are compatible with eqs. (12) and (13), provided we choose $\alpha \sim 0$, hinting at the presence of multifractality. Log-lattices simulations are generally much less intermittent than DNS [13], with one dominating exponent (monofractal behaviour). Some time ago, [34] linked the intermittency properties of NSE with non-local interactions, which is coherent with this observation. Therefore, the difference between log-lattices simulations and DNS could be explained by differences in the amount of non-local interactions.

Acknowledgments

This work received funding from the Ecole Polytechnique, from ANR TILT grant agreement no. ANR-20-CE30-0035, and from ANR BANG grant agreement no. ANR-22-CE30-0025. CC is thankful for the financial support from CEA during his visit to Paris-Saclay, where this work was elaborated. AM was supported by CNPq grant 308721/2021-7 and FAPERJ grants E-26/201.054/2022, E-26/210.874/2014.

References

[1] Uriel Frisch and Rudolf Morf. Intermittency in nonlinear dynamics and singularities at complex times. *Phys. Rev. A*, 23:2673–2705, May 1981.

[2] L. Onsager. Statistical hydrodynamics. *Il Nuovo Cimento (1943-1954)*, 6(2):279–287, 1949.

[3] Philip Isett. A proof of Onsager's conjecture. *Annals of Mathematics*, 188(3):871 – 963, 2018.

[4] John D Gibbon. The three-dimensional euler equations: Where do we stand? *Physica D: Nonlinear Phenomena*, 237(14-17):1894–1904, 2008.

[5] C. L. Fefferman. Existence and smoothness of the Navier-Stokes equation. In *The millennium prize problems*, pages 57–67. AMS, 2006.

[6] G. L. Eyink. Turbulence Theory. http://www.ams.jhu.edu/ eyink/Turbulence/notes/, 2007-2008. course notes, The Johns Hopkins University,.

[7] J-D. Fournier and U. Frisch. L'équation de burgers déterministe et statistique. *Journal de Mécanique Théorique et Appliquée*, 2(5):699–750, 1983.

[8] D Senouf, R Caflisch, and N Ercolani. Pole dynamics and oscillations for the complex burgers equation in the small-dispersion limit. *Nonlinearity*, 9(6):1671–1702, nov 1996.

[9] F. Calogero. Motion of poles and zeros of special solutions of nonlinear and linear partial differential equations and related solvable many-body problems. *Il Nuovo Cimento B (1971-1996)*, 43:177–241, 1978.

[10] U Frisch, T Matsumoto, and J Bec. Singularities of euler flow? not out of the blue! *Journal of statistical physics*, 113:761–781, 2003.

[11] Catherine Sulem, Pierre-Louis Sulem, and Hélène Frisch. Tracing complex singularities with spectral methods. *Journal of Computational Physics*, 50(1):138–161, 1983.

[12] Michael Siegel and RE Caflisch. Calculation of complex singular solutions to the 3d incompressible euler equations. *Physica D: Nonlinear Phenomena*, 238(23-24):2368–2379, 2009.

[13] Ciro S Campolina and Alexei A Mailybaev. Fluid dynamics on logarithmic lattices. *Nonlinearity*, 34(7):4684–4715, jun 2021.

[14] C. Gloaguen, J. Léorat, A. Pouquet, and R. Grappin. A scalar model for mhd turbulence. *Physica D: Nonlinear Phenomena*, 17(2):154–182, 1985.

[15] Luca Biferale. Shell models of energy cascade in turbulence. *Annual Review of Fluid Mechanics*, 35:441–468, 2003.

[16] Ciro S. Campolina and Alexei A. Mailybaev. Chaotic blowup in the 3d incompressible euler equations on a logarithmic lattice. *Phys. Rev. Lett.*, 121:064501, Aug 2018.

[17] C. S. Campolina. Fluid Dynamics on Logarithmic Lattices and Singularities of Euler Flow. Master's Thesis, Instituto de Matemática Pura e Aplicada, 2019.

[18] V. N. Desnyansky and E. A. Novikov. The evolution of turbulence spectra to the similarity regime. *Izv. Akad. Nauk SSSR, Fiz. Atmos. Okeana*, 10:127–136, 1974.

[19] V. S. L'vov, E. Podivilov, A. Pomyalov, I. Procaccia, and D. Vandembroucq. Improved shell model of turbulence. *Phys. Rev. E*, 58(2):1811, 1998.

[20] Alexey Cheskidov. Blow-up in finite time for the dyadic model of the navier-stokes equations. *Transactions of the American Mathematical Society*, 360(10):5101–5120, 2008.

[21] Alexander Kiselev, Fedov Nazarov, and Roman Shterenberg. Blow up and regularity for fractal Burgers equation. *Dynamics of PDE*, 5(3):211–240, 2008.

[22] Nets Katz and Nataša Pavlović. Finite time blow-up for a dyadic model of the euler equations. *Transactions of the American Mathematical Society*, 357(2):695–708, 2005.

[23] Peter Constantin, Boris Levant, and Edriss S Titi. Analytic study of shell models of turbulence. *Physica D: Nonlinear Phenomena*, 219(2):120–141, 2006.

[24] Peter Constantin, Boris Levant, and Edriss S. Titi. Regularity of inviscid shell models of turbulence. *Phys. Rev. E*, 75:016304, Jan 2007.

[25] Alexei A Mailybaev. Spontaneously stochastic solutions in one-dimensional inviscid systems. *Nonlinearity*, 29(8):2238, 2016.

[26] Thierry Dombre and Jean-Louis Gilson. Intermittency, chaos and singular fluctuations in the mixed Obukhov-Novikov shell model of turbulence. *Physica D: Nonlinear Phenomena*, 111(1-4):265–287, 1998.

[27] Alexei A Mailybaev. Bifurcations of blowup in inviscid shell models of convective turbulence. *Nonlinearity*, 26(4):1105, 2013.

[28] Côme Fontaine, Malo Tarpin, Freddy Bouchet, and Léonie Canet. Functional renormalisation group approach to shell models of turbulence, 2022.

[29] P. Orlandi, S. Pirozzoli, and G. F. Carnevale. Vortex events in Euler and Navier-Stokes simulations with smooth initial conditions. *Journal of Fluid Mechanics*, 690:288–320, 2012.

[30] Miguel D. Bustamante and Marc Brachet. Interplay between the beale-kato-majda theorem and the analyticity-strip method to investigate numerically the incompressible euler singularity problem. *Phys. Rev. E*, 86:066302, Dec 2012.

[31] Niklas Fehn, Martin Kronbichler, Peter Munch, and Wolfgang A. Wall. Numerical evidence of anomalous energy dissipation in incompressible Euler flows: towards grid-converged results for the inviscid Taylor-Green problem. *Journal of Fluid Mechanics*, 932:A40, 2022.

[32] Yves Pomeau. On the self-similar solution to the euler equations for an incompressible fluid in three

dimensions. *Comptes Rendus Mécanique*, 346(3):184–197, 2018. The legacy of Jean-Jacques Moreau in mechanics / L'héritage de Jean-Jacques Moreau en mécanique.

[33] Victor Yakhot and Steven A. Orszag. Renormalization-group analysis of turbulence. *Phys. Rev. Lett.*, 57:1722–1724, Oct 1986.

[34] J-P. Laval, B. Dubrulle, and S. Nazarenko. Nonlocality and intermittency in three-dimensional turbulence. *Physics of Fluids*, 13(7):1995–2012, 2001.

[35] Sai Swetha Venkata Kolluru, Puneet Sharma, and Rahul Pandit. Insights from a pseudospectral study of a potentially singular solution of the three-dimensional axisymmetric incompressible euler equation. *Phys. Rev. E*, 105:065107, Jun 2022.

[36] Guo Luo and Thomas Y. Hou. Potentially singular solutions of the 3d axisymmetric euler equations. *Proceedings of the National Academy of Sciences*, 111(36):12968–12973, 2014.

[37] M. E. Brachet, M. Meneguzzi, A. Vincent, H. Politano, and P. L. Sulem. Numerical evidence of smooth self?similar dynamics and possibility of subsequent collapse for three?dimensional ideal flows. *Physics of Fluids A: Fluid Dynamics*, 4(12):2845–2854, 1992.

[38] Bérengère Dubrulle. Multi-fractality, universality and singularity in turbulence. *Fractal and Fractional*, 6(10), 2022.

[39] Dhawal Buaria, Alain Pumir, Eberhard Bodenschatz, and P K Yeung. Extreme velocity gradients in turbulent flows. *New Journal of Physics*, 21(4):043004, apr 2019.

3 - Intermittency on Log-lattices

3.1 . Introduction

In the previous chapters, we investigated the existence of complex singularities in Log-lattices, highlighting the existence of blowup solutions associated to the collapse of a complex singularity onto the real axis. This collapse of a singularity also implies a burst of dissipation, a characteristic feature of intermittency, a key component of turbulence.

The founder of Log-lattices, namely Campolina & Mailybaev, first tackled the question of intermittency on LL (21) through the study of the statistics of Fourier modes in both the inertial and viscous range. Statistics in the inertial range were found to be gaussian indicating the absence of intermittency. Yet, such features were also observed in the statistics of the Fourier transform of intermittent DNS and experimental results meaning that Gaussian statistics do not indicate the absence of intermittency. Therefore to better probe the problem, they defined structure functions through powers of the energy flux. By extracting the exponents of the structure functions in the inertial range, they obtained the Kolmogorov scaling $\xi_p = p/3$ characteristic of non intermittent flow. This first study led to the absence of intermittency, a rather puzzling result. Indeed, 1-D LL with $\lambda = \phi$ corresponds to the well known SABRA shellmodel that exhibits intermittency [1]. Therefore, it is legitimate to wonder if LL really fails at capturing intermittency.

In this chapter, we propose to investigate what hints of intermittency are present in Log-lattices. We first briefly recall the Kolmogorov theory and the multifractal approach. We then study intermittency in the SABRA and dyadic shellmodels to extract, through comparison, the ingredients leading to intermittency. We then move on to 1D LL, applying the same methodology before giving perspectives about generalization to higher dimensions.

3.2 . The Kolmogorov 41 theory

Intermittency is often referred as *deviation from KG41*, a theory derived by A.N Kolmogrov in 1941 based on three hypothesis extracted from (29):

H1: *In the infinite Reynolds numbers, all the possible symmetries of the Navier-Stokes equation, usually broken by the mechanisms producing the turbulent flow, are restored in a statistical sense at small scales and away from boundaries.*

H2: *Under the same assumption as in H1, the turbulent flow is self-similar at small scales, i.e it possesses a unique scaling exponent h.*

H3: *Under the same assumption as in H1, the turbulent flow has a finite non-vanishing mean rate of dissipation ϵ per unit mass.*

We define the velocity increments at scale ℓ as $\delta \boldsymbol{u}(\boldsymbol{r}, \boldsymbol{\ell}) = \boldsymbol{u}(\boldsymbol{r} + \boldsymbol{\ell}) - \boldsymbol{u}(\boldsymbol{r})$. From this definition, one can define the structure function of order p as

$$S_p(\boldsymbol{\ell}) = \langle (\delta \boldsymbol{u}(\boldsymbol{r}, \boldsymbol{\ell}))^p \rangle \,. \tag{3.1}$$

[1] For the usual values $(a, b, c) = (1, -0.5, -0.5)$.

Using these quantities, several results can be derived, under hypothesis H1 to H3. A straightforward dimensional analysis leads to the well known Kolmogorov energy spectrum $S_2(\ell) = C\epsilon^{2/3}\ell^{2/3}$ [2].

In addition, Kolmogorov (30) derived an exact relation for the longitudinal third order structure function, called the *four-fifths law*:

$$S_{\parallel,3}(\boldsymbol{\ell}) = -\frac{4}{5}\epsilon\ell. \tag{3.2}$$

By combining Eq. 3.2 and H2, one can then obtain the scaling property of the structure functions, under Kolmogorov assumptions

$$S_p(\boldsymbol{\ell}) \propto \ell^{p/3}. \tag{3.3}$$

This scaling, and more generally the KG41 theory rely on the *global homogeneity* of the velocity field. Such homogeneity could be locally broken, by a singularity for example, leading to deviation from the so-called Kolmogorov scaling (Eq. 3.3) i.e *deviation from KG41*. Several measurements, in both experiments (31; 32) and numerical simulations (DNS (9), shellmodels (15; 33)) highlight strong deviations from the KG $p/3$ scaling.

Different models were proposed in order to account for the so-called *intermittent corrections* such as the $\beta - model$, the lognormal model and many others. Still, the most consistent remains, as of today, the *multifractal model* (MF) introduced by Parisi & Frisch (34; 3). KG41 relies on a *global scale invariance* implying a unique value $h = 1/3$ [3]. Yet, in the inviscid limit, the Navier-Stokes equations admit an infinite number of values for h which led Parisi & Frisch to instead consider *local scale invariance* implying new scaling exponents:

$$S_p(\boldsymbol{\ell}) \propto \ell^{\xi_p}, \tag{3.4}$$

$$\xi_p = \inf_h[ph + 3 - D(h)], \tag{3.5}$$

where $D(h)$, is the h-dependent dimension of the fractal set associated to h. This model succesfully reproduced the *intermittent corrections* in several studies (4; 5; 6; 7; 8) [4].

Note that in the context of KG41, the flatness of distribution is considered constant, a feature associated to gaussian statistics. Hence, deviation from KG41 can also be understood as deviation from gaussianity.

3.3 . A side note about gaussianity of statistics

In the context of turbulence, intermittency refers to the existence of burst of enstrophy. Although being rare, such extreme events are believed to cause deviation from the Kolmogorov theory 3.3. There are many manisfestation of intermittency in flows, from bursts of dissipation to deviation from the expected KG scaling of the so called structure functions. From a statistical point of view, the rareness of an event depends on the tails

[2] The second order structure function corresponds to the energy spectrum. Note that by taking the Fourier transform of this expression, we obtain the previously mentioned $k^{-5/3}$ spectrum.

[3] The scaling invariance refers to the change $(t, \boldsymbol{r}, \boldsymbol{u}) \rightarrow (\lambda^{1-h}t, \lambda\boldsymbol{r}, \lambda^h\boldsymbol{u})$.

[4] For a more comprehensive derivation of the MF, please refer to (29; 32; 35).

of the probability distribution functions (PDF). By studying the statistics of the velocity increments, one observes, in presence of an intermittent flow, deviation from Gaussianity for PDF tails.

Therefore, a key ingredient to observe intermittency in a model is the existence of a "fat tail" distribution for the velocity increments since purely gaussian statistics limit the existence of extreme events in both amplitude and occurrence.

In this section, we study the existence of non gaussian statistics in Log-lattices through the existence of *non-trivial* fourth order correlators.

3.3.1 . Moments of a Gaussian distribution

Let $X \sim \mathcal{N}(\mu, \sigma)$, then the moments of X are given by:

$$m_n = \mathrm{E}[X^n] = \frac{1}{\sigma\sqrt{2\pi}} \int_{\mathcal{D}} x^n e^{\frac{-1}{2}(\frac{x-\mu}{\sigma})^2}. \tag{3.6}$$

The value of the first four moments of a Gaussian distribution are given in Table. 3.1. In order to find deviations from Gaussianity in the tails of PDFs, one must look at the moment of order 4, namely the *kurtosis* that, for a "fatter tail" should be greater than for the usual normal distribution.

Note that, for a central distribution, we have $\mathrm{E}[X^{2n}_{\mu=0}] = (2n-1)!!\sigma^{2n}$ for even order moments and $\mathrm{E}[X^{2n+1}_{\mu=0}] = 0$ for odd order moments. The first equality can be understood in the following way: the statistics of an n-th order moments are associated to correlators $\delta(\sum_{i=0}^{n} k_i)$. In the case of Gaussianity, the Isserlis' theorem asserts that even order correlator can be decomposed into a product of the correlator of the second order.

As an example, the fourth order moments are associated to the correlators $\delta(k_1+k_2+k_3+k_4)$ as moments can be formally computed through the computation of cumulants. Yet, high order cumulants are non-zero only for $\sum_i \boldsymbol{k}_i = 0$.

Through Iserliss' theorem, we obtain for Gaussian statistics that $\delta(k_1+k_2+k_3+k_4) = \sum_{\theta\in\mathcal{S}_4} \delta(k_{\theta(1)}+k_{\theta(2)})\delta(k_{\theta(3)}+k_{\theta(4)})$ where θ is a cyclic permutation of $\mathcal{S}_4$, the ensemble of 4 elements cyclic permutations.

Deviation from gaussianity can then be seen as the existence of fourth order correlators that can not be decomposed as a product of second order correlators.

Order	Non-central distribution	central distribution
1	μ	0
2	$\mu^2+\sigma^2$	σ^2
3	$\mu^3+3\mu\sigma^2$	0
4	$\mu^4+6\mu^2\sigma^2+3\sigma^4$	$3\sigma^4$

Table 3.1: First four moments of a Gaussian distribution. A central distribution is characterized by a zero mean i.e $\mu = 0$.

3.3.2 . Gaussianity in Desnyansky-Novikov - Dyadic model

The simplest LL model is a n-D generalization of the Dyadic model, obtained for $\lambda = 2$. Modes, in the Fourier space, are then spaced according to a powerlaw of λ:

$$k_n = k_0 2^n, \tag{3.7}$$

where we set $k_0 = 1$.

Let (k, m, n, p) be four wavenumbers such that $0 = k + m + n + p$. Without loss of generality, we set $p = 1$ as it only rescales all other wavenumbers. We must then solve $k + m + n = -1$. In order for the sum to be odd, it is necessary for atleast one of the remaining wave number to be odd. This leaves us with two possibilites:

Case 1: $n = -1$ then $k + m = 0$.

Case 2: $n = 1$ then $k + m = -2$, dividing by 2, we obtain $k' + m' = -1$, where $(k', m') = (k, m)/2$. Keeping in mind that k' and m' are powers of 2, the only possibility to fulfill $k' + m' = -1$ is $(k', m') = (-2, 1)$ leading to $(-4n, 2n, n, n)$.

Therefore, the only *non-trivial* fourth order correlators are permutations of $(-4n, 2n, n, n)$. Still, it might be hard to actually observe deviations from Gaussianity due to the small number of *non-trivial* correlators.

Note that this result extends, by induction, to higher order correlators.

3.3.3 . Gaussianity in SABRA Shell model

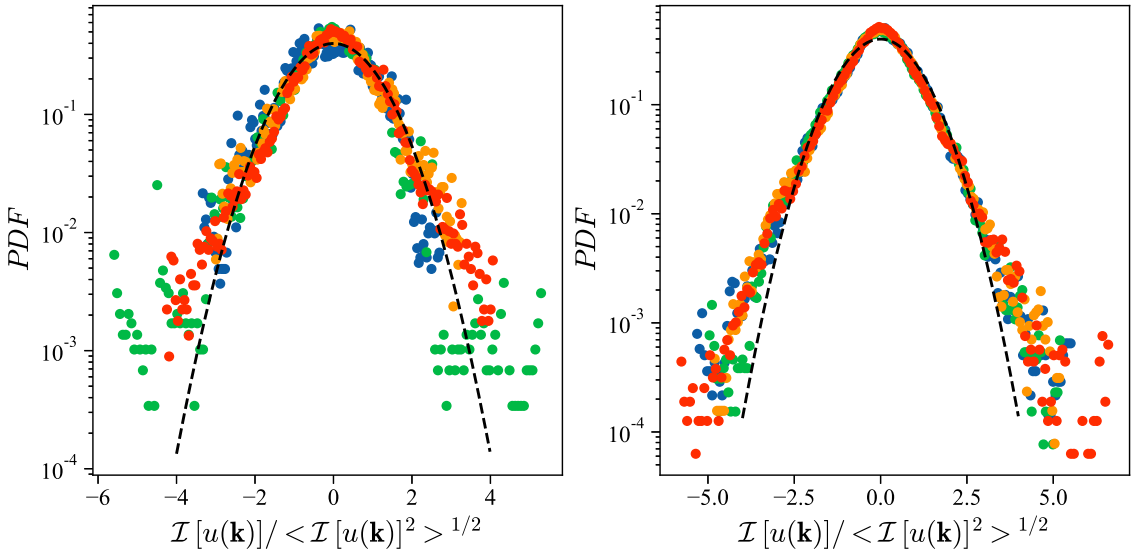

Figure 3.1: **PDF of the velocity fields in the inertial range** for different k. (3.1a) Results for Log-lattices with $\lambda = \phi$ (3.1b) Results for Log-lattices with $\lambda = \phi$ adding a large scale friction. The black dashed lines correspond to a normal distribution. The PDFs highlight deviation from gaussianity in the tails, suggesting intermittent behavior further confirmed through the analysis of structure functions.

We now consider Log-lattices with golden ratio as a spacing parameter (i.e $\lambda = \phi$). This choice of lattice spacing leads to a model equivalent, in 1D, to a SABRA shell model. The golden ratio being defined as $\phi^2 - \phi = 1$, we directly obtain:

$$k_{n+2} - k_{n+1} = k_n. \tag{3.8}$$

From this equation, it is possible to derive 2 other expressions of k_n for a given n (by shifting indices). Then, $k_{n+2} = k_{n+1} + k_n$ can be expressed in 4 different ways, using the various possible expression of k_{n+1} and k_n. One of the possibility being:

$$k_{n+2} = k_{n+1} + k_{n-1} + k_{n-2}. \tag{3.9}$$

From the definition of the lattice, we obtain the existence of several [5] *non-trivial* fourth order correlators, indicating possible deviations from gaussianity.

Fig. 3.1 presents the PDF of the velocity field $u(\boldsymbol{k})$ in the inertial range highlighting distribution with tails fatter than the Gaussian (black dashed line). Deviation from the Gaussian distribution is a first hint towards the presence of intermittency on Log-lattices with $\lambda = \phi$.

Following (17), we analyze intermittency through the existence of charge-discharge scenario, associated to a competition between backward and forward energy cascade. The analysis is first performed on two classical shellmodels, the SABRA and dyadic shellmodels. This analysis is then used to study the intermittency in the 1D-LL.

3.4 . Intermittency in Desnyansky-Novikov - Dyadic model

3.4.1 . Definitions

As mentioned before, by setting $\lambda = 2$, one obtains equations on log-lattices described by the dyadic model (16), reading in its inviscid and unforced form:

$$\partial_t u_n = k_n u_{n-1}^2 - k_{n+1} u_{n+1} u_n. \tag{3.10}$$

The forcing term f_n is once again located on the 5th and 6th shells. In all dyadic simulations, we set $N = 35$ modes and $\nu = 1e-10$ allowing us to observe an extended inertial domain to extract more accurately the exponents of the structure functions.

3.4.2 . Fixed points and energy transfers

Consider once again a solution $u_n = ik_n^\alpha$ of Eq. 3.13. Such solution is a fixed point of the system if the following condition is fulfilled:

$$\lambda^{-2\alpha} - \lambda^{\alpha+1} = 0, \tag{3.11}$$

leading to a unique fixed point $\alpha^{KG} = -1/3$. By deriving a kinetic energy budget and summing up to the n-th shell, one obtains:

$$\Pi_n = k_{n-1} u_n u_{n-1}^2 - C, \tag{3.12}$$

where C is a constant. The system is therefore only driven by a direct cascade. This is indeed what we observe in Fig. 3.2a, where no energy is stored in shells $k \leq k_f$ where k_f is the forcing scale.

Figure 3.2b reports the exponents of the structure functions defined in Eq. 1.6, highlighting no intermittency and a perfect Kolmogorov scaling.

The dyadic model $\lambda = 2$ does not exhibit any intermittent features. Yet, using LL one can set $\lambda = \phi$, formally equivalent in 1D to a SABRA shell model (15) known for its intermittent features. In the following section, we propose to study intermittency in the classical SABRA shellmodel before switching to the *SABRA Log-lattices*.

[5] Note that one has to add every permutations of the previously proposed correlators.

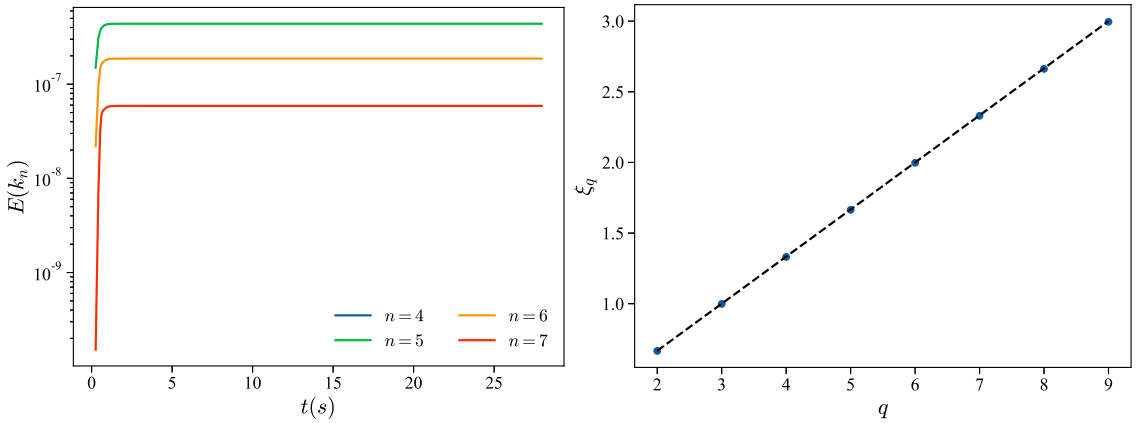

(a) (b)

Figure 3.2: **Time series of the kinetic energy by shell and exponents of the structure functions.** (3.2a) Kinetic energy for shells located around the forcing scale k_f. Due to the absence of backward cascade (Eq. 3.12) we observe no energy in the shells located at scales $k < k_f$. (3.2b) Exponents of the structure functions for the dyadic model Eq. 3.10. The black dashed line corresponds to the KG prediction with slope $1/3$.

3.5 . Intermittency in SABRA shell model

3.5.1 . Definitions

Let us first recall that the SABRA shell model is defined, in the inviscid and unforced case, as follows:

$$\partial_t u_n = i(ak_{n+1}u_{n+2}\overline{u_{n+1}} + bk_n u_{n+1}\overline{u_{n-1}} - ck_{n-1}u_{n-2}u_{n-1}), \tag{3.13}$$

where $(a, b, c) \in \mathbb{R}^3$ such that $a + b + c = 0$ to ensure the kinetic energy conservation in the inviscid and unforced limit. For simplicity, we assume that $a = 1$. Note that the bar is associated to the complex conjugate.

In our simulations, we use a forcing term f_n located on the 5th and 6th shells and a number $N = 35$ of shells. The viscosity is set to $\nu = 1e - 10$ in order to obtain a wide inertial range. The location of the forcing term has been chosen in order to be able to properly quantify the existence of an inverse cascade in the system, starting from zero initial conditions.

3.5.2 . Fixed points and energy transfers

Consider a solution $u_n = ik_n^\alpha$ of Eq. 3.13. Such solution is a fixed point of the system if the following condition is fulfilled:

$$\lambda^{6\alpha} + \frac{b}{\lambda}\lambda^{3\alpha} + \frac{c}{\lambda^2} = 0. \tag{3.14}$$

Then, the system exhibits up to two fixed points for the energy, the first one being the usual Kolmogorov fixed point $\alpha^{KG} = -1/3$. The second fixed point only exists for $c > 0$ and is defined as $\beta = \frac{1}{3}(-1 + \frac{\ln c}{\ln \lambda})$. Note that the vast majority of the studies on the SABRA are performed using $c < 0$, getting rid of the possible effects of that second fixed point.

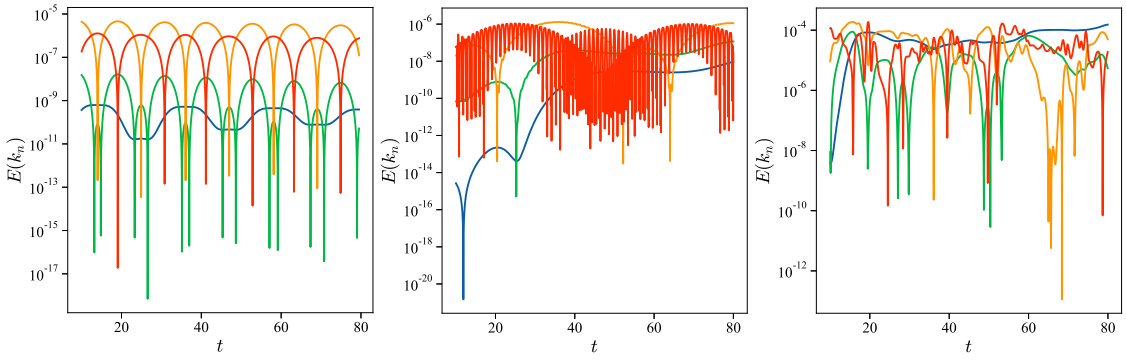

(a) (b) (c)

Figure 3.3: **Time series of the kinetic energy in the first four shells** for different values of b. (3.3a) $b = -0.3$ $(c = -0.7)$ (3.3b) $b = -0.5$ $(c = -0.5)$ (3.3c) $b = -0.7$ $(c = -0.3)$. All simulations are performed using a standard SABRA shell model with $\lambda = 2$. As $b \to 0$, we observe an increased backward cascade leading to energy accumulation in the first modes, located before the forcing term.

By deriving a kinetic energy budget and summing it over the shells, one can show that the energy transfer at shell n is given by:

$$\Pi_n = 2k_{n+1}(D_{n+1} - \frac{c}{\lambda}D_n), \tag{3.15}$$

where $D_n = \Im(\overline{u_{n-1}u_n}u_{n+1})$. The model features both a backward and forward energy cascade, which intensities are directly linked to the chosen value of c. A study (36) on a similar model, the GOY model, underlines that by taking $c \xrightarrow[c<0]{} 0$ the system is more and more chaotic. With such values for c, the inverse cascade D_{n+1} is no longer negligible and leads to energy accumulation at big scales that can suddenly cascade to small scales (Fig. 3.3b & 3.3c). Taking a too big value of $|c|$ would lead to a system only governed by the forward cascade (Fig. 3.3a).

An additionnal fixed point can be defined as "fluxless" consisting of a zero flux fixed point in which the simulations can get trapped. Using this definition, the only solution is once again $\beta = \frac{1}{3}(-1 + \frac{\ln|c|}{\ln\lambda})$ regardless of the sign of c.

The competition between forward and backward cascade could lead to intermittency as it was shown in the GOY model (17) that charge-discharge scenario leads to intermittent features. In the following, we investigate the presence of intermittent features for different parameters c, tuning the balance between the forward and backward cascades.

3.5.3 . Phase space intermittency

This model has been extensively studied (15; 17; 18; 19) but mostly in the domain $-1 < \frac{c}{a} < 0$ in which it exhibits intermittency. In this chapter, we define the structure functions as in Eq. 1.6[6]:

$$S_p(k_n) = \left\langle |\frac{\Pi_n}{k_n}|^{p/3} \right\rangle .$$

[6]The results are independent of the choice of the structure functions' definition.

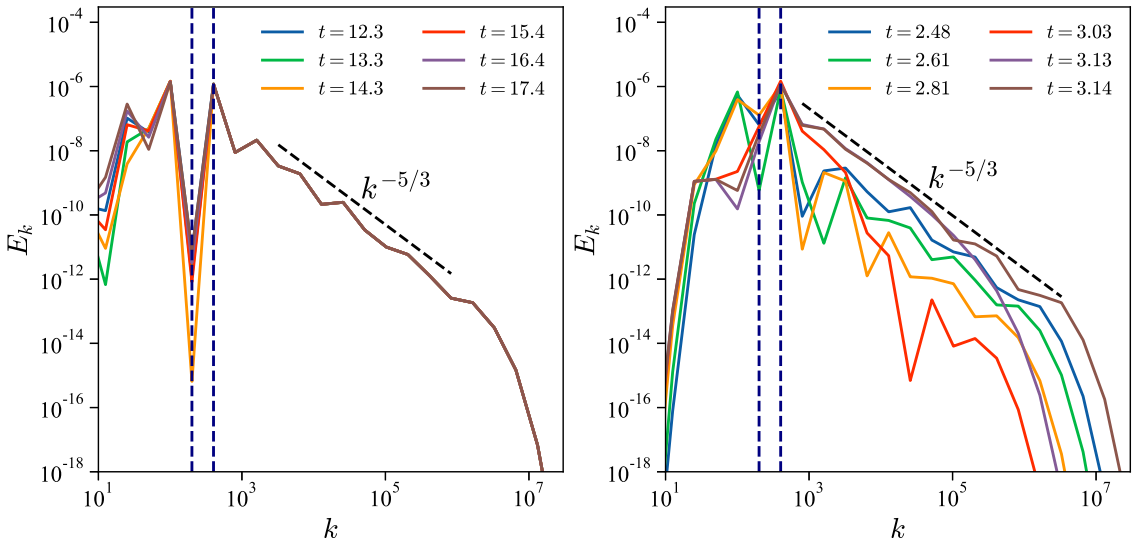

(a) (b)

Figure 3.4: **Energy spectra at different time** for different values of b. (3.4a) $b = -0.3$ $(c = -0.7)$, little to no fluctuation in the inertial range. (3.4b) $b = -0.5$ $(c = -0.5)$, strong fluctuations of the exponent in the inertial range. All simulations are performed using a standard SABRA shell model with $\lambda = 2$. The vertical dashed line represent the forcing term.

In the absence of intermittent features coming from the cascade term (i.e a flat energy transfer), one then expects (1.6) the structure functions to scale as $S_p(k_n) \propto k_n^{-\xi_p}$ with $\xi_p = p/3$. Any deviation from that prediction is interpreted as a sign of intermittency in the Fourier space. As previously mentioned, the choice of the free parameter c is crucial to observe intermittent features in the model. As developped in (36), the existence of a strong enough backward cascade is a necessity as it allows the existence of bursts of energy rapidly cascading from big to small scales, changing the local exponent of the spectrum (Fig. 3.4). Those rapid changes can then lead to deviations from the KG prediction $\xi_p \propto p/3$.

Figure 3.5a shows the extracted exponents for various values of (b, c) highlighting the absence of intermittence in the forward cascade driven case (Fig. 3.3a). However, by taking the classical $(b, c) = (-0.5, -0.5)$ one obtains intermittent exponents that can be associated to the frequent and strong charge-discharge events occuring in the system at big scales (Fig. 3.3b). Still, taking a too low value of b (i.e b close to 0) implies a strong depreciation of the forward cascade meaning that most of the modes at small scales are almost never populated. One then obtains exponents much smaller that KG predictions (Fig. 3.5a orange triangles). Our simulations confirms the finding of previous studies on the GOY model, that shares many features with the SABRA model (15).

Let us define the 1D - instantaneous - energy dissipation $\epsilon = \nu \sum_n k_n^2 \|u_n\|_2^2$. In presence of intermittency, one expects to find intermittent behaviour in the time series of ϵ. Figure 3.5 indeed confirms, through the time series of ϵ for different values of (b, c), the depreciation of intermittency for systems driven by a forward cascade (Fig. 3.5b).

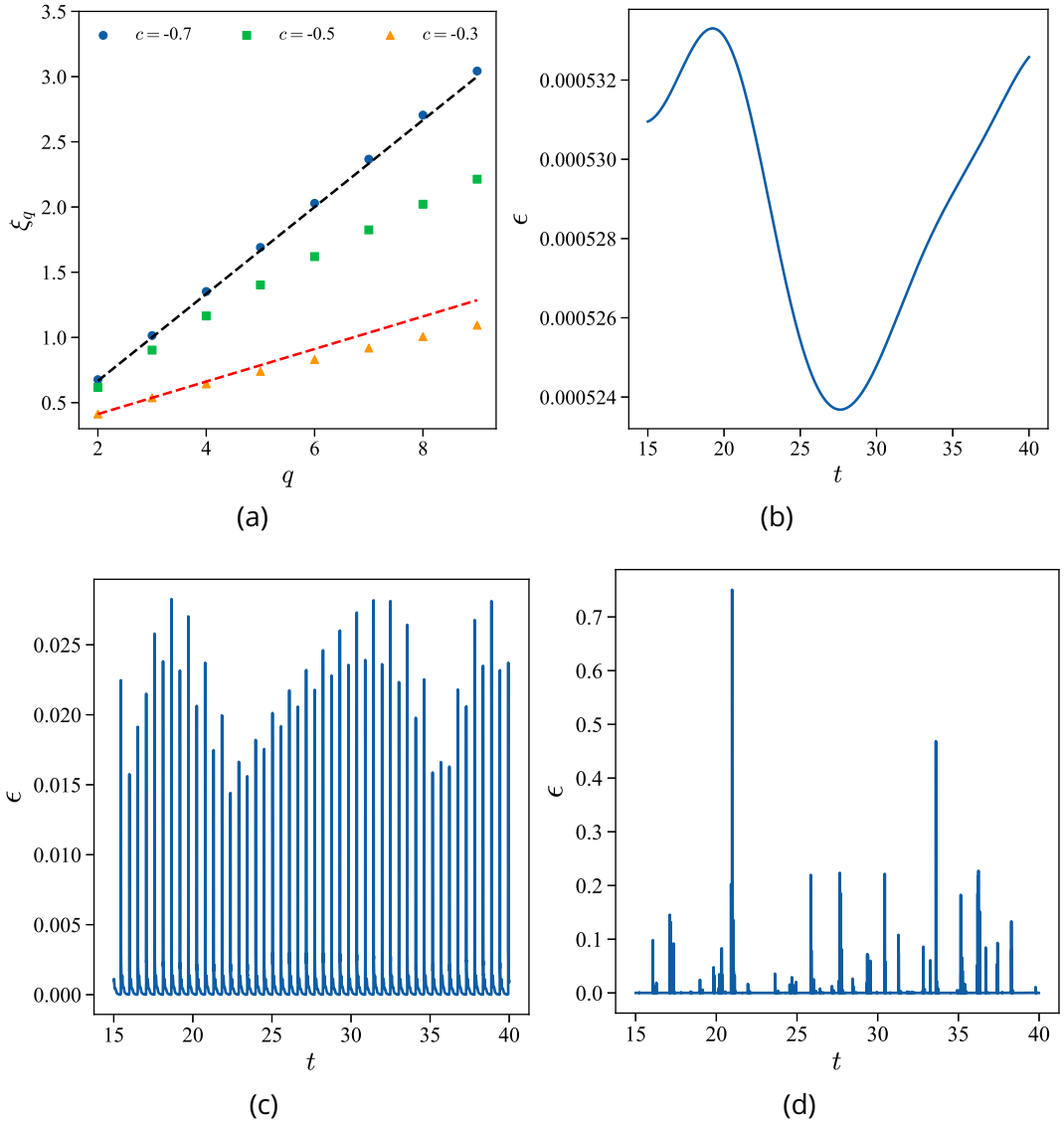

Figure 3.5: **Exponents of the structure functions and time series of the instantaneous energy dissipation** ϵ for different values of b. (3.5a) Exponents of the structure functions (Eq. 1.6). The black dashed line corresponds to the KG prediction with slope $1/3$ while the orange dashed line has a slope of 0.12. Note that the blue dots have a slope slighty steeper that KG with a value of 0.36. (3.5b) $b = -0.3$ $(c = -0.7)$ (3.5c) $b = -0.5$ $(c = -0.5)$ (3.5d) $b = -0.7$ $(c = -0.3)$. All simulations are performed using a standard SABRA shell model with $\lambda = 2$. As $b \to 0$, we observe a depreciation of the intermittent behavior in the time series in agreement with previous findings.

The choice of the parameter c has a great influence over the system. Indeed, its value sets the balance between the forward and backward cascade, allowing or not the charge-discharge scenario piloting intermittency. In the following, we apply the same methodology to study the case of LL as a peculiar case of the SABRA shellmodel.

3.6 . Log-lattices as a SABRA shellmodel

We will now interests ourselves to the log-lattices case. The dyadic model presenting no intermittency, we will limit our study to the $\lambda = \phi$ case.

3.6.1 . Definitions

As mentioned before, in the peculiar case of a 1D log-lattice, with $\lambda = \phi$, one gets a SABRA shellmodel with $(a, b, c) = (-1/\lambda, -1, \lambda)$. One can recover the usual signs by considering the grid's symmetry. Still, such values lie outside of the interval of the usually used parameters (b, c).

Following Section 3.5, one expects the system to be mostly driven by the forward cascade, atleast for modes at scales $k > k_f$[7]. Therefore, the system should exhibit little to no intermittency.

3.6.2 . 1D case with large scale forcing

Before tackling the question of intermittency in 3D log-lattices, it is important to start by a 1D investigation. All simulations presented in this section will be performed in 1D using a forcing term located on the shells (2, 3).

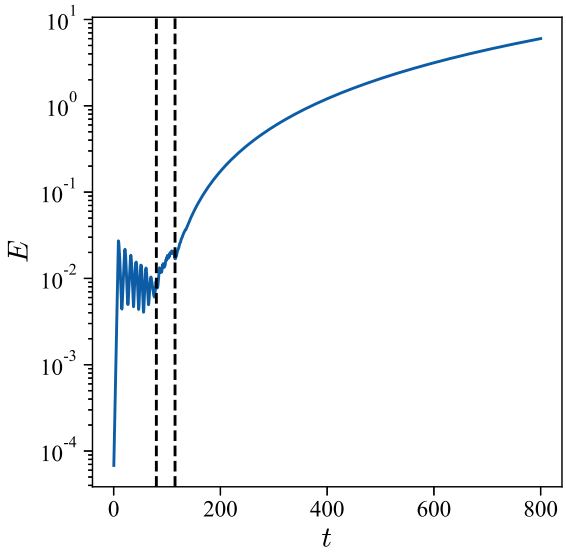

Figure 3.6: **Time series of the total kinetic energy** for a forcing term located near the grid boundary. The system exhibits two behaviors, first reaching a steady state until $t \simeq 80s$ to then switch to an exponential growth at $t > 115s$. The transition area is represented in between black dashed lines.

In this section, we set $k_f = (k_2, k_3)$ such that the forcing acts close to the grid boundaries. As previously underlined in Section 3.5, the system presents both a foward and backward cascade. Such statement still holds true in the log-lattice case and can lead to different scenarios. The peculiar values of the (b, c) parameters should lead to a system mostly driven by a forward cascade. Still, due to the existence of other fixed-point (flux-

[7] k_f being the forcing scale.

less fixed point for example) one can not completely discard the possibility of observing a system driven by a backward cascade.

Figure 3.6 shows the evolution of the system total kinetic energy. Until $t = 80s$, the system is mainly driven by the forward cascade (Fig. 3.7a & 3.7b), reaching a steady state. We then observe a transition area for $t \in [80, 115]s$ after which the system becomes mainly driven by the backward cascade. Hence, we observe an accumulation of energy in the first modes (Fig 3.7d) and a depletion at smaller scales (Fig. 3.7d), leading to the rise of the total kinetic energy (Fig. 3.6 after the dashed lines).

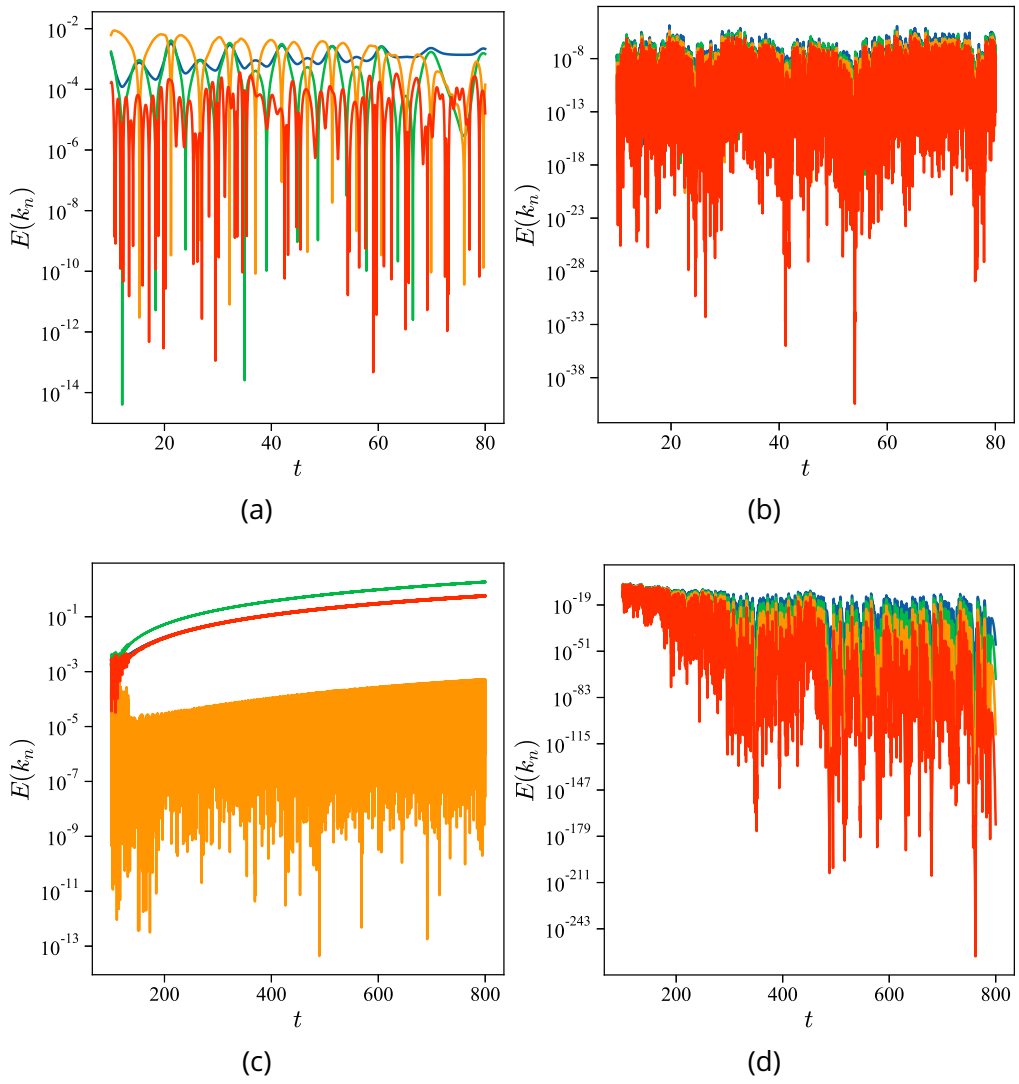

Figure 3.7: **Time series of the energy by shell and intermittency for a "SABRA" log-lattice.** for the two regimes highlighted in Fig. 3.6. (3.7a) & (3.7b) Shell energy at small and big scales in the forward cascade case. (3.7c) & (3.7d) Shell energy at small and big scales highlighting the transition to a backward cascade with energy leaving the small scales to accumulate at larger scales.

Note that in both scenarios, we still observe energy discharges that led to intermittency in Section 3.5. More specifically, Fig. 3.7 highlights (atleast for $n > 2$) a greater

amount of discharge than the $(b, c) = (-0.3, -0.7)$ case (Fig. 3.3a) and less than the $(b, c) = (-0.5, -0.5)$ case. It can then be expected to observe small deviations from KG predictions.

Figure 3.8a shows that indeed, one observes small deviations in both zones from KG prediction. Note that unlike the SABRA $(b, c) = (-0.5, -0.5)$ (Fig. 3.5a green squares) the intermittency is here closer to a bifractal with a second slope of roughly 0.26. In addition, we once again find that the backward cascade case has exponents lower than the forward case as previously highlighted in Section 3.5. The time series of the energy dissipation confirms the presence of intermittent behavior in the forward cascade case (Fig. 3.8b before dashed lines and on the inset). Also note that the energy dissipation in the second zone (after the dashed lines) starts to rise again indicating that the system is starting to switch back to a forward cascade.

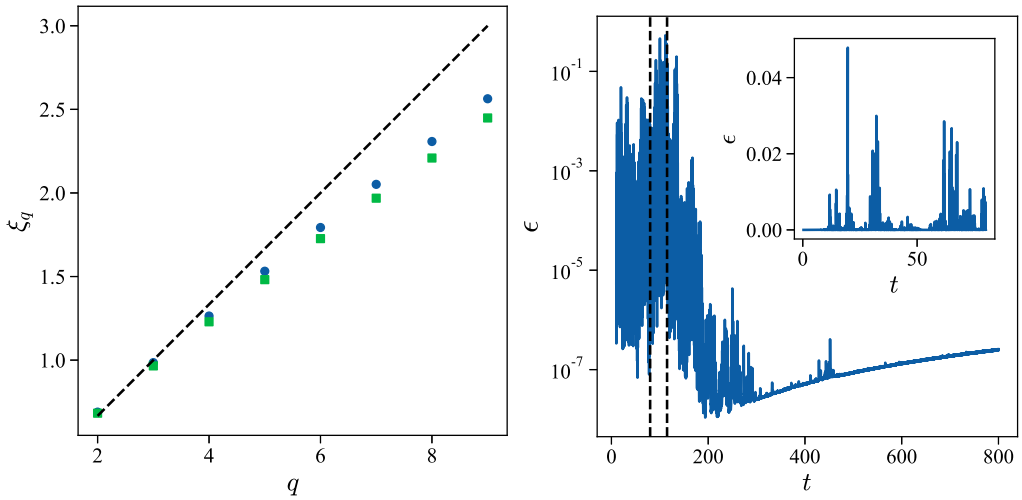

Figure 3.8: **Intermittency on LL SABRA** (3.8a) The blue dots (resp. green squares) represent the structure functions exponents in the first (resp. second) zone of Fig. 3.6 $t < 80s$ (resp. $t > 115s$). The black dashed line corresponds to the KG prediction $\xi_q \propto q/3$. (3.8b) Time series of the instantaneous energy dissipation ϵ. The black dashed lines represent the transition zone between forward $(t < 80s)$ and backward $(t > 115s)$ cascade case of Fig. 3.6. Both cases present intermittent features with bursts of dissipation.

The existence of the backward cascade allows for slightly intermittent exponents but also leads to strong energy accumulation in the first shells that does not cascade for a very long time. Figure 3.8b emphasizes the slow return of the energy in the last shell as the dissipation slightly increases over time. To avoid an excessive stagnation of the energy at large scales, we propose to add a small friction, dissipating a part of this energy.

3.6.3 . Friction at large scale

As previously highlighted, the system can oscillate between two regimes dictated either by a forward or a backward cascade. While both cases contribute to the intermittent behavior of the model, it is important to emphasize the forward cascade case while not completely prevent the existence of the inverse cascade. In fact, a too strong inverse

cascade leads to energy accumulation in the first shells (Fig. 3.6, after dashed lines) and energy depreciation in the last ones.

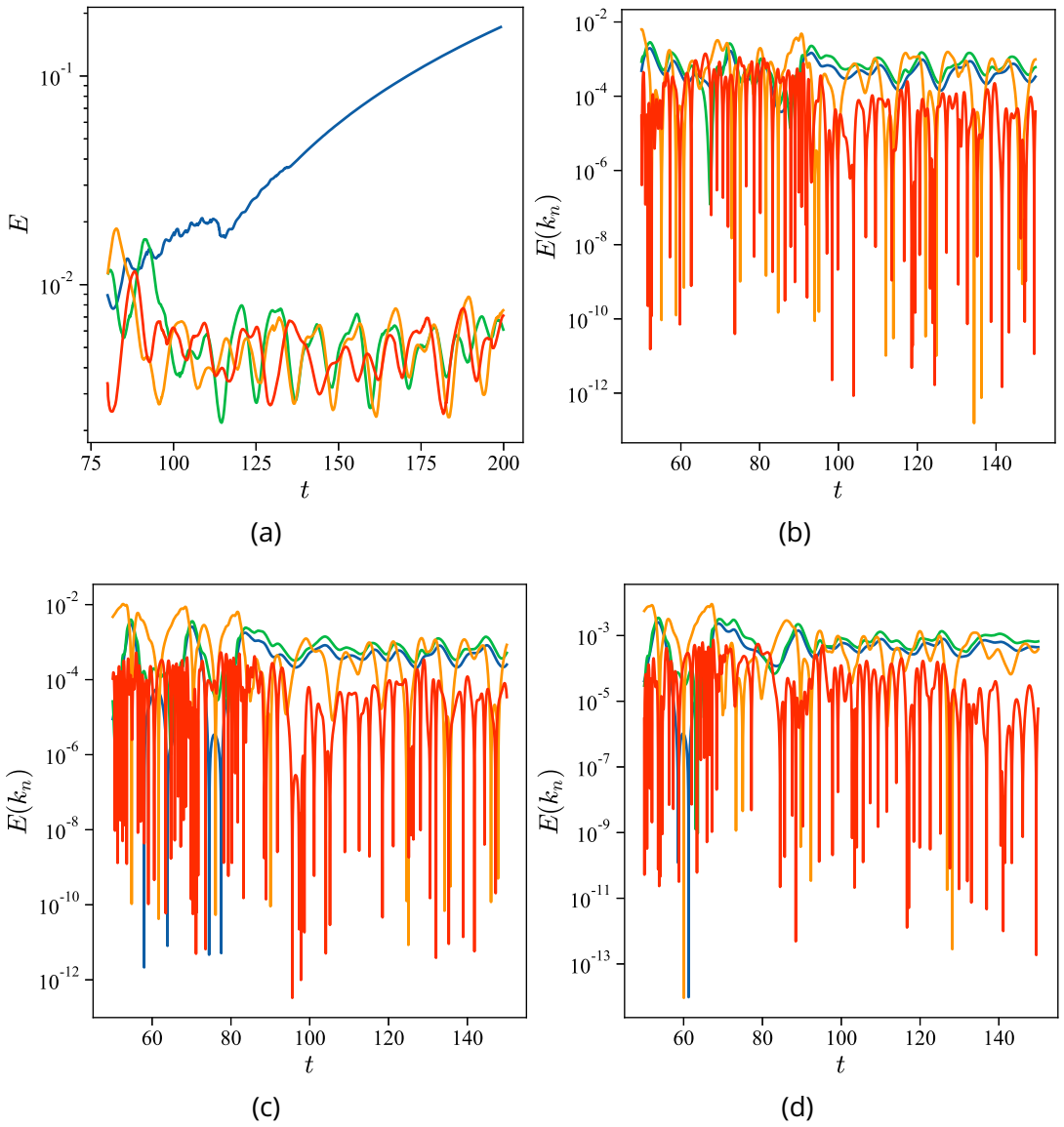

Figure 3.9: **Time series of the total and shell energy.** (3.9a) Time series of the total kinetic energy (blue, green, orange, red) corresponding to ($\alpha_n = 0$, $\alpha_n = 0.2$, $\alpha_n \sim \mathcal{U}(0.1, 0.3)$, $\log \alpha_n \sim \mathcal{N}(0.2, 0.2)$). Figures (b) to (d) correspond to energy in the first shells. (3.9b) Determinist damping at small scales $\alpha_n = 0.2 \; \forall n < 2$. (3.9c) Stochastic damping $\alpha_n \sim \mathcal{U}(0.1, 0.3)$. (3.9d) Stochastic damping $\log \alpha_n \sim \mathcal{N}(0.2, 0.2)$. All the proposed frictions lead to energy oscillations without accumulation.

In order to avoid the excessive accumulation of energy at large scale one can add a small friction on the modes located at $k < k_f$. The equation then reads:

$$\partial_t u_n = i(a k_{n+1} u_{n+2} \overline{u_{n+1}} + b k_n u_{n+1} \overline{u_{n-1}} - c k_{n-1} u_{n-2} u_{n-1}) - \alpha_n u_n + f_n - \nu k_n^2 u_n \quad (3.16)$$

where f_n is the forcing term and $\alpha_n = 0 \; \forall n > n_f$[8]. In our case, we once again set $k_f = (k_2, k_3)$.

By adding a friction term, we keep the energy in the first shell under control (Fig. 3.9), reinforcing the charge-discharge scenario that previously led to intermittency. It is then expected to recover intermittent exponents with stronger deviation from KG prediction. Figure 3.10a presents the extracted exponents, highlighting the presence of intermittent features for various damping form (deterministic and stochastic). Such features are also found in the time series of the dissipation $\epsilon(t)$ (Fig. 3.10b). It is also interesting to underline that ϵ ressembles much more (with respect to the case $(b, c) = (-0.5, -0.5)$ of Section 3.5) the traditional intermittency that can be found in DNS and experiments.

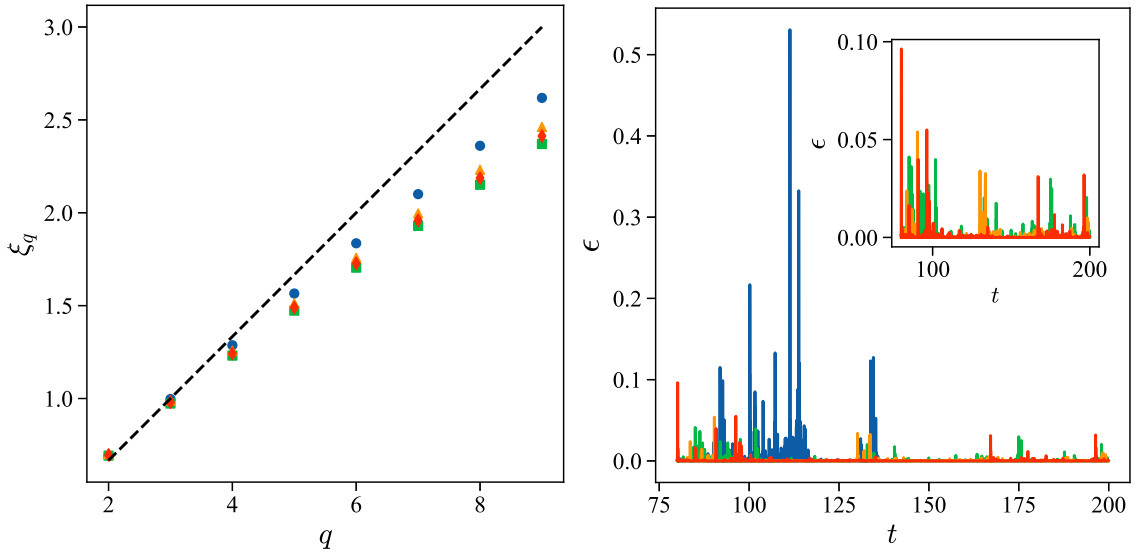

(a) (b)

Figure 3.10: **Intermittency for a "SABRA" log-lattice with large scale friction.** Blue plots corresponds to LL SABRA without damping (data of Fig. 3.8a) other colors (green, orange, red) are associated with ($\alpha_n = 0.2$, $\alpha_n \sim \mathcal{U}(0.1, 0.3)$, $\log \alpha_n \sim \mathcal{N}(0.2, 0.2)$).(3.10a) Exponents of the structure functions highlighting departure from KG prediction $\xi_q \propto q/3$ (black dashed line). (3.10b) Time series of the energy dissipation presenting intermittent features.

Note that the extracted exponents of Fig. 3.10a in the damped case present stronger deviation from KG prediction. A possible explanation being that the damping partially mimics non local interaction that are usually absent in LL.

Throughout this study we found fingerprints of intermittency in 1D "SABRA" Log-lattices through charge-discharge scenario. This charge-discharge leads to deviation, of the exponents of structure functions, from Kolmogorov's prediction. Yet, this study was only performed on 1D systems and must be generalized to n-D systems, $n > 1$. Unfortunately, due to time constraint this extension has been initiated but will be left for the future. In the next section, some perpectives are presented raising hope for intermittency in n-D LL.

[8] n_f is the minimum index of forced shells.

3.7 . Perspectives

This chapter is the subject of on-going work and will be left for future work, either by myself or a colleague. Still here are some perspectives for intermittency in 3D LL.

3.7.1 . 3D case

We now investigate the case of intermittency in 3D LL simulations with spacing parameter $\lambda = \phi$. A first and most naive approach is to compute, just as in the 1D case, the structure functions (Eq. 1.5). By doing so, we observe no deviation from the Kolmogorov exponents (Fig. 3.12, blue circles).

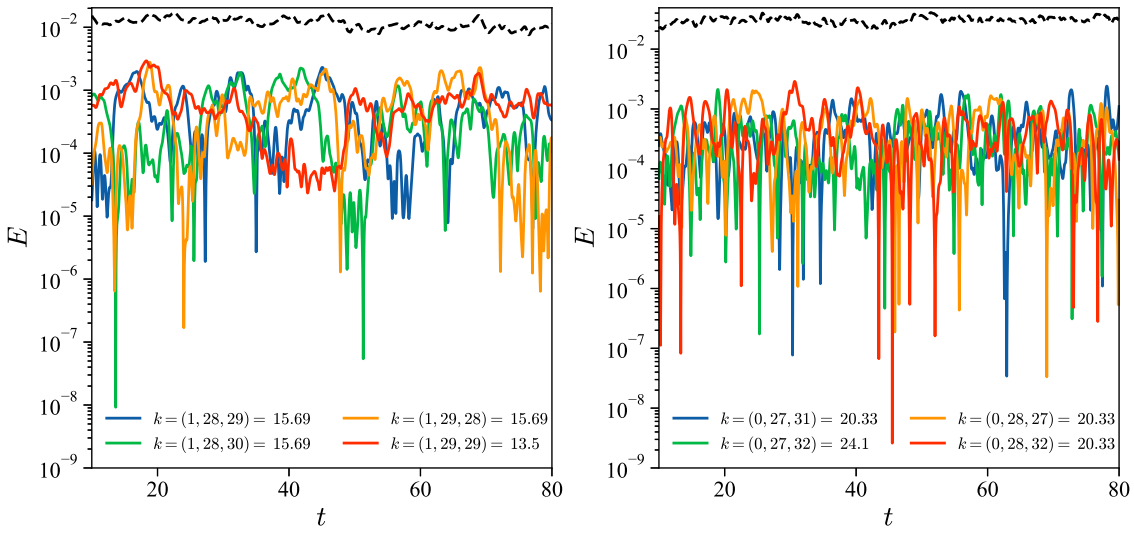

(a) (b)

Figure 3.11: **Time series of the "wavenumber like" energy in a 3D NSE simulation** with $\nu = 1e-09$, $N = 30^3$. (3.11a) Modes located in the first shell. (3.11b) Modes located in the second shell. The black dashed lines correspond to the total contribution of all mode, i.e the sum of all the energy inside the considered shell. One observes, while considering every mode in a shell, an averaging effect killing the charge-discharge scenario due to summation over uncorrelated modes.

An explanation to this phenomenon is that the n-D extension of LL can be understood as a collection of weakly coupled shell models. Therefore, performing a summation over all modes of wavenumber belonging to a shell $k^i \leq \|\boldsymbol{k'}\|_2 < \lambda k^i$ leads to the summation of non-correlated wavenumbers (i.e belonging to different shellmodels that are not coupled together). As a result, the summed energy presents no charge-discharge scenario and appears smoother (Fig.3.11) while the "wavenumber-like" energy varies similarly to the 1D case (Fig. 3.3a).

These wavenumber-like variations raise hope for intermittency in n-D LL. Everything comes down to wisely choosing the definition of the structure functions. A naive approach is to fix, in 3D, (k_y, k_z) and only navigate the grid in the x direction. By doing so, we extract intermittent exponents, with ξ_2 slightly lower from the usual $\xi_2^{KG} = 2/3$ and$\xi_2^{int} = 0.72$. Still, we observe deviations from KG41 (Fig. 3.12, green squares) likely due to less averaging

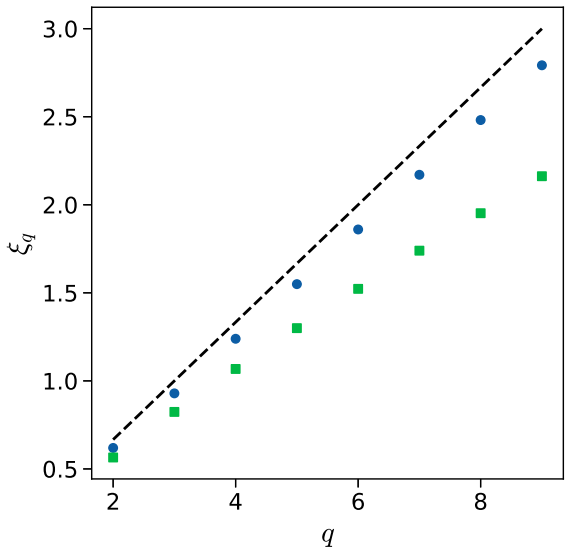

Figure 3.12: **Exponents of structure functions in a 3D NSE simulation** with $\nu = 1e-09$, $N = 30^3$. Blue circles correspond to exponents extracted from the structure functions of Eq. 1.5 (i.e averaging over every modes). Green squares correspond to the exponent extracted from structure functions along the x-direction i.e fixed $(k_y, k_z) = (k_0, k_0)$ varying k_x.

effect. Nevertheless, only navigating the x-direction is not equivalent to a 1D shellmodel as modes are not fully correlated. In addition, the effects of varying the frozen directions (k_y, k_z) is unclear and therefore must be studied.

3.7.2 . Backward adaptative grid

As previously seen in the 1D case, LL with $\lambda = \phi$ exhibits both a forward and backward cascade, leading to the accumulation of energy in the first shells (Fig.3.6).

The current framework allows us to adapt the grid size to reach smaller and smaller scales during a simulation. Applying that same methodology backward (i.e building bigger and bigger scales) could reduce the energy stacking and therefore substitute the large scale friction previously added.

4 - Onsager's conjecture and the existence of weak solutions

4.1 . Introduction

In previous chapters, we investigated the presence of potential singularities through the development of blowup solutions in 1D and 3D Log-lattices simulations. We showed that the development of the blowup is associated to a collapse of a complex singularity onto the real axis, leading to a strong increase of enstrophy. This increase takes form of enstrophy bursts that manisfest in dissipation usually leading to intermittency. Intermittency or *deviation from KG41* can be explained using multi-fractal theory (3). This theory allows to measure the probability of apparition of a singularity with a given exponent, characterizing how the velocity gradients diverge in the inviscid limit, possibly under the shape of a dissipative singular solution.

Dissipative weak solutions are special in the sense that they support a new types of conversion of mechanical energy into heat, piloted by their singular behavior. In the presence of a force, such solution may be able to absorb completely the energy input by the work of the force, allowing establishment of a stationary inviscid forced state. We can then reach a situation where it is possible to sustain an arbitrarily large amount of mechanical energy in the fluids, for any given force, without any viscosity. The non-dimensional parameter characterizing such process is the efficiency $\mathcal{E} = E/E_i$, where E is the stored kinetic energy per unit mass and $E_i = f_0 \ell_f$ is a measure of the mechanical injected energy input per unit mass due to an applied force of amplitude f_0 over a characteristic scale ℓ_f. The existence of weak dissipative solutions is of great interest as it connects potential singularities of the underlying equations of fluid motions to the observed *anomalous dissipation* [1] through the Onsager conjecture (2).

In this chapter, we show that that the efficiency can be used to explore and unfold the phase space of possible inviscid singular solutions. This idea is difficult to implement using direct numerical simulations because the development of irregular solutions generates finer and finer structures, that can only be resolved by mesh refinement procedures, at an increasing numerical cost. We thus explore this idea on a simple but tractable system, made of fluids projected on Fourier log-lattices (LL) with effective resolutions up to 402620^3 Fourier modes.

4.2 . Definitions

We consider the forced incompressible Navier-Stokes equations given by:

$$\partial_t \boldsymbol{u} + (\boldsymbol{u} \cdot \boldsymbol{\nabla})\boldsymbol{u} = -\boldsymbol{\nabla} p + \nu \boldsymbol{\Delta} \boldsymbol{u} + \boldsymbol{f}, \tag{4.1}$$

$$\nabla \cdot \boldsymbol{u} = 0, \tag{4.2}$$

where $\boldsymbol{u}$ is the velocity, p is the pressure, $\boldsymbol{f}$ is a force and ν is the viscosity. We have set the constant density equal to 1.

[1] Please, refer to the general introduction for a reminder on anomalous dissipation.

We define the spatial average of any function $\psi(x,t)$ as $\langle\psi\rangle = (\int d\boldsymbol{x})^{-1}\int d\boldsymbol{x}\psi$ and define the efficiency $\mathcal{E}$ by:

$$\epsilon_I = \langle|\boldsymbol{f}\cdot\boldsymbol{u}|\rangle, \tag{4.3}$$

$$\mathcal{E} = \frac{\langle\boldsymbol{u}\cdot\boldsymbol{u}\rangle}{L_f\langle\boldsymbol{f}\cdot\boldsymbol{f}\rangle^{1/2}}, \tag{4.4}$$

where L_f is a characteristic scale of forcing, defined e.g. as $(2\pi/L_f)^2 = (1/3)\langle\nabla\boldsymbol{f}\cdot\nabla\boldsymbol{f}\rangle/\langle\boldsymbol{f}\cdot\boldsymbol{f}\rangle$.

In the sequel, we denote: $E = \langle\boldsymbol{u}\cdot\boldsymbol{u}\rangle$ and $f_0 = \langle\boldsymbol{f}\cdot\boldsymbol{f}\rangle^{1/2}$. Based on Isett theorem, we call non dissipative a solution of Eq. 4.1 such that $E(k)\propto k^{-1-2h}$ with $h > 1/3$. Considering that the solutions may extend from a cut-off $1/L_f$ to infinity in case of blow-up, we further restrict the physically admissible solutions to $h > 0$, so that the total energy stored in the fluids $2\int_{2\pi/L_f}^{\infty} E_K(k)dk$ remains finite.

It follows, using an energy spectrum $E(k) = C_K\epsilon_I^{2/3}k^{-1-2h}$, that the total kinetic energy stored is given by:

$$E(h,\epsilon_I) = 2\int_{2\pi/L_f}^{\infty} E_K(k)dk = C_k\epsilon_I^{2/3}h^{-1}(\frac{L_f}{2\pi})^{2h}, \tag{4.5}$$

where C_K is the Kolmogorov constant.
By Cauchy-Schwartz inequality, we obtain an exact bound linking ϵ_I and $\mathcal{E}$:

$$\frac{\epsilon_I L_f}{E^{3/2}} \leq \frac{1}{\mathcal{E}}, \tag{4.6}$$

the equality being achieved when $\boldsymbol{f}$ is parallel to $\boldsymbol{u}$.

Finally, we can derive another bound involving ϵ_I for a solution of INSE which energy is bounded by the ideal Kolmogorov case $E(1/3,\epsilon_I)$ (Eq.4.5). Injecting this energy in 4.6, we obtain:

$$\frac{\epsilon_I L_f}{E^{3/2}} \geq \frac{2\pi}{(3C_K)^{3/2}} = \frac{1}{\mathcal{E}^*}, \tag{4.7}$$

where $\mathcal{E}^*$ is a critical efficiency below which one necessarily has $h > 1/3$.

4.3 . Reversible Navier-Stokes

4.3.1 . Motivations

To reach solutions at finite efficiency, one must add a non-zero forcing. If the viscosity is further held constant, interplay between forcing and viscous dissipation in the presence of non-linearities results in fluctuations of the total energy. To remain in a framework of solutions at constant energy E, like in the inviscid case, we allow a time-dependent viscosity $\nu_r(t)$, and monitor it at each time-step so as to keep energy constant in time (20; 37). We call this viscosity the reversible viscosity $\nu_r(t)$ as it is the viscosity that is necessary to ensure the time reversibility.

4.3.2 . Time reversibility and reversible viscosity

We recall that the Navier-Stokes equations describing a fluid of viscosity ν, subject to a force $\boldsymbol{f}$, are given by:

$$\partial_t \boldsymbol{u} + (\boldsymbol{u} \cdot \boldsymbol{\nabla})\boldsymbol{u} = -\boldsymbol{\nabla} p + \nu \boldsymbol{\Delta} \boldsymbol{u} + \boldsymbol{f}, \tag{4.8}$$

where **u** is the velocity, p is the pressure, and we have set the constant density equal to 1. Due to the presence of the dissipative term $\nu \boldsymbol{\Delta} \boldsymbol{u}$, the dynamics induced are clearly irreversible as (4.8) is not left-invariant under the time-reversal symmetry:

$$\mathcal{T} : t \to -t; \boldsymbol{u} \to -\boldsymbol{u}; p \to p. \tag{4.9}$$

This is true even in the presence of a force that is symmetric by time-reversal (which will be the case of every forcing used in this thesis).

Following the work of Shukla et al. (20), we introduce a reversible version of the NSE by defining a (time dependent) reversible viscosity ν_r, which conserves the total kinetic energy $E = \frac{1}{2}\int_{\mathcal{D}} \|\boldsymbol{u}\|_2^2 \, \mathrm{d}\boldsymbol{x}$ over our domain $\mathcal{D}$. The expression of ν_r can be derived from an energy budget under the constraint $\partial_t E = 0$:

$$\nu_r[\boldsymbol{u}] = \frac{\int_{\mathcal{D}} \boldsymbol{f} \cdot \boldsymbol{u} \, \mathrm{d}\boldsymbol{x}}{\int_{\mathcal{D}} \|\boldsymbol{\nabla} \times \boldsymbol{u}\|_2^2 \, \mathrm{d}\boldsymbol{x}}. \tag{4.10}$$

It is also possible to define another framework, where the viscosity is still time-dependent, but adjusted to conserve the total enstrophy $\partial_t \Omega = 0$, where $\Omega = \int_{\mathcal{D}} \|\nabla \times \boldsymbol{u}\|_2^2 \, \mathrm{d}\boldsymbol{x}$ (1). The corresponding expression of the viscosity is obtained by taking the Fourier transform of (4.8), multiplying by $k^2 \bar{\hat{u}}_i$ and summing over $\boldsymbol{k}$, leading to :

$$\nu_r[\boldsymbol{u}] = \frac{\sum_{\boldsymbol{k}} \|\boldsymbol{k}\|_2^2 \, \hat{\boldsymbol{f}}_{\boldsymbol{k}} \cdot \hat{\boldsymbol{u}}_{-\boldsymbol{k}} + \Lambda(\hat{\boldsymbol{u}})}{\sum_{\boldsymbol{k}} \|\boldsymbol{k}\|_2^4 \, \|\hat{\boldsymbol{u}}_{\boldsymbol{k}}\|_2^2}, \tag{4.11}$$

where $\Lambda(\hat{\boldsymbol{u}})$ comes from the non-linear term of the Navier-Stokes equations. While it is yet unclear whether viscid or inviscid Navier-Stokes equations with regular initial conditions and finite energy are subject to a finite-time blow-up, it is known that controlling the enstrophy is sufficient to prevent a blow-up (38). Therefore, the enstrophy conserving scheme is associated with more regular solutions than the energy conserving scheme. In particular, it rules out a spontaneous breaking of the time-reversal symmetry mediated by dissipating singularities as conjectured by Onsager (2). In the chapter, we focus on the energy conserved scheme. Still, it is interesting to explore the properties of both conservation schemes and such study will be performed in the following chapters.

Replacing the usual viscosity ν with its "reversible" counterpart ν_r in (4.8), we obtain the reversible Navier-Stokes (RNS) equations:

$$\partial_t \boldsymbol{u} + (\boldsymbol{u} \cdot \boldsymbol{\nabla})\boldsymbol{u} = -\boldsymbol{\nabla} p + \nu_r \boldsymbol{\Delta} \boldsymbol{u} + \boldsymbol{f}. \tag{4.12}$$

Taking into account that $\boldsymbol{f}$ is invariant by the time-reversal symmetry, it is then easy to check that the whole equation is also invariant by the symmetry (4.9), hence its name.

Since the viscosity is no longer a constant, the Reynolds number $\mathrm{Re} = \frac{LU}{\nu}$ is no longer a valid control parameter. Therefore, in the fixed energy case we introduce the dimensionless control parameter $\mathcal{R}_\mathrm{r}$[2] (20) given by:

$$\mathcal{R}_\mathrm{r} = \frac{f_0}{E_0 k_f}, \tag{4.13}$$

[2]This definition of the control parameter is equivalent to $1/\mathcal{E}$.

where f_0 is the forcing amplitude, $k_f = \frac{2\pi}{L_f}$ the wavenumber at which the forcing occurs and E_0 the constant, total kinetic energy.

4.4 . 1D Burger's equation and stochastic regularization

Disclaimer: In this chapter, the definiton of $\mathcal{R}_r = 1/\mathcal{E}$ differs from the rest of the thesis by a multiplicative factor due to a new computation method.

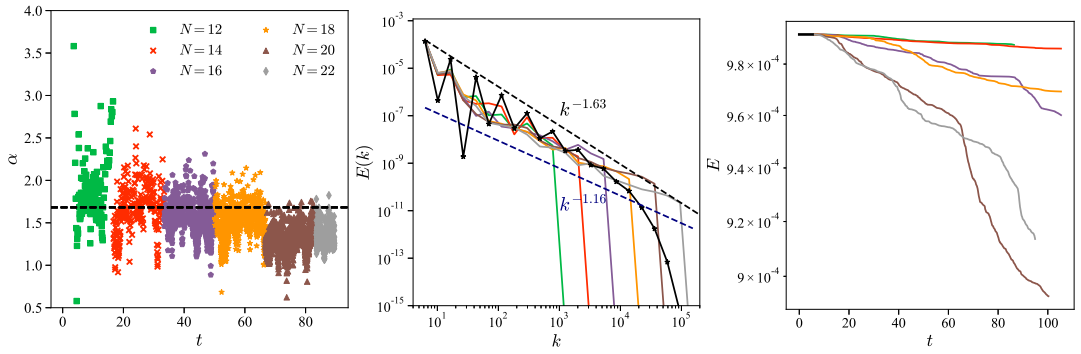

(a) (b) (c)

Figure 4.1: (4.1a) Time series of the slopes in presence of regularization. (4.1b) Energy spectra for the inviscid 1D Burgers equation. (4.1c) Time series of the total kinetic energy highlighting the presence of dissipation. N is the number of modes, all figures shares the same legend as Fig. 4.1a).

Before tackling the 3D case, we start by investigating the 1D inviscid Burgers equation. It is known that solutions of the inviscid Burgers equation blows-up in finite time t_b with pre-blowup exponent, on LL, $\alpha_{t<t_b} = -5/3$ (22; 24). In order to pass the blowup t_b, one usually adds a small viscous regularization, reaching a post blowup state with same exponent $\alpha_{t>t_b} = -5/3$.

Here, we propose to use a stochastic regularization to overcome the blowup state. To do so, we first perform a blowup simulation using an adaptative grid, with the desired parameters. Time steps at various resolutions are saved and stored. They are then used as an initial conditions to launch regularized simulations at fixed resolution N corresponding to the instantaneous resolution of the blowup simulation at time t.

In addition, we add a multiplicative noise, in the last shell, to pass the blowup time t_b without thermalizing.
Following (39), we define the last shell such that it reads, in the regularized framework:

$$u_{i,N-1}(t+dt) = u_{i,N-1}(t)\eta(t),$$
$$\forall t\ \eta(t) \sim \mathcal{U}[-1,1],$$

where i accounts for the direction (x, y or z in 3D) and $N-1$ is the last shell. Meaning that before computing the new time-step, the last shell is first modified by the noise.
The regularization vanishes by taking $N \to \infty$ as the energy in the last mode reaches 0 in the infinite grid limit.

Figure 4.1b presents the averaged energy spectra for different resolutions N, highlighting departure from the pre-blowup state (black line). The slopes of the regularized spectra slowly converge (Fig. 4.1a) to $\alpha > -5/3$ (i.e $h < 1/3$) being dissipative solutions. We recall that the viscosity is still set to $\nu = 0$ yet the regularized solutions all present dissipation as highlighted in Figure 4.1c being the sign of irregular solutions.

By applying a stochastic regularization in the last shell of a 1D inviscid Burgers system, we are able to pass the blowup time t_b while converging to dissipative solutions as the number of modes N increases. These preliminary results encourage us to extend the study to the 3D Log-lattices Navier-Stokes equations.

4.5 . Weak solutions on 3D Log-lattices

4.5.1 . Background

Taking advantage of the huge available resolutions, Campolina & Mailybaev were able to show that inviscid unforced fluids on LL are characterized by a chaotic blow-up in finite time (13). The blow-up proceeds in a self-similar manner, with a power law energy spectrum $E(k,t) \sim k^{-1-2h}$ widening towards smaller and smaller scale as time proceeds, and reaching $k = \infty$ in a finite time. During the blow-up, the energy is conserved at all time, so that the corresponding singular solution at $t = t_b$ is non-dissipative. This observation is in agreement with the observed value of h, which is very close to $h = 2/3$ (13; 24). This value is larger than the minimal value $h_* = 1/3$ excluding any dissipative weak solutions by Isett theorem (40). On the other hand, it guarantees that the solution remains on finite energy at the blow-up time, providing the spectrum does not propagate to $k = 0$. Given that it is obtained at zero-forcing, it corresponds to a non-dissipative solution that has an infinite efficiency. Let us now show that there exists other blowing-up solutions, with finite efficiency.

4.5.2 . Pre-blowup

We have performed numerical simulations of Eq. 4.1 on LL with given forcing (f_0, L_f) inside a triply-periodic cubic domain $\mathcal{D}$ of side 2π using adaptative grid, for different values of the efficiency and starting with energy spanning the first few modes in order to ensure the convolutions. For RNS simulations, a forcing term is added (with respect to Euler), details are given in Section 1.3. Depending on the value of $\mathcal{E}$, we obtain typically two types of solutions: finite time blow-up solutions for $\mathcal{E} > \mathcal{E}_*$, and stationary viscous solution for $\mathcal{E} \leq \mathcal{E}_*$, with $\mathcal{E}_* \approx 0.14$. Exemple of spectra of the two type of solution is provided in the small left panel of Fig. 4.2a, black triangles corresponds to a developping blowup while brown triangle (inset) is a stable viscous solution. Blow-up solutions are characterized by a power-law spectrum $E(k,t) \sim k^{-1-2h}$, that gradually widens towards $k = \infty$ as $\nu(t)$ gradually decreases towards 0. The asymptotic solution at the finite blow-up time t_b then corresponds to a singular solution to Euler equation. The spectral index of the blow-up depends on the efficiency, as shown in Figure 4.2b. It varies from $2/3$ to $1/3$ as $\mathcal{E}$ goes from ∞ to $\mathcal{E}_*$, so that all the solutions are non-dissipative. Stationary viscous solutions are characterized by an energy spectrum that is a power-law with index $h \sim 1/3$ at small k, with exponential cut-off at large wavenumber. During the simulation, the viscosity first decreases steadily, like in the blow-up stage, making the spectrum extends towards large wavenumber. After a certain time, the viscosity suddenly stops decreasing, and goes up

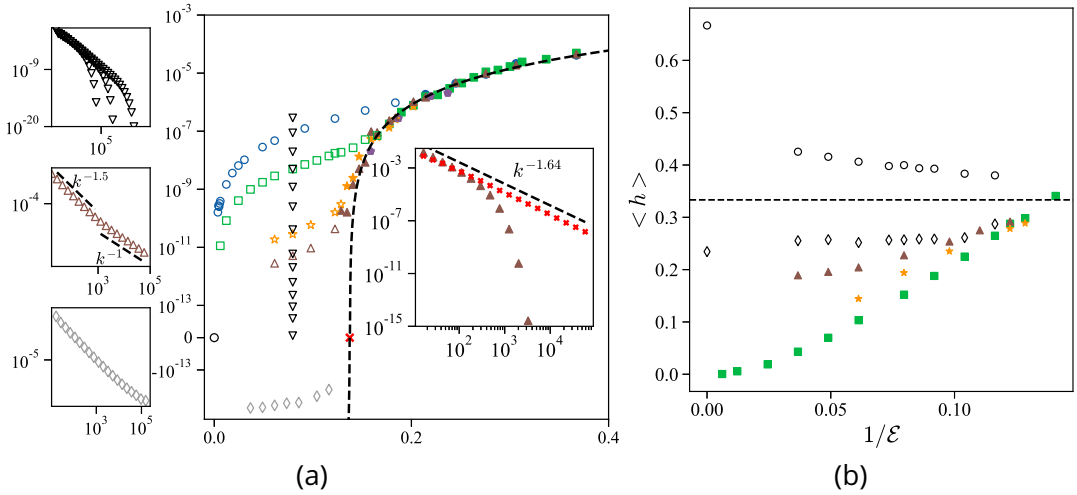

Figure 4.2: Phase space of the reversible fluids on log-lattices. In each figures colors and markers are associated to different grid size N. blue dots, green squares, red crosses, purple pentagons, orange stars, brown triangles, grey diamonds and pink are respectively associated to $N = 8^3, 12^3, 14^3, 16^3, 18^3, 20^3, 22^3$ and 24^3 while black symbols correspond to blowup solutions with adaptative N. (4.2a) The central panel shows the adimensionnalized reversible viscosity as a function of the inverse of the efficiency $1/\mathcal{E}$. The side panels and insert show the spectra of the corresponding solutions. The vertical dashed lines located at $1/\mathcal{E}^*$ separates the warm and hydrodynamic phase. Solutions in the hydrodynamic phase (full symbols, and inset) collapse on a mastercurve of equation $\nu_* \sim (1/\mathcal{E} - 1/\mathcal{E}^*)^3$ (black dashed lines) regardless of the resolution. Solution in the warm phase (open symbol) depend on the resolution: at finite resolution, they stabilize to a thermalized state, characterized by a finite viscosity and a spectrum with two slopes (left panel empty brown triangles). The slope at large scale is reported on Fig. 4.2b with filled symbol. At infinite resolution, the solutions first blow-up in a self-similar manner (left panel, empty black downward triangle), with exponent reported on Fig. 4.2b (empty black circles). After blow-up and stochastic regularization, the solution converges towards a power-law spectrum (left panel, empty grey diamonds), with another exponent. (4.2b) Blowup exponents as a function of $1/\mathcal{E}$. The infinite efficiency case corresponds to Euler. Empty black circles corresponds to exponents during blowup while empty black diamond are the exponents obtained through stochastic regularization.

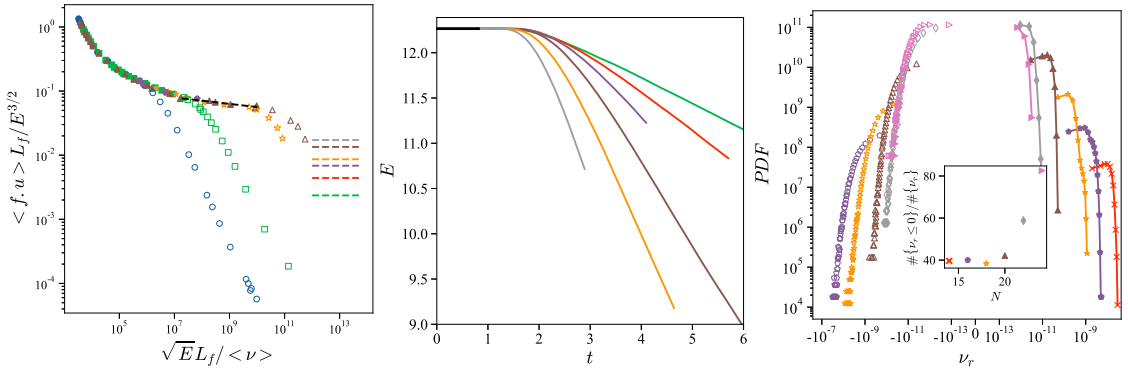

(a) (b) (c)

Figure 4.3: Colors and symbols: same as Figure 4.2. (4.3a) Adimensionnalized energy dissipation. The horizontal dashed lines represent the energy dissipation in regularized Euler for various N. (4.3b) Post-blow up decay of the energy at different resolution. The rate of the exponential decay computed fro this figure is reported by dashed line on Fig. 4.3a. (4.3c) Probability distribution of the viscosity for $\mathcal{E} \approx 0.12$, at different resolution.

until it reaches a finite value ν_*, where the solution becomes statistically stationary. The finite value depends on $\mathcal{E}$, and follows a curve of equation $\nu_* \sim (1/\mathcal{E}^{-1} - 1/\mathcal{E}^*)^3$. This curve therefore corresponds to an attractor of the dynamics for $\mathcal{E} \leq \mathcal{E}_*$. We checked that the corresponding solutions corresponds to stationary solution of the Navier-Stokes equations at fixed viscosity, that are attractive in the following sense: if at some time during a blow-up development for $\mathcal{E} > \mathcal{E}^*$ we freeze the viscosity, then the solution converges towards the stationary viscous solution corresponding to this viscosity by gradually decreasing its efficiency (see Fig. 4.4b in Supplementary). The stationary viscous solutions are not irregular enough to produce anomalous dissipation in the limit $\nu \to 0$ as their exponent h is slightly larger than $1/3$. Indeed, when we plot the energy dissipation rate ϵ as a function of viscosity (Fig. 4.3a), we observe a steady decrease as $\nu_* \to 0$, meaning no anomalous dissipation. The data can be fitted with a power law. with a very small exponent $\epsilon \sim \nu_*^{0.05}$, meaning that the dissipation eventually vanishes as $\nu_* \to 0$.

The adaptative resolution allows for the development of blowups solutions until a blowup time t_b. To pass this blowup time and access a post blowup state, it is necessary to regularize the solution. As mentioned before, the blowup state is associated to the increasing grid size. Therefore, we propose to study the post blowup state by freezing the gridsize N.

4.5.3 . Post-blowup via thermalization

We now concentrate on the solutions for $\mathcal{E} \geq \mathcal{E}_*$, that converge to a non-dissipative inviscid solution as $t \to t_b^-$. We now show that the corresponding solutions are unstable, and transform into other solutions as we go past the blow-up. There are a number of ways to extend the solution past the blow-up time. A first method is to freeze the resolution at a fixed number N (or equivalently freezing the maximum wavenumber k_{max}) just before blow-up, and let the solution evolves. What we observe is that the viscosity starts evolving, and saturates at a given value depending on both the resolution and efficiency

$\nu_{th}(N, \mathcal{E}$ (see Figure 4.2a). The energy coming from the small wavenumbers then accumulates at the largest wavenumbers k_{max}, producing a reflected wave of thermalization that is halted at a finite wavenumber k_{th}, depending on ν_{th}. Below k_{th}, the spectrum becomes more shallow, reaching a new exponent h_{pp} (Fig. 4.2a, brown curve in the left panel). This behavior is the counterpart on LL of what has been observed on direct numerical simulations of Navier-Stokes equations (41) at much smaller resolutions. This dynamic is also observed for Leith model of turbulence (42), where it corresponds to a switch between an unstable fixed point to a stable one. In our case, the post-blow up exponent h_{pp} is smaller than the pre-blow up exponent (Fig. 4.2b), and actually becomes less than $1/3$, corresponding to a dissipative solution. For $N = 12^3$ it goes down from $1/3$ at $\mathcal{E} = \mathcal{E}_*$ to 0 at $\mathcal{E} \to \infty$. For a larger value of the resolution, the curve $h_{pp}(\mathcal{E}$ shifts upwards and gets closer to $h_{pp} = 1/3$, the Kolmogorov dissipative solution. Due to computational burden, the infinite resolution limit of h_{pp} is however difficult to reach using this type of regularization. So we decided to switch towards a stochastic regularization.

4.5.4 . Post-blowup via stochastic regularization

The stochastic regularization has already been used in shell models of turbulence (39). The protocol consists in freezing the resolution at a given N, and add a multiplicative noise at the largest wavenumber. Details are provided in Section 4.4.

The system then undergoes a transient dynamic, after which a new statistically stationary state is obtained, with a new value of the mean viscosity $< \nu_{pp} >$ and local slope. h_{pp}. The value of N is then progressively increased, until reaching convergency of the results. For the range of efficiency we considered, this was achieved for $N = 22^3$. In the Euler case, ν is fixed to zero. The converged spectrum is shown in Fig. 4.2a (grey diamonds, left panel). It corresponds to a spectrum with $h_{pp} \sim 0.25$, lower than the pre-blow up exponent. Another striking feature of the dynamics is that the energy is not conserved anymore, as illustrated in Fig 4.3b: it decays linearly after regularization, corresponding to a constant energy dissipation rate that increases with resolution. The corresponding values are added on Fig. 4.3a. As resolution increases, it tends towards the value observed for viscous solutions, showing that the dynamics have become dissipative. This feature is also observed for other values of efficiency, when using the RNS equations. Due to the constraint of energy conservation, viscosity has to take negative values to compensate for the existence of a dissipative mechanism. This can be seen on Fig. 4.3a, showing the probability distribution for the viscosity in the case $\mathcal{E} \approx 0.12$, for various resolutions. As the latter increases from $N = 8^3$ to $N = 24^3$ [3], the proportion of negative values shifts from 40% to 80% (see inset of Fig. 4.3c), making the average value of the positive viscosities two orders of magnitudes less than the average value of negative ones. This property holds true whenever $\mathcal{E} > \mathcal{E}_*$, as shown in Figure 4.2a. Implying that the mean value of the viscosity after the blow-up always stays negative. The dissipative nature of the solution can also be investigated by computing the post blow-up spectral exponent, shown in Fig. 4.2b. It indeed satisfies $h_{pp} \leq 1/3$. For large efficiency, the value of h_{pp} saturates around $h_{pp} \sim 0.25$, and converges towards $h_{pp} = 1/3$ as $\mathcal{E} \to \mathcal{E}_*$. This reinforce the interpretation of Kolmogorov solution as being the attracting fixed point at $\mathcal{E} = \mathcal{E}_*$.

[3] We recall that the power exponent is associated to the dimension D used in the considered simulation.

4.5.5 . Discussion

We have used fluids on log-lattice and a reversible framework to investigate the influence of the efficiency on the behaviors of solutions. We observe a phase transition at a given efficiency, separating regular, viscous solution, from singular inviscid solutions. The singular solutions experienced self-similar blow-up with exponent characterizing non-dissipative solutions. We use stochastic regularization to go pass the blow-up, and show that the resulting solutions converge to power-law solutions, with exponents characterizing dissipative solutions. Globally, the range of different exponents we find are comparable to exponents found in ordinary fluids, thereby providing a dynamical scenario for their construction. The occurence of possible dissipative singular solutions is intimately linked to the breaking of the symmetries of the equations of motions. In general, Euler equations are invariant both by time translation and by time-reversal. By Noether theorem, the first symmetry leads to energy conservation. Moreover, time homogeneity means that no special time can be singled out by the dynamics, so that time-reversal can be performed around any time without adding any new information. In the presence of a finite-time blow-up, the time translation is broken, offering the possibility for energy to vary. Moreover, the time-reversal applied at the blow-up time allows us to connect physical solutions before and after blow-up. This explains the success of our procedure, based on reversible Navier-Stokes equation, to unfold the parameter space of singular Euler equations. By construction, the reversible viscosity we introduced changes sign under time-reversal. Therefore, to each non-dissipative singular solution of RNS with positive viscosity corresponds a dissipative singular solution of RNS, with negative viscosity. We have shown how to capture these solutions using a stochastic regularization, that allows to go pass the blow-up. We conjecture that these solutions converge to dissipative singular solutions of Euler equation. All of results have been obtained for fluids projected on log-lattices. It would be very interesting to test whether they still hold on fluids on regular Fourier lattices. Indeed, current construction of dissipative singular solutions is usually done via convex integration methods (43), which are delicate to implement. If the conjecture holds true also for regular lattices, it means that the reversible protocol could provide a new way of constructing those solutions through a controlled limit procedure. As such, it would probably pave the way to new exact results regarding the existence and properties of dissipative singular solutions of Euler.

4.6 . Supplementary: stability of solutions

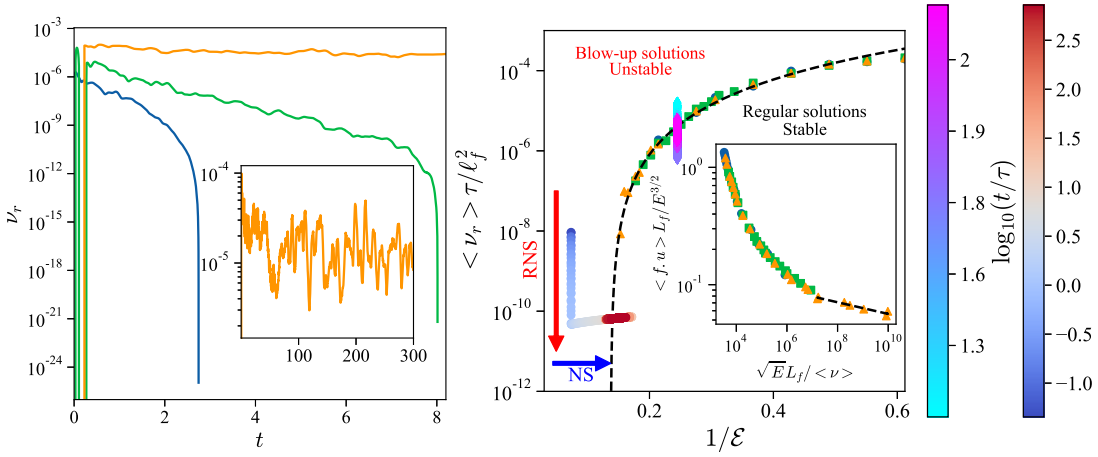

(a) (b)

Figure 4.4: (4.4a) Time series of the reversible viscosities $\nu_r(t)$ for different efficiency highlighting two scenarios, blowup at high effiency and regular solutions for lower values. (4.4b)Stability of solutions in the two phases. Two trajectories of solutions as a function of time (colorcoded) are presented highligthing the instability (resp. stability) of the warm (resp. hydrodynamic) phase.

Both Euler and RNS equations present blowup solutions in the range $\mathcal{E} > \mathcal{E}^*$. In order to go beyond the blowup time t_b, one might be tempted to simply fix the resolution N. It has already been shown that, under resolved solutions exhibit thermalization at small scales (44). By thermalizing, the solutions reach a stable "thermalized" branch that corresponds to truncation effects and hence strongly depends on N (Fig. 4.2a empty symbols in the warm phase).

Note that when reached, this thermalized branch is stable by switching between NSE and RNSE as a consequence of the Gallavotti conjecture (37) that will be studied later in this thesis. However, the instanteneous RNS solutions (i.e non thermalized) are unstable under such switch, see Fig. 4.4b. The solution then converges to the stable branch $(1/\mathcal{E} - 1/\mathcal{E}^*)^3$.

In addition, performing RNS simulations with adaptative resolution in the hydrodynamic phase leads to the same solutions as the one obtained with fixed N. Fig. 4.4a presents the time series of the reversible viscosities highlitighting blowups in the unstable phase (blue and green lines) as $\nu_r \propto \Omega^{-1}$. The orange curve shows that there are no blowups in the hydrodynamic phase as ν_r achieves a steady state. Note that the amplitude of the oscillations are correlated to the position in the phase transition that the system exhibits (20; 37). Such transition will be studied later in this thesis.

5 - Singularity induced instability

As highlighted in previous chapters, the existence of complex singularities have many impacts on the behavior of the flow (blowups, intermittency).

In this chapter, we study the existence and properties of a singularity driven instability. We show that the LLRNS system exhibits two stable attractors, located at $\mathcal{R}_\mathrm{r} \gg \mathcal{R}_\mathrm{r}{}^*$ and $\mathcal{R}_\mathrm{r} \to 0$. The first one is the standard "Navier-Stokes" spectrum, exhibiting both an inertial domain $k^{-5/3}$ and a dissipative region. The second one is associated to the singularity getting closer to the real axis in the complex plane. In this range ($\mathcal{R}_\mathrm{r} < \mathcal{R}_\mathrm{r}{}^*$) as shown in the previous chapter, the system converges for fixed grids, to fully thermalized spectrum " as $\mathcal{R}_\mathrm{r} \to 0$ associated to the collapse of a complex singularity on the real axis.

Systems, at fixed grid size, are free to oscillate between the two attractors, with exit times $t_{a\to b}$ depending on $\mathcal{R}_\mathrm{r}$. Figure 5.1 presents the KDE plots of the enstrophy for various values of $\mathcal{R}_\mathrm{r}$ highlighting stronger oscillations pointing towards variation of the exit times as one gets further away from the attractors. Note that the enstrophy is a good indicator as the development of a singularity is associated to an enstrophy blow-up.

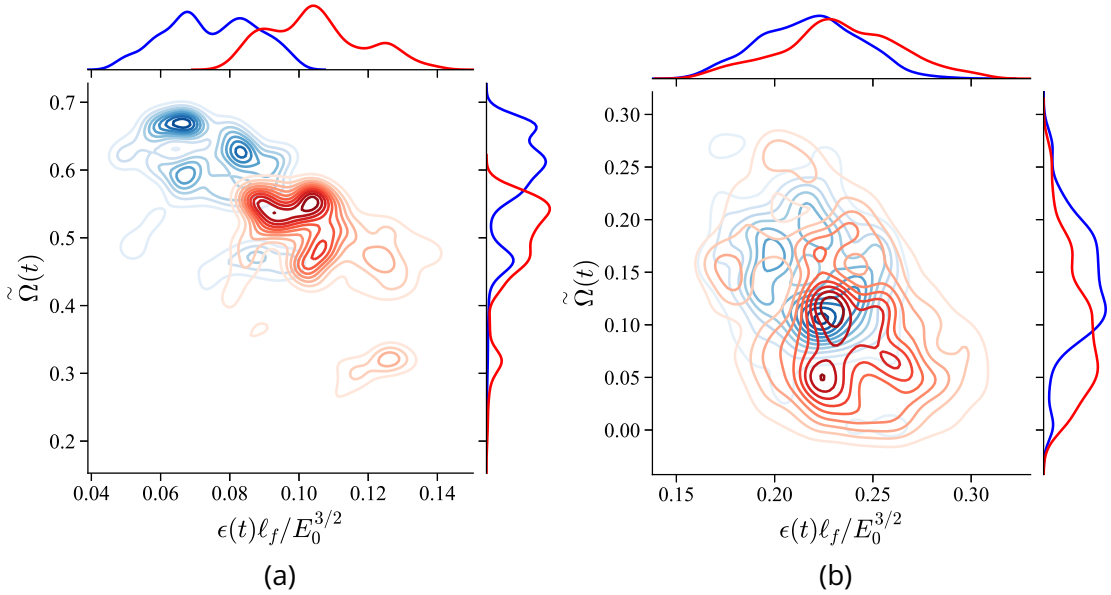

Figure 5.1: **Attracting sets**. (5.1a) KDE plot at low $\mathcal{R}_\mathrm{r}$, $\mathcal{R}_\mathrm{r} \approx 1.11, 1.45$. (5.1b) KDE plot in between the two attractors, $\mathcal{R}_\mathrm{r} \approx 2.34, 2.45$, showing a much wider range of values for the enstrophy. Simulations are performed using $N = 20^3$.

As in Chapter 2, the position in the complex plane, of the complex singularity is extracted using the analiticity strip method. The blowup state $\delta = 0$ is referred to as state 1, while $\delta > 0$ is referred as state 2.

Fig. 5.2 shows the time series of δ for simulations at various $\mathcal{R}_\mathrm{r}$. As highlighted in the previous chapter, there exists a threshold $\mathcal{R}_\mathrm{r}{}^*$ below which the system, with adaptative grid, blows-up. Due to the fixed size of the grid, the proper blowup is prevented and leads

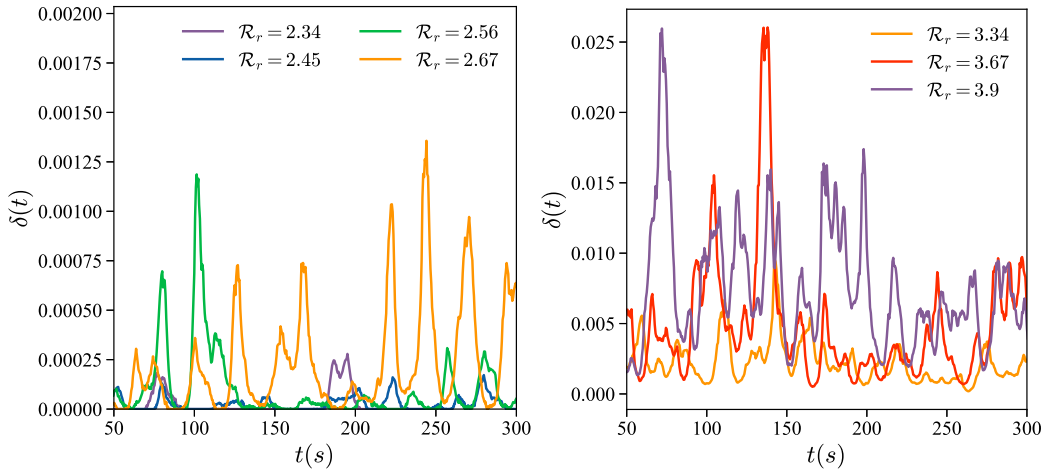

Figure 5.2: **Time series of δ.** Simulations are performed for $\lambda = \phi$, $N = 20^3$.(5.2a) δ oscillates between state 1 ($\delta = 0$) and 2 ($\delta > 0$). (5.2b) For bigger $\mathcal{R}_\mathrm{r}$ (see Eq. 4.13) the system remains permanently in state 2 as it is repelled by a strong enough viscosity, preventing the collapse on the real axis.

to thermalization (26), considered as state 1. By increasing $\mathcal{R}_\mathrm{r}$, one reaches the stable phase of Fig. 4.2a, where δ still oscillates but never reaches 0. Note also that the singularity is more strongly repelled as $\mathcal{R}_\mathrm{r}$ increases. Indeed Fig. 5.2 shows increasing values for δ with a difference of several order of magnitude between $\mathcal{R}_\mathrm{r} = 2.34$ and $\mathcal{R}_\mathrm{r} = 3.9$.

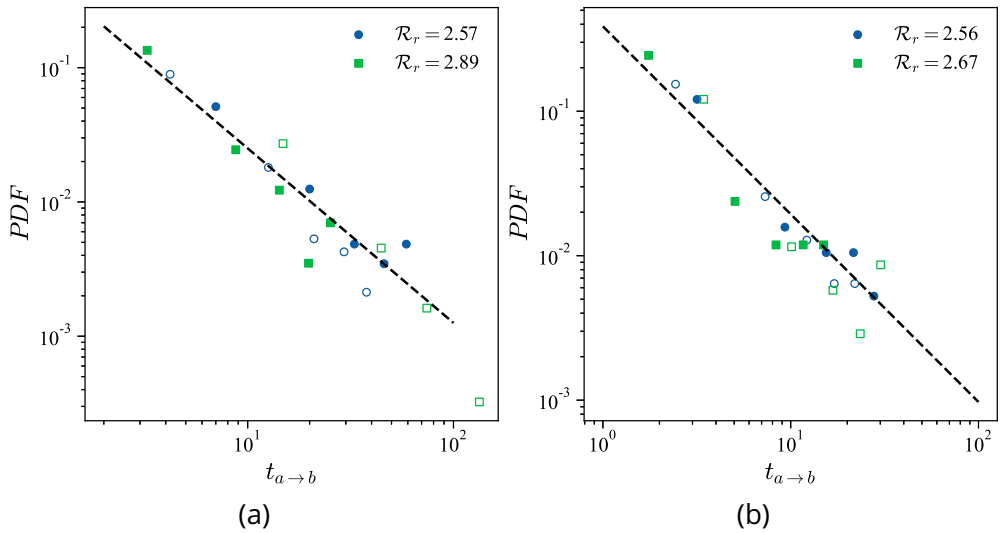

Figure 5.3: **PDF of characteristic times of the transition** between state 1 (warm) and state 2 (hydrodynamical). (5.3a) $N = 16^3$ (5.3b) $N = 20^3$. The extracted PDFs are accurately described by a powerlaw of exponents $\alpha = -1.3$ represented by the black dashed lines. The empty (resp. full) symbols are associated to the transition from hydrodynamical (resp. warm) to warm (resp. hydrodynamical).

It is then possible to define transition times $t_{a\to b}$ as a kind of exit time from state a. Fig. 5.3 shows the PDFs of $t_{1\to 2}$ (full symbols) and $t_{2\to 1}$ (empty symbols). PDFs are quite well [1] described by a powerlaw of exponent $\alpha \sim -1.3$. The PDFs also highlight a previously mentioned behavior. Indeed, at $\mathcal{R}_\mathrm{r} < \mathcal{R}_\mathrm{r}{}^*$, the system leaves the warm state for short periods of time implying a PDF located at low values of τ. The inverse observation is also made for $\mathcal{R}_\mathrm{r} > \mathcal{R}_\mathrm{r}{}^*$. Note that in those case the low values of τ can be over-represented as the system struggles to take distance from the attractor.

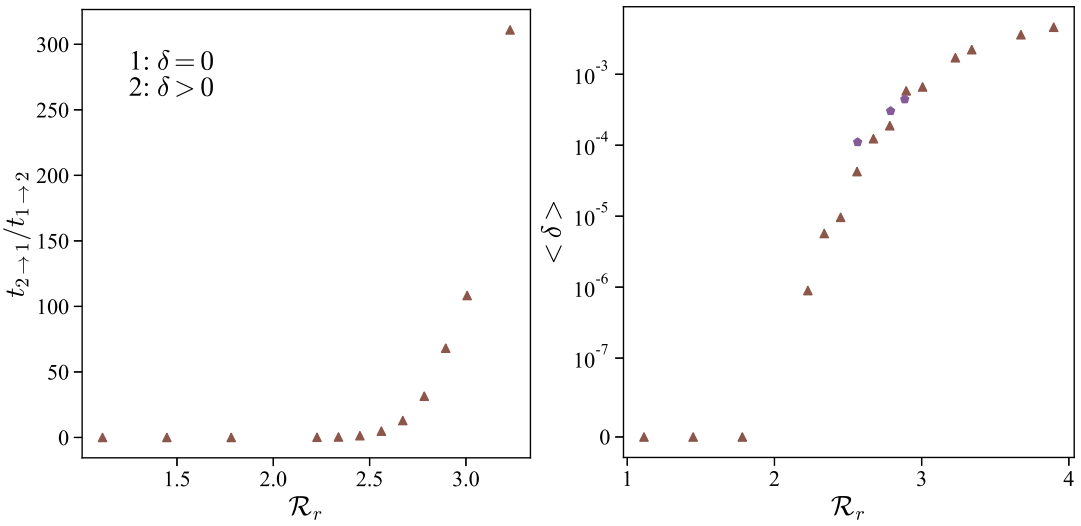

(a) (b)

Figure 5.4: **Statistics for $N = 20^3$.** (5.4a) Ratio of the transition times between state 1 (warm) and state 2 (hydrodynamical) as a function of $\mathcal{R}_\mathrm{r}$. (5.4b) Mean value of δ as a function of $\mathcal{R}_\mathrm{r}$.

Such effect can also be seen in Fig. 5.4a that shows the evolution of the ratio $\tau_{2\to 1}/\tau_{1\to 2}$ as a function of $\mathcal{R}_\mathrm{r}$. Note that for $\mathcal{R}_\mathrm{r} < 2$ the system never departs (atleast in our simulations) from the warm state. Fig. 5.4b presents the value of δ as a function of $\mathcal{R}_\mathrm{r}$ confirming the presence of the two phases introduced in the previous chapter.

The existence of two attractors and the possibility to oscillate back and forth between them points toward a possible phase transition in the RNS system. This intuition is further supported by the shape of $\log\langle\delta(\mathcal{R}_\mathrm{r})\rangle$ that recalls those of phase transitions. It is therefore interesting to analyze the behavior of the RNS equations in the framework of phase transition as its reversible nature allows for the use of the traditional statistical mechanics.

[1] Obtaining extremely accurate PDFs is complicated due to the bursty behavior of δ (see Fig. 5.2).

6 - Phase transition in Reversible Navier-Stokes equations

We have seen that there exists a critical efficiency $\mathcal{E}^*$ beyond which the unregularized system blows up. Below this threshold the system reaches a steady state of finite enstrophy. We confirm the intuition of the previous chapter showing that this results can be understood within the framework of phase transitions upon defining the efficiency $\mathcal{E}$ as a control parameter or equivalently the "Reversible Reynolds number" $\mathcal{R}_{\mathrm{r}}$.
All the results presented in this chapter are obtained in the conserved energy case, i.e. for $\mathcal{G} = E$.

We recall that RNSE stands for the *Reversible Navier-Stokes Equations*, defined in Section 4.3.

6.1 . Numerical details to study the RNS transition

Initial conditions and form of the forcing term have already been presented in Chapter 1. This sections presents the supplementary details of the simulations used to perform the analysis of chapter 6 & 7.

The minimum wavenumber of the grid is set to $k_{\min} = 2\pi$. The maximum grid size $N = 20^3$ is chosen such the hydrodynamic branch, introduced later on, is well-enough resolved. We set a maximum time-step $dt = 0.005$, in order to avoid under-resolving some very stiff moments when the viscositiy tends to zero. As a result, whenever the viscosity is not very small, the time-step is a constant equal to dt. The reversible viscosity ν_r is obtained by solving the equation $\mathcal{G}(\nu_r, t + dt) = \mathcal{G}_0$ such that $\mathcal{G}$ is conserved with floating-point accuracy: $|\,\mathcal{G}(t+dt) - \mathcal{G}_0\,| < 10^{-14}\,\mathcal{G}_0$. It is then taken into account following the procedure of Section 1.2.

The range of parameters studied is chosen such that it is possible to observe the two regimes previously observed in DNS by Shukla et al.
All the simulations ran on one core of a consumer-grade computer, for a few (< 4) CPU days at most.

6.2 . Dynamics

Fig. 6.1a illustrates the time-evolution of the normalized enstrophy $\widetilde{\Omega}$ (properly defined in Appendix. 6.8) for many modes $N = 20^3$. As in (20), different regimes are observed. At low values of the control parameter $\mathcal{R}_{\mathrm{r}}$, the solutions converges to a constant mean value of $\widetilde{\Omega}$ with little to no fluctuations. This regime is associated with a lower branch of mean viscosity $\langle \nu_r \rangle$ (Fig. 6.1b) that develops a power-law $\langle \nu_r \rangle \propto {\mathcal{R}_{\mathrm{r}}}^{\alpha}$, where $\alpha \approx 2$. This result was already obtained in DNS (20), and can be justified using a Kubo fluctuation dissipation theorem, that also applies on log-lattices. As the size of the grid increases, it becomes harder to reach the limit $\mathcal{R}_{\mathrm{r}} \to 0$ as the low values of viscosity require smaller time-steps. This limit is associated to a thermalized steady state, as it is characterized by a

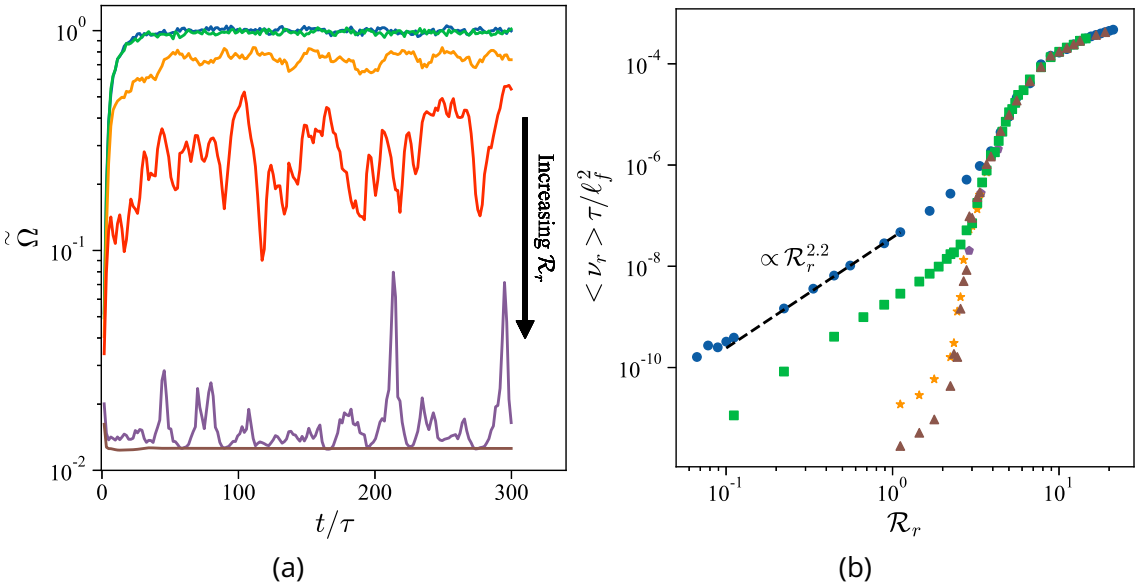

Figure 6.1: **Behaviors of order parameters using $\lambda = \phi$.** (6.1a) Time series of the normalized enstrophy $\widetilde{\Omega}$ for different values of the control parameter $\mathcal{R}_\mathrm{r}$, with $N = 8^3$. (6.1b) Time averaged reversible viscosity as a function of the control parameter $\mathcal{R}_\mathrm{r}$. The dashed line represents a linear fitting in the warm regime, exhibiting a power-law behavior. The dimensionless time is $\tau = \ell_f/\sqrt{E_0}$, where ℓ_f is the scale at which the forcing occurs.

vanishing energy injection and therefore, in order to conserve the energy, to a vanishing viscosity.

As $\mathcal{R}_\mathrm{r}$ increases, the system fluctuations continually increase up to a certain value of ${\mathcal{R}_\mathrm{r}}^*$ at which fluctuations reach their maximum. Beyond this critical value, fluctuations slowly decrease to zero, towards a lower branch of enstrophy (Fig. 6.1a). This branch corresponds to a branch of large viscosity (Fig. 6.1b). Before vanishing completely, the enstrophy fluctuations appear as "bursts" of enstrophy.

Note that defined in such a way, ${\mathcal{R}_\mathrm{r}}^*$ depends on the resolution N. Indeed, both the value of $\mathcal{R}_\mathrm{r}$ at which the system leaves the collapsed branch (Fig. 6.1b) and the location of maximum fluctuations (Fig. 6.2d) clearly depends on the resolution. Also note that both definition of ${\mathcal{R}_\mathrm{r}}^*$ (from fluctuations and the asymptote in Fig. 6.1b) and are equivalent in the limit $N \to \infty$ as the thermalized branch can never be reached.

6.3 . Phase transitions

In Shukla et al. (20), the various regimes of the enstrophy dynamics are associated with the existence of a second order phase transition, described by a Landau mean field theory. Specifically, the time-averaged normalized enstrophy $\left\langle \widetilde{\Omega} \right\rangle$ exhibits a power-law $\left\langle \widetilde{\Omega} \right\rangle = \left(1 - \dfrac{\mathcal{R}_\mathrm{r}}{{\mathcal{R}_\mathrm{r}}^*}\right)^\beta$, with $\beta \simeq 0.5$, while the normalized standard deviation of the renormalized enstrophy $\sigma_{\widetilde{\Omega}}$ presents a divergence around ${\mathcal{R}_\mathrm{r}}^*$, following a power-law

$\sigma_{\widetilde{\Omega}} = \left(1 - \frac{\mathcal{R}_\mathrm{r}}{\mathcal{R}_\mathrm{r}^*}\right)^{-\gamma}$ with $\gamma \simeq 1$. As it is possible to observe different values of γ on each side of the transition, we define γ_l and γ_r where l and r stand for left and right, respectively. In our case, we also observe at $N = 20^3$ behaviors for the enstrophy that are

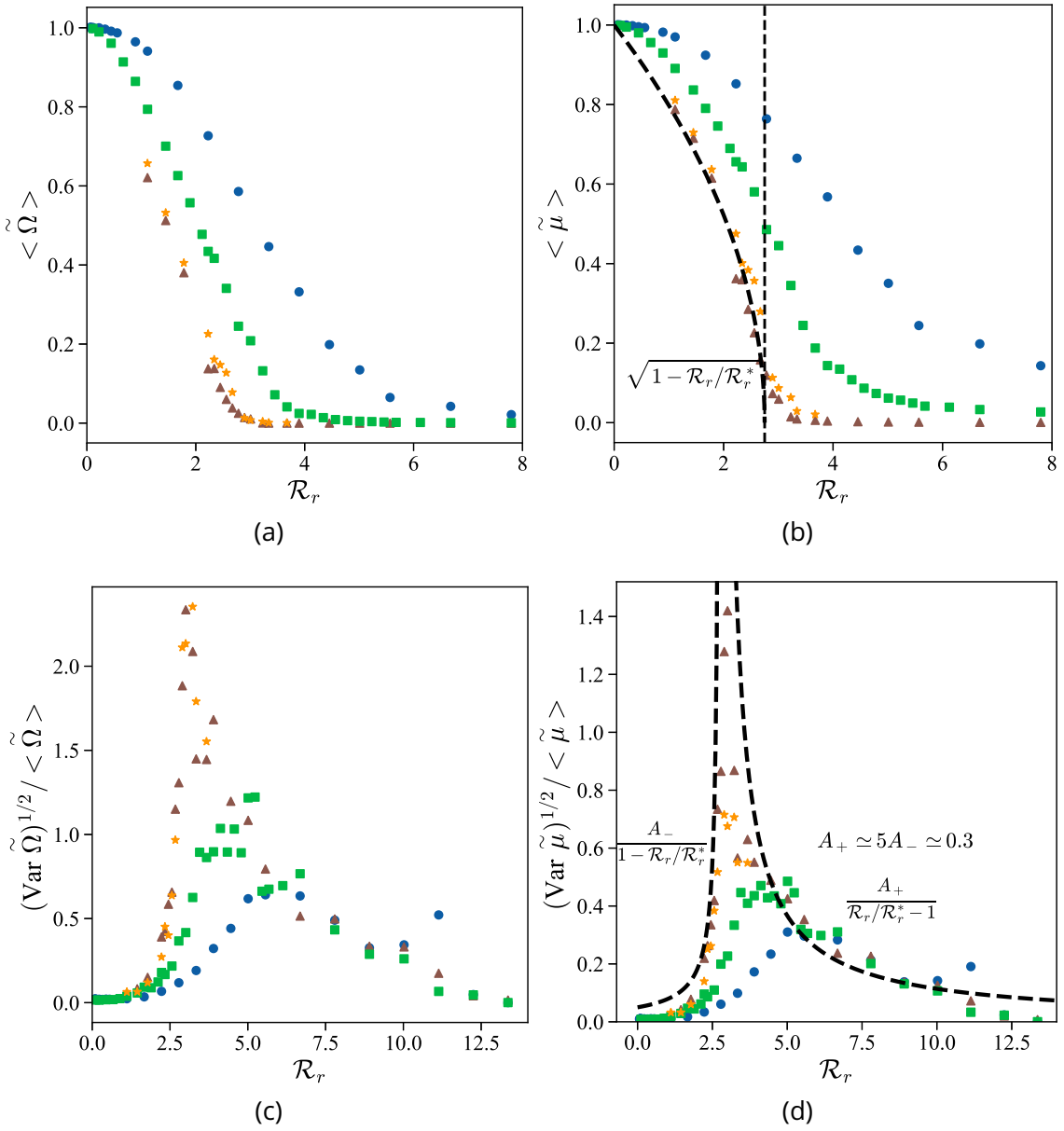

Figure 6.2: **Second order transition for $\lambda = \phi$.** Evolution of (6.2a) the renormalized mean enstrophy and (6.2b) $\widetilde{\mu}$ as a function of $\mathcal{R}_\mathrm{r}$. Variance of (6.2c) the renormalized enstrophy and of (6.2d) $\widetilde{\mu}$ as a function of $\mathcal{R}_\mathrm{r}$. The dashed lines associated with the equations corresponds to a Landau mean field formulation of the phase transition.

reminiscent of a second-order phase transition, albeit with exponents that do not correspond to the mean field description (Fig. 6.2a & 6.2c and Tab. 6.1). Indeed, we observe a power-law with exponent $\beta \simeq 1$, which is larger than its mean-field version (Fig. 6.2a). In the case of the variance, we observe a divergence at $\mathcal{R}_\mathrm{r}^*$ with a critical exponent corresponding to the mean field value $\gamma_l = 1$, like in (20).

Table 6.1: **Critical exponents as a function of h.** For $\lambda = 2$, values of γ_r were not extracted as the variance does not vanish, but converges to a constant on a domain extending quite far away from ${\mathcal{R}_\mathrm{r}}^*$.

λ	N	h	β_Ω	$\gamma_{r,\Omega}$	$\gamma_{l,\Omega}$	β_μ	$\gamma_{r,\mu}$	$\gamma_{l,\mu}$
2	8^3	$7 \cdot 10^{-3}$	-	-	-	-	-	-
	12^3	$4 \cdot 10^{-4}$	$\simeq 0.8$	-	1.6	$\simeq 0.4$	-	1.6
	16^3	$3 \cdot 10^{-5}$	$\simeq 1$	-	1.0	$\simeq 0.5$	-	1.0
ϕ	8^3	$3 \cdot 10^{-2}$	-	1.0	2.2	-	1.0	1.6
	12^3	$5 \cdot 10^{-3}$	$\simeq 0.5$	1.0	1.8	$\simeq 0.27$	1.0	1.4
	20^3	$1 \cdot 10^{-4}$	$\simeq 1$	1.0	1.0	$\simeq 0.5$	1.0	1.0
Shukla **DNS** (20)	128^3	$2.4 \cdot 10^{-2}$	$\simeq 0.5$	$\simeq 1$	$\simeq 1$	-	-	-
Landau Mean field	-	-	0.5	1	1	-	-	-

Our results show that, while the nature of the transition is unaffected by the details of the interactions between modes, the value of the critical exponents depends on those details. One should see Tab. 6.1 for different values of λ, and recall that on log-lattices, different values of λ correspond to different numbers of local interactions.

In that respect, it is interesting to see whether our result fits in the cruder description of the interactions provided by the Leith model. In this model, the mean-field description is found by taking the square root of the enstrophy as an order parameter. In our case, upon defining $\widetilde{\mu} = \widetilde{\Omega}^{1/2}$, we indeed observe a mean field behavior for $\left\langle \widetilde{\mu} \right\rangle$ in the limit of large grids $k_{\max} \to \infty$ (e.g. Fig. 6.2b & 6.2d). Its critical order parameters depend on the lattice spacing λ as ${\mathcal{R}_\mathrm{r}}^* \approx 3.75$ for $\lambda = 2$ and ${\mathcal{R}_\mathrm{r}}^* \approx 2.75$ for $\lambda = \phi$. The computed exponents associated with this model are presented in Tab. 6.1 (left columns). Note however that the mean field description is not entirely valid in our model, as we do not observe the peculiar link between pre- and post-transitions prefactors: $A_+ = 2A_-$. Still, it seems that as the number of interactions grows (i.e. as λ decreases), we are getting closer and closer to this description.

Finally, we stress that as soon as $\mathcal{R}_\mathrm{r} > {\mathcal{R}_\mathrm{r}}^*$, both the variance and the mean viscosity (Fig. 6.1b) become independent of the grid size. Therefore, only β and γ_l depend on $k_{\max}$.

6.4 . Characterizing the various phases with spectra

As shown in (20), the nature of the different phases before and after the transition can be elucidated by looking at energy spectra. Examples are provided in Fig. 6.3. Before the transition, we observe a spectrum that is characterized by two slopes: one at low wavenumbers, with an exponent close to $-5/3$ and one at large wavenumbers, with an exponent closer to -1. As already discussed in (21; 26), the -1 slope corresponds to ther-

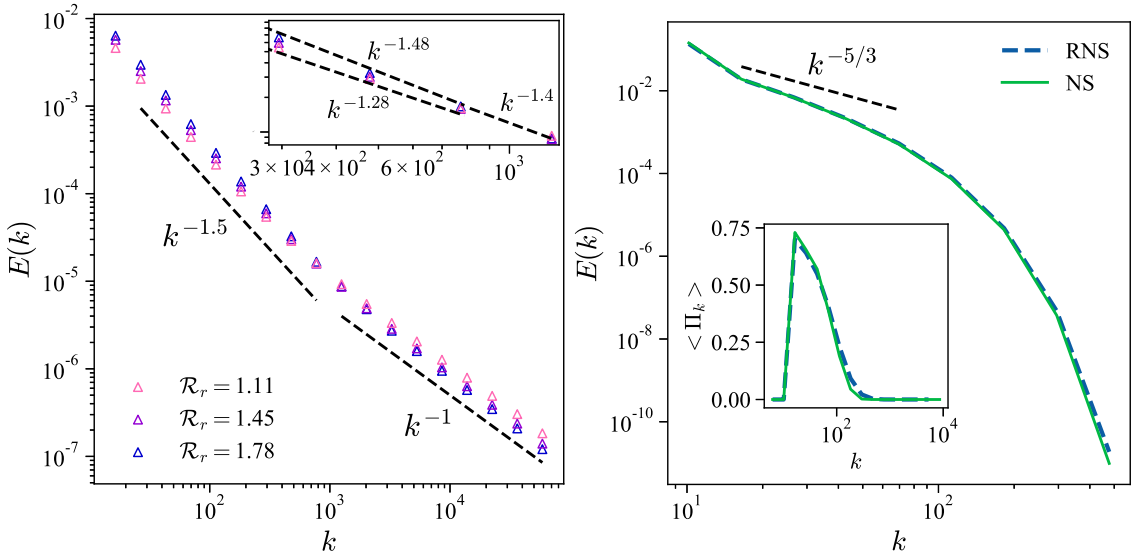

(a) (b)

Figure 6.3: **Time averaged energy spectra vs $\mathcal{R}_\mathrm{r}$, $\lambda = \phi$, $N = 20^3$ Modes**. (6.3a) Warm regime, with coexistence of two phases. The dotted line represents the slope of the two coexisting regime, a pseudo Kolmogorov regime at large scales and a thermalized regime at small scales exhibiting a -1 slope. The inset shows a zoom in the crossover area, highlighting the difference in slopes with respect to $\mathcal{R}_\mathrm{r}$ associated to the contamination of the bigger scales by the thermalization. (6.3b) Laminar state, with dominant dissipative range, and no thermalization. The inset shows the energy transfer Π_k.

malization on log-lattices, characterized by equipartition of energy among the modes. The $-5/3$ regime corresponds to a classical spectrum due to a positive flux of energy, as evidenced by the insert of Fig. 6.3b. We call this phase with a coexistence of two cascades the "warm cascade" regime. As $\mathcal{R}_\mathrm{r}$ decreases, the thermalized phase extends further towards lower k, and the pseudo-Kolmogorov phase disappears. Conversely, as $\mathcal{R}_\mathrm{r}$ increases, the thermalized phase progressively disappears, to leave room for an increasingly laminar state as the reversible viscosity increases. Such state is shown in Fig. 6.3b.

6.5 . Structure functions

The nature of the various phases can be further characterized using higher orders of the velocity field, via the structure functions (Eq. 1.5). In classical shell models, such structure functions are subject to intermittency, as they exhibit scaling laws $F_q(k) \sim k^{-\xi_q}$ that deviate from the monofractal behavior $\xi_q = q\xi_1$ (17; 45; 33; 5).

In our case, it is difficult to measure the exponents of the structure functions for all phases: at large values of $\mathcal{R}_\mathrm{r}$ the viscosity rises quickly, and the inertial range becomes very small. At small values of $\mathcal{R}_\mathrm{r}$, the scaling laws are polluted by the coexistence of the pseudo-Kolmogorov regime and the thermalized state, as illustrated in Fig. 6.3a. This invalidates the classical method of computing exponents via extended self similarity (46) as the structure functions can present multiple slopes at different scales. We extracted exponents via the following method: we first determine the inertial range by computing the

time-averaged energy transfer Π_k through Eq. 1.4. Then, we define the inertial range as the range of wavenumber where it is flat. If this range is large enough (at least a decade), we fit the scaling exponents of the structure functions on this range only. This provides us with an unambiguous determination of ξ_q. The extracted exponents are shown in Fig. 6.4a, for value of $\mathcal{R}_\mathrm{r}$ in various regimes, as illustrated in Fig. 6.4b.

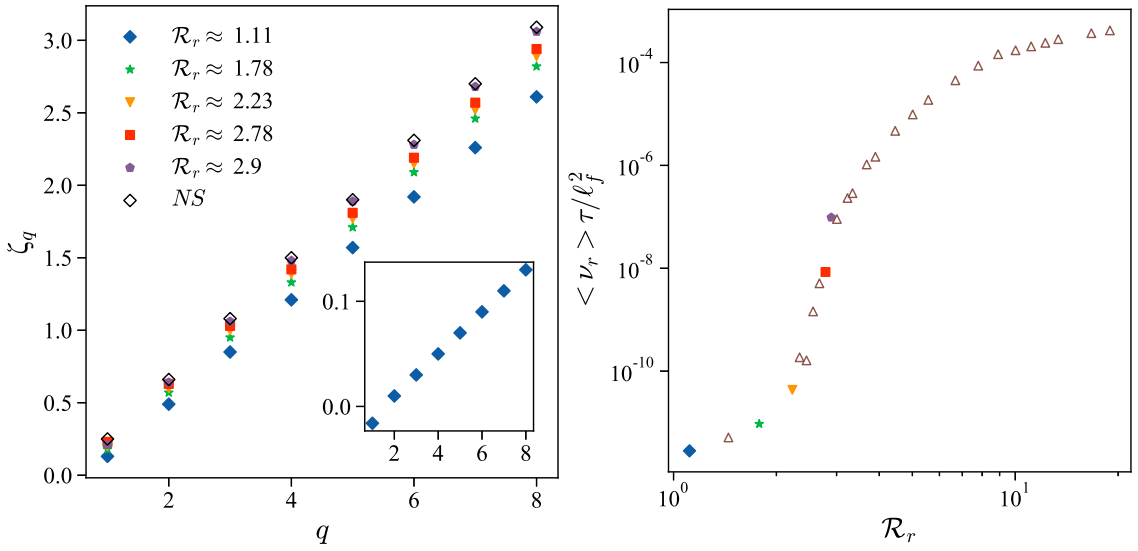

Figure 6.4: **Extracted exponents of the structure functions and localization in the transition for $\lambda = \phi$, $N = 20^3$ Modes.** Both figures share the same legend. (6.4a) Exponents of the structure function of order q for various RNS simulations and comparison to a NS simulation. The inset presents the exponents, extracted at small scales, in the case of a quasi-thermalized state. (6.4b) Color coded version of the ν_r vs $\mathcal{R}_\mathrm{r}$ diagram, showing where the various results are located with respect to the transition. The color of the data points are the same as those from panel (a).

In the limit of low $\mathcal{R}_\mathrm{r}$, the ξ_q exponents appear to be significantly lower than the usual exponents (Fig. 6.4, blue, green and orange curves). This phenomenon can be explained by the fact that, in such a limit, the system tends to follow equipartition, associated with an energy spectrum of $E(k) \sim k^{-1}$ (Fig. 6.3). This is indeed what we observe: as $\mathcal{R}_\mathrm{r}$ gets closer to o a quasi-thermalized spectra appears, first at low scales, and then progresses towards the larger scales, impacting the slope even at larger scales (as illustrated in Fig. 6.3a and the inset of Fig. 6.4a). There is no intermittency in this regime, with all exponents aligning onto a perfect line. In the other limit, as $\mathcal{R}_\mathrm{r}$ rises, the RNS exponents increase (Fig. 6.4). However, there is still no intermittency in this regime. To check whether it was a feature of the RNS system, we computed the same exponents from a simulation of NSE with fixed viscosity. The result is also shown in Fig. 6.4a (brown curve). We see that the resulting exponents are very close to the exponents we observe in RNS, reaching a quasi perfect agreement for both exponents and slope (Tab. 6.2) located around the middle of the transition area.

This absence of intermittency is not surprising, as the used definition of the structure function is very crude. Indeed, due to the 3 dimensionnality of the simulations, the shell

Table 6.2: **Slopes of the exponents of the structure functions** for both RNS and NS equations. Values were extracted by fitting the structure functions in the inertial range, determined by the domain of constant energy transfer.

Equation	RNS					NS
$\mathcal{R}_\mathrm{r}$	1.11	1.78	2.23	2.78	2.9	-
Slopes	0.36	0.38	0.4	0.4	0.42	0.42

averaging process implies summing non correlated quantities. By doing so, the strong variations that usually give birth to intermittency in the SABRA (15) and GOY (36) vanish along with the fingerprints of intermittency. Further investigations are on going to better define the structure functions for more information refer to Chapter 3.

Note finally that in the log-lattices simulations, the usual Kolmogorov prediction $\xi_q \propto q/3$ does not hold. Indeed, even for NS equation, the slope is roughly equal to 0.42 (Tab. 6.2).

6.6 . Universal and non universal laws

In previous sections, we described the dependence of $\langle\nu\rangle\,\tau/\ell_f^2$ (or $\left\langle\widetilde{\Omega}\right\rangle$) on $\mathcal{R}_\mathrm{r}$ for LLRNS models with constant energy. Surprisingly, such behavior extends to both LLRNS models with conserved enstrophy and to irreversible LL-Navier-Stokes models (Fig. 6.5) upon defining $\mathcal{R}_\mathrm{r} = \frac{f_0}{\langle E\rangle k_f}$. This property is interesting as it provides information on the steady state of the system, and on whether the system is well resolved. Indeed, if the system is under-resolved (i.e $k_\mathrm{max} \ll k_\eta$, k_η being the Kolmogorov scale), it is characterized by a thermalization of the small scales, and corresponds to a state located before the transition at $\mathcal{R}_\mathrm{r} < {\mathcal{R}_\mathrm{r}}^*$, on the linear part of Fig. 6.5a.

However, neither the LLRNS with conserved enstrophy, nor the LL-Navier-Stokes model display the divergence of fluctuations observed in the LLRNS with fixed energy (see Fig. 6.2d). Indeed, the LL-Navier-Stokes model exhibits bounded values of energy and enstrophy fluctuations, as shown in Fig. 6.5c & 6.5d. The LLRNS model with constant enstrophy cannot, by construction, display any enstrophy fluctuations. However, it does not present diverging fluctuations for the energy either (see Fig. 6.5d). This shows that the phase transition feature observed in the LLRNS model with constant energy is non-trivial. We conjecture that these events are linked with the existence of events of quasi-blow-up in the vorticity, that are naturally present in the inviscid blow-up (13; 24). These quasi-blow-ups can propagate from low wavenumbers to large wavenumbers when the viscosity is low, provoking events of large vorticity. In the case where the enstrophy is fixed, such quasi blow-ups cannot exist anymore. In addition, these events are blocked by normal constant viscosity, but not by hypoviscosity (24). A time-dependent viscosity like in the RNS case could be viewed as a hypo-viscosity, leaving room for these events to develop, in contrast with LL-Navier-Stokes. This therefore explains why we only observe these events in the LLRNS with constant energy.

6.7 . Comparison with a 1D diffusive model

6.7.1 . The Leith model

The Leith model is a toy model based on a non-linear diffusive equation, which in its inviscid description (42), approximates the dynamics of the energy spectrum of a Euler flow. it exhibits both an inertial domain with scaling $k^{-5/3}$ and a quasi-thermalization at small scales characterized by a Gibbsian equipartition with scaling $E(k,t) \propto k^2$. Such model is described by a well-chosen second order diffusive operator:

$$\begin{aligned}\partial_t E(k,t) &= -\partial_k \Pi(k,t) - \nu k^2 E(k,t)\\ \Pi(k,t) &= -Ck^{11/2}\sqrt{E(k,t)}\partial_k\left(\frac{E(k,t)}{k^2}\right).\end{aligned}$$

Note that C is a dimensional constant that we set to 1 in this article.

This model has been adapted by (20) to accommodate reversible viscosities by changing ν into ν_r, given by Eq. 4.10. Its solutions confirm the existence of a mean field second order phase transition, albeit for an order parameter equal to $\sqrt{\Omega}$. Moreover, it showed that the resolution of the simulation could have a large impact on the nature of the transition, the latter becoming imperfect as the resolution is decreased. In this article, we adopt the same convention for the dimensionless number representing the influence of resolution, namely $h = k_0/k_{\max}$, where k_0 and $k_{\max}$ are respectively the minimum and maximum wave number in our simulation.

In our system, the thermalization is no longer associated with an energy spectrum following $E(k,t) \propto k^2$ but instead to a k^{-1} behavior. It is then necessary to adapt the previous definition of the energy transfer to our system:

$$\Pi(k,t) = -Ck^{5/2}\sqrt{E(k,t)}\partial_k\left(kE(k,t)\right).$$

Solving $\partial_k \Pi(k,t) = 0$, we obtain an energy spectrum of the form $E(k,t) \propto (Ak^{-5/2} + Bk^{-3/2})^{2/3}$, where (A,B) are two constants taking into account boundary conditions and governing the scale at which the thermalization occurs.

6.7.2 . Influence of the resolution

While performing simulations on log-lattices, it is possible to reach high resolutions ($k > 10^{20}$) at a moderate numerical cost, making it possible to analyze the effect of the resolution on the transition. Such a study could not be done using DNS.

A first influence of resolution can be obtained on the value of the mean reversible viscosity, illustrated in Fig. 6.1b: as $k_{\max}$ (or equivalently the number of modes, N) is increased, the viscosity decreases for a same value of $\mathcal{R}_{\mathrm{r}}$, as there is more room for the cascade to operate. Therefore, the time-averaged viscosity gives us some insights on the dependence of the system on the resolution. Indeed, before the transition, for $\mathcal{R}_{\mathrm{r}} < \mathcal{R}^*_{r,-}$ (being the lower-bound of the transition) the viscosity exhibits a very large dependence on the size of the grid. As we reach the transition area, that we locate at the beginning of the quick rise of viscosity, all the data then collapses on the same universal curve, independent of $k_{\max}$. Note that $\mathcal{R}^*_{r,-}$ shifts to lower values as the size of the grid increases (Tab. 6.3).

Another influence of the resolution is given by the nature of the transition, that shifts from a second-order transition to an imperfect transition as the number of modes is de-

Table 6.3: **Values of various quantities around the transition area.** $\mathcal{R}^*_{r\_}$ defines the value at which the transition area starts, defined by the quick rise in viscosity. $\Delta\nu$ represents the difference in viscosity between the two asymptotic regimes separated by the transition area. $h = \frac{k_0}{k_{\max}}$ is a parameter used to quantify the influence of the resolution and N is the number of spectral modes.

λ	N	h	$\Delta\nu_r$	$\mathcal{R}^*_{r\_}$	$\mathcal{R}^*_r$
2	8^3	$7 \cdot 10^{-3}$	10^4	≈ 4.3	≈ 7
	12^3	$4 \cdot 10^{-4}$	10^6	≈ 3.6	≈ 5
	16^3	$3 \cdot 10^{-5}$	10^8	≈ 3.1	≈ 3.75
ϕ	8^3	$3 \cdot 10^{-2}$	10^2	≈ 4.4	≈ 5
	12^3	$5 \cdot 10^{-3}$	10^4	≈ 2.8	≈ 4
	20^3	10^{-4}	10^8	≈ 1.8	≈ 2.75
Shukla **DNS** (20)	128^3	$2.4 \cdot 10^{-2}$	-	$\simeq 2.0$	2.75

creased (see Fig. 6.2c & 6.2d). This effect was a prediction of the Leith model introduced in (20), and we observe the same typical features found in this model.

Indeed, for $N < 20^3$, neither the mean enstrophy nor its square root follow a power-law. Such description is only accurate upon reaching $N = 20^3$. In the case of the variance, we observe in Fig. 6.2d a scenario that resembles the one predicted by the Leith model: at low resolution, the standard deviation exhibits a "bump" (Fig. 6.2d, circle and triangle markers). In this case, extracting a γ exponent is questionable. Nevertheless, Tab. 6.1 gathers all the extracted critical exponents. At larger resolution, the divergence of the variance becomes more visible, with a critical exponent converging to the mean field value $\gamma_l = 1$. Note that even while using log-lattices, there are still finite size effects, as the limit $\mathcal{R}_\mathrm{r} \to 0$ exhibits truncated Euler dynamics, characterized by equipartition $E(k) \propto k^{-1}$ (Fig. 6.3).

6.7.3 . Further comparison with the Leith model

It appears that, so far, our results and observations are in general agreement with the Reversible Leith model proposed in (20). It is then interesting to compare more quantitatively those two systems. The only quantity from the RNS runs that can be compared to the Leith model is the energy transfer. Therefore, our comparison will rely on computing the Leith-like energy transfers Π_{Leith} (see section 6.7.1) from the RNS energy spectra and comparing it to the RNS transfers Π_{RNS}.

The comparison between the two quantities is presented in Fig. 6.6. We see that the Leith-like transfer is able to mimic the RNS transfer in the inertial domain, but drops more quickly in the dissipative domain. This effect is probably caused by the Leith-like computation not taking into account the strong oscillations of the viscosity (and therefore of the Kolmogorov length) naturally present in RNS. Such oscillations tend to straighten the transfer a bit further outside the inertial range. Overall, it seems that the Leith models shares features with the RNS equations without completely reproducing its dynamics.

6.8 . Appendix A - Enstrophy renormalization

The case of $\mathcal{R}_\mathrm{r} \to 0$, is associated to a vanishing energy injection and therefore, in order to keep the total energy constant, to a vanishing viscosity. The system thus behaves as a truncated Euler equation and should exhibit an equipartition of energy. In our model, this equipartition is characterized by an energy spectrum developing a power law k^{-1} that we will be using in order to compute the total enstrophy Ω_max.

We start by assuming that the kinetic energy in a shell can be written as $E_k = \frac{A}{k}$, where A is a constant obtained through the total kinetic energy E_0:

$$E_0 = \sum_k E(k)\Delta\mu_k = A\sum_k \frac{1}{k}(\lambda k - k) = AN(\lambda - 1),$$

where $\Delta\mu_k$ is the measure of the space, which is $(\lambda k - k)$ for the 1D shells here. This leads to $A = \frac{E_0}{N(\lambda-1)}$, where N is the number of modes used on the grid.
We then compute the total enstrophy Ω_max.

$$\begin{aligned}\Omega_\mathrm{max} &= \sum_k k^2 E(k)(\lambda k - k) = \frac{E_0}{N}\sum_k k^2, \\ &= \frac{E_0 k_0^2}{N}\sum_{p=0}^{N-1}\lambda^{2p} \simeq \frac{E_0\lambda^2 k_\mathrm{max}^2}{N(\lambda^2-1)}.\end{aligned}$$

We can now define the renormalized enstrophy:

$$\widetilde{\Omega} = \frac{\Omega}{\Omega_\mathrm{max}}. \tag{6.1}$$

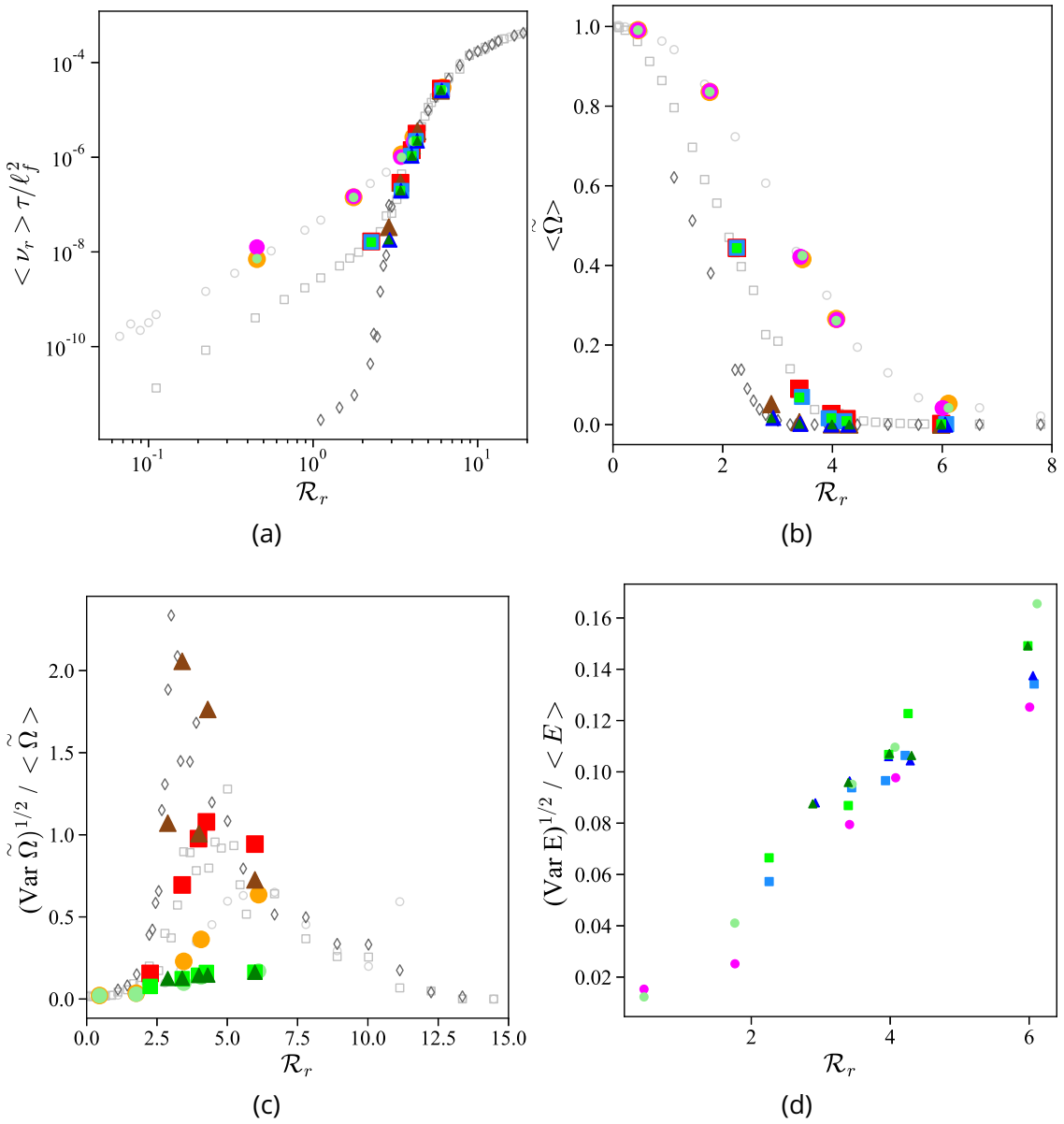

Figure 6.5: **Existence of a phase transition in the different systems for different order parameter**.(6.5a) Renormalized viscosity function of the previously introduced control parameter $\mathcal{R}_\mathrm{r}$. (6.5b) Renormalized enstrophy as a function of the control parameter $\mathcal{R}_\mathrm{r}$. (6.5c) Rescaled variance of the normalized enstrophy as a function of $\mathcal{R}_\mathrm{r}$. (6.5d) Rescaled variance of the energy, as a function of $\mathcal{R}_\mathrm{r}$, for the LLRNS conserved enstrophy case and LLNS. In all four figures, the empty gray symbols are the data of Fig. 6.1b & 6.2a. Circles, squares and triangles are associated to $N = 8^3, 12^3, 16^3$, respectively. The conservation schemes are coded by color, with light green to dark green being the irreversible LL-Navier-Stokes model, purple to dark blue LLRNS model with conserved enstrophy, orange to brown LLRNS model with conserved energy. Note that in the non-conserved energy case, we define $\mathcal{R}_\mathrm{r}$ using the averaged kinetic energy. Also note that the difference between the grey and blue symbols lies in the numerical details, both are associated to conserved energy case. But, grey symbols are obtained varying the forcing amplitude f_0 while blue symbols are associated to a fixed f_0 and varying initial condition i.e varying E_0. Fig. 6.5a & 6.5b show that all mean viscosities and enstrophy collapse on an universal law. While Fig. 6.5c & 6.5d highlight the absence of transition for LL-Navier-Stokes and LL-RNS with conserved enstrophy.

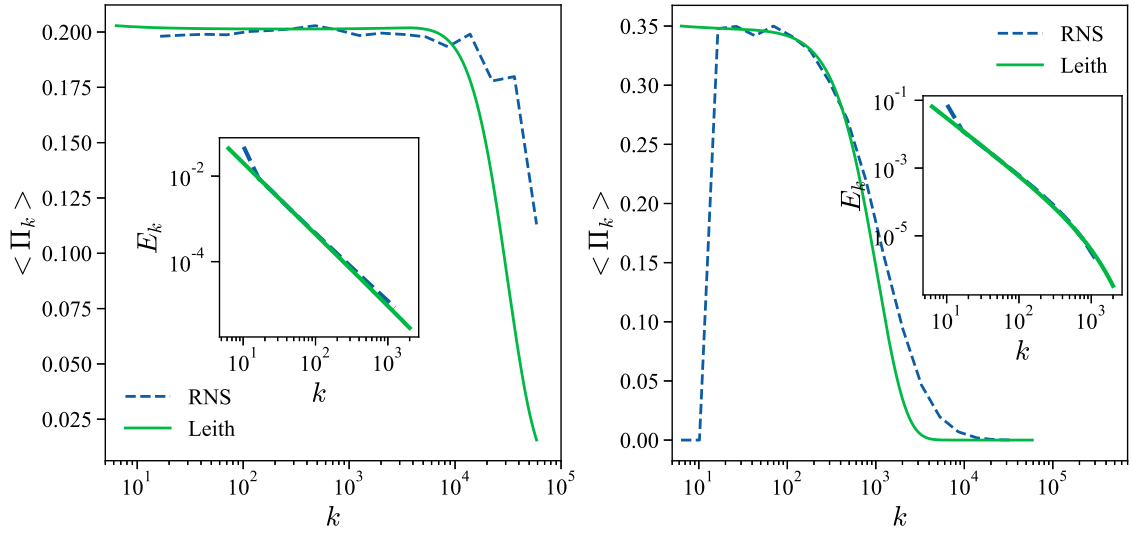

Figure 6.6: **Quantitative comparison of the energy transfers** between RNS (dashed lines) and Leith-like transfers (full lines). The main figures present the two energy transfers, while the insets show the fitted energy spectra. The two figures are obtained for different values of $\mathcal{R}_\mathrm{r}$ (6.6a) $\mathcal{R}_\mathrm{r} \approx 2.34$ (6.6b) $\mathcal{R}_\mathrm{r} \approx 3.34$.

7 - Equivalence of ensembles and statistics

In this section, we study the equivalence conjectures postulated by Gallavotti (1). This equivalence was studied using 2D (47) and 3D (48) DNS in the context of the *Reversible Navier-Stokes at constant enstrophy* (RNSW). However, due to unsufficient resolution, exploring high Reynolds regime remains a challenge. We propose to use LL to investigate the Gallavotti conjectures for both conserved quantities (i.e for RNSE and RNSW). We then make use of the time reversibility to apply the Gallavotti-Cohen theorem.

7.1 . Definitions and conjectures

Following (48), we introduce the collection $\mathcal{E}^{\mathcal{I},N}$ of the stationary distributions $\mu_\nu^{\mathcal{I},N}$, where $\mathcal{I}$ characterizes the irreversible equation (with time-independent viscosity i.e. LL-Navier-Stokes), with N modes. Similarly, we define the collection $\mathcal{E}^{\mathcal{R},N}$ of the stationary distributions $\mu_G^{\mathcal{R},N}$, associated with the LLRNS model of N modes, where G is the conserved quantity (total enstrophy, total kinetic energy…). For any observable $\mathcal{O}$, $\langle\mathcal{O}\rangle_\nu^{\mathcal{I},N}$ and $\langle\mathcal{O}\rangle_\mathcal{G}^{\mathcal{R},N}$ denote the averages over the distributions $\mu_\nu^{\mathcal{I},N}$ and $\mu_G^{\mathcal{R},N}$, respectively.

As in (47; 48), a set of parameters ν, G and N will be said to be "in correspondence" if

$$\langle\mathcal{G}(\boldsymbol{u})\rangle_\nu^{\mathcal{I},N} = G \tag{7.1}$$

G is associated to a conserved, and therefore constant, quantity in the RNS model while $\mathcal{G}$ is its irreversible counterpart in regular NS.
The adaptation of the two Gallavotti conjectures to our models can then be formulated as:

Conjecture 1: *If ν, G and N are in correspondence, then for any local observable (i.e. depending on a limited number of modes) $\mathcal{O}(\boldsymbol{u})$ one has*

$$\forall N, \lim_{\nu\to 0}\langle\mathcal{O}\rangle_\mathcal{G}^{\mathcal{R},N} = \lim_{\nu\to 0}\langle\mathcal{O}\rangle_\nu^{\mathcal{I},N} \tag{7.2}$$

Conjecture 2: *Let $\mathcal{O}(\boldsymbol{u})$ be a local observable depending on $\boldsymbol{u}(\boldsymbol{k})$ for $k < K$, then if ν, G and N are in correspondence one has*

$$\lim_{N\to\infty}\langle\mathcal{O}\rangle_\mathcal{G}^{\mathcal{R},N} = \lim_{N\to\infty}\langle\mathcal{O}\rangle_\nu^{\mathcal{I},N} \tag{7.3}$$

$\forall\nu$ and $K < c_\nu k_\eta$, $c_\nu \xrightarrow[\nu\to 0]{} c_0 < \infty$, where k_η is the Kolmogorov scale.

Those two conjectures are associated to different regimes. Indeed, by fixing the resolution N and sending the viscosity to 0, one reaches the warm regime, characterized by thermalization (*Conjecture 1*). In contrast, by sending first the resolution N to infinity, then viscosity to 0, one prevents the thermalization from occurring (as it is associated to under-resolved simulations). Therefore, *Conjecture 2* is associated to hydrodynamical regimes, and better describes turbulence in the limit of low viscosities.

7.2 . Numerical procedure

In order to investigate the equivalence of ensemble, we start by running a LL-Navier-Stokes simulation, with time independent viscosity of $\nu = 10^{-4}, 10^{-5}, 5 \cdot 10^{-6}, 10^{-6}, 10^{-7}$ for different values of N. After reaching a steady state for a sufficient number of time-steps (to ensure the possibility of doing statistics), we use the LL-Navier-Stokes field as an initial condition for the LLRNS equation, in both conservation case. We then let both reversible and irreversible simulations run for 4.10^5 time-steps.

This procedure enables us to highlight any divergence of the reversible solution from the irreversible solution, while allowing us to characterize the simulations by viscosity ν or equivalently by their Reynolds number (Re).

7.2.1 . Using scores to compare PDFs

In the next sections, we need to compare PDFs. To quantify their similarity, we introduce a scalar parameter – a score –, defined as:

$$\mathcal{S}(\mathcal{O}) = 1 - \sum_{i=1}^{p} \frac{|\mathcal{O}_{\mathcal{R}}^{(i)} - \mathcal{O}_{\mathcal{I}}^{(i)}|}{\mathcal{O}_{\mathcal{I}}^{(i)}} \mathcal{B}^{-i+1} \tag{7.4}$$

where $\mathcal{O}^{(i)}$ stands for the i-th moment of the local observable $\mathcal{O}$, p for the number of moments we take into account and $\mathcal{B}$ for a decomposition basis ($\mathcal{B} = 10$, being a decimal basis in our case).

A score of one implies little errors between irreversible and reversible moments and leads to matching PDFs. We will restrict the computation of the score to the first three moments because of large statistical errors in our kurtosis. Therefore, the score should be roughly 1 whenever the 3 first moments coincide, i.e. whenever the distributions are identical around the mean value. Thus, $\mathcal{S}$ appears as a good indicator to qualify to what extent the conjecture holds.

7.3 . Analysis of the conjectures

7.3.1 . Statistics of the reversible viscosity

Because of its presence in the limits, the viscosity plays a special role in the conjectures. However it is a non-local observable. There is therefore no reason that mean reversible viscosities should be equivalent to irreversible viscosities, even when only small values are considered. However, there are several differences between the conservation schemes that may temper this observation. First, the total kinetic energy is concentrated at the large scales whereas enstrophy is a small scale quantity, resulting in completely different statistics of the viscosity. In fact, a major difference between the two cases arises in the possible occurrence of negative viscosities. At low viscosities, there is almost no occurrence of negative viscosities in the conserved energy case, even in systems presenting a quasi-thermalized spectrum (Fig. 7.1a). This is no longer true for the conserved enstrophy case as we observe many occurrences of negative viscosities in well thermalized regimes (Fig. 7.1b).

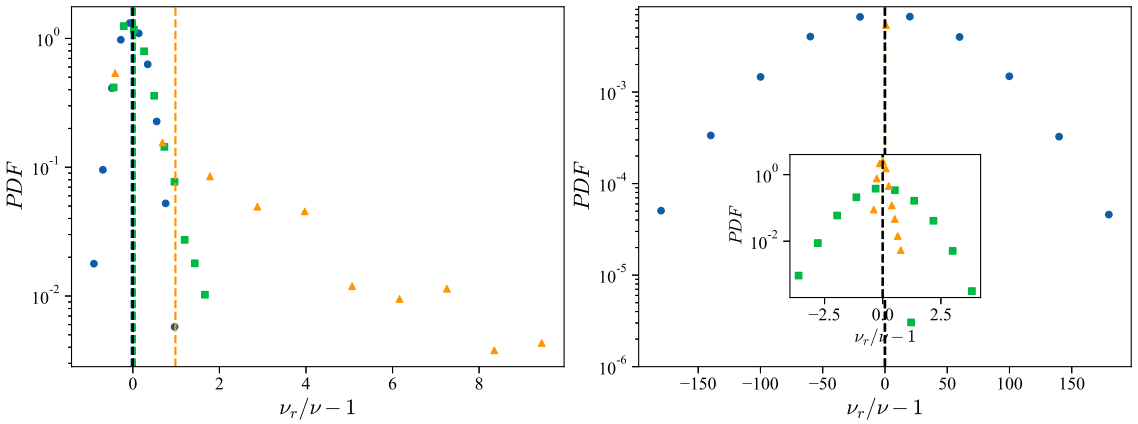

Figure 7.1: **PDF of the ratio ν_r / $\nu - 1$** where ν_r stands for the reversible viscosity, for $N = 8^3$ (blue dots), 12^3 (green squares), 16^3 (orange diamonds), $\nu = 10^{-7}$. Fig. 7.1a shows the results associated to $\mathcal{G} = E$, while Fig. 7.1b is associated to $\mathcal{G} = \Omega$. Colored dashed lines represents the mean values of the PDF while the black dashed line is associated to $\langle \nu_r \rangle = \nu$.

In addition, conserving the enstrophy is a strong constraint, that implies additional equivalence for the viscosity. Indeed, if the first conjecture holds, we should observe conservation of the mean work of the forcing term $\mathcal{W} = \langle \boldsymbol{f}.\boldsymbol{u} \rangle$, because it is local at large scales (more details in section 7.4.1 and Tab. 7.1. Using the energy budget, this yields $\langle \nu_r \rangle = \nu$ in the constant enstrophy case (48), even though ν_r is not a local observable. The property is not true for the conserved energy case, so that the *Conjecture 1* should not hold a priori for the viscosity.

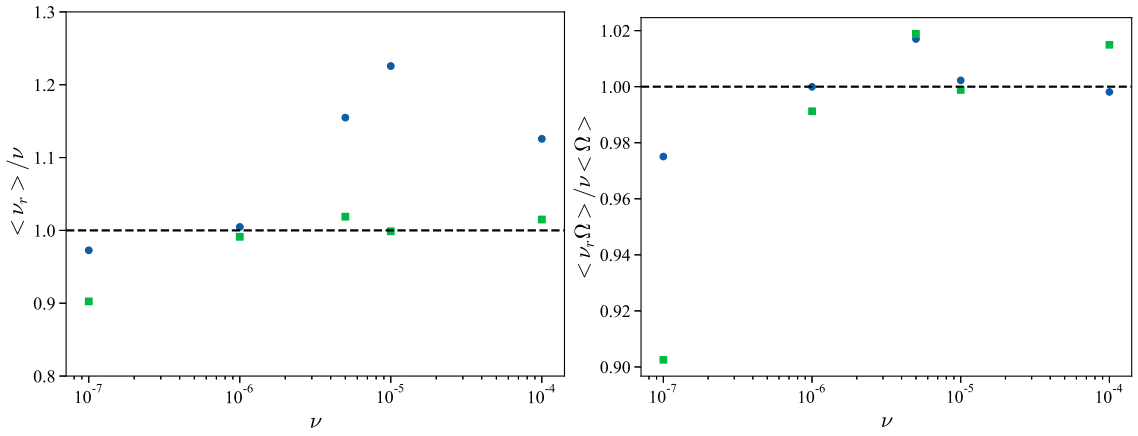

Figure 7.2: **Equivalence between the viscosities**. (7.2a) Ratio of the mean reversible viscosity over the standard NS viscosity. (7.2b) Ratio of the mean dissipation $\nu\Omega$. Both figures are obtained for $N = 8^3$, blue dots correspond to conserved energy while green squares are associated with conserved enstrophy.

Our measurements are generally in agreement with these theoretical predictions, with some exceptions (Fig. 7.2a). In the conserved enstrophy LLRNS model, we observe that the condition $\langle \nu_r \rangle = \nu$ holds for most values of ν, except for very low viscosity. In the conserved energy case, the situation is opposite: the property does not hold a priori for large enough values of viscosity. However, for small enough values of ν, we recover $\langle \nu_r \rangle \approx \nu$.

Note that since injection is a local observable, and since we are in a stationary state, where on average injection equals dissipation, we expect that $\nu_r \Omega$ obeys *Conjecture 1* & *2*. In the case of constant enstrophy, this condition is equivalent to $\langle \nu_r \rangle \approx \nu$, as we just saw. However, in the conserved energy case, this is not true anymore. Indeed, as we see in Fig. 7.2b, we have $\langle \nu_r \Omega \rangle \approx \nu \langle \Omega \rangle$ for the conserved energy case, even though the equivalence is not fulfilled for the viscosity alone.

7.3.2 . Energy and enstrophy

The first obvious quantities to investigate are energy E and enstrophy Ω. Results are reported in Tab. 7.1, where we give the mean ratios between reversible and irreversible values at various ν for the two conservation schemes.

Table 7.1: **Ratio of various quantities for both conservation scheme.** $\mathcal{W}$ stands for the work of the forcing term.

N	ν	$\langle E_\mathcal{R} \rangle_E / \langle E_\mathcal{I} \rangle_\nu$	$\langle \Omega_\mathcal{R} \rangle_E / \langle \Omega_\mathcal{I} \rangle_\nu$	$\langle W_\mathcal{R} \rangle_E / \langle W_\mathcal{I} \rangle_\nu$	$\langle E_\mathcal{R} \rangle_\Omega / \langle E_\mathcal{I} \rangle_\nu$	$\langle \Omega_\mathcal{R} \rangle_\Omega / \langle \Omega_\mathcal{I} \rangle_\nu$	$\langle W_\mathcal{R} \rangle_\Omega / \langle W_\mathcal{I} \rangle_\nu$
8^3	10^{-4}	100.0%	125.6%	99.9%	98.2%	100.0%	98.5%
	10^{-5}	100.0%	102.1%	99.7%	99.8%	100.0%	99.9%
	5.10^{-6}	100.0%	98.2%	98.6%	98.9%	100.0%	98.3%
	10^{-6}	100.0%	100.0%	99.9%	99.8%	100.0%	99.4%
	10^{-7}	100.0%	100.0%	97.3%	100.0%	100.0%	96.3%
12^3	10^{-4}	100.0%	135.4%	99.6%	98.5%	100.0%	98.1%
	10^{-5}	100.0%	160.0%	99.3%	99.0%	100.0%	98.9%
	5.10^{-6}	100.0%	164.6%	99.1%	98.8%	100.0%	98.6%
	10^{-6}	100.0%	132.3%	99.7%	98.6%	100.0%	98.9%
	10^{-7}	100.0%	100.4%	99.8%	100.0%	100.0%	99.7%
16^3	10^{-4}	100.0%	142.9%	97.5%	98.8%	100.0%	98.0%
	10^{-5}	100.0%	156.1%	98.4%	99.6%	100.0%	99.3%
	5.10^{-6}	100.0%	145.1%	98.9%	99.7%	100.0%	99.8%
	10^{-6}	100.0%	315.2%	98.8%	99.5%	100.0%	99.8%
	10^{-7}	100.0%	313.4%	97.9%	98.7%	100.0%	98.5%

In all cases, the ratio of $\langle \mathcal{G} \rangle / G$ is very close to 1, showing the validity of Eq. 7.1 for both conservation schemes. It is interesting to note that the mean energy is well described even in the conserved enstrophy case. On the other hand, in the conserved energy case the enstrophy is correctly reproduced only in the quasi-thermalized state (Tab. 7.1 & Fig. 6.5a). In particular, at high resolution ($N = 16^3$), we observe enstrophy ratio above 100%.

7.4 . Analysis of Conjecture 1 - Warm regime

In this subsection, we focus on the *Conjecture 1*. We consider various local quantities, and analyze results at fixed number of modes $N = 8^3$ and decreasing viscosity of $\nu =$

10^{-4}, 10^{-5}, $5 \cdot 10^{-6}$, 10^{-6} and 10^{-7}.

7.4.1 . Work of the forcing term

We now consider the work $\mathcal{W} = \langle \boldsymbol{f}.\boldsymbol{u} \rangle$. This quantity appears as a good candidate for *Conjecture 1*, as the forcing term is localized around $k_f = 15$ (see Eq. 1.10). Tab. 7.1 summarize the ratio of mean values between reversible and irreversible values, and show that almost all simulations fulfill correspondence conditions Eq. 7.1, with either conserved energy or conserved enstrophy. A finer understanding of this correspondence can be obtained by exploring the properties of its PDF in both the hydrodynamical case ($\nu = 10^{-4}$) and quasi-thermalized ($\nu = 1 \cdot 10^{-6}$). This is shown in Fig. 7.3. In both case and with both schemes, the PDF shows good agreement between the reversible and irreversible case, except for the high viscosity case, where tails are different. This difference is due to the difference in standard deviations. Nevertheless, in the quasi-thermalised regime (Fig. 7.3b), the PDF presents quasi perfect agreement between irreversible and reversible cases, which is a signature that *Conjecture 1* holds for the local observable $\mathcal{W}$.

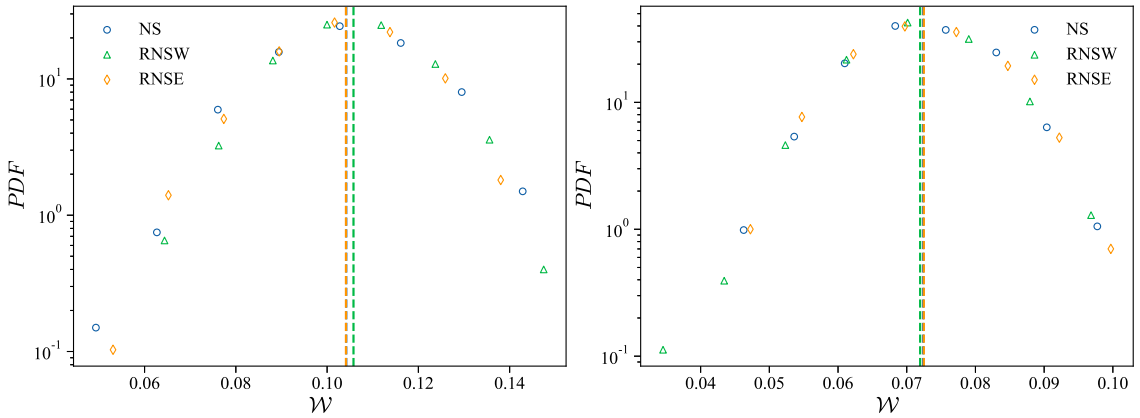

Figure 7.3: **PDF of the work of the forcing term $\mathcal{W}$.** Simulations are performed with $N = 8^3$. (7.3a) $\nu = 10^{-4}$ (7.3b) $\nu = 10^{-6}$. Dashed lines represent the mean values of the PDF. Both conservation schemes show good agreement for the mean values. At higher viscosities, tails differ.

To further support this claim, we analyze the ratio of the two first order moments $\frac{\langle \mathcal{W}_\mathcal{R} \rangle}{\langle \mathcal{W}_\mathcal{I} \rangle}$ and $\frac{\sigma^\mathcal{W}_\mathcal{R}}{\sigma^\mathcal{W}_\mathcal{I}}$. Fig. 7.4 gathers those results, obtained for $N = 8^3$. One observes that for any value of ν, the mean value of $\mathcal{W}$ corresponds to the mean value of the reversible equations, within a 5% error margin (Fig. 7.4a). This property does not hold however for the standard deviation, where the ratios lie outside the confidence interval in the hydrodynamical case (Fig. 7.4b). As the viscosity decreases, both ratios enter the confidence interval, and thus both PDFs match in the inviscid limit.

7.4.2 . Energy spectra

We now consider the equivalence for the distribution of energy in the wavenumber space, through the instantaneous energy spectra $E(\boldsymbol{k})$. As time varies, and for each given

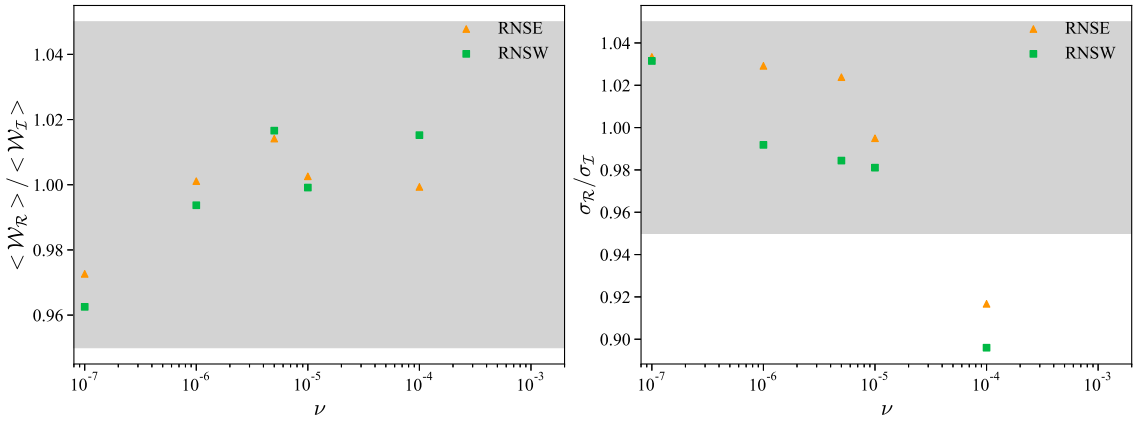

Figure 7.4: **Ratios of the two first moments of $\mathcal{W}$ as a function of the viscosity ν.** Simulations are performed with $N = 8^3$. (7.4a) Ratio $\langle \mathcal{W}_\mathcal{R} \rangle \,/\, \langle \mathcal{W}_\mathcal{I} \rangle$, (7.4b) Ratio $\sigma^\mathcal{W}_\mathcal{R}/\sigma^\mathcal{W}_\mathcal{I}$, where σ stands for the standard deviation. The gray shaded area represents the 5% confidence interval.

k, $E(k)$ fluctuates in time, and we can study its statistics through our score function. Fig. 7.5 gathers the different scores $\mathcal{S}(E)$, obtained for different ν at various k_s. In the conserved energy case (Fig. 7.5a), *Conjecture 1* holds quite well. Indeed, as $\nu \to 0$, the score is almost equal to one (purple pentagons) over the whole space, highlighting good moments matching. For higher viscosities (blue dots, green squares…) the score starts to drop at smaller k, indicating that only the first shells display equivalence. Note that the statistics around the first and last data points might be biased by side effect associated to the sampling process. The conserved enstrophy case (Fig. 7.5b) shares some similar features, as the score indeed appears to grow as ν decreases, progressively spanning the whole grid.

According to the score, one should observe PDF matching (outside the tails) for $\nu = 10^{-4}$ at big scales ($k_s \approx 16.5$) and PDF differences at small scales ($k_s \approx 182.6$). This is indeed what we observe in Fig. 7.6a & Fig. 7.6b. In addition, one expects near identical PDF in both conservation schemes, at all scales for $\nu = 10^{-7}$. This statement is confirmed in Fig. 7.6c& Fig. 7.6d, where the PDFs are almost indistinguishable.

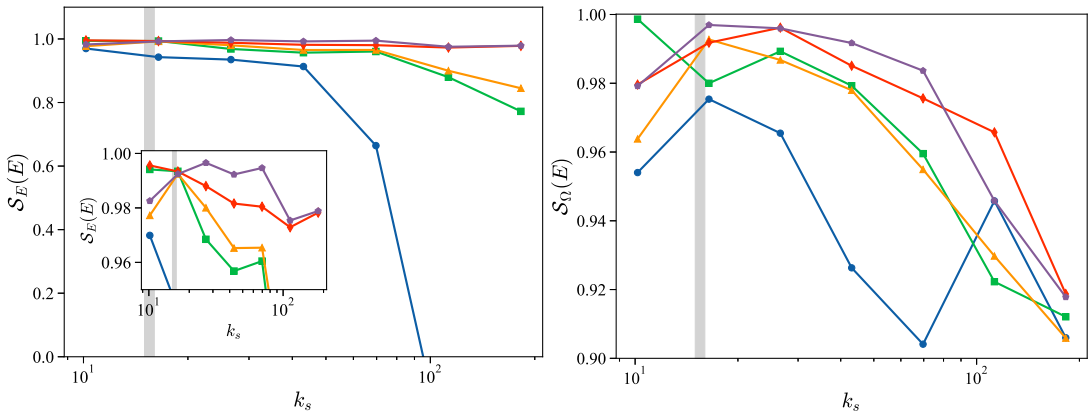

(a) (b)

Figure 7.5: **Score $\mathcal{S}(E)$ of the energy in each shell** Figures (7.5a) corresponds to the conserved energy case while (7.5b) is associated to the conserved enstrophy case. The gray shaded areas show where the forcing term is localized. Figures are obtained for $N = 8^3$. Blue dots, green squares, orange triangles, red diamonds and purple pentagons are respectively associated to $\nu = 10^{-4}$, 10^{-5}, $5 \cdot 10^{-6}$, 10^{-6} and 10^{-7}.

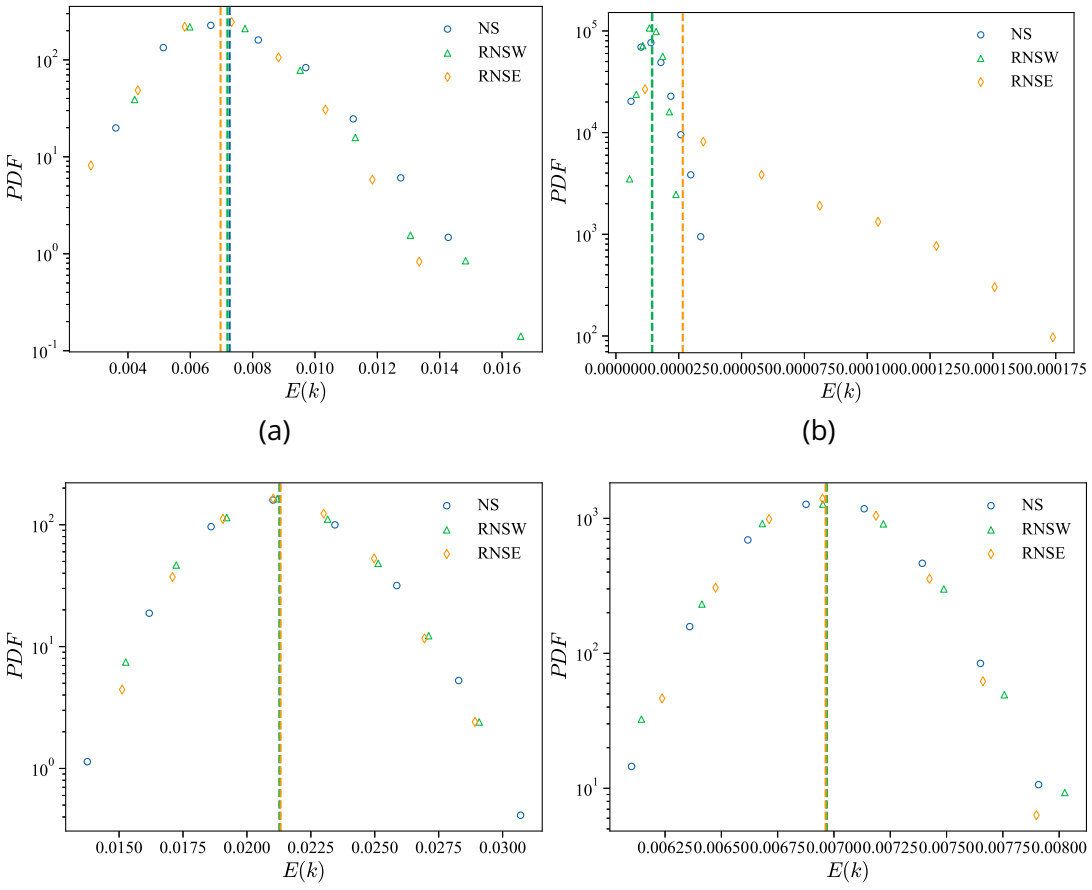

(a) (b)

(c) (d)

Figure 7.6: **Energy PDF** Results are obtained for different values of k_s and ν, with $N = 8^3$. (7.6a & 7.6b) $\nu = 10^{-4}$, $k_s \approx 16.5$, $k_s \approx 182.6$; (7.6c & 7.6d) $\nu = 10^{-7}$, $k_s \approx 16.5$, $k_s \approx 182.6$. Dashed lines represent the mean values of the PDF.

7.5 . Analysis of Conjecture 2 - Hydrodynamical regime

In this section, we analyze the *Conjecture 2*, i.e. equivalence at fixed ν and varying N in the case of the hydrodynamical regime, in the thermodynamic limit $h \to 0$ ($k_{\max} \to \infty$).

In the analysis of this conjecture, there appears a strong difference between the conserved energy case, and the conserved enstrophy case. Indeed, the former presents a phase transition whose characteristics depend on N (Fig. 6.5). This dependence complicates the analysis on the impact of $k_{\max} \to \infty$ ($N \to \infty$) in *Conjecture 2*. In fact, for a given $\mathcal{R}_r$, increasing N implies switching phase (Fig. 6.5a), going from quasi-thermalized regimes ($\mathcal{R}_{\mathrm{r}} < \mathcal{R}_r^*$, in which *Conjecture 1* holds) to hydrodynamical ones ($\mathcal{R}_{\mathrm{r}} \geq \mathcal{R}_r^*$). Therefore, one must be careful while comparing similar Re for different resolutions as the validity of the conjecture is related to the position in the transition, as will be highlighted later.

7.5.1 . Energy spectra

We now focus on the statistics of the energy spectrum, at given values of k_s. In the hydrodynamical regime, *Conjecture 2* implies that the score of $\mathcal{E}(k)$ should be equal to 1 in the thermodynamic limit $h \to 0$ ($k_{\max} \to \infty$). In practice, we shall see that this will be true only for a given range of wavenumber $k < K_\nu$ (49; 48).

In the conserved enstrophy case the analysis is straightforward. We show in Fig. 7.7 the evolution of the score $\mathcal{S}_\Omega(E)$ at various resolutions. At lower resolution, $\mathcal{S}_\Omega(E)$ drops quickly (Fig. 7.7, blue dots) highlighting the absence of equivalence between the reversible and irreversible ensemble. By increasing N, we obtain scores closer to 1 on intervals up to K_ν, defined as the value of k such that $\forall k > K_\nu, \mathcal{S}_\mathcal{G}(\mathcal{O}) < 0.9$. We also observe that for low values of viscosity, the scores are similar for $N = 12^3$ and $N = 16^3$, supporting the second conjecture, in the conserved enstrophy case. For $k > K_\nu$, scores start to "oscillate", this is associated to the fact that the reversible moments fluctuate around the irreversible ones and sometimes lies in confidence interval, leading to artificially higher scores.

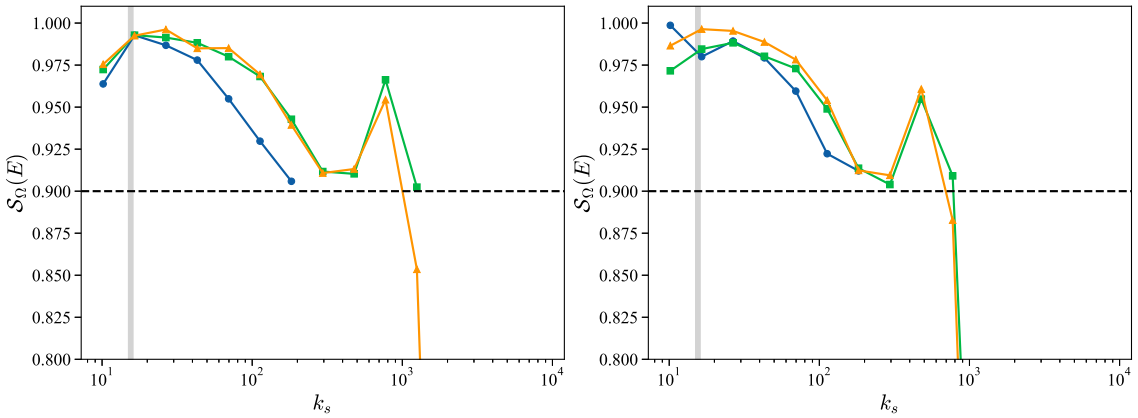

(a) (b)

Figure 7.7: **Score $\mathcal{S}(E)$ of the energy in each shell for $\mathcal{G} = \Omega$.** (7.7a) $\nu = 5 \cdot 10^{-6}$; (7.7b) $\nu = 10^{-5}$. Blue dots, green squares and orange triangles correspond to $N = 8^3, 12^3, 16^3$, respectively. Black dashed lines correspond to a score of 0.9.

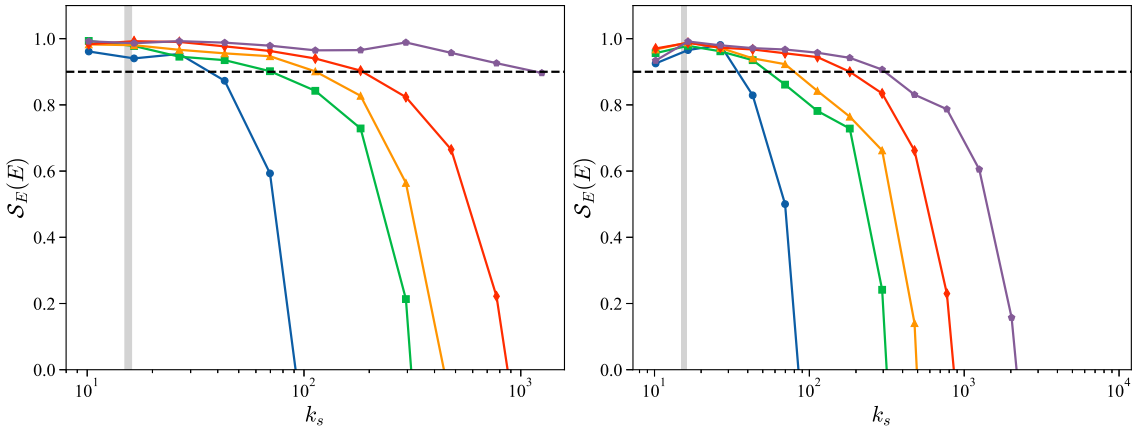

Figure 7.8: **Score $\mathcal{S}(E)$ of the energy in each shell for $\mathcal{G} = E$.** (7.8a) $N = 12^3$; (7.8b) $N = 16^3$. Blue dots, green squares, orange triangles, red diamonds, and purple pentagons correspond to $\nu = 10^{-4}$, $\nu = 10^{-5}$, $5 \cdot 10^{-6}, 10^{-6}$, 10^{-7}, respectively. Note that in (7.8a), the purple pentagons are associated with a quasi-thermalized state, being a crossover region between the two conjectures. Black dashed lines correspond to a score of 0.9.

In the conserved energy case, the analysis is complicated by the phase transition, as detailed below. According to the *Conjecture 2*, one expects to observe scores $\mathcal{S}_{\mathcal{G}}(E) > 0.9$ on bigger and bigger domains as $\nu \to 0$. Fig. 7.8 shows the scores, in the case of conserved energy E, for various viscosities and $N = 12^3$ (Fig. 7.8a) or $N = 16^3$ (Fig. 7.8b). Our results indeed highlight a dependency of K_ν on ν (Fig. 7.7 & 7.8). Note that the red diamonds

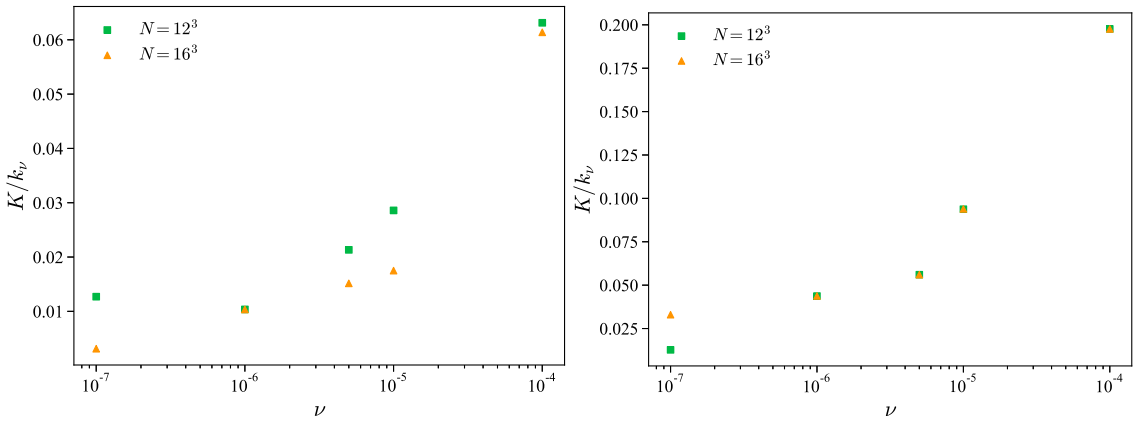

Figure 7.9: **Ratio K/k_ν in the context of Conjecture 2** (7.9a) corresponds to conserved total kinetic energy while (7.9b) corresponds to conserved enstrophy. The thresholds K were extracted directly from the score at the considered k. The thresholds were not extracted for $N = 8^3$ since the resolution is insufficient as most simulations lie on the thermalized branch (Fig. 6.5a, colored circles).

in Fig. 7.8a are associated with a crossover regime where thermalization at small scales starts to occur, leading to results similar to *Conjecture 1* (Fig. 7.5a) but with a slight drop.

Fig. 7.9 shows the extracted thresholds divided by the Kolmogorov scale for both conservation schemes, at different resolutions and different viscosities. Unlike in (48), c_ν is no longer a constant but depends on the value of ν and does not grow as fast as the Kolmogorov scale k_η (Fig. 7.9).

Note that for $\nu = 10^{-7}$, the $N = 12^3$ are under-resolved, leading to an upper-bound $K = k_{\max}$ for the threshold, that can not grow anymore as ν decreases. Such phenomenon explains the difference between the two first points of Fig. 7.9b.

In the thermodynamic limit of the conserved energy case, the equivalence is best achieved for $\mathcal{R}_\mathrm{r} \to {\mathcal{R}_\mathrm{r}}^*(N)$. As mentioned before, such properties make the comparison between resolutions difficult, as the value of $\mathcal{R}_\mathrm{r}$ at which the transition between warm and hydrodynamical regimes occurs also depends on N. Nevertheless, Fig. 7.9a gathers the results for the conserved energy case, confirming the validity of *Conjecture 2*, on smaller domains with respect to those observed in the conserved enstrophy case.

7.6 . Irreversibility and Gallavotti-Cohen's fluctuation theorem

Disclaimer: This section presents the current results of an on-going work, new results are to be expected in the future.

One of the assets of studying the RNS equations lies in the time reversibility. For time reversible systems, one can apply the Gallavotti-Cohen theorem obtaining various informations on the system, such as phase space contraction rate... Coupling this result to the equivalence conjecture, one can study some non trivial underlying properties of the NSE.

7.6.1 . Anosov systems and fluctuation theorem

A differential dynamical system is defined by the existence of a bijection $S_t : \mathcal{C} \to \mathcal{C}$, $\mathcal{C}$ being the phase space, such that for any initial condition x_0, there exists a unique futur at time t:

$$x(t) = S_t(x_0). \tag{7.5}$$

Varying t, one obtains a flow in the phase space $\mathcal{C}$ such that [1]:

$$S_0 = \mathrm{Id}, \tag{7.6}$$

$$\forall (t,s) \in \mathbb{R}^2,\ S_t \circ S_s = S_{t+s}. \tag{7.7}$$

An *Anosov system*, is a *smooth* dynamical system $(\mathcal{C}, S)$ such that the phase space $\mathcal{C}$ can be decomposed in $\mathcal{C} = E_0 \bigoplus E_S \bigoplus E_I$, where E_0 is a 1D manifold in the flow direction while E_S (resp. E_I) is a stable (resp. unstable) manifold that exponentially constracts (resp. expands) corresponding to negative (resp. positive) Lyapunov exponents.
In addition, an *Anosov system* is said *transitive* if the stable and unstable manifolds are dense in $\mathcal{C}$ (50).

For such systems, the following theorem holds:

[1] A simple example is the Hamiltonian flow of classical mechanic.

Theorem (51): if a system is a transitive Anosov system then it admits a Sinai-Ruelle-Bowen (SRB) distribution.

We recall that a SRB distribution μ is defined such that (52):

$$\lim_{T\to\infty}\frac{1}{T}\sum_{i=0}^{T-1} f(S^i(x)) = \int_{\mathcal{C}} \mu(dy) f(y), \tag{7.8}$$

for all smooth function f and all $x \in \mathcal{C}$. In particular, Eq. 7.8 assesses the existence of the time-average of any macroscopic observable, defined at a point x of the phase space $\mathcal{C}$.

For a time reversible, dissipative (i.e $\langle\sigma\rangle > 0$, σ being the phase space contraction rate), transitive Anosov system, the probability distribution $P_\tau(p)$ of the variable

$$p = \frac{1}{\tau}\int_0^\tau \frac{\sigma(S^t x)}{\langle\sigma\rangle} dt, \tag{7.9}$$

verifies the large deviation relation $P_\tau(p) = e^{\zeta(p)\tau + \mathcal{O}(1)}$ (51), with the symmetry property $\zeta(p) - \zeta(-p) = p\,\langle\sigma\rangle$ for all p within the definition domain of ζ.

This fluctuation theorem although interesting has only been rigorously proven for idealized systems such as Anosov systems. The extension to real systems, made of many particles is therefore non trivial. In the following, we tackle the subject of the *Gallavotti-Cohen Fluctuation Theorem*, obtained through less restrictive hypothesis.

7.6.2 . The Gallavotti-Cohen Fluctuation Theorem

In order to extend the *Fluctuation theorem* of the previous section to more realistic systems, Gallavotti (50) introduced the *chaotic hypothesis* defined as follows:

Chaotic hypothesis (CH): *a reversible many-particle system in a stationary state can be regarded as a transitive Anosov system for the purpose of computing the macroscopic properties of the system.*

Through the use of (CH), it is then possible to apply the results of the previous section and derive the *Gallavotti-Cohen Fluctuation Theorem* (GCFT).

Upon satisfying the following properties (A)-(C):

(A) *Dissipation:* The phase space volume undergoes a contraction at a rate, on the average, equal to $D\,\langle\sigma(x)\rangle_+$, where 2D is the phase space $\mathcal{C}$ dimension and $\sigma(x)$ is a model dependent "rate" per degree of freedom.

(B) *Reversibility:* There is an isometry, i.e., a metric preserving map i in phase space, which is a map $i : x \to ix$ such that if $t \to x(t)$ is a solution, then $i(x(-t))$ is also a solution and furthermore i^2 is the identity.

(C) *Chaoticity:* The chaotic hypothesis holds and we can treat the system $(\mathcal{C}, S)$ as a transitive Anosov system.

One can then apply the GCFT, stating that the probability $P_\tau(p)$ that the total entropy production over a time interval τt_0 (t_0 being the average time between timing events) has a value $Dt\,\langle\sigma(x)\rangle_+\,p$ satisfies the large-deviation

$$\ln\frac{P_\tau(p)}{P_\tau(-p)} = Dt\,\langle\sigma(x)\rangle_+\,p + \mathcal{O}(1), \tag{7.10}$$

where we recall that 2D is the dimension of the phase space $\mathcal{C}$.

If the GCFT holds true then one should observe a linear dependance for $\ln \frac{P_\tau(p)}{P_\tau(-p)}(\tau)$. This theorem was succesfully applied in wind tunnel experiments (53) with p being the pressure force over an objet of area S but also in granular media (54). In (53), PDFs were also successfully rescaled, applying Sinai's theory (51), into τ independent distributions. This result holds great importance as the probability of observing negative fluctuations decreases as τ increases.

7.6.3 . Application of the GCFT

By construction, the *Reversible Navier-Stokes equations* satisfy properties (A)-(C). It is therefore possible to apply the GCFT to a variable related to the phase space contraction.

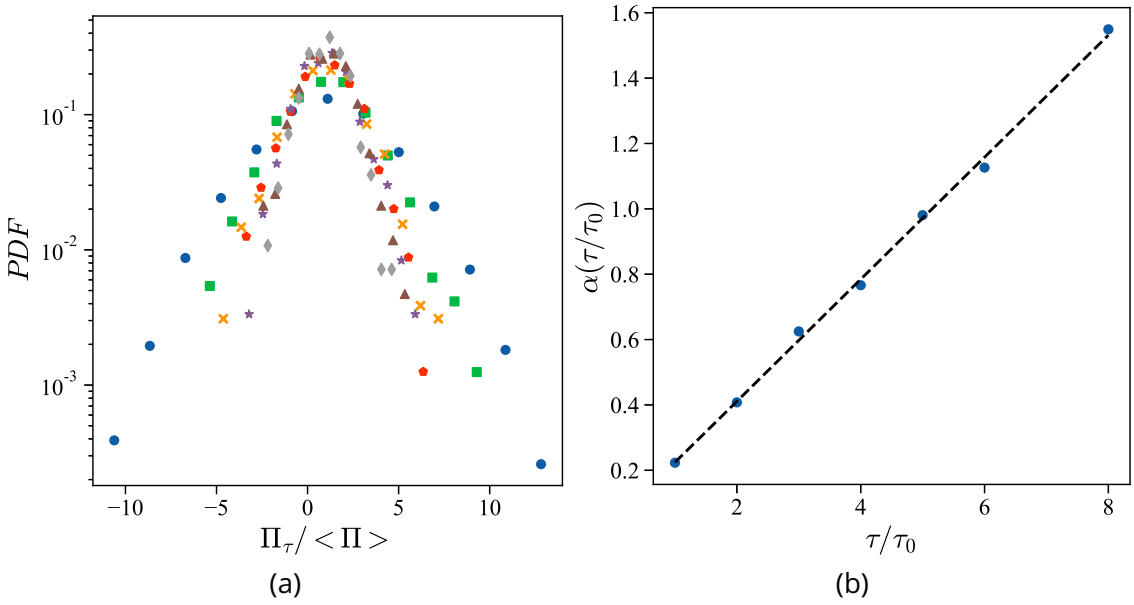

Figure 7.10: **An application of the GCFT** the considered simulation is performed using $N = 12^3$ and $\mathcal{R}_\mathrm{r} = 1.89$. (7.10a) PDF of $\Pi_\tau / \langle \Pi \rangle$. Blue dots, green squares, orange crosses, red pentagons, purple stars, brown triangles and grey diamonds correspond to τ/τ_0 ranging from 1 to 7. (7.10b) presents the extracted slopes α confirming the linearity predicted by Eq. 7.12.

We apply the GCFT to the energy transfer at scale k, Π_k (see Eq. 1.4), more specifically in the last shell. The following procedure is used, first we compute the energy transfer according to Eq. 1.4. The considered variable is obtained by averaging over a time interval τ such that:

$$\Pi_\tau(t) = \frac{1}{\tau} \int_t^{t+\tau} \Pi(t')dt'. \tag{7.11}$$

Then, we extract the PDF from the data to perform a best fitting of the PDF. The GCFT is

then performed over the extrapolated data [2] for the variable $Y = \Pi_\tau / \langle \Pi \rangle$:

$$\ln \frac{P_\tau(Y = y)}{P_\tau(Y = -y)} = \alpha(\tau) y. \tag{7.12}$$

Note that we also define τ_0 as the sampling time of the simulation (i.e the average time between two consecutive save).

Fig. 7.10a presents a set of PDF of Y obtained for various values of τ. It is to be noted that the PDFs are non necessarily gaussian. If the GCFT (Eq. 7.10) holds, then $\alpha(\tau)$ (see Eq. 7.12) should be linear in τ. This property is indeed observed (Fig 7.10b) allowing for the extraction of σ such that $\alpha(\tau) = \sigma\tau$. [3]

This same protocol can be applied varying $\mathcal{R}_\mathrm{r}$ [4] to obtain the evolution of $\sigma = f(\mathcal{R}_\mathrm{r})$.

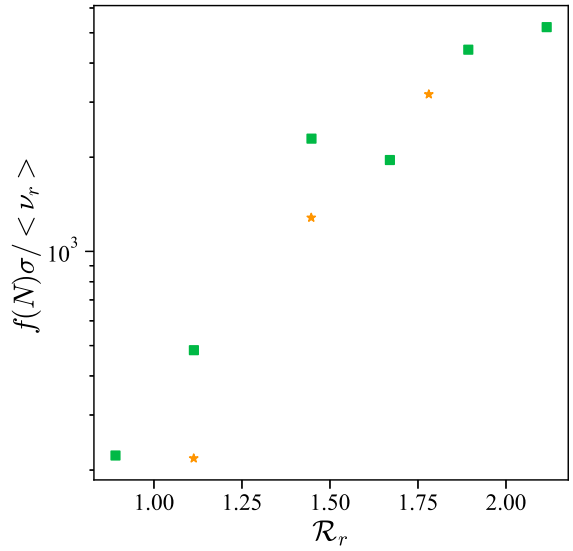

Figure 7.11: **Ratio of the phase rate contraction over the average reversible viscosity.** Green squares correspond to $N = 12^3$ and orange stars to $N = 18^3$. $f(N)$ is a rescaling function, ensuring the collapse of $\langle \nu_r \rangle$ in the limit $\mathcal{R}_\mathrm{r} \to 0$, such that $f(N) \propto \sqrt{N} k_{max}$.

At the current time, we did not manage to link σ to another physical quantity, Fig. 7.11 seems to highlight a connection to the averaged reversible viscosity $\langle \nu_r \rangle$ with a collapse, for the two considered resolutions ($N = 12^3, 18^3$), for the highest presented values of $\mathcal{R}_\mathrm{r}$. This is quite puzzling as the proposed rescaling function $f(N)$ assures the collapse of viscosities in the limit $\mathcal{R}_\mathrm{r} \to 0$. The analysis of this phenomenon and more generally the analysis of σ is left for future work.

As previously mentioned, the proof of the fluctuation theorem relies on the time reversibility of the system. Yet, such restrictive hypothesis is hardly met in experimental setups. It is therefore interesting to check if the symmetry of Eq. 7.12 also holds for irreversible dynamics.

[2] The theorem is only applied on a small interval around 0 where the best fitting is perfectly accurate.

[3] We actually perform a fitting of the form $\alpha(\tau) = \sigma\tau + B$, where B is found to be close to zero.

[4] We recall that $\mathcal{R}_\mathrm{r} = 1/\mathcal{E}$ corresponds to the ratio of the energy injection over the total kinetic energy, see Eq. 4.13.

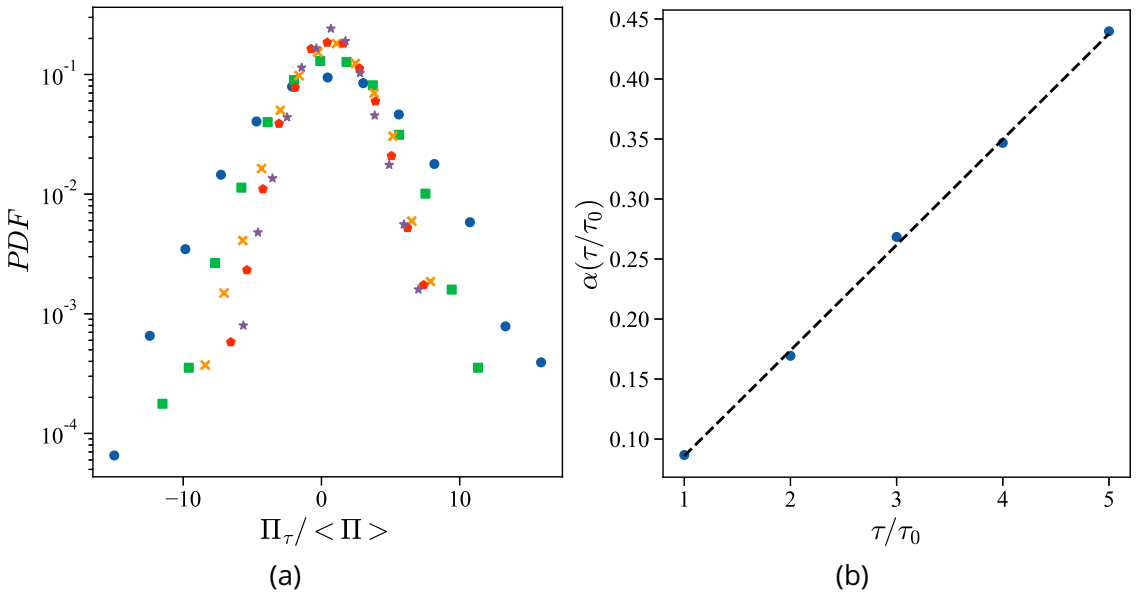

Figure 7.12: **Applying the GCFT to NSE.** The considered simulation is performed using $N = 8^3$, corresponding to the second orange circle of Fig. 6.5a. (7.12a) PDF of $\Pi_\tau / \langle \Pi \rangle$. (7.12b) presents the extracted slopes $\alpha(\tau)$ confirming the linearity predicted by Eq. 7.12.

Once again, we apply the GCFT to the energy transfer, averaged over interval of length τ : $Y = \Pi_\tau / \langle \Pi \rangle$, for simulations of the NSE. Figure 7.12 presents the results of the application of the GCFT to one simulation, highlighting the acceptable linear behavior for $\alpha(\tau)$, therefore confirming the symmetry of Eq. 7.12. This result is surprising as the NSE systems is inherently irreversible. Although being an interesting result, it is still unclear if the validity of the GCFT in this particular case is not due to the truncature effects as the considered simulations lie in the unstable phase defined in Chapter 4.

7.6.4 . Rescaling PDF according to large deviation

The difficulty in using the GCFT lies in the observation of negative fluctuations that are quite rare. Indeed, due to the the rareness or even absence of negative fluctuations as $\mathcal{R}_\lambda$ increases, it becomes impossible to apply the GCFT. This statement is confirmed by the results of Fig 7.10a, where the number of negative fluctuations decreases as τ increases. Sinai (51) (see Section 7.6.1) proposed a rescaling of $P_\tau(Y)$ that no longer depends on τ, through a large deviation rate $\zeta(p)$.

The rescaling is based on the previously extracted $\alpha(\tau)$ such that:

$$P_\tau(Y) = A_\tau e^{-\zeta(Y)\alpha(\tau)}, \tag{7.13}$$

where A_τ is a constant depending on τ.

Fig. 7.13 (RNSE) and 7.14 (NSE) present rescaled PDFs $\zeta(Y)$ constructed using Eq. 7.13 highlighting a collapse of PDFs in the small interval around 0 but also for the rest of the PDFs. Note that for two small values of τ, $\alpha(\tau)$ can be non linear, such values of τ should therefore be discarded (53). The existence of a rate function [5] $\zeta(Y)$ further supports the

[5] In the context of the large deviation principle.

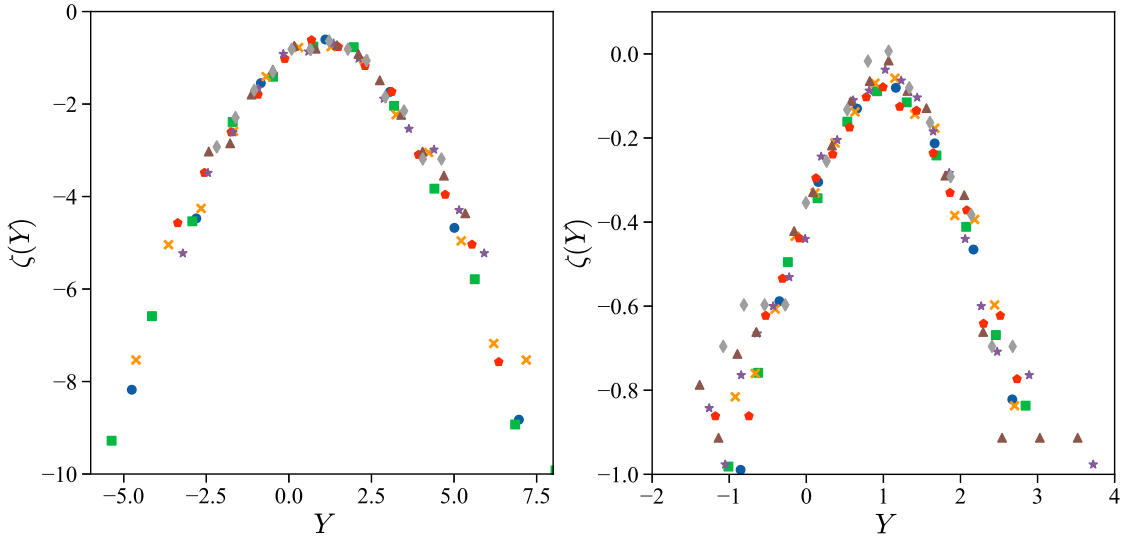

Figure 7.13: **Large deviation rate** $\zeta(Y)$**,** $Y = \Pi_\tau / \langle \Pi \rangle$ the considered simulations are performed using $N = 12^3$. Blue dots, green squares, orange crosses, red pentagons, purple stars, brown triangles and grey diamonds correspond to increasing values of τ/τ_0. (7.13a) Rescaling of the PDF of Fig. 7.10a, $\mathcal{R}_\mathrm{r} = 1.89$. (7.13b) $\mathcal{R}_\mathrm{r} = 2.56$. Both figures highlight a collapse of the PDFs onto a τ-independent PDF.

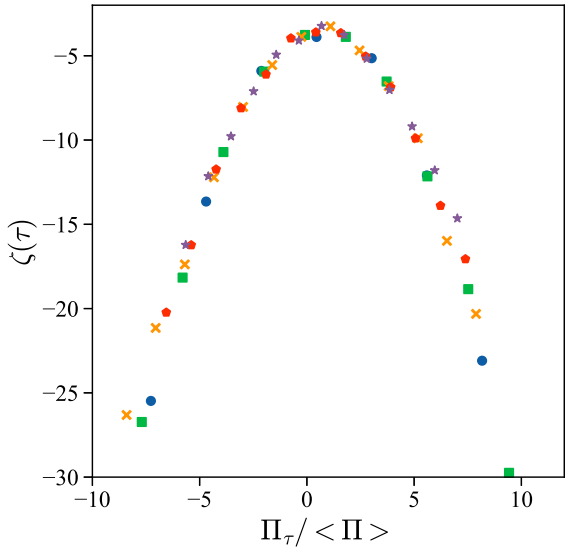

Figure 7.14: **Large deviation rate** $\zeta(Y)$**,** $Y = \Pi_\tau / \langle \Pi \rangle$ **for NSE dynamics.** Rescaling the PDF of Fig. 7.12a obtaining $\zeta(Y)$, $Y = \Pi_\tau / \langle \Pi \rangle$. Once again, $\zeta(Y)$ is independent of τ and allows for the extract of the probability of negative events in the limit $\tau \to \infty$.

validity of the GCFT that technically holds for $\tau \to \infty$ and allows for the estimation of the probability of negative fluctuations in the limit of $\tau \to \infty$.

8 - Unrelated contributions

This chapter is a collection of articles whose subjects are unrelated to the main scientific subject of this PhD (Reversible Navier-Stokes and weak solutions). Still, there is a plethora of topics that are yet to be tackled. As we believe that science is a team effort, the following articles have been written in collaboration with other PhD students and researchers of the group. While not being the primary author of the papers, I contributed during the scientific discussions and reviews.

8.1 . Log-lattices for atmospheric flows

This section is made of a self-sufficient article, published in Atmosphere 2023, 14(11), 1690; https://doi.org/10.3390/atmos14111690.

In this article, Log-lattices are applied to geophysics through the equation describing the heat transport in a dry atmosphere making full use of the achievable parameters (Reynolds, Rayleigh...) to confirm a theoretical scaling of the critical Rayleigh number. In addition, we highlight the existence of two regime of convection and derive general scaling laws in both of them.

MDPI

Article

Log-lattices for atmospheric flows

Quentin Pikeroen [1], Amaury Barral [1], Guillaume Costa [1] and Bérengère Dubrulle[1]*

[1] University Paris-Saclay, CEA, CNRS, SPEC, 91191, Gif-sur-Yvette, France
* Correspondence: berengere.dubrulle@cea.fr

Abstract: We discuss how projection of geophysical equations of motion onto an exponential grid allows to achieve realistic values of parameters, at a moderate cost. This allows to perform many simulations over a wide range of parameters, thereby leading to general scaling laws of transport efficiency that can then be used to parametrize the turbulent transport in general climate models for Earth or other planets. We illustrate this process using the equation describing the heat transport in a dry atmosphere, to obtain the scaling laws for onset of convection as a function of rotation. We confirm the theoretical scaling of the critical Rayleigh number $\mathrm{Ra}_c \sim E^{-4/3}$ over a wide range of parameter. We have also demonstrate the existence of two regimes of convection, one laminar extending near the convection onset, and one turbulent, occurring as soon as the vertical Reynolds number reaches a value of 10^4. We derive general scaling laws for these two regimes, both for transport of heat, dissipation of kinetic energy, and value of the anisotropy and temperature fluctuations.

Keywords: convection; rotation; turbulence

1. Forewords by B. Dubrulle

I met Jack in 1999, when I came to the MMM division of NCAR for a one-year sabbatical. I had been attracted there by Jack's reputation, from conversation with Annick Pouquet, Uriel Frisch and Maurice Meneguzzi. Being a theoretician of turbulence, interested in geophysical application, I then knew that I would find in Jack a very good interlocutor, and benefit greatly of his physical insight, his broad knowledge about turbulence and geophysical flows, and his open mind. I met Jack regularly during my stay, and we spoke of all sorts of topics. It was after a discussion with him that I started to investigate Rayleigh Bénard flows and heat transfer properties-I published two papers on that topic that year. About Jack, I keep the memory of a true "gentleman of science", very kind to junior scientist (as I still was at that time), with a great sense of humor and an immense knowledge that he was keen to share. It is certainly thanks to Jack that I jumped into the modeling of geophysical flows, and I will always be grateful to him for this.

2. Introduction

Ultra-high Reynolds number flows are ubiquitous in geosciences, due to small viscosity, large dimensions or velocity. They are described by the Navier-Stokes Equations (NSE). A natural control parameter of NSE is the Reynolds number $Re = LU/\nu$ built using the viscosity ν and characteristic length L and velocity U. Classical turbulent flows are thought to be described by NSE, with $Re \gg 1$. In 1941, Kolmogorov [K41] used such equations to predict the shape of the energy spectrum $E(k)$ derived from the Fourier transform of the velocity correlation function for isotropic and homogeneous turbulence stirred at a constant rate ϵ. He found that it should scale like $E(k) \sim \epsilon^{2/3}k^{-5/3}$ in the range $1/L \ll k \ll \nu^{-3/4}\epsilon^{1/4}$ where k is the wave-number. This prediction was verified in 1962 on data from a turbulent flow in Seymour Narrows [1] and appears to be one of the most robust laws of turbulence [2,3] being independent of the boundaries or on the stirring process. At large wave-numbers, viscous processes take over, and the spectrum decays very fast, so that the energy contained in wave-numbers greater than $k_d = \nu^{-3/4}\epsilon^{1/4}$ is

Citation: Pikeroen,Q.; Barral, A.,Costa, G.,Dubrulle, B. Log-lattices for atmospheric flows. *Atmosphere* **2023**, *1*, 0. https://doi.org/

Received:
Revised:
Accepted:
Published:

negligible. The overall behavior of $E(k)$ can be used to infer the typical number of dynamically active modes as $N = (k_d L)^3$. In geophysical flows such number can be quite large: for example, the atmosphere has $L = 10^3 km$ (the size of the large typhoons or cyclones), while k_d^{-1} is smaller than 10 mm, resulting in $k_d L > 10^8$. Direct numerical simulations of the Navier-Stokes equations for such flows are thus impossible, as the total computational cost of reading-in/writing-out and coupling all these modes exceeds by many orders of magnitude the capability of the present most powerful computers.

If one wishes to simulate ultra-large Reynolds numbers like the atmosphere, one has no other way out than to empirically decimate modes via a clever selection of grid points or modes. Simulating viscous flows with just as many scales as needed to "get the physics right" has been and still is the holy grail of all researchers in the computational fluid community. If a well-established theory of turbulence were available, including a deep understanding of all interactions between scales, the quest would probably be over by now. In the absence of such complete theory, we need empirical yet clever strategies for mode number reduction. Jack Herring worked many years on such issue, using e.g. two-point closure (see e.g. [4]).

Nowadays, the most popular approach is to use a Large Eddy simulation strategy, in which only the large scales are simulated: present climate models have a grid size of 10 km, allowing to handle the data volume in 2 CPU seconds per time step. However, there is no free lunch: the price to pay for such a mode reduction is the addition of a (sometime very large) damping, to avoid accumulation of energy at the smallest simulated scale. In LES type climate simulations, the damping is the same as if the atmosphere were made of peanut butter and the ocean of honey, so that no fluctuations can develop. This is problematic to capture possible bifurcations, such as those observed in von Karman flows [5].

In this paper, we consider another class of model in which the modes reduction is achieved by keeping modes following a geometric progression. Such approximation leaves out a lot of possible interactions, as we shall see. However, it allows reaching very small scales with a very small number of modes. In the atmosphere, for example, only 27 modes are necessary to go from $k_0 = 1/L$ to $10^8/L$ by a geometrical progression of step 2 (38 with a step being the golden number). This means, that we can perform a "resolved" 3D simulation of an atmospheric flow with less than 2×10^4 modes (respectively less than 6×10^4), corresponding to the number of modes involved in a LES simulation at a resolution of 37km. The corresponding models correspond to Fluid dynamics on Log-Lattices, the properties of which were detailed in [6]. For example, they respect classical and basic properties of Navier-Stokes equation, such as constancy of energy flux in the inertial range. Given the potential of such models to describe ultra-high Reynolds number flow at a cheap prize, we investigate here further properties of such models with respect to one important open problems of atmospheric flows, which was dear to Jack, namely the influence of rotation on convection.

3. Log-Lattices framework

Consider a velocity field that obeys Navier-Stokes equation (NSE), with viscosity ν and forcing. Its Fourier transform, noted $u(t,k)$ is a complex field that obeys the equation:

$$\begin{aligned} \mathbf{i}k_j u_j &= 0, \\ \partial_t u_i + \mathbf{i}k_j u_i * u_j &= -\mathbf{i}k_i p - \nu k^2 u_i + f_i, \\ u(k,t) &= u^*(-k,t). \end{aligned} \tag{1}$$

where $*$ denotes the traditional convolution product, that involves for each k, coupling of modes $u(t,p)$ and $u(t,q)$, such that $k_i = p_i + q_i$ for any i^{th} component. The (constant) density has been set to 1 for convenience, and thus disappears in front of the pressure term in Eq. (1). The convolution sum is computed directly, but is less costly than a Fast Fourier Transform because only a limited amount of local interaction are kept [6].

In traditional spectral simulation of NSE, the wave-numbers are discretized on a linear grid, and can be written as $k = (m_1, \dots m_3)$ with $m_i \in \mathbb{Z}^3$. The convolution being ensured by the condition $m = n + q$ for any $(m, n, q) \in \mathbb{Z}^3$, it allows a lot of interactions between Fourier modes.

In the log-lattice framework, we now impose that the wave-numbers follow a geometric progression as

$$k = (\lambda^{m_1}, \dots, \lambda^{m_3}), \tag{2}$$

with $m_i \in \mathbb{Z}^3$, where λ is a parameter yet to be defined. It is imposed by the condition that the convolution product appearing in Eq. (1) has some non-zero solution, which is only possible if the equation:

$$\lambda^m = \lambda^p + \lambda^q, \tag{3}$$

has some solutions for any $m, p, q \in \mathbb{Z}^3$. As discussed by [6], Eq. (3) can only be achieved provided λ takes some specific values, among which $\lambda = 2$, $\lambda \equiv \phi = (1 + \sqrt{5})/2 \approx 1.618$, the golden mean and $\lambda \equiv \sigma =\approx 1.325$, the plastic number[1]. Different values of λ correspond to different number of coupling between modes: they become more and more numerous and less and less local as $\lambda \to 1$ [6]. In this sense, log-lattices can be seen as a special case of the sparse Fourier model [7], the REWA model [8] or fractal decimated models [9,10], in which the non-linear interactions of NSE is projectively decreased randomly or in a scale invariant manner.

The choice of λ is fixed by several considerations: larger values of λ are cheaper, both in computation time and in memory. However, lower values of λ give rise to more interactions, thus more fluctuations, which is more realistic for simulating a turbulent flow. As discussed by [11], the case $\lambda = 2$ should be avoided when simulating incompressible dynamics because it lacks backs scatter. On the other hand, [12] checked that scaling law properties, such as spectral slope, or blow-up exponent, do not depend on the value of λ. Therefore, we work below with $\lambda = \phi$, which is the best compromise between all constraints.

3.1. Energy spectra

It is possible to write the mean energy, that measures the scaling properties of the mode at $k_n = \lambda^n$ as:

$$E_m(n) =< ||u(k)||^2 >_{S_n}, \tag{4}$$

where the average is taken over wave numbers in the shell delimited by spheres with radii λ^{n-1} and λ^n. Specifically:

$$< ||u(k)||^2 >_{S_n}, = \frac{1}{N_k} \sum_{\lambda^{n-1} \leq ||k|| < \lambda^n} \sum_{\alpha=1}^{d} |u_\alpha(k)|^2, \tag{5}$$

where d is the space dimension and $N_k \sim (\log(k))^{d-1}$ is the number of wave-numbers in the shell S_n.

[1] σ is defined as the common real root to $\sigma^3 - \sigma - 1 = 0$ and $\sigma^5 - \sigma^4 - 1 = 0$

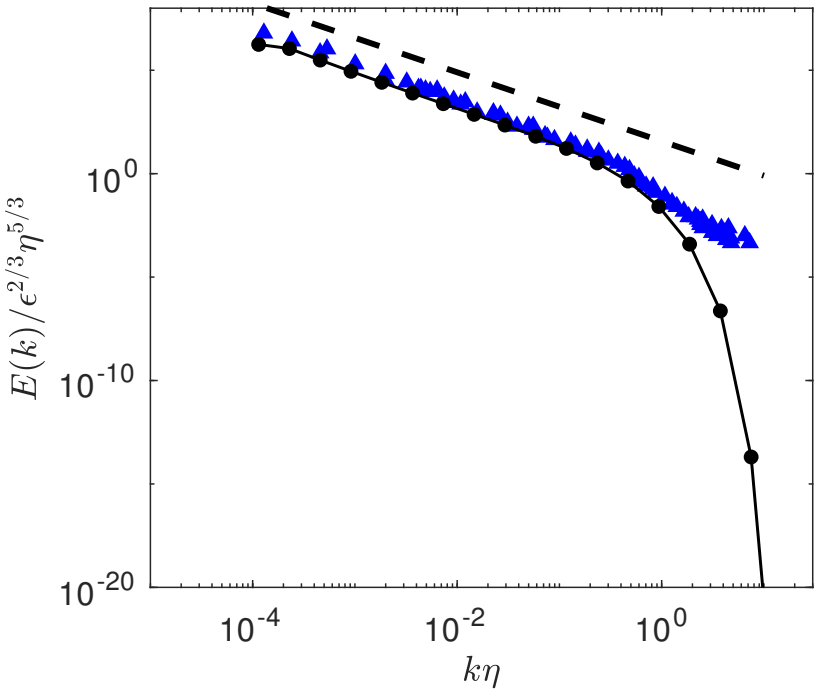

Figure 1. Renormalized energy spectrum $E(k)/\epsilon^{2/3}\eta^{5/3}$ as a function of renormalized wavenumber $k\eta$ for a simulation of Navier-Stokes on a 20^3 log-lattice (black dotted line) and for a turbulent flow in Seymour Narrows (Ocean) (blue squares). The black dashed line corresponds to $E(k) \sim k^{-5/3}$. This figure has been drawn by the authors using data extracted from the published graph shown in [1].

From this quantity, one can define a pseudo-energy spectrum as:

$$E(k) = \frac{\lambda^{-n}}{\lambda - 1} < ||u(k)||^2 >_{S_n}, \tag{6}$$

Examples of such spectrum in $d = 3$ are shown in fig. 1 for $\lambda = 2$. One sees that it is self-similar and display a very clear $k^{-5/3}$ law. This spectrum has been obtained by simulating eq. (1) with 20^3 modes, which can easily be done on a PC. Due to the exponential spacing, it enables to reach resolutions and inertial range even larger than what is achieved by oceanic measurements, a performance which is out-of-reach of DNS simulations of NSE. This shows the interest of FDLL in geophysics.

3.2. Generalizations

The equations (1), (2) and (3) define Navier-Stokes equation on log-lattice. By extension, any equation of fluid dynamics on log-lattice can be defined by performing the two steps [6]: (i) write the equation in the Fourier-space. (ii) replace any convolution product by the convolution on log-lattice. This construction guarantees that the resulting equation obeys all the conservation laws and symmetries of the original equations [6].

3.3. Limitations of log-lattices

Computations on log-lattices involve a number of limitations. First, due to the local nature of the convolution in Fourier space, log-lattice are unable to describe the so-called "non-local" interactions that are involved for example in the shearing of small eddies by large eddies [13]. This may explain why lo-lattices simulation do not display intermittency for the structure functions [14]. Due to their sparsity, log-lattices cannot describe dispersive wave resonances, like inertial or gravity waves. This mans that they cannot capture dissipative phenomena induces by those waves, and that it can only capture the dissipation due to small scale turbulent eddies. Finally, due to the spectral nature of the construction, it

may appear that the log-lattice framework is only appropriate for homogeneous flows, i.e. far from boundaries. In a recent work, [15] have however shown that the extension to flow with boundaries is possible, via lattice symmetrization around the boundary and careful treatment of the resulting discontinuity. Despite the high relevance of this situation for geophysical flow, we here concentrate on the simpler case of homogenous flow, and show how log-lattice simulation enable to recover some well known features of homogeneous rotating convection.

4. Homogeneous rotating convection on log-lattices

4.1. Definitions

We now consider a rotating homogeneous fluid, with coefficient of thermal dilation α, viscosity ν and diffusivity κ, subject to a temperature gradient ΔT over a length H and vertical gravity g. Its dynamic is given by the HRB set of equations [11,16–18],

$$\partial_t \boldsymbol{u} + \boldsymbol{u}\cdot\nabla\boldsymbol{u} + \frac{1}{\rho_0}\boldsymbol{\nabla} p + 2\boldsymbol{\Omega}\times\boldsymbol{u} = \nu\nabla^2\boldsymbol{u} + \alpha g\theta\vec{\boldsymbol{z}} - f\boldsymbol{u}, \tag{7}$$

$$\partial_t\theta + \boldsymbol{u}\cdot\boldsymbol{\nabla}\theta = \kappa\nabla^2\theta + u_z\frac{\Delta T}{H} - f\theta, \tag{8}$$

$$\nabla\cdot\boldsymbol{u} = 0, \tag{9}$$

where $\boldsymbol{u}$ is the velocity, θ the temperature deviation from the equilibrium profile (where $\theta = 0$), which means by definition $T = -\Delta T z/H + \theta$, $\boldsymbol{\Omega}$ the rotation vector, ρ_0 is the (constant) reference density, p is the pressure and f is a (Rayleigh) friction term, accounting for the friction at the boundary layer that cannot be resolved by the present framework. We will assume below that this friction is concentrated only on large scale. As proved in [11], this friction is mandatory to allow the system to reach well-defined stationary states. Indeed, for periodic boundary conditions, exponential instabilities can grow because there is no wall to stop them. They are characterized by the accumulation of energy at large scale. Introducing a large scale friction allows damping of the inverse cascade and avoids the concentration of energy at the large scale. This set of equation has to be completed with boundary conditions. In this paper, we consider periodic boundary conditions and focus on the case when rotation is aligned with the z-axis, $\boldsymbol{\Omega} = \Omega e_z$.

4.2. Non-dimensional numbers

We can build 5 independent non-dimensional numbers to characterize the system:

the Rayleigh number $\mathrm{Ra} = \alpha g H^3\Delta T/(\nu\kappa)$, that characterizes the forcing by the temperature gradient.

the Prandtl number $\mathrm{Pr} = \nu/\kappa$, which is the ratio of the fluid viscosity to its thermal diffusivity.

the Nusselt number $\mathrm{Nu} = JH/\kappa\Delta T$. that characterizes the mean total heat flux is the z direction is $J = \partial_z < u_z\theta > -\kappa\Delta T$.

the Ekman number $\mathrm{E} = \nu/(2\Omega H^2)$, measuring the importance of the rotation with respect to diffusive process.

the Rossby number $\mathrm{Ro} = \sqrt{\alpha g\Delta T}/(2\Omega\sqrt{H})$, measuring the importance of the rotation with respect to buoyancy. In terms of other variables, we have $\mathrm{Ro} = \mathrm{E}\sqrt{\mathrm{Ra}}/(\sqrt{Pr})$.

the friction coefficient $F = f\sqrt{H}/\sqrt{\alpha g\Delta T}$, that provides the intensity of the Rayleigh damping.

4.3. Equations on log-lattice

The regimes we want to explore are very turbulent regimes where the viscosity and diffusivity do not play any role anymore. Therefore, it is natural to adimensionalize the equation in terms of "inertial quantities", i.e. using the vertical width H as a unit of length, the free fall velocity $U = \sqrt{\alpha g\Delta T H}$ as a unit of velocity, and ΔT as a unit of temperature.

Then, to define the Rotating Homogeneous Rayleigh-Benard (RHRB) equations on log-lattice, we take the Fourier transform of Eq. (7) that can be written in non-dimensional form as (with the Einstein convention on summed repeated indices):

$$\mathbf{i}k_j u_j = 0, \tag{10}$$

$$\begin{aligned}\partial_t u_i + \mathbf{i}k_j u_i * u_j = & -\mathbf{i}k_i p + \theta\delta_{i3} - F u_i \delta_{k\approx k_{\min}} \\ & - \sqrt{\frac{\mathrm{Pr}}{\mathrm{Ra}}} k^2 u_i - \frac{1}{\mathrm{Ro}}\epsilon_{i3k}u_k\end{aligned} \tag{11}$$

$$\partial_t \theta + \mathbf{i}k_j \theta * u_j = u_z - \frac{k^2\theta}{\sqrt{\mathrm{Ra}\,\mathrm{Pr}}} - F\theta\delta_{k\approx k_{\min}}, \tag{12}$$

$$u(k,t) = u^*(-k,t), \tag{13}$$

$$\theta(k,t) = \theta^*(-k,t). \tag{14}$$

where the Dirac $\delta_{k\approx k_{\min}}$ filters out the small scales.

In these equations, the convolution product is taken over the log-lattice, see Eq. 3.

4.4. Convection onset

Convection is an instability, so it sets-up at a certain critical value of the parameter Ra_c. Detailed computation of this parameter is performed in [19] for the case $F = 0$. In a nutshell, we assume that we are very near the threshold, so that deviations from the "equilibrium state" $u = \theta = 0$ are small. This will allow us to neglect all non-linear terms in the equations 14. Then, we look for solutions behaving like:

$$\begin{aligned}\mathbf{u}(k,t) &= (u(k), v(k), w(k))e^{\sigma t}, \\ p(k,t) &= p(k)e^{\sigma t}, \\ \theta(k,t) &= \theta(k)e^{\sigma t},\end{aligned} \tag{15}$$

where σ is the growth rate of the instability: if σ has a negative real part, then all perturbation decay, while the instability develop when the real part of $\sigma > 0$. Plugging this decomposition into eq. (14) and neglecting non-linear terms, we get:

$$\begin{aligned} ik_x u + ik_y v + ik_z w &= 0, \\ \sigma u - \frac{v}{Ro} &= -ik_x p - \sqrt{\frac{\mathrm{Pr}}{\mathrm{Ra}}} k^2 u, \\ \sigma v + \frac{u}{Ro} &= -ik_y p - \sqrt{\frac{\mathrm{Pr}}{\mathrm{Ra}}} k^2 v, \\ \sigma w &= -ik_z p - \sqrt{\frac{\mathrm{Pr}}{\mathrm{Ra}}} k^2 w + \theta, \\ \sigma\theta &= w - \frac{1}{\sqrt{\mathrm{Ra}\,\mathrm{Pr}}} k^2\theta. \end{aligned} \tag{16}$$

This represents a linear, homogeneous system of equations in the variable (u, v, w, p, θ). If we want this system to have other solutions than $(0, 0, 0, 0, 0)$, we must impose the determinant of the system to be zero, which provides us with an expression linking σ, k and the parameters of the system. Taking $Pr = 1$ for simplicity [2], we get:

$$\sigma^2 + 2k^2\,\mathrm{Ra}^{-1/2}\,\sigma + \frac{k^4}{\mathrm{Ra}} + (1+\mu^2)^{-1}\left(\frac{\mu^2}{\mathrm{Ro}^2} - 1\right) = 0, \tag{17}$$

[2] The general case leads to the same conclusions with different prefactors.

where $\mu^2 = k_z^2/(k_x^2+k_y^2)$. This is a second order equation for σ, there are therefore two solutions. Since the prefactor of σ is positive, it means that the sum of the two solution is negative. To ensure that there exists at least one solution with a positive real part, we must then ensure that the product of the solution, given by term independent of σ is negative. To study the consequences of this condition, we consider two limiting cases.

4.4.1. Onset at zero rotation

We first consider the case with no rotation, $\mathrm{Ro} \to \infty$. Then, the condition for instability is: $\frac{(1+\mu^2)k^4}{\mathrm{Ra}} - 1 < 0$. Since $(1+\mu^2)k^4$ is minimum when $k_{\min} = (2\pi, 2\pi, 2\pi)$, where $k_{\min}$ is the minimal wavenumber, this is achieved whenever $Ra > \frac{3}{2}k_{\min}^4$. In our simulations, $k_{\min} \sim 2\pi\sqrt{3}$, this gives $Ra_c \sim 2.1\ 10^4$.

4.5. Onset at large rotation

In the limit of large rotation, $Ro \to 0$ and the condition for instability now reads: $\frac{k^4}{\mathrm{Ra}} + (1+\mu^2)^{-1}(\frac{\mu^2}{\mathrm{Ro}^2} - 1) < 0$. Introducing $\alpha = k^4/Ra$, we may further simplify the condition by noting that at the instability threshold μ is close to 1, and $k_z^2 \ll k_x^2 + k_y^2 \sim Ra$. The condition for instability then becomes $\mathrm{Ra}^{3/2} > 4\pi^2\,\mathrm{E}^{-2}\,\frac{1}{(1-\alpha)\sqrt{\alpha}}$. The instability criterion is given by the condition that there exists at least α such that the equality is satisfied i.e. when the minimum of the r.h.s. of the condition of instability is achieved. This is true for $\alpha = 1/3$, resulting in $\mathrm{Ra}^{3/2} > 4\pi^2\,\mathrm{E}^{-2}\,\frac{3\sqrt{3}}{2}$, giving a critical Rayleigh number

$$\mathrm{Ra}_c = (6\pi^2\sqrt{3})^{2/3}\,\mathrm{E}^{-4/3} \approx 22\,\mathrm{E}^{-4/3}\,. \tag{18}$$

We note that this eq. is similar to eq. 184 p.106 of [19]. This means that the larger the rotation (the smaller E), the more difficult it is to get convection: rotation stabilizes the flow.

4.6. Phenomenology when $F = 0$

In the case $F = 0$, there are a number of simple physical argument that provide scaling laws relation between the non-dimensional numbers.

4.6.1. Non-rotating case

We first consider the non-rotating case, $\mathrm{E} = \infty$. In this case, the phenomenology of homogeneous convection distinguishes 3 regimes for the behavior of the heat flux, as a function of the forcing [11,16]:

(I): when $\mathrm{Ra} \leq \mathrm{Ra}_c$, we are in the laminar case. The fluid is at rest, $< u_z\theta >= 0$ and the heat flux is only piloted by the Fourier law, so that $J = \kappa\Delta T/H$ and $Nu = 1$.

(II) : above the critical threshold for instability, when $\mathrm{Ra} >\sim \mathrm{Ra}_c$, convection sets in, $< u_z\theta >$ starts becoming positive, and we have $\mathrm{Nu} \sim (\mathrm{Ra} - \mathrm{Ra}_c)^\chi$, where χ is an exponent characterizing the (super)-critical transition to convection.

(III) : when $\mathrm{Ra} \gg \mathrm{Ra}_c$, the turbulence become fully developed, and we are entering an "ultimate" regime (also called Spiegel regime), in which the heat flux does not depend anymore on the viscosity or the diffusivity. In that case, we have $\mathrm{Nu} \sim (\mathrm{Ra}\,\mathrm{Pr})^{1/2}$ [20–22] and $\mathrm{Re} \sim (\mathrm{Ra}\,/\,\mathrm{Pr})^{1/2}$[23]. This regime is very difficult to observe in DNS, because of the need for high resolutions, to be able to cope with $\mathrm{Ra} \gg \mathrm{Ra}_c$. In the atmosphere Ra is typically of the order of $\mathrm{Ra} \sim 10^{18-22}$ so we expect the atmosphere to be in this ultimate regime.

Note that in the case where boundaries are present, there is the possibility of an intermediate regime (the Malkus regime), where the heat flux is piloted by the boundary layers and $\mathrm{Nu} \sim \mathrm{Ra}^\gamma$, $\gamma \sim 1/3$. This regime is frequently observed in laboratory experiments, but it does not apply to homogeneous turbulence, because of the absence of boundaries.

4.6.2. Rotating case

Let us consider the case with rotation. As shown by many studies, the rotation has a stabilizing influence on the flow, so that the threshold for instability now increases with increasing rotation. Detailed studies show that $\mathrm{Ra}_c \sim \mathrm{E}^{-4/3}$ [24]. In addition, the rotation modifies the structure of the convective cells, that become aligned with the vertical axis in the case of strong rotation. This changes profoundly the heat transfer. To account for this effect, [25] suggest performing the same phenomenology as in the non-rotating case, using $\mathrm{Ra}\, E^{4/3}$ instead of Ra. The two turbulent regimes in the presence of rotation are now:

(R1) in the presence of boundaries, a rotating Malkus regime, where the heat flux is independent of the height of the cell, and in which $\mathrm{Nu} \sim \mathrm{Ra}^3\, \mathrm{E}^4$. This regime cannot be present in HRB.

(R2) at Reynolds number larger than the threshold for onset of turbulence in the boundary layers, or when boundaries do not limit the heat flux, like in HRB, a rotating ultimate regime, also called Geostrophic Turbulent (GT) regime. This regime is then found by stating that the relation between Nu and $\mathrm{Ra}\, \mathrm{E}^{4/3}$ and Pr should be such that the energy flux J is independent of κ and ν, resulting in [25].

$$\mathrm{Nu} \sim \mathrm{Ra}^{3/2}\, \mathrm{E}^2\, \mathrm{Pr}^{-1/2}\,. \tag{19}$$

An interesting property of the geostrophic turbulent regime is that it can be expressed as a universal law, independent of the rotation and the Prandtl number, using the "turbulent" coordinates [25]:

$$\begin{aligned} \mathrm{Nu}_* &= \frac{\mathrm{Nu}\, \mathrm{E}}{\mathrm{Pr}}, \\ \mathrm{Ra}_* &= \frac{\mathrm{Ra}\, \mathrm{E}^2}{\mathrm{Pr}}. \end{aligned} \tag{20}$$

In that case, the relation (19) becomes:

$$\mathrm{Nu}_* \sim \mathrm{Ra}_*^{3/2}\,. \tag{21}$$

In this regime, we further have $\mathrm{Re} \sim \mathrm{Ra}\, \mathrm{E}^2 \,/\, \mathrm{Pr}$[23].

4.6.3. Log-lattice simulation details

To simulate these equations, we can perform log-lattice simulations. The minimum wave vector of the grid is set to $k_{\mathrm{min}}^{1D} = 2\pi$ to match a simulation on a box of size $\tilde{L} = 1$. Note that the absence of wavenumbers $k = 0$ in our simulation means that we will not be able to capture large-scale vertical structures that are often observed in rotating turbulence. However, as shown below, this does not seem to affect the scaling laws of the transport of heat and momentum that we observe. The grid size N (such that the maximum wavenumber in the x, y or z direction is proportional to λ^N) is then set to reach the dissipative scale for both velocity and temperature. We have verified that the size of the grid for 3D simulations ($N \geq 13$) does not affect the mean value of the observables Nu, Re, ..., which are already converged for grids of size $N \geq 6$. However, the tail of the pdfs does depend on N. Another 3D simulation set at $N = 20$ (not shown here, both vs Ra and Pr) displays the same scaling laws as the $N = 13$ case, confirming this analysis.

5. Results

5.1. Non-rotating case

As reference, we have performed simulations without rotation, for various Ra up to 10^{25} at $\mathrm{Pr} = 1$ and $\mathrm{Pr} = 0.7$ and for $F = 1$. Note that present direct numerical simulation for these Prandtl number are limited to $\mathrm{Ra} \approx 10^{15}$ [26]. The resulting heat transfer Nu as a function of Rayleigh-number Ra is shown in fig. 2. In that case, we observe that the convection starts as $\mathrm{Ra}_c = 6 \times 10^5$, which is larger than the value predicted by the linear

theory at $F = 0$, and observed in previous log-lattice simulations [11]. This means that friction stabilizes the convection in the non-rotating regime. In addition, we observe a near onset regime $\mathrm{Nu} \sim (\mathrm{Ra} - \mathrm{Ra}_c)^{3/2}$, then turning into an asymptotic regime where $\mathrm{Nu} \sim \sqrt{\mathrm{Ra}}$. This regime itself splits in two distinct regimes, characterized by the same scaling law $\mathrm{Nu} \sim \mathrm{Ra}^{1/2}$, but with very different amplitude: (i) a *laminar regime*, characterized by low fluctuations of the heat transfer. This laminar regime is well-fitted by an empirical law

$$\mathrm{Nu} = A(\mathrm{Ra} - \mathrm{Ra}_c)^{3/2}/(\mathrm{Ra} \,/\, \mathrm{Ra}_t + 1), \tag{22}$$

where $A = 7$, $\mathrm{Ra}_c = 5 \times 10^5$ is the critical number for convection onset and $\mathrm{Ra}_t = 5 \times 10^6$ is the transition number from near-onset to asymptotic regime. This laminar regime is followed by (ii) a *turbulent regime*, with much larger fluctuations. Typical time behavior of the heat transfer in the two regimes is displayed in fig. 3 which showcases both regimes. The laminar regime is stable up to $\mathrm{Ra} \approx 10^{12}$, and unstable above: if we wait long enough, the solution jumps from the laminar regime to the turbulent regime, as illustrated in fig. 3. Looking at Nu as a function of time in this regime in fig. 3, we observe that the simulation first follows a rather long evolution along the laminar regime, before suddenly transitioning towards the turbulent regime as an instability develops, increasing its energy by several orders of magnitude in the process.

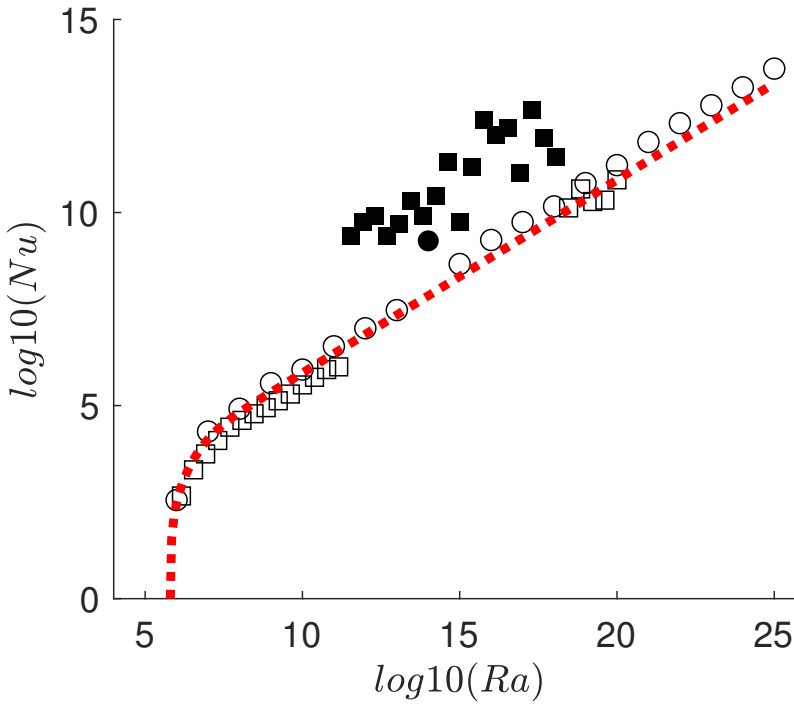

Figure 2. Non-dimensional heat transfer Nu vs Rayleigh number Ra in 3D for $\mathrm{Pr} = 0.7$ (circle) and $\mathrm{Pr} = 1$ (squares). The dotted line corresponds to the empirical law: $\mathrm{Nu} = 7(\mathrm{Ra} - \mathrm{Ra}_c)^{3/2}/(\mathrm{Ra} \,/\, \mathrm{Ra}_t + 1)$, with $\mathrm{Ra}_c = 6 \times 10^5$ and $\mathrm{Ra}_t = 5 \times 10^6$ that connects the near-convection onset regime to the asymptotic law $\mathrm{Nu} \sim 20\sqrt{\mathrm{Ra}}$ for large Ra, corresponding to asymptotic non-rotating ultimate regime scaling. This regime is itself split into a laminar regime (open symbols) and a turbulent regime (filled symbols).

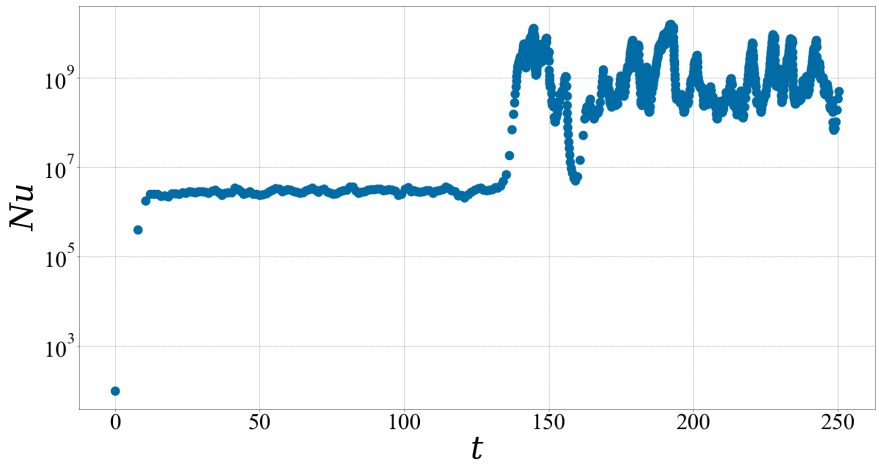

Figure 3. Non-dimensional heat transfer Nu versus time t for Ra $= 3.46 \cdot 10^{11}$. The flow starts in a laminar regime, then abruptly transitions to a turbulent regime.

5.2. Rotating case

5.2.1. Parameter space and critical Rayleigh number

We turn now to the case with rotation. Figure 4 shows the parameter space we have explored, with E ranging from 10^{-9} to 10^{-1} and Ra up to 10^{14}. In this range of parameters, we observe typically three types of behaviors: (i) conductive behaviors, where both velocity and temperature fluctuations are zero, and Nu $= 1$. These cases are reported as white symbols on fig. 4; (ii) transitional regimes, where velocity and temperature fluctuations are decaying very slowly but steadily, along with Nu over the time of simulation, so that asymptotically, they are likely to converge to the conductive limit. The typical timescale to reach this limit increases as E decays, and Ra increases. To save computational time, we have stopped the simulation before reaching the limit for E $\geq 10^{-6}$, but have reported this points as yellow points on fig. 4; (iii) convective regimes, where both velocity and RMS velocities reach a stationary state; these points are reported as black points in fig. 4. This representation allows seeing clearly the stabilizing influence of rotation on the convection threshold. In the asymptotic regime of large rotation, E $\ll 1$, such influence is very-well described by the prediction of the linear theory at $F = 0$, Eq. 18, which is reported as a red line on the diagram. This means that, as rotation increases, the friction becomes less important in the dynamics.

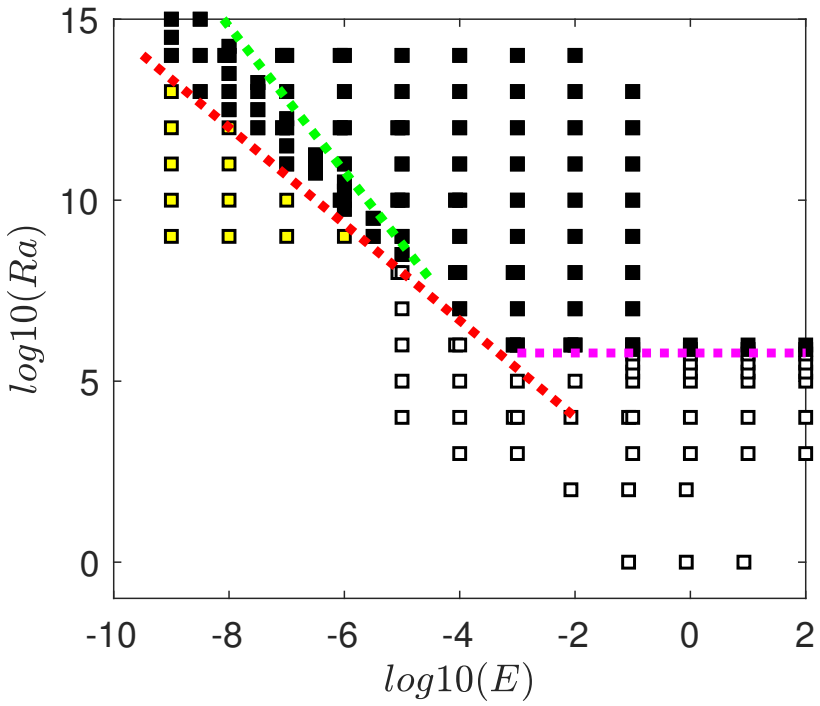

Figure 4. Parameter space covered by our log-lattices simulations at Pr $= 0.7$. The color of the symbols codes the 3 possible regimes: conductive (white), transitional (yellow) and convective (black). The red line is the theoretical asymptotic prediction given by Eq. (18). The magenta line is the theoretical convection threshold in the absence of rotation $Ra = 6 \times 10^5$. The green line has equation$Ra = 0.06E^{-2}$ and delineates regions of the parameter space where turbulent is influenced by rotation (below the line) or not influenced by rotation (above the line), as diagnosed by the behavior of the kinetic energy dissipation, see fig. 8. The geostrophic turbulent regime is observed in between the red and the green-line.

5.3. Influence of friction

To elucidate this observation, we computed the ratio of the kinetic energy dissipated by friction FU^2 to the kinetic energy dissipated by in the flow by viscous processes ϵ_u. It is reported in fig. 5. We see indeed observe two regimes: one at low value of Ra $< 10^{11}$, where the friction dominated the dissipation and one at larger Ra $> 10^{11}$ where the friction is negligible. We will see below that this induce two different regimes termed "laminar" and "turbulent". In addition, we observe that as the rotation becomes larger, the influence of friction decreases.

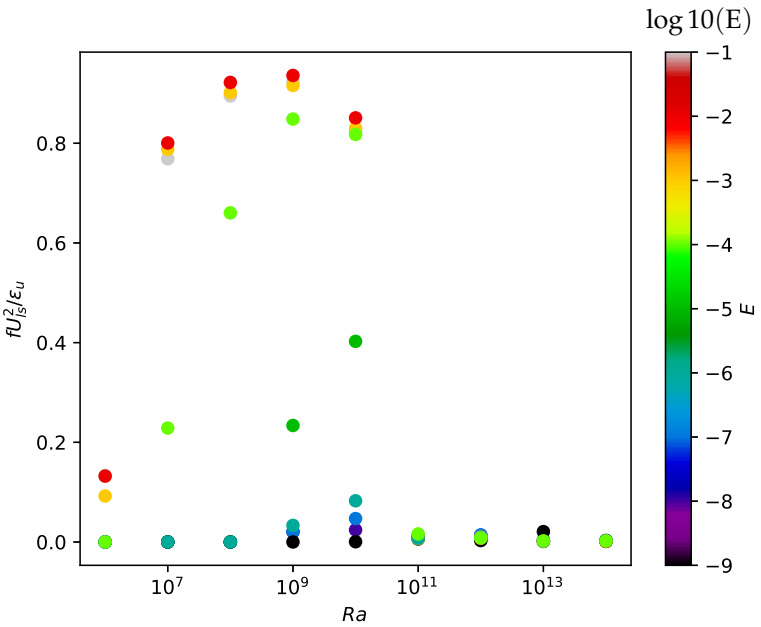

Figure 5. Ratio of the kinetic energy dissipated by friction FU^2 to the kinetic energy dissipated by viscous processes ϵ_u, as a function of the Rayleigh number Ra, and the Ekman number E. The points are color-coded by $\log 10(\mathrm{E})$. The friction dominates for low-rotation and for $\mathrm{Ra} < 10^{11}$.

5.3.1. Laminar vs turbulent regime

Figure 6 reports the heat transport Nu as a function of Rayleigh Ra and Ekman number E. One sees that larger Ekman numbers correspond to smaller heat transport, at a given Ra. However, the rotation does not suppress the existence of the laminar to turbulent transition, already present in the non-rotating case. Like in the non-rotating case, it is happening when the vertical Reynolds number exceeds $u_z^{rms} L/\nu = \mathrm{Re}_c = 10^4$, corresponding to $\mathrm{Ra} \sim 10^{12}$, with a bi-stability occurring around $\mathrm{Ra} = 10^{11}$, see fig. 7. This critical value separates two different scaling regime: one such that $\mathrm{Re} \sim \mathrm{Ra}^{1/2}$, and one such that $\mathrm{Re} \sim \mathrm{Ra}$.

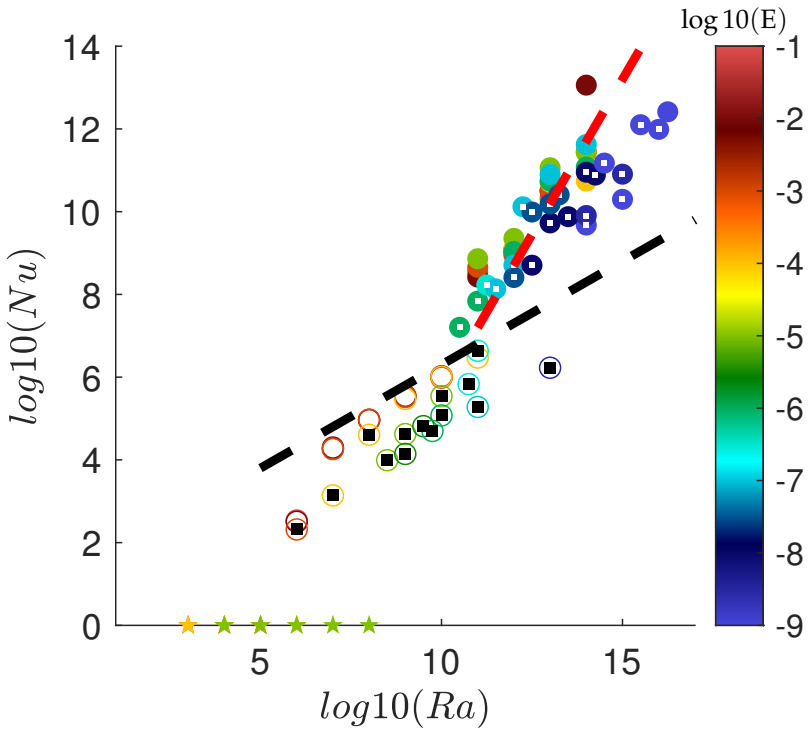

Figure 6. Non-dimensional heat transfer Nu vs Rayleigh number Ra in 3D for Pr $= 0.7$ for simulations of rotating HRB simulations on log-lattice. The symbols are colored according to their Ekman number E. The stars traces the conductive regime. The open symbols trace the laminar regime, while the filled symbol trace the turbulent regime. The rotation dominated regimes are tagged by a black (respectively white) square for the laminar (respectively turbulent) regime. The black dashed line is Nu $= 20\sqrt{\text{Ra}}$, corresponding to asymptotic non-rotating ultimate regime scaling. The red dotted line is Nu $\sim \text{Ra}^{3/2}$ corresponding to the geostrophic turbulent regime, see fig. 13 for an exact representation of the corresponding scaling law.

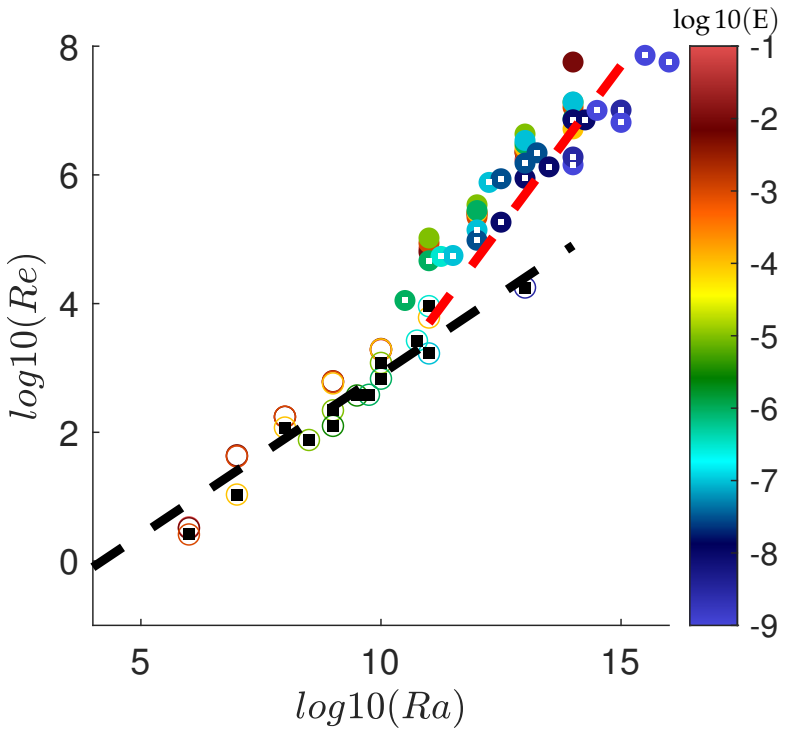

Figure 7. Vertical Reynolds number Re $= \sqrt{< u_z^2 >} H/\nu$ as a function of Rayleigh number Ra in 3D for Pr $= 0.7$ for simulations of rotating HRB simulations on log-lattice. The symbols are colored according to their Ekman number E. The open symbols trace the laminar regime, while the filled symbol trace the turbulent regime. The rotation dominated regimes are tagged by a black (respectively white) square for the laminar (respectively turbulent) regime. The black (respectively red) dashed line follows the equation $y \sim x^{1/2}$ (respectively $y \sim x^1$).

5.3.2. Influence of rotation and onset of rotation dominated regimes

The influence of rotation onto the turbulence is well documented (see e.g. [27,28]), and is characterized by a *decrease* of the efficiency of the transport properties with respect to the non-rotating case. For the case of the heat transport, this is already clear from fig. 6, as already discussed. In the case of the turbulent kinetic energy dissipation $\nu < (\nabla u)^2 >$, it is known that the decrease is proportional to the vertical Rossby number, $\mathrm{Ro}_z = u_z/2H\Omega$ when Ro_z goes to zero [28]. We indeed observe this effect in our simulations, as illustrated in fig. 8, where the non-dimensional turbulent kinetic energy dissipation $\epsilon_u = \nu < (\nabla u)^2 > H/U^3$ is shown, as a function of the vertical Rossby number. We see that in both the laminar and turbulent regime, the energy dissipation indeed decreases for sufficiently low-vertical Rossby number. In the turbulent regime, the decrease is indeed proportional to Ro_z, indicated by the black dotted line. In the laminar regime, however, the decrease is milder, going like $\mathrm{Ro}_z^{1/2}$. In the turbulent case, the rotation dominated regime starts below $\mathrm{Ro}_z \sim 0.1$, while in the laminar case, it starts at $\mathrm{Ro}_z \sim 0.03$. We can use this change of regime to tag the simulations that are or are not influenced by the rotation. We denote them below by a white dot inside the filled symbol, for the turbulent regime, and a black dot inside an open symbol, for the laminar regime. Reporting this on figs. 6 and 7, we see that this regime corresponds to lower heat transport, and smaller vertical Reynolds number, in agreement with the general findings that rotation impedes heat transport and vertical velocities. Note that the vertical Rossby number scales like the global Rossby number, following $\mathrm{Ro}_z \sim \mathrm{Ra}^{1/2}\,\mathrm{E}$ in both the laminar and the turbulent regime, see fig. 9.

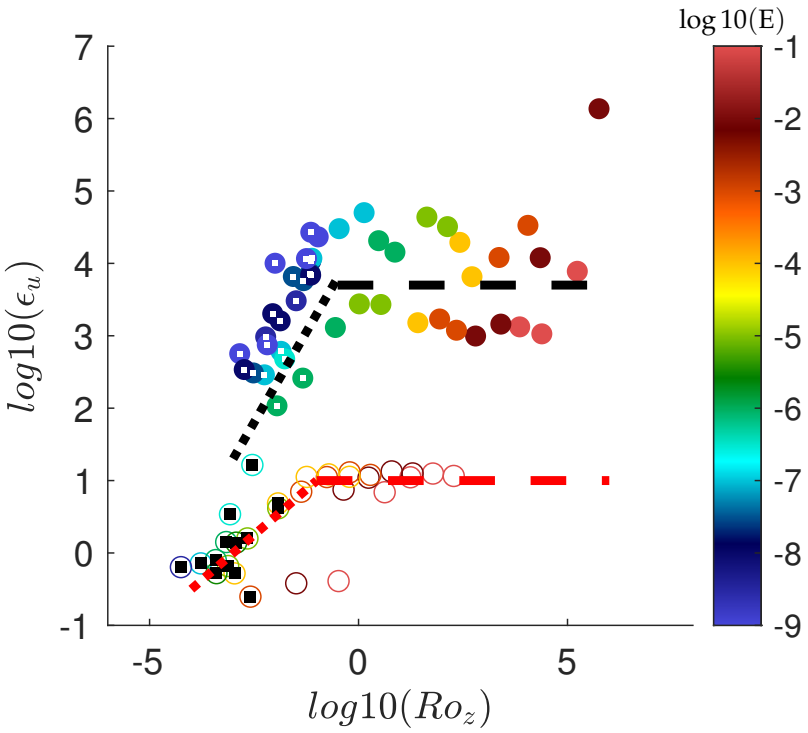

Figure 8. Non-dimensional energy dissipation $\epsilon_u = \nu < (\nabla u)^2 > H/U^3 = \mathrm{Ra}\,\mathrm{Nu}\,\mathrm{Pr}^{-2}/(\mathrm{Ra}\,\mathrm{Pr})^{3/2}$ vs vertical Rossby number Ro_z in 3D for $\mathrm{Pr} = 0.7$ for simulations of rotating HRB simulations on log-lattice. The symbols are colored according to their Ekman number E. The open symbols trace the laminar regime, while the filled symbol trace the turbulent regime. The rotation dominated regimes are tagged by a black (respectively white) square for the laminar (respectively turbulent) regime. . The black (respectively red) dotted line corresponds to $\epsilon_u \sim \mathrm{Ro}_z$ (respectively $\epsilon_u \sim \mathrm{Ro}_z^{1/2}$), while the black (respectively red) dashed line correspond to $\epsilon_u = 3.7$ (respectively $\epsilon_u = 1$).

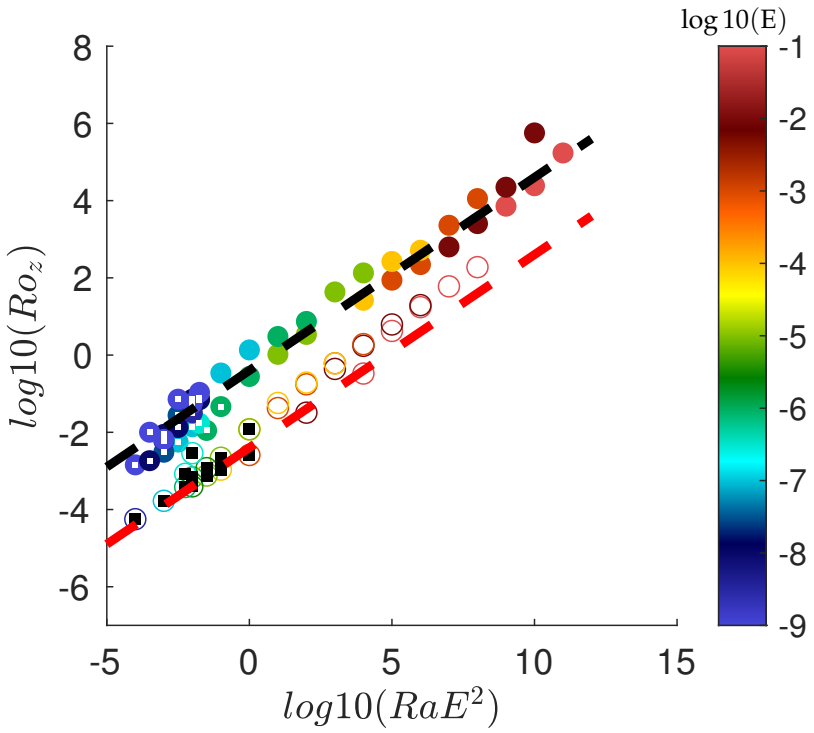

Figure 9. Vertical Rossby number Ro_z vs "turbulent" Rayleigh number $\mathrm{Ra}\,E^2$ in 3D for $\mathrm{Pr} = 0.7$ for simulations of rotating HRB simulations on log-lattice. The symbols are colored according to their Ekman number E. The open symbols trace the laminar regime, while the filled symbol trace the turbulent regime. The rotation dominated regimes are tagged by a black (respectively white) square for the laminar (respectively turbulent) regime. The black (respectively red) dashed line follows $0.4\,\mathrm{Ra}^{1/2}\,E$ (respectively $0.04\,\mathrm{Ra}^{1/2}\,E$).

5.3.3. Temperature fluctuation and anisotropy

Another interesting indicator of the influence of rotation on convection is given by the behavior of the temperature fluctuations, displayed in fig. 10. In the laminar case, they are plateauing at a low value (less than 0.01) as Ra increases, showing that the dynamic is indeed laminar. The rotation tends to even decrease the size of the fluctuations. In the laminar case, the temperature fluctuations are increasing with Ra, showing that convection is more and more vigorous, even so large rotation tends to somehow impede the development of too large fluctuations. The rotation also influences the anisotropy of the turbulence, as seen in fig. 11. Both in the laminar and turbulent case, the anisotropy is well above the value 1/2, that would correspond to a situation where kinetic energy is split evenly between motions along and perpendicular to the rotation axis. Due to the special nature of our projection, we cannot get a meaningful representation of what this result means in the physical space. It might however be interpreted as the influence of strong up (respectively down)-drafts that are observed in direct numerical simulations to carry the heat from bottom to top (respectively the cold fluid from top to bottom). The values we obtain here for the anisotropy are much larger to what is usually observed in simulation or experiment of RB convection with boundaries, but they are compatible with observation of radiative convection [29] or convection with no-slip boundary conditions [25], that observe the formation of very extended plumes extending towards the whole bulk of the flow. The decrease of anisotropy observed at decreasing E can be connected with the stabilizing influence of rotation, that impedes vertical fluctuations [27].

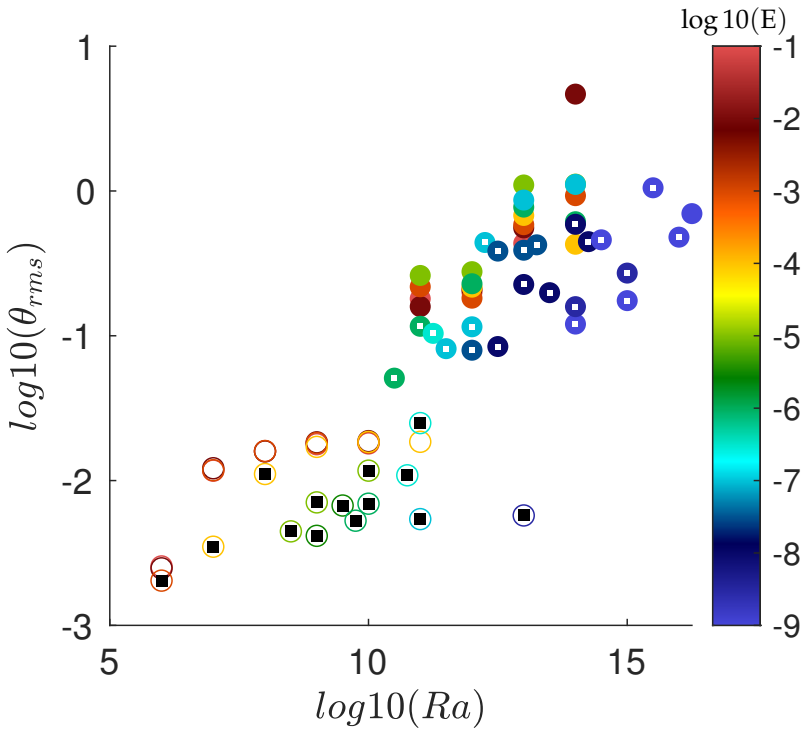

Figure 10. Temperature fluctuations $\theta_{rms} = \sqrt{< \theta^2 >}$ vs Rayleigh number Ra in 3D for Pr $= 0.7$ for simulations of rotating HRB simulations on log-lattice. The symbols are colored according to their Ekman number E. The open symbols trace the laminar regime, while the filled symbol trace the turbulent regime. The rotation dominated regimes are tagged by a black (respectively white) square for the laminar (respectively turbulent) regime.

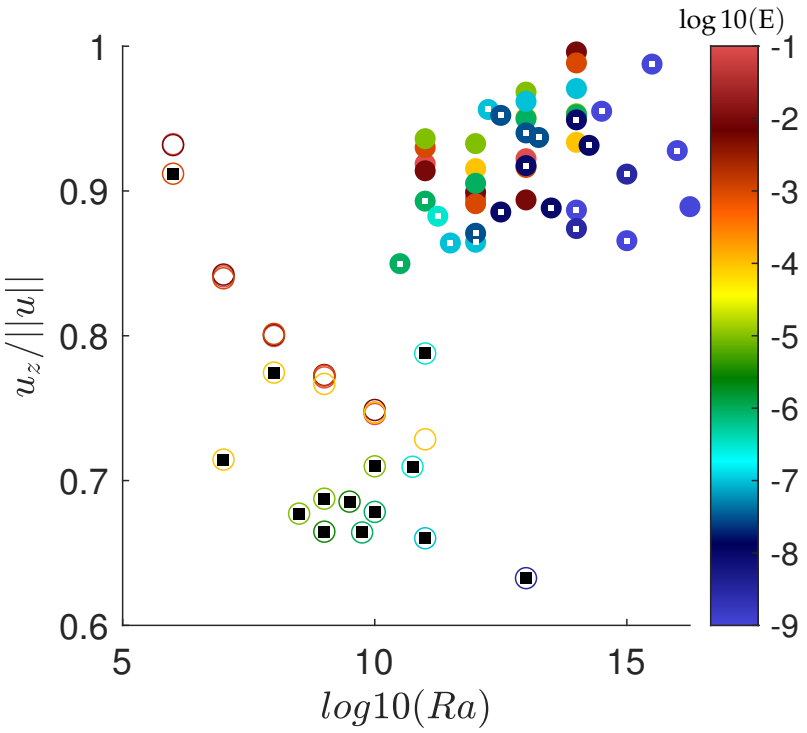

Figure 11. Velocity anisotropy $\sqrt{< u_z^2 >}/\sqrt{< u^2 >}$ vs Rayleigh number Ra in 3D for Pr $= 0.7$ for simulations of rotating HRB simulations on log-lattice. The symbols are colored according to their Ekman number E. The open symbols trace the laminar regime, while the filled symbol trace the turbulent regime. The rotation dominated regimes are tagged by a black (respectively white) square for the laminar (respectively turbulent) regime.

5.3.4. Laminar and turbulent scaling laws and GT regimes

The laminar regime starts from the convection onset. It is therefore likely that it is influenced by near onset dynamics. A natural idea is then to try to see whether it also follows the near-onset scaling law of the non-rotating case, Eq. (22), albeit with Ra_c being replaced by its rotating value $22\,\mathrm{E}^{-4/3}$ and Ra_t being replaced by $B\,\mathrm{E}^{-4/3}$, where the constant B needs to be determined. With this hypothesis, we then find that in the laminar regime, Nu $E^{2/3}$ should be a function of Ra $\mathrm{E}^{4/3}$, where the function satisfies Eq. (22), with $A = 7$, $\mathrm{Ra}_c = 22$ and $\mathrm{Ra}_t = 5 \times 10^2$, see fig. 12. The turbulent regime corresponds to large Reynolds number, in which viscosity and diffusivity should not play a role anymore. It is then natural to represent it in the turbulent variable Nu E and Ra E^2 (where we have omitted the Pr dependence, since it a constant in all our data set), which is done in fig. 13. This representation indeed collapses the data on two different scaling laws: one with exponent $3/2$ for regimes influenced by rotation -this is the GT regime- and one with exponent $1/2$ corresponding to the turbulent regime not influenced by rotation. The precise location in parameter space where the GT regime occurs can be computed using the fit of the vertical Rossby number as a function of Ra E^2, see fig. 9. The condition $\mathrm{Ro}_z < 0.1$ then translates into the condition $\mathrm{Ra} \leq 0.06E^{-2}$, which is the green line reported on fig. 4. The GT regime is then to be found in-between the blue and the green line, which is the region where we concentrate additional numerical simulations.

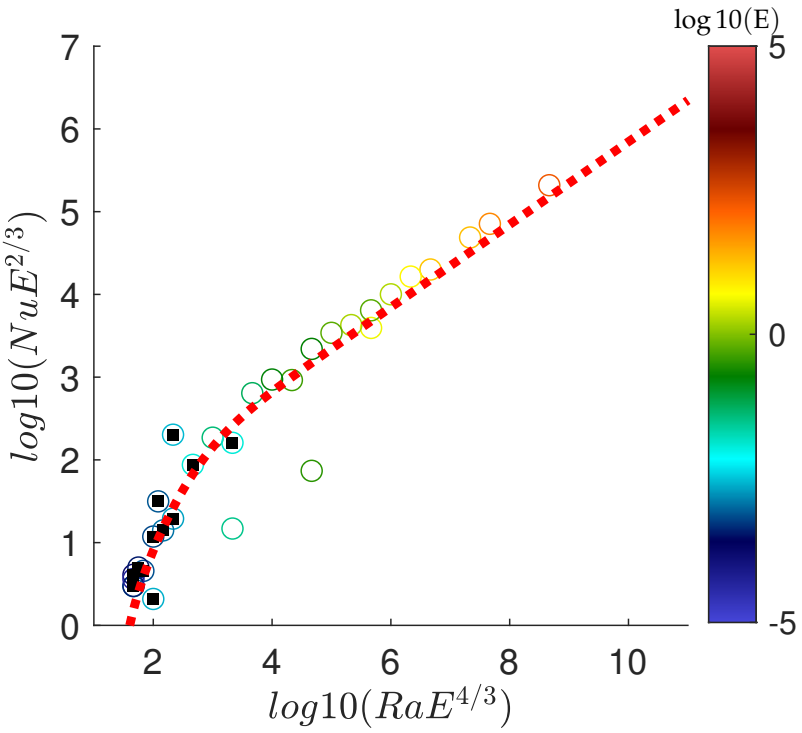

Figure 12. Universal law governing the heat transfer in the laminar regime $\mathrm{Nu}\,\mathrm{E}^{2/3}$ as a function of $\mathrm{Ra}\,\mathrm{E}^{4/3}$ in 3D for $\mathrm{Pr} = 0.7$ for simulations of rotating HRB simulations on log-lattice. The symbols are colored according to their Ekman number E. The open symbols tagged by a black square trace the rotation dominated regime, while the open symbols trace the rotation independent regime. The red dotted line follows Eq. 22, whith $A = 7$, $\mathrm{Ra}_c = 22$ and $\mathrm{Ra}_t = 5 \times 10^2$.

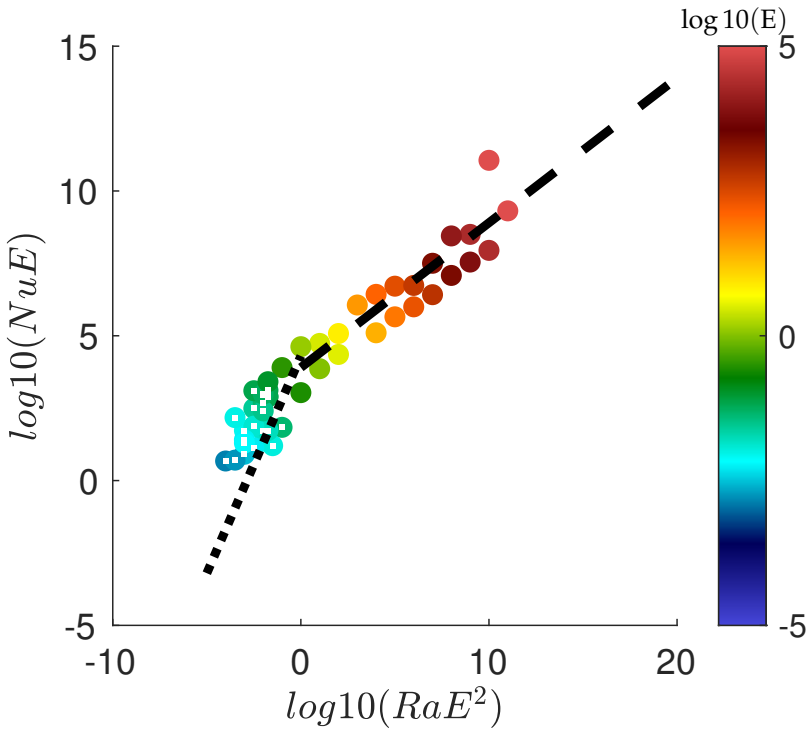

Figure 13. Universal law governing the heat transfer in the turbulent regime Nu E as a function of Ra E^2 in 3D for Pr $= 0.7$ for simulations of rotating HRB simulations on log-lattice. The symbols are colored according to their Ekman number E. The symbols tagged by a white square trace the rotation dominated regime, while the filled symbols trace the rotation independent regime. The black dotted (respectively dashed) line follows the equation $y \sim x^{3/2}$ (respectively $y \sim x^{1/2}$).

6. Discussion

We have shown that projection of geophysical equations of motion allow achieving realistic values of parameters, at a moderate cost. This allows to perform many simulations over a wide range of parameters, thereby leading to general scaling laws of transport efficiency that can then be used to parametrize the turbulent transport in general climate models for Earth or other planets. We have illustrated this process using the equation describing the heat transport in a dry atmosphere, to obtain the scaling laws for onset of convection as a function of rotation, and confirmed the theoretical results $\mathrm{Ra}_c \sim E^{-4/3}$ over a wide range of parameters. We have also demonstrated the existence of two regimes of convection, one laminar extending near the convection onset, and one turbulent, occurring as soon as the vertical Reynolds number reaches a value of 10^4. We have derived general scaling laws for these two regimes, both for transport of heat, dissipation of kinetic energy, and value of the anisotropy and temperature fluctuations. The set-up we have used here is far from reproducing the full complexity of the atmosphere, as it models the friction at the bottom with a simple law, and ignores the moist dynamics. We plan to include these features in a future work. Finally, it is not clear how the projection of the dynamics on log-lattice influences the results we are deriving. It is quite remarkable that the procedure is able to capture the scaling laws, since we recover here some results already obtained in experiments [29] numerical simulations [25] of convection without boundary layers, albeit with different prefactors. This of course has some important implications when translating these scaling laws as parametrization in models. However, if we believe that the scaling laws themselves are robust, it only takes comparison with a few direct numerical simulation to recalibrate the constants and turn our laws into useful parametrization.

Author Contributions: Conceptualization, all authors; methodology, all authors; software, A.B. , G.C; and Q.P.; validation, all authors; formal analysis, B.D.; investigation, Q.P.; resources, A.B.; data curation, all authors; writing—original draft preparation, B.D.; writing—review and editing, all

authors.; visualization, B.D.; supervision, B.D.; project administration, B.D..; funding acquisition, B.D. All authors have read and agreed to the published version of the manuscript.

Funding: This work received funding through the PhD fellowship programs of the Ecole Polytechnique and Ecole Normale Superieure Paris-Saclay, and through the ANR, via the grants ANR TILT grant agreement no. ANR-20-CE30-0035 and ANR BANG grant agreement no. ANR-22-CE30-0025.

Data Availability Statement: Data are available upon request to the author.

Conflicts of Interest: The authors declare no conflict of interest.

References

1. Grant, H.L.; Stewart, R.W.; Moilliet, A. Turbulence spectra from a tidal channel. *Journal of Fluid Mechanics* **1962**, *12*, 241–268. https://doi.org/10.1017/S002211206200018X.
2. Frisch, U. . In *Turbulence, the legacy of A. N. Kolmogorov*; Cambridge University Press, 1996.
3. Dubrulle, B. Beyond Kolmogorov cascades. *Journal of Fluid Mechanics* **2019**, *867*, P1. https://doi.org/10.1017/jfm.2019.98.
4. Herring, J.R. Some Contributions of Two-Point Closure to Turbulence. In Proceedings of the Frontiers in Fluid Mechanics; Davis, S.H.; Lumley, J.L., Eds., Berlin, Heidelberg, 1985; pp. 68–87.
5. Dubrulle, B.; Daviaud, F.; Faranda, D.; Marié, L.; Saint-Michel, B. How many modes are needed to predict climate bifurcations? Lessons from an experiment. *Nonlinear Processes in Geophysics* **2022**, *29*, 17–35. https://doi.org/10.5194/npg-29-17-2022.
6. Campolina, C.S.; Mailybaev, A.A. Fluid dynamics on logarithmic lattices. *Nonlinearity* **2021**, *34*, 4684–4715. https://doi.org/10.1088/1361-6544/abef73.
7. Meneguzzi, M.; Politano, H.; Pouquet, A.; Zolver, M. A Sparse-Mode Spectral Method for the Simulation of Turbulent Flows. *Journal of Computational Physics* **1996**, *123*, 32–44. https://doi.org/https://doi.org/10.1006/jcph.1996.0003.
8. Grossmann, S.; Lohse, D.; L'vov, V.; Procaccia, I. Finite size corrections to scaling in high Reynolds number turbulence. *Phys. Rev. Lett.* **1994**, *73*, 432–435. https://doi.org/10.1103/PhysRevLett.73.432.
9. Frisch, U.; Pomyalov, A.; Procaccia, I.; Ray, S.S. Turbulence in Noninteger Dimensions by Fractal Fourier Decimation. *Phys. Rev. Lett.* **2012**, *108*, 074501. https://doi.org/10.1103/PhysRevLett.108.074501.
10. Lanotte, A.S.; Benzi, R.; Malapaka, S.K.; Toschi, F.; Biferale, L. Turbulence on a Fractal Fourier Set. *Phys. Rev. Lett.* **2015**, *115*, 264502. https://doi.org/10.1103/PhysRevLett.115.264502.
11. Barral, A.; Dubrulle, B. Asymptotic ultimate regime of homogeneous Rayleigh-Bénard convection on logarithmic lattices. *Journal of Fluid Mechanics* **2023**, *962*, A2. https://doi.org/10.1017/jfm.2023.204.
12. Pikeroen, Quentinand Costa, G.; Barral, A.; Dubrulle, B. Tracking complex singularities of fluids on log-lattices. *Nonlinearity* **2023**, *submitted*.
13. Laval, J.P.; Dubrulle, B.; Nazarenko, S. Nonlocality and intermittency in three-dimensional turbulence. *Physics of Fluids* **2001**, *13*, 1995–2012, [https://pubs.aip.org/aip/pof/article-pdf/13/7/1995/12739203/1995_1_online.pdf]. https://doi.org/10.1063/1.1373686.
14. Costa, G.; Barral, A.; Dubrulle, B. Reversible Navier-Stokes equation on logarithmic lattices. *Phys. Rev. E* **2023**, *107*, 065106. https://doi.org/10.1103/PhysRevE.107.065106.
15. Campolina, C.S. Fluid dynamics on logarithmic lattices. PhD thesis, IMPA, 2022.
16. Calzavarini, E.; Lohse, D.; Toschi, F.; Tripiccione, R. Rayleigh and Prandtl number scaling in the bulk of Rayleigh-Bénard turbulence. *Physics of Fluids* **2005**, *17*, 055107, [https://doi.org/10.1063/1.1884165]. https://doi.org/10.1063/1.1884165.
17. Calzavarini, E.; Doering, C.R.; Gibbon, J.D.; Lohse, D.; Tanabe, A.; Toschi, F. Exponentially growing solutions in homogeneous Rayleigh-Bénard convection. *Phys. Rev. E* **2006**, *73*, 035301. https://doi.org/10.1103/PhysRevE.73.035301.
18. Calzavarini, E.; Lohse, D.; Toschi, F. Homogeneous Rayleigh-Bénard Convection. In Proceedings of the Progress in Turbulence II; Oberlack, M.; Khujadze, G.; Günther, S.; Weller, T.; Frewer, M.; Peinke, J.; Barth, S., Eds., Berlin, Heidelberg, 2007; pp. 181–184.
19. Chandrasekhar, S. *Hydrodynamic and hydromagnetic stability*; Courier Corporation, 2013.
20. Spiegel, E.A. A Generalization of the Mixing-Length Theory of Turbulent Convection. *The Astrophysical Journal* **1963**, *138*, 216.
21. Kraichnan, R.H. Turbulent Thermal Convection at Arbitrary Prandtl Number. *The Physics of Fluids* **1962**, *5*, 1374–1389, [https://aip.scitation.org/doi/pdf/10.1063/1.1706533]. https://doi.org/10.1063/1.1706533.
22. Grossmann, S.; Lohse, D. Scaling in thermal convection: a unifying theory. *Journal of Fluid Mechanics* **2000**, *407*, 27–56. https://doi.org/10.1017/S0022112099007545.
23. Ecke, R.E.; Shishkina, O. Turbulent Rotating Rayleigh–Bénard Convection. *Annual Review of Fluid Mechanics* **2023**, *55*, 603–638, [https://doi.org/10.1146/annurev-fluid-120720-020446]. https://doi.org/10.1146/annurev-fluid-120720-020446.
24. Cheng, J.S.; Stellmach, S.; Ribeiro, A.; Grannan, A.; King, E.M.; Aurnou, J.M. Laboratory-numerical models of rapidly rotating convection in planetary cores. *Geophysical Journal International* **2015**, *201*, 1–17, [https://academic.oup.com/gji/article-pdf/201/1/1/2149282/ggu480.pdf]. https://doi.org/10.1093/gji/ggu480.
25. Plumley, M.; Julien, K. Scaling Laws in Rayleigh-Bénard Convection. *Earth and Space Science* **2019**, *6*, 1580–1592, [https://agupubs.onlinelibrary.wiley.com/doi/pdf/10.1029/2019EA000583]. https://doi.org/https://doi.org/10.1029/2019EA000583.

26. Iyer, K.P.; Scheel, J.D.; Schumacher, J.; Sreenivasan, K.R. Classical 1/3 scaling of convection holds up to Ra = 10¹⁵. *Proceedings of the National Academy of Sciences* **2020**, *117*, 7594–7598, [https://www.pnas.org/doi/pdf/10.1073/pnas.1922794117]. https://doi.org/10.1073/pnas.1922794117.
27. Dubrulle, B.; Valdettaro, L. Consequences of rotation in energetics of accretion disks. *Astronomy and Astrophysics* **1992**, *263*, 387–400.
28. Campagne, A.; Machicoane, N.; Gallet, B.; Cortet, P.P.; Moisy, F. Turbulent drag in a rotating frame. *Journal of Fluid Mechanics* **2016**, *794*, R5. https://doi.org/10.1017/jfm.2016.214.
29. Bouillaut, V.; Miquel, B.; Julien, K.; Aumaître, S.; Gallet, B. Experimental observation of the geostrophic turbulence regime of rapidly rotating convection. *Proceedings of the National Academy of Sciences* **2021**, *118*, e2105015118, [https://www.pnas.org/doi/pdf/10.1073/ https://doi.org/10.1073/pnas.2105015118.

9 - Conclusions and perspectives

In this PhD, through the use of Log-lattices, a new framework developped by Campolina & Mailybaev, we studied various properties of turbulence.

9.1 . Technical aspects of Log-lattices

Due to the recent nature of LL, some properties fall in the category of *technical aspects*. This has to be understood as "Can LL reproduces this feature of real flows?".

Throughout our journey, we investigated the presence of intermittent features in Log-lattices. Through a 1D comparison with the SABRA shell model, we showed that n-D LL, with $\lambda = \phi$, share the same characteristics that lead to intermittency in both the SABRA and GOY model. In addition, we extracted 1D structure functions exponents highlighting deviation from the Kolmogorov scaling and therefore, intermittency on LL. The real challenge lies in the extension of those results in upper dimensions as n-D LL ($n > 1$) can be understood as a collection of weakly coupled shellmodels. Therefore, the naive approach of summing the contribution of every mode lying in a shell leads to an averaging effect that effectively kills the strong fluctuations. It is then necessary to wisely choose the definition of the structure functions in order to avoid excessive averaging. Unfortunately, due to time constraint, this part of the work is left for the hopefully near future as it is still an on-going piece of work.

To make full use of the available resolution that offers LL, we used the analiticity-strip method to track the position of singularities, in the complex plane, of the flow. This method relies on the fitting of the exponential dissipation of the energy spectrum. Yet, it is known that shellmodels exhibit exponential stretching in the dissipative range, impeding the proper fitting of the dissipation. Through a numerical analysis, we showed that unlike shellmodels, LL presents an exponential dissipation without stretching. However, due to the high available resolutions, one has to be careful as to only fit *well-resolved modes* (according to CFL conditions) in order to obtain meaningful results. We successfully derived a fitting procedure, able to fit the whole spectrum including both the inertial and dissipative domains. By doing so, we highlighted the presence of small bottleneck effects, aggravated by the use of hyperviscosity that slightly change the shape of the energy spectrum in the transition range between the two previously mentioned domains. This result is interesting as it allows for a better extraction of exponents in the context of intermittency. Indeed, a complete fitting of the structure functions leads to a more accurate value of the slopes, getting rid of the possible yet small effects of the exponential dissipation.

9.2 . Log-lattices as a tool for mathematicians

The development of this fitting procedure and the huge available resolutions that LL offers allows for the study of singularities through the fitting of the dissipative range. This method, developed by Frisch & Morf, was first performed on DNS but quickly abandonned

due to the lack of resolution, impeding the good estimation of the δ prefactor in the exponential decay. Resolution no-longer being a problem on LL, we extracted the values of δ in various scenarios, highlighting the development of blowup solutions as $\delta \to 0$ in both inviscid 1D Burgers equation and inviscid 3D Navier-Stokes. The addition of a viscous dissipation repels the singularity, preventing the collapse of the singularity onto the real axis therefore preventing the formation of blowup solutions. Yet, we showed that for hypodissipative processes with exponent $\gamma < 1/3$, the dissipation is no longer strong enough to repel the singularity and viscous blowups start to develop. This study highlights the possibilities that offers LL for the study of singularities and more generally of phenomena requiring higher resolutions than the current DNS.

9.3 . Log-lattices as a tool for physicists

The other part of this PhD focuses on applying LL to the study of various phenomena. As mentioned before, we investigated the link between the development of singularities in the flow and blowup scenarios in 1D Burgers equation and 3D Navier-Stokes. We showed that the addition of viscosity prevents the development of blowups by repelling the singularity. However, in the case of hypoviscous dissipation, for $\gamma < 1/3$, the dissipative process is no longer able to repel the singularity and blowups can be observed.

This work led us to wonder if singularities and blowups could be observed in presence of a forcing term. To answer this question, we built, following the work of Gallavotti, a Reversible Navier-Stokes equation, that conserves the total kinetic energy through a time dependent viscosity. By doing so, we obtain a time reversible system that conserves energy even in presence of a forcing term. We showed that this system exhibits two phases, as previously highlighted in small DNS, one unstable and one stable. In the former, performing RNSE simulations with adaptative grid size leads to the formation of blowups in finite time with exponents that differ from the usual Euler blowup. We showed that these new exponents actually depend on the efficiency $\mathcal{E}$, ratio of the stored kinetic energy over the mechanical injected energy. Such construction allows for the observation of energy spectra with exponents h ranging from 0 to $1/3$, $1/3$ being the usual NSE exponent, predicted by KG41. The use of LL allowed to make some preliminary assumptions about the link between NSE and Euler through a whole range of unstable solutions, stabilized through a stochastic procedure. We expect to observe the same trend using the same procedure in DNS, at smaller resolutions.

The existence of unstable solutions leads to an instability associated to two attractors between which the system can oscillate. Upon defining the two attractors using the previously mentioned δ, we showed that there seems to exist a critical efficiency $\mathcal{E}^*$ above which the system never departs from the *warm state* (introduced by Shukla et.al), characterized by a null value of δ. The existence of this critical efficiency and the shape of $\langle\delta\rangle$ led us to investigate this transition using the framework of phase transitions, highlighting the existence, in the limit of infinite grid size, of a Landau mean field second order phase transition.

Finally, we investigated the conjecture of Gallavotti, stating an equivalence of ensemble between Navier-Stokes equations and its reversible counterpart. The conjecture holds true in the both phases, up to a certain threshold depending on $\mathcal{R}_\mathrm{r}$. Therefore, one can

obtain interesting informations about NS using its time reversible counterpart, on which usual statistical mechanics can be applied. To illustrate this property, we succesfully applied the Gallavotti-Cohen fluctuation dissipation theorem to RNS simulations extracting values of σ. Although σ usually (in the GCFT) refers to the phase contraction rate, it is still interesting to try to link it to other physical quantities of interest such as energy dissipation, temperature... Yet, further study is needed to better establish and understand this link. In addition, the GCFT was also successfully applied to NSE simulations, in presence of truncature effects, it is still unclear if these results extend to fully resolved NSE.

The last part of this thesis concerns the application of LL to atmospheric flows, highlighting the possibilities that Log-lattices offer in the context of geophysics, where resolution is extremely important.

9.4 . Perspectives

Due to time constraint, some of my work is left unfinished. The investigation of intermittency on n-D ($n > 1$) LL is still on-going as one must properly define the structure functions in order to avoid averaging effects over non-correlated modes. In addition, I will pursue my work on the GCFT theorem, more specifically on the link between σ and other quantities. As only a small part of my work is currently published, I will also focus on writting several articles on the topics presented in this PhD.

The framework being still new, the investigation of its limitations and of the fields to which it could be applied is still on going. During this¨PhD, Log-lattices prooved to be a powerful tool to study the Reversible Navier-Stokes equation but also atmospheric flows. In addition, in his PhD, Amaury Barral showed that thanks to their huge resolutions, Log-lattices also allow for the study of the ultimate regime in homogenous Reyleigh-Bénard (55; 56). Furthermore, some other properties and flaws of the model were studied highlighting the absence of Rossby wave resonance.

It is important to note that Log-lattices are a class of statistical models that shares similarities with 1D shellmodels meaning that there might not be an exact correspondance between the observations made in LL and in DNS. Still, it appears as a remarkable tool to study properties, yet out of reach of current DNS, that might motivate further studies using other modeling methods.

Bibliography

[1] Giovanni Gallavotti. Equivalence of dynamical ensembles and navier-stokes equations. *Physics Letters A*, 223(1-2):91–95, 1996.

[2] Lars Onsager. Statistical hydrodynamics. *Il Nuovo Cimento (1943-1954)*, 6(2):279–287, 1949.

[3] U Frisch. On the singularity structure of fully developed turbulence. *Turbulence and predictability in geophysical fluid dynamics and climate dynamics*, 1985.

[4] P. Debue, V. Shukla, D. Kuzzay, D. Faranda, E.-W. Saw, F. Daviaud, and B. Dubrulle. Dissipation, intermittency, and singularities in incompressible turbulent flows. *Phys. Rev. E*, 97:053101, May 2018.

[5] Massimo De Pietro, Luca Biferale, Guido Boffetta, and Massimo Cencini. Time irreversibility in reversible shell models of turbulence. *The European Physical Journal E*, 41(4):1–12, 2018.

[6] P. Kestener and A. Arneodo. Generalizing the wavelet-based multifractal formalism to random vector fields: application to three-dimensional turbulence velocity and vorticity data. *Phys. Rev. Lett.*, 93(4):044501, 2004.

[7] J. F. Muzy, E. Bacry, and A. Arneodo. Wavelets and multifractal formalism for singular signals: Application to turbulence data. *Phys. Rev. Lett.*, 67(25):3515, 1991.

[8] H. Faller, D. Geneste, T. Chaabo, A. Cheminet, V. Valori, Y. Ostovan, L. Cappanera, Ch. Cuvier, F. Daviaud, J.-M. Foucaut, and et al. On the nature of intermittency in a turbulent von karman flow. *Journal of Fluid Mechanics*, 914:A2, 2021.

[9] Hugues Faller. *Dissipation, cascade et singularités en turbulence*. PhD thesis, Université Paris-Saclay, 2022.

[10] E.-W. Saw, P. Debue, D. Kuzzay, F. Daviaud, and B. Dubrulle. On the universality of anomalous scaling exponents of structure functions in turbulent flows. *J. Fluid Mech.*, 837:657–669, 2018.

[11] Uriel Frisch and Rudolf Morf. Intermittency in nonlinear dynamics and singularities at complex times. *Phys. Rev. A*, 23:2673–2705, May 1981.

[12] Tristan Buckmaster, Camillo De Lellis, László Székelyhidi Jr, and Vlad Vicol. Onsager's conjecture for admissible weak solutions. *arXiv preprint arXiv:1701.08678*, 2017.

[13] Ciro S Campolina and Alexei A Mailybaev. Chaotic blowup in the 3d incompressible euler equations on a logarithmic lattice. *Physical review letters*, 121(6):064501, 2018.

[14] Michio Yamada and Koji Ohkitani. Lyapunov spectrum of a chaotic model of three-dimensional turbulence. *Journal of the Physical Society of Japan*, 56(12):4210–4213, 1987.

[15] V. S. L'vov, E. Podivilov, A. Pomyalov, I. Procaccia, and D. Vandembroucq. Improved shell model of turbulence. *Phys. Rev. E*, 58(2):1811, 1998.

[16] V. N. Desnyansky and E. A. Novikov. The evolution of turbulence spectra to the similarity regime. *Izv. Akad. Nauk SSSR, Fiz. Atmos. Okeana*, 10:127–136, 1974.

[17] Luca Biferale. Shell models of energy cascade in turbulence. *Annual review of fluid mechanics*, 35(1):441–468, 2003.

[18] Peter Constantin, Boris Levant, and Edriss S Titi. Analytic study of shell models of turbulence. *Physica D: Nonlinear Phenomena*, 219(2):120–141, 2006.

[19] PD Ditlevsen. Symmetries, invariants, and cascades in a shell model of turbulence. *Physical Review E*, 62(1):484, 2000.

[20] Vishwanath Shukla, Bérengère Dubrulle, Sergey Nazarenko, Giorgio Krstulovic, and Simon Thalabard. Phase transition in time-reversible navier-stokes equations. *Physical Review E*, 100(4):043104, 2019.

[21] Ciro S Campolina and Alexei A Mailybaev. Fluid dynamics on logarithmic lattices. *Nonlinearity*, 34(7):4684, 2021.

[22] CS Campolina. Fluid dynamics on logarithmic lattices and singularities of euler flow. Master's thesis, IMPA, 2019.

[23] G. L. Eyink. Turbulence Theory. http://www.ams.jhu.edu/ eyink/Turbulence/notes/, 2007-2008. course notes, The Johns Hopkins University,.

[24] Q.Pikeroen, A.Barral, G.Costa, C.Campolina, A.Mailybaev, and B.Dubrulle. Tracking complex singularities of fluids on log-lattices. *to be published*, 2023.

[25] Miguel D. Bustamante and Marc Brachet. Interplay between the beale-kato-majda theorem and the analyticity-strip method to investigate numerically the incompressible euler singularity problem. *Phys. Rev. E*, 86:066302, Dec 2012.

[26] Dmytro Bandak, Nigel Goldenfeld, Alexei A Mailybaev, and Gregory Eyink. Dissipation-range fluid turbulence and thermal noise. *Physical Review E*, 105(6):065113, 2022.

[27] Richard Courant, Kurt Friedrichs, and Hans Lewy. Über die partiellen differenzengleichungen der mathematischen physik. *Mathematische annalen*, 100(1):32–74, 1928.

[28] Rahul Agrawal, Alexandros Alexakis, Marc E Brachet, and Laurette S Tuckerman. Turbulent cascade, bottleneck, and thermalized spectrum in hyperviscous flows. *Physical Review Fluids*, 5(2):024601, 2020.

[29] Uriel Frisch. *Turbulence: the legacy of AN Kolmogorov*. Cambridge university press, 1995.

[30] Andrei Nikolaevich Kolmogorov. Dissipation of energy in the locally isotropic turbulence. *Proceedings of the Royal Society of London. Series A: Mathematical and Physical Sciences*, 434(1890):15–17, 1991.

[31] F Anselmet, Yl Gagne, EJ Hopfinger, and RA Antonia. High-order velocity structure functions in turbulent shear flows. *Journal of Fluid Mechanics*, 140:63–89, 1984.

[32] Bérengère Dubrulle. Beyond kolmogorov cascades. *Journal of Fluid Mechanics*, 867, 2019.

[33] MH Jensen, G Paladin, and A Vulpiani. Intermittency in a cascade model for three-dimensional turbulence. *Physical Review A*, 43(2):798, 1991.

[34] Uriel Frisch and Giorgio Parisi. Fully developed turbulence and intermittency. *New York Academy of Sciences, Annals*, 357:359–367, 1980.

[35] Roberto Benzi and Luca Biferale. Fully developed turbulence and the multifractal conjecture. *Journal of Statistical Physics*, 135(5):977–990, Jun 2009.

[36] L Biferale, A Lambert, R Lima, and G Paladin. Transition to chaos in a shell model of turbulence. *Physica D: Nonlinear Phenomena*, 80(1-2):105–119, 1995.

[37] Guillaume Costa, Amaury Barral, and Bérengère Dubrulle. Reversible navier-stokes equation on logarithmic lattices. *Physical Review E*, 107(6):065106, 2023.

[38] Peter Constantin. On the euler equations of incompressible fluids. *Bulletin of the American Mathematical Society*, 44(4):603–621, 2007.

[39] Alexei A Mailybaev. Spontaneous stochasticity of velocity in turbulence models. *Multiscale Modeling & Simulation*, 14(1):96–112, 2016.

[40] Philip Isett. A proof of Onsager's conjecture. *Annals of Mathematics*, 188(3):871 – 963, 2018.

[41] Alexandros Alexakis and Marc-Etienne Brachet. Energy fluxes in quasi-equilibrium flows. *Journal of Fluid Mechanics*, 884:A33, 2020.

[42] Colm Connaughton and Sergey Nazarenko. Warm cascades and anomalous scaling in a diffusion model of turbulence. *Physical review letters*, 92(4):044501, 2004.

[43] László Székelyhidi. Weak solutions to the incompressible euler equations with vortex sheet initial data. *Comptes Rendus Mathematique*, 349(19):1063–1066, 2011.

[44] Giorgio Krstulovic and Marc-Étienne Brachet. Two-fluid model of the truncated euler equations. *Physica D: Nonlinear Phenomena*, 237(14-17):2015–2019, 2008.

[45] Tomas Bohr, Mogens H Jensen, Giovanni Paladin, and Angelo Vulpiani. *Dynamical systems approach to turbulence*. 1998.

[46] R Benzi, S Ciliberto, Raffaele Tripiccione, C Baudet, F Massaioli, and S Succi. Extended self-similarity in turbulent flows. *Physical review E*, 48(1):R29, 1993.

[47] Giovanni Gallavotti. Ensembles, turbulence and fluctuation theorem. *The European Physical Journal E*, 43:1–10, 2020.

[48] Georgios Margazoglou, Luca Biferale, Massimo Cencini, Giovanni Gallavotti, and Valerio Lucarini. Non-equilibrium ensembles for the 3d navier-stokes equations. *arXiv preprint arXiv:2201.00530*, 2022.

[49] Giovanni Gallavotti. Finite thermostats in classical and quantum nonequilibrium. *The European Physical Journal Special Topics*, 227(3-4):217–229, 2018.

[50] Giovanni Gallavotti and Ezechiel Godert David Cohen. Dynamical ensembles in stationary states. *Journal of Statistical Physics*, 80:931–970, 1995.

[51] Ya G Sinai. Lectures in ergodic theory. *Lecture notes in Mathematics. Princeton University Press, Princeton*, 4:1121–1131, 1977.

[52] Giovanni Gallavotti. Srb distribution for anosov maps. In *Chaotic Dynamics and Transport in Classical and Quantum Systems: Proceedings of the NATO Advanced Study Institute on International Summer School on Chaotic Dynamics and Transport in Classical and Quantum Systems Cargèse, Corsica 18–30 August 2003*, pages 87–105. Springer, 2005.

[53] Sergio Ciliberto, Nicolas Garnier, S Hernandez, Cédrick Lacpatia, J-F Pinton, and G Ruiz Chavarria. Experimental test of the gallavotti–cohen fluctuation theorem in turbulent flows. *Physica A: Statistical Mechanics and its Applications*, 340(1-3):240–250, 2004.

[54] Klebert Feitosa and Narayanan Menon. Fluidized granular medium as an instance of the fluctuation theorem. *Physical review letters*, 92(16):164301, 2004.

[55] Amaury Barral and Berengere Dubrulle. Asymptotic ultimate regime of homogeneous rayleigh–bénard convection on logarithmic lattices. *Journal of Fluid Mechanics*, 962:A2, 2023.

[56] Amaury Barral. *A numerical framework for geophysical flows on logarithmic lattices*. PhD thesis, Université Paris-Saclay, 2023.

10 - Synthèse en français

Introduction

La dynamique des fluides simples est décrite par l'équation de Navier-Stokes:

$$\begin{aligned} \partial_t \boldsymbol{u} + (\boldsymbol{u} \cdot \boldsymbol{\nabla})\boldsymbol{u} &= -\boldsymbol{\nabla} p + \nu \boldsymbol{\Delta} \boldsymbol{u}, \\ \nabla \cdot \boldsymbol{u} &= 0. \end{aligned}$$

En l'absence de viscosité, appelée ν, le système est réversible dans le temps car il est laissé invariant par la transformation $\mathcal{T} : t \to -t; \boldsymbol{u} \to -\boldsymbol{u}$. L'ajout de la viscosité entraîne une dissipation d'énergie au travers du terme $\nu \Delta \boldsymbol{u}$. Il s'ensuit que l'équation n'est plus laissée invariante par la transformation $\mathcal{T}$. La dynamique des fluides visqueux est alors intrinsèquement irréversible, en raison de la présence d'une viscosité constante ν qui brise la symétrie temporelle. Les écoulements turbulents sont donc intrinsèquement des systèmes *hors équilibres*, un domaine d'étude plutôt nouveau. De ce fait, ils ne peuvent donc pas être étudiés avec précision en utilisant la plupart des principes physiques bien connus, ceux-ci ne s'appliquant qu'aux systèmes *à l'équilibres*.

Afin de remédier à ce problème, Gallavotti (1) a introduit une version réversible des équations de Navier-Stokes, appelée RNSE, rétablissant la symétrie temporelle $\mathcal{T} : t \to -t; \boldsymbol{u} \to -\boldsymbol{u}$, au travers de la conservation de l'enstrophie totale obtenue par le biais d'une viscosité dépendante du temps $\nu_r(t)$. Du fait de la restauration de la réversibilité temporelle, il est alors possible d'étudier cette nouvelle équation avec les outils usuels de la mécanique statistique. Un point fondamental de cette équation réside dans la conjecture de Gallavotti (1). Cette dernière affirme que les équations RNS et NS seraient, sous certaines conditions, statistiquement équivalentes. Cette conjecture est très importante car les propriétés statistiques de l'équation RNS, trouvées à l'aide de nos outils habituels, pourraient être transposées à l'équation de Navier-Stokes, là où ces mêmes outils ne fonctionnent plus. Plus précisément, cette conjecture et l'utilisation de l'équation réversible pourraient éclairer un phénomène déroutant connu sous le nom de *dissipation anormale*. Ce phénomène fait référence au comportement de la dissipation d'énergie ϵ des fluides dans la limite des grands nombres de Reynolds. Un simple coup d'œil à l'Eq. 1 indique une dissipation d'énergie ϵ proportionnelle à la viscosité ν. Cependant, cette propriété n'est valable que dans le régime laminaire (c'est-à-dire aux nombres de Reynolds modérés), alors qu'en atteignant la limite turbulente (c'est-à-dire les nombres de Reynolds élevés), la dissipation atteint un plateau et devient indépendante de la viscosité. Ce scénario suggère une rupture spontanée de la symétrie par renversement du temps qui pourrait être étudiée par le biais de l'équation réversible.

L'existence d'une dissipation dans la limite turbulente fait référence à la conjecture d'Onsager, selon laquelle les solutions de l'équation de Navier-Stokes, non visqueuses, suffisamment irrégulières pourraient dissiper de l'énergie même en l'absence de viscosité (2). Contrairement à son équivalent visqueux, l'effet dissipatif des singularités est supposé se produire au travers de "bursts" de dissipation, un phénomène appelé *intermittence*. Une caractérisation empirique de ces solutions dissipatives peut être obtenue grâce à la théorie multifractale (3). Cette théorie permet de mesurer la probabilité d'apparition

d'une singularité avec un exposant donné, caractérisant la façon dont les gradients de vitesse divergent dans la limite inviscide. Les résultats des données expérimentales et numériques (4; 5; 6; 7; 8) révèlent un large intervalle d'exposants possibles (Fig. 10.1 $C(h) = 3 - D(h)$, où $D(h)$ est la dimension de l'ensemble fractal dans la théorie multifractale), avec une probabilité maximale pour la valeur de Kolmogorov $1/3$, et avec des valeurs correspondant à des solutions faibles dissipatives ($h < 1/3$) ou non-dissipatives ($h > 1/3$) des équations d'Euler.

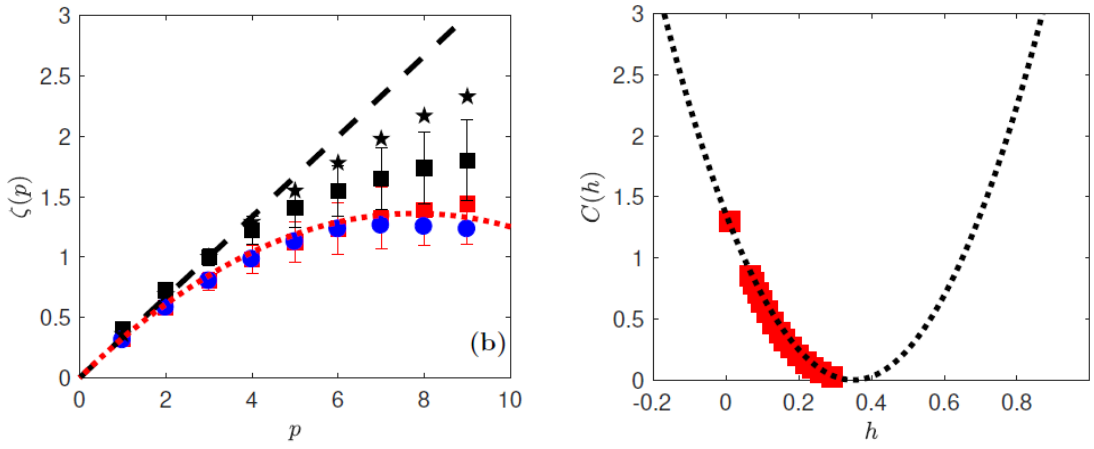

(a) (b)

Figure 10.1: **Déviations de KG41 et théorie multifractale, résultats extraits de la thèse de Hugues Faller (9).** (1a) Exposants des fonctions de structure. Les cercles bleus correspondent à des simulations numériques tandis que les carrés rouges sont associés à des données expérimentales. Les résultats sont obtenus sur des transformées en ondelettes pour lesquelles $\zeta(3) \neq 1$. Les carrés noirs correspondent donc à la mise à l'échelle $\zeta(p)/\zeta(3)$ des carrés rouges. Les étoiles noires correspondent à la mise à l'échelle des résultats expérimentaux de (10). (1b) Spectre multifractale des données expérimentales de la Fig. 1a. $C(h)$ est obtenu par une transformée de Legendre inverse de $\zeta(p)$ et correspond à $3 - D(h)$, où $D(h)$ est la dimension fractale de l'ensemble fractal associé à h.

En 1981, Frisch et Morf (11) ont proposé une méthode de suivi des singularités complexes basée sur l'ajustement de la décroissance exponentielle du spectre d'énergie. Grâce à l'étude d'un système de Langevin non linéaire à 1D, ils ont mis en lumière le lien possible entre l'intermittence et l'effondrement des singularités complexes sur l'axe réel générant des "bursts" de dissipation. Malgré leurs diverses manifestations, l'observation des singularités reste un véritable défi, tant dans les expériences que dans les simulations numériques, en raison de la nécessité d'atteindre des nombres de Reynolds extrêmement élevés. En effet, la complexité des DNS étant d'environ $\mathcal{O}(\mathrm{Re}^3)$, approcher la limite turbulente avec les DNS reste, pour l'instant, un exploit impossible car $\mathrm{Re} \to \infty$. Il est alors nécessaire d'écarter les plus petites échelles en introduisant une "coupure" (i.e une résolution maximale) ayant un impact sur la dynamique des singularités (11). Du fait de ces limitations, cette méthode a été abandonnée.

Néanmoins, la *dissipation anormale* et les singularités font toujours l'objet de recherches

actives. En effet, la conjecture d'Onsager a été récemment prouvée par Buckmeister (12), qui a construit des solutions faibles de l'équation d'Euler capables de dissiper une quantité finie d'énergie. Le lien exact entre les solutions réelles de l'équation de Navier-Stokes et cette construction reste cependant à éclaircir.

Dans cette thèse, nous proposons de réaliser des simulations en utilisant *les grilles logarithmiques*, un nouveau modèle développé par Campolina & Mailybaev (13). Son espacement exponentiel des modes, dans l'espace de Fourier, permet la réalisation de simulations à haute résolutions au prix d'une réduction du nombre d'interactions entre les modes. Cette construction rappelle les *shellmodels* (GOY (14), SABRA (15), Desnyansky-Novikov (16)), une classe de modèles 1D utilisant également un espacement exponentiel des modes dans l'espace de Fourier. Ces derniers ont notamment été largement étudiés (15; 17; 18; 19) [1] car, bien qu'à une dimension, ils compensent le manque de résolution des DNS. Cependant, en raison de l'absence de certaines symétries fondamentales (du fait de leur nature 1D inhérente), ils ne parviennent pas à reproduire certaines caractéristiques de l'équation de Navier-Stokes (telle que l'intermittence dans le modèle dyadique). C'est ici que les grilles logarithmiques entrent en jeu, car elles permettent la réalisation de simulations à n-dimensions, avec une équivalence formelle aux shellmodels habituels pour $n = 1$, tout en conservant la plupart des symétries de l'équation de Navier-Stokes. Ces caractéristiques nous permettent d'étudier des propriétés encore hors de portée des DNS actuelles, comme le développement de singularités complexes par la méthode de Frisch & Morf mentionnée précédemment, mais aussi d'étendre diverses études sur l'équation de Navier-Stokes réversible, comme par exemple l'existence d'une transition de phase dans le cas de l'énergie conservée (20) ou la conjecture de Gallavotti (1).

Grilles logarithmiques et détails numériques

Avec le développement rapide des ordinateurs, les simulations sont devenues un outil primordial pour les physiciens afin d'aborder des sujets encore hors de portée des expériences.

Cependant, la manière la plus traditionnelle et la plus directe d'effectuer des simulations est plutôt coûteuse. En effet, les simulations numériques directes (DNS) d'un écoulement simple ont une complexité de l'ordre de $\mathcal{O}(\mathrm{Re}^3)$, rendant fastidieuse la tâche de simuler les plus petites échelles de ce dernier. Afin surmonter les limitations de résolution des DNS, Campolina & Mailybaev (13) ont proposé un nouveau modèle dans lequel l'espace de Fourier est discrétisé selon une progression géométrique $k_n = k_0\lambda^n$. Une telle construction rappelle immédiatement la discrétisation des *shellmodels* (14; 15; 16) permettant des simulations à haute résolution en utilisant un nombre limité de modes. La principale amélioration des grilles logarithmiques réside dans l'extension de ces *shellmodels* à des dimensions plus élevées. Elles permettent donc des simulations d'écoulements 3D à haute résolutions tout en conservant intégralement les symétries du système.

Dans ce chapitre, nous définirons brièvement les grilles logarithmiques et leurs propriétés. De plus, nous introduirons les différentes grandeurs que nous servirons au cours de cette thèse, à savoir le spectre d'énergie $E(k)$, l'enstrophie totale Ω, le transfert d'énergie

[1] Pour n'en citer que quelques-uns

inter-échelles $\Pi(k)$ et bien d'autres... Entre autre, nous introduirons brièvement le schéma numérique utilisé dans nos simulations.

Singularités et blowup

En 1981, Frisch & Morf (11) ont postulé l'existence de singularités complexes dans les solutions des équations de Navier-Stokes. A l'aide d'un système de Langevin non linéaire unidimensionnel simple, ils ont démontré que la dynamique de ces singularités complexes pouvait être directement liée à l'intermittence, car des *bursts* de dissipation se produisent chaque fois qu'une singularité complexe s'approche, dans le plan complexe, de l'axe réel. Le scénario a ensuite été exploré dans l'équation de Burgers unidimensionnelle - un substitut 1D de l'équation de Navier-Stokes. Il a été découvert que des singularités réelles peuvent être observées dans la limite inviscide et se manifester sous forme de chocs, c'est-à-dire de sauts finis dans la vitesse dissipant de l'énergie en accord avec l'anomalie de dissipation (23). L'extension de ces résultats à la 3D représente un véritable défi. En 3D, les singularités d'Euler émergent comme des *blowups*, dont la réalisation pourrait se produire en temps fini, de la vorticité. L'ajout d'une viscosité ν agit comme un répulsif, empêchant les singularités d'atteindre l'axe réel en bloquant la croissance infinie de la vorticité.

Par conséquent, l'observation des singularités nécessite des nombres de Reynolds élevés (c'est-à-dire de faibles viscosités), impliquant des simulations à haute résolutions numériques, car la troncature pourrait affecter la dynamique des singularités (11). Cependant, la puissance de calcul nécessaire à la réalisation de telles DNS est hors de portée des ordinateurs actuels, entravant les progrès dans ce domaine. C'est là que les grilles logarithmiques entrent en jeu. Leur coût numérique modéré, permettant des simulations dont les résolutions dépassent de loin celles des DNS actuelles, couplé à la méthode de l'*analiticity strip*, ouvrent de nouvelles perspectives sur ces questions.

Ce chapitre est décomposé en deux parties, tout d'abord un préambule, illustrant la pertinence de la méthode de l'*analiticity strip* dans le cadre des grilles logarithmiques. En effet, dans certains *shellmodels* (dont les grilles logarithmiques s'inspirent) la dissipation d'énergie n'est pas exactement une exponentielle. Cette caractéristique empêchent ainsi l'application de la méthode de Frisch et Morf. Nous illustrons dans cette sous-partie que les grilles logarithmiques ne sont pas sujettes à ce phénomène et présentent bien une décroissance purement exponentielle de l'énergie, pour les modes bien résolus du point de vue numérique (conditions CFL).

La deuxième partie de ce chapitre consiste en un article, actuellement en révision dans *Non-linearity* (24). Il s'agit d'un travail collaboratif avec d'autres doctorants du groupe et les fondateurs des grilles logarithmiques, à savoir C.Campolina et A.Mailybaev.

Dans cet article nous proposons d'étudier le lien entre *blowups* et singularités en utilisant la méthode de l'*analiticity strip*. Nous traiterons tout d'abord le cas 1D de l'équation de Burgers dans divers scénarios (inviscide, visqueux, hypervisqueux, hypovisqueux) mettant en lumière, l'existence de *blowups* et le développement de singularités dans les cas inviscide et hypovisqueux (pour un facteur d'hypoviscosité $\gamma < 1/3$). Cette même étude sera ensuite étendue en 3 dimensions à l'équation de Navier-Stokes sur grilles logarithmiques, confirmant les observations obtenues à une dimension.

Intermittence sur les grilles logarithmiques

Suite aux résultats du chapitre précédent, indiquant l'existence de *blowup* dans divers scénarios, et donc le développement de singularités complexes se rapprochant de l'axe des réels, nous nous intéressons à l'intermittence, phénomène pouvant naître de la dynamique de ces singularités complexes. Nous discuterons donc de l'intermittence sur les grilles logarithmiques, dans un premier temps d'un point de vue purement statistique puis au travers de l'étude des fonctions de structure.

L'intermittence, dans le contexte de la turbulence, se réfère à l'existence de "burst" (i.e augmentation soudaine) de la vorticité. De tels événements extrêmes, bien que rares, sont considérés comme des causes d'écarts à la théorie de Kolmogorov. Il existe de nombreuses manifestations de l'intermittence dans les écoulements, des "burst" de dissipation à l'existence d'exposants anormaux pour les fonctions structures. D'un point de vue statistique, la rareté d'un événement dépend des queues des densités de probabilité (PDF). En étudiant les statistiques des incréments de vitesse, on observe, en présence d'un écoulement intermittent, des PDFs dont les queues sont plus larges que celle d'une distribution gaussienne. Par conséquent, un ingrédient clé dans l'observation de l'intermittence réside dans l'existence de distributions "fat tail" pour les incréments de vitesse. En effet, les statistiques purement gaussiennes limitent l'existence d'événements extrêmes en termes d'amplitude et d'occurrence et sont donc, à priori, incompatibles avec l'intermittence. Dans cette section, nous étudions l'existence de statistiques non gaussiennes dans les grilles logarithmiques à travers l'existence de corrélateurs non triviaux du quatrième ordre.

Les grilles logarithmiques étant formellement équivalente, en 1D, à certains *shellmodels*, nous analysons le caractère intermittent de ces *shellmodels* avant de traiter le cas de l'intermittence sur des grilles logarithmique à 1D. Fort des résultats obtenus dans les cadres des grilles logarithmiques à une dimension pour $\lambda = \phi$, nous proposons d'étendre l'étude à 3 dimensions et donnons des premières pistes à explorer afin d'approfondir nos connaissances de ce phénomène sur nos grilles.

Conjecture d'Onsager et existence de solutions faibles

Le chapitre deux a révélé l'existence, ou non, de *blowup* dans divers scénarios de l'équation de Navier-Stokes. En cas d'existence, ces derniers se sont tous révélés non dissipatifs, signifiant une conservation de l'énergie totale et donc la présence de singularités non-dissipatives. Cependant, il est bien connus que dans la limite inviscide, la dissipation moyenne d'énergie devient indépendante du Reynolds. Ce phénomène connu sous le nom d'anomalie de dissipation suggère une brisure spontanée de la symétrie par renversement du temps. L'existence d'une telle dissipation, en l'absence de viscosité, fait l'objet d'une conjecture de Onsager (2), suggérant que des solutions irrégulières de l'équation de Navier-Stokes inviscides seraient capables de dissiper de l'énergie en l'absence de viscosité au travers du développement de singularités.

Cette conjecture a récemment été prouvée par Buckmeister (12), qui a construit à l'aide de l'intégration convexe, des solutions faibles de l'équation d'Euler. Ces dernières étant notamment capable de dissiper une faible quantité d'énergie et ce en l'absence de vis-

cosité. Une caractéristique notable étant un spectre d'énergie évoluant selon $E(k) \propto k^{-1-2h}$ avec une infinité de valeur possible pour h dans l'intervalle $]0, 1/3[$. La construction de ces solutions reste toutefois ardue et leurs lien avec la véritable équation d'Euler n'est pas encore parfaitement établi. C'est pourquoi, dans ce chapitre, nous essaierons de construire des solutions faibles à l'aide de simulations plus traditionnelles.

Les *blowups* trouvés lors du chapitre précèdent étant tous non-dissipatifs, nous proposons d'utiliser l'équation de Navier-Stokes Réversible, introduite par Gallavotti (1) en 1996, afin de construire des solutions à énergie constante, et ce même en présence de forçage. Pour se faire, nous rendons la viscosité ν dépendante du temps, de telle façon qu'à chaque instant l'énergie soit conservée. Une viscosité négative impliquera donc une création d'énergie, dans le but de compenser la dissipation associée à une autre mécanisme. Nous mettrons ainsi en lumière l'existence de *blowup* en temps fini pour l'équation d'Euler mais aussi de Navier-Stokes Réversible, et proposons une régularisation stochastique permettant de dépasser le temps de *blowup* t_b.

Instabilité associé à la présence de singularités

Dans ce court chapitre, nous effectuons un bilan des effets des singularités complexes, précédemment étudiés, sur l'équation Navier-Stokes réversible et montrons l'existence d'une potentielle transition de phase dans ce nouveau système en introduisant un nouveau paramètre de contrôle $\mathcal{R}_{\mathrm{r}}$.

Transition de phase dans l'équation de Navier-Stokes Réversible

Suite aux résultats préliminaires obtenus au chapitre précédent, nous proposons d'étudier la potentielle transition de phase du système. Cette étude vise à compléter des premiers résultats obtenus sur des petites DNS (20) à l'aide des grilles logarithmiques. Nous montrerons notamment que le système est sujet à une transition de phase du second ordre dont les exposants dépendent de la résolution. A faible résolution cette dernière est imparfaite et les exposants sont, dans la limite de grande résolution, bien décris par une théorie de champs moyens de Landau. Nos résultats seront confrontés à des résultats obtenus sur des modèles plus simples, notamment le modèle de Leith, un modèle diffusif à une dimension.

En outre, nous mettrons en lumière l'existence de lois universelles, en fonction du paramètre de contrôle $\mathcal{R}_{\mathrm{r}}$, pour les simulations de l'équation de Navier-Stokes et de son équivalent réversible.

Equivalence d'ensemble et statistiques

L'existence de lois universelles, valable pour les deux équations pointe dans le sens de la validité de la conjecture de Gallavotti (1), statuant une équivalence d'ensemble (i.e équivalence statistique) entre les deux modèles. A l'aide des grilles logarithmiques, nous étudions l'équivalence d'ensemble dans les différentes phases précédemment trouvées et confirmons son existence, pour différents modèles de conservation (énergie ou enstrophie conservée). Au cours de cette étude, nous étendons notamment des résultats (48),

obtenus pour l'équation réversible, à enstrophie conservée, dans de petites DNS.

Ayant numériquement démontré la conjecture de Gallavotti (pour nos grilles logarithmiques), nous proposons d'appliquer le théorème de fluctuation dissipation (Gallavotti-Cohen) à notre équation réversible. En appliquant ce théorème aux transferts d'énergie, nous montrons que les statistiques de ces derniers obéissent à la théorie des grandes déviations et qu'il est alors possible d'extraire une densité de probabilité maîtresse, indépendante de l'intervalle de temps. Une première tentative d'application du théorème au cadre irréversible (i.e Navier-Stokes) est présentée.

Autres contributions

Ce chapitre comporte les contributions auxquelles j'ai pu participer avec mes collaborateurs. N'ayant uniquement les grilles logarithmiques comme lien avec mon sujet de thèse, elles consisteront en un chapitre à part.

L'article *Log-lattices for atmospheric flows* montre comment les grilles logarithmiques peuvent être utilisées pour modéliser des fluides dans le contexte de la géophysique notamment dans le cadre d'écoulement atmosphériques nécessitant de très grandes résolutions. Dans le but de démontrer les capacités de ce nouvel outil, l'article se concentre sur l'étude de la convection en rotation, retrouvant des résultats déjà obtenus sur des résolutions plus faibles et apportant, grâce aux grandes résolutions accessibles, de nouveaux résultats.

Conclusion et perspectives

Dans cette thèse, nous avons étudié diverses propriétés de la turbulence à l'aide de grilles logarithmiques, un nouveau modèle de simulations numériques développé par Campolina & Mailybaev.

Point de vue technique

En raison de la nature récente de ces grilles, certaines propriétés relèvent des *aspects techniques*, à comprendre "Les grilles logarithmiques peuvent-elles reproduire cette caractéristique d'un écoulement réel?".

Au cours de cette thèse, nous avons notamment étudié la présence de caractéristiques intermittentes sur les grilles logarithmiques. Grâce à une comparaison 1D avec le modèle SABRA (*shellmodel*), nous avons montré que les grilles logarithmiques à n-D, avec $\lambda = \phi$, partagent les mêmes caractéristiques conduisant à l'intermittence à la fois dans le modèle SABRA et GOY. En outre, nous avons extrait les exposants des fonctions de structure à 1D mettant en évidence la déviation de la prédiction de Kolmogorov et, par conséquent, l'intermittence sur nos grilles. Le véritable défi réside dans l'extension de ces résultats aux dimensions supérieures, car une grille logarithmique à n-D ($n > 1$) peut être considérée comme une collection de *shellmodels* faiblement couplés. Par conséquent, l'approche naïve consistant à sommer la contribution de chaque mode se trouvant dans une *shell* conduit à un effet de moyennage effaçant les fluctuations fortes. Il est donc nécessaire de choisir judicieusement la définition des fonctions de structure afin d'éviter un moyennage excessif. Malheureusement, en raison des contraintes de temps, cette partie du

travail est laissée pour le futur.

Afin d'utiliser pleinement la résolution disponible qu'offre ces grilles, nous avons utilisé la méthode de l'*analiticity strip* pour suivre, dans le temps, la position des singularités, dans le plan complexe, de l'écoulement. Cette méthode repose sur l'ajustement de la dissipation exponentielle du spectre d'énergie. Or, il est connu que les *shellmodels* présentent une dissipation *stretched*, ce qui empêche l'ajustement correct du spectre d'énergie dans la zone dissipative. Grâce à une analyse numérique, nous avons montré que, contrairement aux *shellmodels*, nos grilles présentent une dissipation purement exponentielle. Cependant, en raison de la haute résolution disponible, il faut veiller à n'ajuster que *les modes bien résolus* (selon les conditions CFL) afin d'obtenir des résultats significatifs. Nous avons dérivé avec succès une procédure d'ajustement, capable d'ajuster l'ensemble du spectre, y compris les domaines inertiels et dissipatifs. Ce faisant, nous avons mis en évidence la présence de petits effets de *bottleneck*, aggravés par l'utilisation de l'hyperviscosité, qui modifient légèrement la forme du spectre d'énergie dans la plage de transition entre les deux domaines précédemment mentionnés. Ce résultat est intéressant car il permet une meilleure extraction des exposants dans le contexte de l'intermittence. En effet, un ajustement complet de la fonction de structure conduit à une valeur plus précise de la pente, en se débarrassant des effets possibles de la dissipation exponentielle.

Les grilles logarithmiques pour les mathématiciens

Le développement de cette procédure d'ajustement et les énormes résolutions atteignables permettent l'étude des singularités par l'ajustement de la zone dissipative. Cette méthode, développée par Frisch & Morf, a d'abord été réalisée sur DNS mais a été rapidement abandonnée en raison du manque de résolution, empêchant une bonne estimation du préfacteur δ dans la décroissance exponentielle. La résolution n'étant plus un problème sur les grilles logarithmiques, nous avons extrait les valeurs de δ dans différents scénarios, mettant en évidence le développement de solutions *blowup* lorsque $\delta \to 0$ dans l'équation de Burgers 1D inviscide et dans l'équation d'Euler 3D. L'ajout d'une dissipation visqueuse repousse la singularité, empêchant cette dernière de rejoindre l'axe réel et empêche donc la formation de *blowup*. Cependant, nous avons montré que pour les processus hypodissipatifs avec un exposant $\gamma < 1/3$, la dissipation n'est plus assez forte pour repousser la singularité et des *blowups* visqueux commencent à se développer. Cette étude met en évidence les possibilités qu'offrent les grilles logarithmiques pour l'étude des singularités et plus généralement des phénomènes nécessitant des résolutions plus élevées que les DNS actuelles.

Les grilles logarithmiques pour les physiciens

L'autre partie de ce doctorat se concentre sur l'utilisation des grilles logarithmiques dans le but d'étudier divers phénomènes. Comme mentionné précédemment, nous avons étudié le lien entre le développement de singularités dans les écoulements et les scénarios de *blowup* dans l'équation de Burgers 1D et de Navier-Stokes 3D. Nous avons montré que l'ajout de viscosité empêche le développement du *blowup* en repoussant la singularité. Cependant, dans le cas d'une dissipation hypovisqueuse, pour $\gamma < 1/3$, le processus dissipatif n'est plus capable de repousser la singularité et des *blowups* peuvent être observés.

Ce travail nous a amené à nous demander si les singularités et les *blowups* pouvaient

être observées en présence d'un terme de forçage. Pour répondre à cette question, nous avons construit, en suivant les travaux de Gallavotti, une équation de Navier-Stokes réversible (RNS), conservant l'énergie cinétique totale par le biais d'une viscosité dépendante du temps. Ce faisant, nous obtenons un système réversible, conservant l'énergie en présence d'un terme de forçage. Nous avons montré que ce système présente deux phases, comme précédemment mis en évidence dans de petites DNS, l'une instable et l'autre stable. Dans la première, l'exécution de simulations RNS avec une taille de grille adaptative conduit au développement de *blowups* en temps finis avec des exposants qui diffèrent de ceux observés habituellement pour l'équation d'Euler. Ces exposants dépendent de l'efficacité $\mathcal{E}$, rapport de l'énergie cinétique stockée sur l'énergie mécanique injectée. De telles constructions permettent d'observer des spectres d'énergie avec des exposants h allant de 0 à $1/3$, $1/3$ étant l'exposant usuellement observé pour l'équation de Navier-Stokes, prédit par KG41. L'utilisation de ces grilles a permis d'émettre quelques hypothèses préliminaires sur le lien entre Navier-Stokes et Euler à travers toute une gamme de solutions instables, stabilisées par une procédure stochastique. Nous nous attendons à observer les mêmes tendances en utilisant la même procédure dans les DNS, à des résolutions plus faibles.

L'existence de solutions instables conduit à une instabilité associée à deux attracteurs entre lesquels le système peut osciller. En définissant les deux attracteurs à l'aide des δ mentionnés précédemment, nous avons montré qu'il semble exister une efficacité critique $\mathcal{E}^*$ au-dessus de laquelle le système ne s'éloigne jamais de l'état dit *warm* (Shukla et.al), caractérisé par une valeur nulle de δ. L'existence de cette efficacité critique et la forme de $\langle\delta\rangle$ nous ont conduit à étudier cette transition dans le cadre des transitions de phases, mettant en évidence l'existence d'une transition de phase du second ordre, dont les exposants, dans la limite d'une taille de grille infinie, correspondent à une théorie de champ moyen de Landau.

Enfin, nous avons étudié la conjecture de Gallavotti, énonçant une équivalence d'ensemble entre les équations de Navier-Stokes et les versions réversibles. La conjecture se vérifie dans les différentes phases. Par conséquent, il est possible d'obtenir des informations intéressantes sur l'équation de Navier-Stokes en utilisant la version réversible, sur laquelle les outils de la mécanique statistique peuvent être appliqués. Pour illustrer cette propriété, nous avons appliqué avec succès le théorème de fluctuations-dissipations de Gallavotti-Cohen aux simulations RNS en extrayant les valeurs de σ. Bien que σ se réfère habituellement (dans la GCFT) au taux de contraction de phase, il est toujours intéressant d'essayer de le relier à d'autres quantités physiques d'intérêt telles que la dissipation d'énergie, la température... D'autres études sont encore nécessaires afin d'établir proprement, et mieux comprendre ce lien. En outre, la GCFT a également été appliquée avec succès à des simulations de Navier-Stokes, en présence d'effets de troncature, il n'est cependant pas encore clair si ces résultats s'étendent aux simulations de Navier-Stokes entièrement résolues.

La dernière partie de cette thèse concerne l'application des grilles logarithmiques aux écoulements atmosphériques, mettant en évidence les possibilités qu'offre ce modèle dans le contexte de la géophysique, où la résolution est extrêmement importante.

Perspectives

En raison de contraintes de temps, certains de mes travaux sont restés inachevés. L'étude de l'intermittence à n-D ($n > 1$) sur les grilles logarithmiques est toujours en cours. En effet, il reste encore à définir correctement les fonctions de structure afin d'éviter l'effet de moyennage sur les modes non corrélés. En outre, je poursuivrai mon travail sur le théorème GCFT, plus particulièrement sur le lien entre σ et d'autres quantités. Comme seule une petite partie de mon travail est actuellement publiée, je me concentrerai également sur la rédaction de plusieurs articles sur les sujets présentés dans ce doctorat.

Ce modèle numérique étant encore nouveau, la recherche de ses limites et des domaines auxquels il pourrait être appliqué est encore en cours. Au cours de cette thèse, les grilles logarithmiques se sont révélés être un outil puissant pour étudier l'équation de Navier-Stokes réversible mais aussi les écoulements atmosphériques. De plus, dans sa thèse, Amaury Barral a montré que grâce à leurs énormes résolutions, les *Log-lattices* permettent également l'étude du régime ultime dans l'équation de Rayleigh-Bénard homogène (55; 56). En outre, d'autres propriétés et défauts ont été étudiés, mettant notamment en évidence l'absence de résonance des ondes de Rossby.

Il est important de noter que les grilles logarithmiques constituent une classe de modèles statistiques qui leur est propre et qui présente des similitudes avec les *shellmodels* 1D. Ce qui signifie qu'il pourrait ne pas y avoir de correspondance exacte entre les observations faites sur les *Log-lattices* et dans les DNS. Néanmoins, elles apparaissent comme un outil remarquable pour étudier des propriétés encore hors de portée des DNS actuelles et pourraient motiver des études plus approfondies de certains phénomènes, en utilisant d'autres méthodes de modélisation.